A Measurement of the Weak Charge of the Proton through Parity Violating Electron Scattering using the Qweak Apparatus: A 21% Result

A dissertation presented to

the faculty of

the College of Arts and Sciences of Ohio University

In partial fulfillment

of the requirements for the degree

Doctor of Philosophy

Rakitha S. Beminiwattha

August 2013

This dissertation titled

A Measurement of the Weak Charge of the Proton through Parity Violating Electron Scattering using the Qweak Apparatus: A 21% Result

by

RAKITHA S. BEMINIWATTHA

has been approved for

the Physics and Astronomy Department

and the College of Arts and Sciences by

Julie Roche

Associate Professor of Physics

Robert Frank

Dean of the College of Arts and Sciences

Abstract

BEMINIWATTHA, RAKITHA S., Ph.D., August 2013, Physics

A Measurement of the Weak Charge of the Proton through Parity Violating Electron Scattering using the Qweak Apparatus: A 21% Result (250 pp.)

Director of Dissertation: Julie Roche

After a decade of preparations, the Q_{weak} experiment at Jefferson Lab is making the first direct measurement of the weak charge of the proton, Q_W^p. This quantity is suppressed in the Standard Model making a good candidate for search for new physics beyond the SM at the TeV scale. Operationally, we measure a small (about -0.200 ppm) parity-violating asymmetry in elastic electron-proton scattering in integrating mode while flipping the helicity of the electrons 1000 times per second.

Commissioning took place Fall 2010, and we finished taking data in early summer 2012. This dissertation is based on the data taken on an initial two weeks period (Wien0). It will provide an overview of the Q_{weak} apparatus, description of the data acquisition and analysis software systems, and final analysis and results from the Wien0 data set. The result is a 16% measurement of the parity violating electron-proton ($\vec{e}p$) scattering asymmetry, $A = -0.2788 \pm 0.0348(\text{stat.}) \pm 0.0290(\text{syst.})$ ppm at $Q^2 = 0.0250 \pm 0.0006$ $(\text{GeV})^2$. From this a 21% measurement of the weak charge of the proton, $Q_w^p(\text{msr}) = +0.0952 \pm 0.0155(\text{stat.}) \pm 0.0131(\text{syst.}) \pm 0.0015(\text{theory})$ is extracted. From this a 2% measurement of the weak mixing angle, $\sin^2\hat{\theta}_W(\text{msr}) = +0.2328 \pm 0.0039(\text{stat.}) \pm 0.0033(\text{syst.}) \pm 0.0004(\text{theory})$ and improved constraints on isoscalar/isovector effective coupling constants of the weak neutral hadronic currents are extracted. These results deviate from the Standard Model by one standard deviation. The Wien0 results are a proof of principle of the Q_{weak} data analysis and a highlight of the road ahead for obtaining full results.

Dedicated to my father and mother

Acknowledgments

I would like to start by thanking my advisors Julie Roche and Paul King for mentoring me to reach this far in my career as graduate student. This includes the enormous amount of time they spent on guiding my research work, listening and correcting my research talks, and reading and correcting my academic writings including my dissertation. Especially through countless skype meetings. Without them, I would not have come so far in my research career so thank you Paul and Julie. Next, I should thank David Mack at Jefferson Lab. From the very first time I moved to the laboratory up to now, for the numerous one-to-one meetings at his office trying to explain physics that I have missed on my analysis or guide me to do an analysis, the correct way. I really appreciate amount of time he spent on guiding my dissertation writing to provide best possible suggestions and correcting my not so good English skills.

In my graduate career, I have only spent just two years at my university just so I can finish compulsory courses but that time was very valuable for my research career. I enjoyed the intense discussion held during nuclear physics pizza seminars that helped to grew my interest on nuclear and particle physics. I would like to thank Daniel Phillips and Madappa Prakash for enlightening me about the importance of fundamental nuclear and particle physics during the graduate courses I took with them and during the nuclear physics pizza seminars.

After two years, I have moved across states to Jefferson Lab which have been my home for last four years. At Jefferson Lab, I got the opportunity to work with laboratory staff scientists and faculty members, postdoctoral fellows, and students from many different universities whom are part of the the Qweak collaboration. I would like to thank all the members of the Qweak collaboration for the valuable experience I gained working with such a diverse group of talented scientists. I would like to specially mention Roger Carlini, David Armstrong, Mark Pitt, David Mack, David Gaskell, Kent Paschke, Stephen Wood, Michael Gericke, and Wouter Deconinck

for their valuable guidance during the Qweak experiment. A special thank goes to Jeong Han Lee for all the support given to me.

No physics endeavour is successful without all the valuable contribution from the graduate students and I would like to thank all the graduate students in the Qweak collaboration for their important contributions. I would like to specially mention John Leacock, Katherine Myers, Amrendra Narayan, Scott MacEwan, Emmanouil Kargiantoulakis, Josh Magee, Josh Hoskins, Donald Jones, John Leckey, Josh Hoskins, Nuruzzaman, Wade Duvall, Anna Lee, and Adesh Subedi for all the wonderful experience I had working with all of you. I also have to specially mention all the Wien0 thesis students (25percenters: John Leacock, Katherine Myers, John Leckey, Jie Pan, and PeiQuing Wan) who did an excellent job in data analysis towards finalizing Wien0 results.

I have been so lucky to have my soulmate and wife Buddhini Waidyawansa alongside me in my life and in the research works. We both started our graduate research work with Qweak experiment under same supervisors. I would like to give my gratitude to her for being there for me all the time and for all the important contribution she has made to the Q_{weak} experiment.

I wish to thank my mother and father for all the support given me to pursue a good education. Without their hard work and encouragements to pursue higher education, my journey so far would not have possible. I also want to thank my three wonderful sisters for all the joy and support I keep receiving.

Finally I thank my undergraduate advisors U. Karunasiri and B. S. B. Karunarathne for guiding me to pursue higher education in the USA. On concluding, I would like to thank again my advisors, Roger Carlini, Mark Pitt, Kent Paschke, David Mack, and Juliette Mammei for all the career guidance support given to advance my research career.

Table of Contents

List of Tables

List of Figures

List of Acronyms

CEBAF	Continuous Electron Beam Accelerator Facility
linac	linear accelerator
srf	superconducting radio-frequency
rf	radio-frequency
QE	Quantum Efficiency
HC	Helicity Correlated
BCM	Beam Charge Monitor
S/N	Signal to Noise ratio
ADC	Analog to Digital Conversion
BPM	Beam Position Monitor
LH2	Liquid Hydrogen
ESR	End Station Refrigerator
CHL	Central Helium Liquefier
JLab	Jefferson Lab
CFD	Computational Fluid Dynamics
QTOR	Q_{weak} TORoidal
R2	Region 2
R3	Region 3
HDC	Horizontal Drift Chamber
VDC	Vertical Drift Chamber
CAD	Computer Aided Drawing
ppm	parts per million
PMT	photomultiplier tube
DAQ	Data Acquisition
CODA	CEBAF On-line Data Acquisition

ROC	Read-Out-Controller
ADC	Analog to Digital Converter
TDC	Time to Digital Converter
TRIUMF	TRI-University Meson Facility
MT	meantime
MPS	Macro Pulse Signal
QRT	quartet
TS	Trigger Scintillator
GUI	Graphical User Interface
EM	electromagnetic
PE	Photo-Electron
IHWP	Insertable Half Wave Plate
RHWP	Rotatable Half Wave Plate
VME	VERSAModule Eurocard
TS	Trigger Supervisor
CPU	Central Processing Unit
EB	Event Builder
ET	Event Transfer
ER	Event Recorder
EPICS	Experimental Physics and Industrial Control System
LV1	LeVel 1
SM	Standard Model
HCBA	Helicity Correlated Beam Asymmetry
RMS	Root Mean Square
PVES	Parity Violating Electron Scattering
APV	Atomic Parity Violating

PV	Parity Violating
SUSY	Super Symmetry

1 Introduction

The Standard Model (SM) is a very successful elementary particle theory developed based on decades of experimental evidence. After the discovery of the neutral weak currents in the Gargamelle neutrino experiment [1], the electroweak theory of particle physics developed by Sheldon Glashow, Steven Weinberg and Abdus Salam was accepted as the SM of the particle physics [2]. The trio was awarded the Nobel Prize in Physics in 1979 for their contribution to the development of the SM. The SM was further confirmed by the 1978 SLAC measurement of the weak mixing angle, $\sin^2\theta_{\mathrm{W}}$ [3]. The $\mathrm{Q}_{\mathrm{weak}}$ experiment itself uses the experimental technique developed by this experiment. The theory was further established after the discoveries of weak gauge bosons and the measurement of their masses in collider experiments [4]. But missing phenomena like matter antimatter asymmetry, neutrino flavor oscillations, and dark matter and energy suggest that the SM is only a "low energy" effective theory. The recently observed $3\,\sigma$ deviation of the anomalous magnetic moment of muon [5] could also be related to new physics extensions beyond the SM.

Experiments testing the SM can be categorized into three main branches: the energy frontier, the precision frontier, and the cosmological frontier. The high energy frontier experiments are designed to detect particles that are predicted by the SM or to detect new physics particles. The most prominent discovery machines include the Super Proton Synchrotron (SPS), the Large Electron Positron (LEP) collider also known as the Z factory, the Large Hadron Collider (LHC), and the Tevatron. They have discovered SM particles including the W and Z bosons [6] (at SPS), a Higgs like boson [7, 8] (at LHC), and the top quark [9, 10] (at Tevatron). The precision frontier experiments measure SM predicted quantities (ideally suppressed) to high precision or detect rare processes predicted by the SM. Therefore, precision frontier

experiments are very diverse and vary from table-tops to colliders. Their results for SM predicted quantities can be used to constraint or develop new physics models beyond the SM. Examples of high precision measurements include the measurement of the anomalous magnetic moment of the electron or the muon [5, 11], the measurements of neutrino oscillations [12], the Electric Dipole Moment (EDM) measurements of leptons and nucleons [13], and the measurement of the weak charge of the proton by Q_{weak} . Examples of attempted rare process detections include Majorana neutrino searches by using neutrinoless double β decays [14], dark matter searches [15], and matter anti-matter asymmetry studies performed at Large Hadron Collider beauty (LHCb) experiment [16]. The cosmological frontier experiments observe the visible and the dark universe using: cosmic ray studies [17], cosmic wave background measurements [18, 19], gravitational wave searches [20], dark matter searches [21], and matter anti-matter asymmetry direct and indirect measurements in space by Alpha Magnetic Spectrometer (AMS) experiment [22]. In summary, the energy frontier experiments are mainly discovery experiments where particles predicted by the SM or new particles can be discovered. The precision and cosmological frontier experiments mainly detect certain footprints or signatures that signal new physics and ultimately may lead to discoveries of new physics particles at the energy frontier. Therefore, all three branches of SM experiments are closely related. They test the SM and new physics theories essential to our understanding of the universe and a theory of everything.

The Q_{weak} experiment is a precision frontier experiment [23] designed to measure the Parity Violating (PV) asymmetry of the electron proton elastic scattering cross section using a high intensity longitudinally polarized electron beam. Its goal is to provide the first precision measurement of the weak charge of the proton and use this result to constraint new PV physics beyond the SM at the TeV scale (section 2.2.1).

The Q_{weak} experiment has benefited from technical advancements achieved by the world class Parity Violating Electron Scattering (PVES) experiments performed since the pioneering Prescott experiment at SLAC, and by the high intensity polarized electron beam development at the Jefferson Lab (JLab). The weak charge of the proton measurement is only possible because of the successful PVES physics programs conducted by SAMPLE [24], A4 [25, 26], HAPPEX [27, 28], and G0 collaborations [29] whose goal were to study the electroweak neutral currents of the nucleons in order to measure the strange quark contribution to nucleon structure. The success of the Q_{weak} experiment will provide the technical expertise for the next generation of the PV physics program starting with the proposed 12 GeV Møller experiment [30] whose goal is to measure the weak mixing angle three times more precisely than the Q_{weak} experiment.

The Q_{weak} experiment took data in two sets. Run 1 data were taken from January 2011 to May 2011. Run 2 data were taken from November 2011 to May 2012. During the Run 1 period, the initial data set which included enough data to measure the weak charge of the proton to about 25% relative precision, was marked as an independent data set known as the Wien0 or 25% data set. The Wien0 data analysis can be considered as a test of the important analysis techniques, tools, and procedures towards extracting the final results. The main results, conclusions, and discussions of this dissertation are based on the Wien0 data set.

As a graduate student working with the Q_{weak} collaboration, I have contributed to many aspects of the experiment mainly for the data acquisition and analysis software development, polarimetry measurements, and data analysis to extract the weak charge of the proton. I took about 60 8-hour long experimental shifts contributing to the data-taking. I have provided technical help as 24-hour on-call expert for software and data acquisition issues. During the course of the

Q_{weak} experiment, I wrote and executed run plans with special procedures to take data for systematics studies related to neutral backgrounds, charge feedback system, and Møller polarimetry measurements. This dissertation summarizes my contributions to the Q_{weak} experiment and provides the results and discussion for the Wien0 data set.

The formalism of parity violating electron scattering and the physics motivations for the Q_{weak} experiment are presented in Chapter 2. Chapter 3 discusses the Q_{weak} experimental techniques and the apparatus. Chapter 4 introduces the data acquisition and analysis software systems with additional sections for the projects that I have contributed to. Chapter 5 provides an overview of the Q_{weak} polarimetry and discusses the Møller polarimeter analysis projects that I have worked on. It also documents the electron beam polarization measurement for the Wien0 data set. In Chapter 6, the PV asymmetry from electron proton scattering is extracted. Additional details are included for analysis projects that I have completed. At the end of Chapter 6, the kinematics of the Q_{weak} experiment are also presented. Chapter 7 includes a preliminary analysis and the results for the weak charge of the proton, weak mixing angle, and constraints on effective quark couplings. I will provide a discussion on analysis issues, impact of the results, and the foreseeable work to be performed by the Q_{weak} collaboration in order to obtain the final result based on the whole data set.

The author acknowledges the support of NSF under grant numbers 065342 and 0969788. The data discussed in this thesis were taken at JLab, a facility operated currently by Jefferson Science Associates, LLC under U.S. DOE Contract No. DE-AC05-06OR23177.

2 Formalism and Physics Motivation

This chapter introduces the Standard Model (SM) formalism for Parity Violating (PV) electron scattering and presents the SM prediction of the weak charge of the proton and the weak mixing angle. I will also discuss an important energy dependent electroweak radiative correction applied to the measured weak charge of the proton. Then the physics motivations for Q_{weak} experiment as a test of the SM and possible new physics beyond the SM accessible from the Q_{weak} experiment are summarized.

2.1 The Formalism

The lepton hadron interaction at energies smaller than the mass of the Z-boson ($|Q^2| < M_Z^2$) can be interpreted using an admixture of electromagnetic (EM) and weak neutral currents (NC) (Figure 2.1). The one-photon-exchange scattering amplitude is defined as,

$$M^{EM} = \frac{4\pi\alpha}{Q^2} Q_\ell l^\mu J_\mu^{EM} \tag{2.1}$$

where Q_ℓ is the leptonic electric charge , Q^2 is the momentum transfer square for the interaction, α is the fine structure constant, J_μ^{EM} is the the matrix element from the electromagnetic (EM) hadronic current and l^μ is the leptonic vector Dirac current.

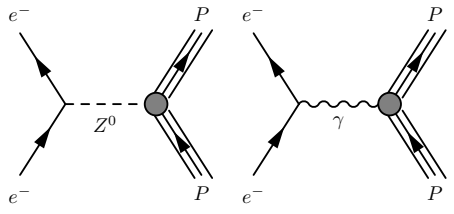

Figure 2.1: Leading order (tree-level) parity conserving and parity violating semi-leptonic electroweak interactions.

Table 2.1: SM predictions for weak vector, and weak axial-vector charges (coupling constants) for leptons and quarks. For quarks, $g_V^f = -2C_{1f}$ and $g_A^f = -2C_{2f}$.

Particle (f)	g_V^f	g_A^f
ν_e	1	-1
e^-	$-1 + 4\sin^2\theta_W$	1
u-quark	$1 - \frac{8}{3}\sin^2\theta_W$	-1
d,s-quark	$-1 + \frac{4}{3}\sin^2\theta_W$	1

The Z-boson exchange scattering amplitude is defined as,

$$M^{NC} = \frac{-G_F}{2\sqrt{2}}(g_V^\ell \ell^\mu + g_A^\ell \ell^{\mu 5})(J_\mu^{NC} + J_{\mu 5}^{NC}) \tag{2.2}$$

where g_V^ℓ and g_A^ℓ are leptonic weak vector, and weak axial-vector charges, respectively (see Table 2.1), G_F is the Fermi constant, ℓ^μ and $\ell^{\mu 5}$ are leptonic vector and axial-vector Dirac currents, respectively, and J_μ^{NC} and $J_{\mu 5}^{NC}$ are matrix elements from neutral hadronic currents. Only the PV components of the neutral current amplitude (M^{NC}) contribute to the PV asymmetry. The PV amplitude is given by,

$$M^{PV} = \frac{-G_F}{2\sqrt{2}}(g_V^\ell \ell^\mu \cdot J_{\mu 5}^{NC} + g_A^\ell \ell^{\mu 5} \cdot J_\mu^{NC}) \tag{2.3}$$

where the leptonic vector and axial-vector Dirac currents are defined as,

$$\ell^\mu \equiv \bar{u}_\ell \gamma_\mu u_\ell \text{ and,}$$
$$\ell^{\mu 5} \equiv \bar{u}_\ell \gamma_\mu \gamma^5 u_\ell \tag{2.4}$$

The hadronic matrix elements (J_μ^{EM}, J_μ^{NC} and $J_{\mu 5}^{NC}$) can be constructed using EM, vector, and axial-vector quark current operators, which are defined as,[†]

$$\hat{J}_\mu^{EM} \equiv \sum_q Q_q \bar{u}_q \gamma_\mu u_q, \quad \hat{J}_\mu^{NC} \equiv \sum_q g_v^q \bar{u}_q \gamma_\mu u_q, \quad \hat{J}_{\mu 5}^{NC} \equiv \sum_q g_A^q \bar{u}_q \gamma_\mu \gamma_5 u_q \tag{2.5}$$

[†]The matrix elements from neutral or electromagnetic hadronic currents of any hadron are defined as, $J_{\mu/\mu 5}^{NC/EM} = < H|\hat{J}_{\mu/\mu 5}^{NC/EM}|H >$ where $|H >$ is any hadronic state.

where the sum is over quark flavors, q $(u, d, s, \cdots)$, the g_V^q and g_A^q are SM predictions for weak vector, and weak axial-vector quark charges (or coupling constants), respectively (see Table 2.1).

The hadronic dynamics of the proton are dominated by lightest quarks (u,d, and s quarks) at the small momentum transfer where the Q_{weak} experiment is carried out. Therefore heavier quarks are neglected and the hadronic currents are parametrized into isoscalar and isovector currents using SU(3) octet and singlet current components [31](see Appendix A.1 for details). The results from the Q_{weak} experiment will test the effective couplings of these isoscalar and isovector hadronic currents.

The quantity of interest in the Q_{weak} experiment is the electron-proton (lepton-nucleon) scattering PV asymmetry, and it results from the interferences of the M^{EM} and the M^{PV} amplitudes. (The parity conserving contributions get canceled.) The PV asymmetry is defined as,

$$\begin{aligned} A_{LR} &= \frac{\frac{d\sigma^R}{d\Omega} - \frac{d\sigma^L}{d\Omega}}{\frac{d\sigma^R}{d\Omega} + \frac{d\sigma^L}{d\Omega}} \equiv A_{LR}^0 \frac{W^{(PV)}(\tau,\varepsilon)}{F_p^2(\tau,\varepsilon)} \\ &\propto \frac{M^{EM} \cdot M^{PV}}{|(M^{EM})^2|} \end{aligned} \tag{2.6}$$

where $\frac{d\sigma^{R/L}}{d\Omega}$ are the total differential cross sections in the right (R) and left (L) helicity states (helicity is discussed in Section 3.1), $W^{(PV)}(\tau,\varepsilon)$ is the PV response of the scattering amplitude, and $F_p^2(\tau,\varepsilon)$ is the total EM response of the scattering amplitude [31]. A_{LR}^0 is defined as,

$$A_{LR}^0 = \frac{G_F |Q^2|}{2\pi\alpha\sqrt{2}} \tag{2.7}$$

and ε and τ are dimensionless functions of the scattering angle θ and momentum transfer square, respectively. They are defined as,

$$\varepsilon = \frac{1}{1+2(1+\tau)\tan^2\frac{\theta}{2}},\ \tau = \mathrm{Q}^2/4M^2 \tag{2.8}$$

where M is the proton mass. The F_p^2 and $\mathrm{W}^{(\mathrm{PV})}$ can be expressed using the electric and magnetic Sachs form factors of the nucleon ($\mathrm{G}_\mathrm{E}^{\mathrm{p,n}}(\tau)/\mathrm{G}_\mathrm{M}^{\mathrm{p,n}}(\tau)$), EM strange form factors ($\mathrm{G}_\mathrm{E/M}^{(\mathrm{s})}$), and weak axial-vector form factor of the proton ($\tilde{\mathrm{G}}_\mathrm{A}^\mathrm{p}(\tau)$) [31, 32]. The F_p^2 is derived to be,

$$\mathrm{F}_\mathrm{p}^2(\tau,\varepsilon) = \frac{\varepsilon \mathrm{G}_\mathrm{E}^\mathrm{p}(\tau)^2 + \tau \mathrm{G}_\mathrm{M}^\mathrm{p}(\tau)^2}{\varepsilon(1+\tau)} \tag{2.9}$$

and $\mathrm{W}^{(\mathrm{PV})}$ is given by,

$$\begin{aligned}
&\mathrm{W}^{(\mathrm{PV})}(\tau,\varepsilon) = \\
&-\frac{1}{2\varepsilon(1+\tau)}\Bigg[\mathrm{g}_\mathrm{A}^\mathrm{e}\Big(\ \mathrm{Q}_\mathrm{W}^\mathrm{p}[\varepsilon \mathrm{G}_\mathrm{E}^\mathrm{p}(\tau)^2 + \tau \mathrm{G}_\mathrm{M}^\mathrm{p}(\tau)^2] + \varepsilon \mathrm{G}_\mathrm{E}^\mathrm{p}(\tau)[\mathrm{Q}_\mathrm{W}^\mathrm{n}\mathrm{G}_\mathrm{E}^\mathrm{n}(\tau) + \xi_\mathrm{V}^{(0)}\mathrm{G}_\mathrm{E}^{(\mathrm{s})}(\tau)] + \\
&\tau \mathrm{G}_\mathrm{M}^\mathrm{p}(\tau)[\mathrm{Q}_\mathrm{W}^\mathrm{n}\mathrm{G}_\mathrm{M}^\mathrm{n}(\tau) + \xi_\mathrm{V}^{(0)}\mathrm{G}_\mathrm{M}^{(\mathrm{s})}(\tau)]\ \Big)\ + \mathrm{g}_\mathrm{V}^\mathrm{e}\sqrt{1-\varepsilon^2}\sqrt{\tau(1+\tau)}\mathrm{G}_\mathrm{M}^\mathrm{p}(\tau)\tilde{\mathrm{G}}_\mathrm{A}^\mathrm{p}(\tau)\Bigg]
\end{aligned} \tag{2.10}$$

where $\xi_\mathrm{V}^{(0)} = (\mathrm{g}_\mathrm{v}^\mathrm{u} + \mathrm{g}_\mathrm{v}^\mathrm{d} + \mathrm{g}_\mathrm{v}^\mathrm{s})$ (see Table 2.1) is the strange quark weak neutral coupling constant, see Appendix A.1 for more on the derivation. The weak charges (coupling constants) of the proton, neutron, and electron can be defined using the SM predictions for weak vector, and weak axial-vector quarks charges as,

$$\mathrm{Q}_\mathrm{W}^\mathrm{p} = 2\mathrm{g}_\mathrm{V}^\mathrm{u} + \mathrm{g}_\mathrm{V}^\mathrm{d},\quad \mathrm{Q}_\mathrm{W}^\mathrm{n} = 2\mathrm{g}_\mathrm{V}^\mathrm{d} + \mathrm{g}_\mathrm{V}^\mathrm{u},\quad \mathrm{Q}_\mathrm{W}^\mathrm{e} \equiv \mathrm{g}_\mathrm{V}^\mathrm{e}, \tag{2.11}$$

where the quark and lepton weak charges were defined in Table 2.1. The PV asymmetry can now be expressed in terms of EM Sachs form factors of the proton and neutron, strange quark form factors, and axial-vector weak form factor with the contributions from weak charges of proton, neutron, and electron separated. The

expression for the PV asymmetry is,

$$\mathrm{A_{LR}}(\vec{\mathrm{e}}\mathrm{p}) = -\frac{1}{2}\mathrm{A^0_{LR}}\Bigg[\mathrm{Q^p_W} + \mathrm{Q^n_W}\cdot\frac{[\varepsilon \mathrm{G^p_E}(\tau)\mathrm{G^n_E}(\tau) + \tau \mathrm{G^p_M}(\tau)\mathrm{G^n_M}(\tau)]}{\varepsilon \mathrm{G^p_E}(\tau)^2 + \tau \mathrm{G^p_M}(\tau)^2} + \xi^{(0)}_{\mathrm{V}}\cdot\frac{[\varepsilon \mathrm{G^p_E}(\tau)\mathrm{G^{(s)}_E}(\tau) + \tau \mathrm{G^p_M}(\tau)\mathrm{G^{(s)}_M}(\tau)]}{\varepsilon \mathrm{G^p_E}(\tau)^2 + \tau \mathrm{G^p_M}(\tau)^2} + \mathrm{Q^e_W}\cdot\frac{\sqrt{1-\varepsilon^2}\sqrt{\tau(1+\tau)}\mathrm{G^p_M}(\tau)\tilde{\mathrm{G}}^{\mathrm{p}}_{\mathrm{A}}(\tau)}{\varepsilon \mathrm{G^p_E}(\tau)^2 + \tau \mathrm{G^p_M}(\tau)^2}\Bigg]. \tag{2.12}$$

For forward angle scattering ($\theta \to 0$) and small momentum transfer ($\mathrm{Q}^2 \to 0$), where $\varepsilon \to 1$ and $\tau << 1$, the PV asymmetry can be written as,

$$\mathrm{A_{LR}}(\vec{\mathrm{e}}\mathrm{p}) \simeq -\frac{1}{2}\mathrm{A^0_{LR}}\Big[\mathrm{Q^p_W} \ + \ \mathrm{Q^2 B}\Big], \tag{2.13}$$

where the leading contribution to the PV asymmetry is coming from the weak charge of the proton ($\mathrm{Q^p_W} = 1 - 4\cdot\sin^2\hat{\theta}_{\mathrm{W}}(0)$ at tree level, where $\sin^2\hat{\theta}_{\mathrm{W}}(0)$ will be discussed later) and it is about 75%. The next to leading order contribution, B is related to proton, neutron, strange quark, and axial form factors (equation 2.12) and it is about 25%. There are two methods to remove the hadronic contribution (B) from the measured asymmetry and extract the weak charge of the proton. The hadronic contribution can be estimated from a global data analysis based on measured asymmetries from Parity Violating Electron Scattering (PVES) experiments [24–29, 33, 34] to a better precision than the uncertainty on the measured asymmetry or it can be estimated from existing parametrization of EM and electroweak form factors. The main difference between the two methods is related to the treatment of the strange form factors which are poorly known relative to other form factors. I will discuss both these methods towards the end of this section. With a better estimation of the hadronic contribution, a measurement of the asymmetry, $\mathrm{A_{LR}}(\vec{\mathrm{e}}\mathrm{p})$, at forward angle scattering and small momentum transfer can be used to probe the weak charge of the proton free of any nuclear theoretical uncertainties, which is the goal of the

Q_{weak} experiment. The asymmetry contribution from the hadronic term (B) increases as a function of Q^4 and dilutes the PV asymmetry at higher momentum transfer. Going to lower momentum transfer reduces the hadronic asymmetry but it also reduces the asymmetry from the weak charge of the proton making its measurement more challenging. Therefore, with the goal of extracting a statistically dominated measurement of the Q_W^p at about 4% level, the optimum momentum transfer for the Q_{weak} experiment was determined to be to Q^2 of 0.025 $(GeV)^2$.

A proof of principle of the global data analysis based on measured asymmetries from PVES was published in references [35, 36] which provided the first method to estimate the hadronic contributions using PVES asymmetries. In this world data analysis, EM strange form factors ($G_{E/M}^{(s)}$), proton and neutron weak axial-vector form factors ($\tilde{G}_A^{p/n}$), and the weak charge of the proton are fitted using the PVES measurements from all the PVES experiments [24–29, 33, 34] at Q^2 less than 0.3 GeV^2 on nuclear targets (proton, helium, and deuterium). For PVES experiments, the normalized PV asymmetry is defined as,

$$\overline{A_{LR}}(\vec{e}p) \simeq (Q_W^p + B \cdot Q^2) \tag{2.14}$$

where $\overline{A_{LR}}(\vec{e}p) = A_{LR}(\vec{e}p)/\frac{1}{2}A_{LR}^0$. The range of PVES measurements in the range of $0.1 < Q^2 < 0.3$ GeV^2 enable $Q^2 \to 0$ GeV^2 extrapolation and extraction of the weak charge of the proton independent of any models of nucleon structure (see Figure 2.2). The fit curve and 1-σ uncertainty band only contain experimental constraints on hadronic contributions including strange form factor and weak axial form factors. The alternate fit to the data with the anapole form factor theoretical constraints (the dashed-line in Figure 2.2) is within the 1-σ error band [36], and makes no significant difference to the final result.

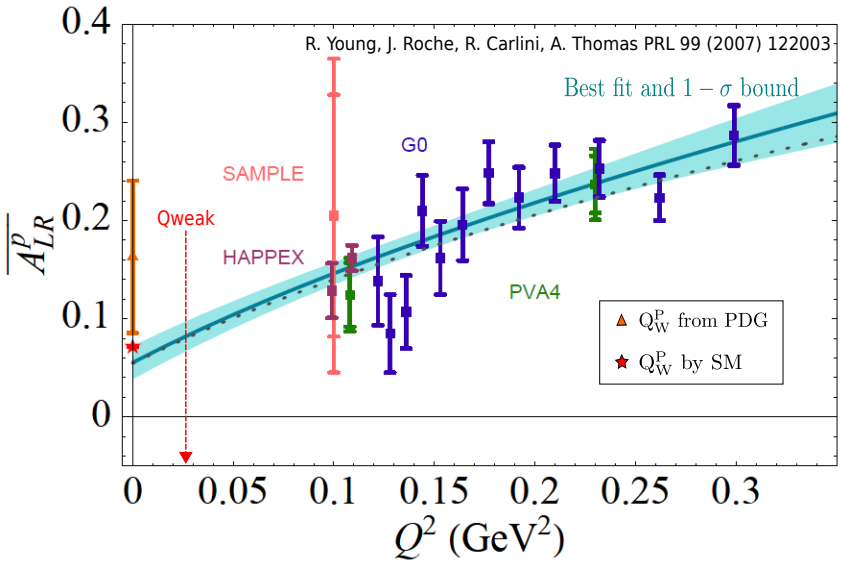

Figure 2.2: The proton target asymmetries are plotted after being extrapolated to zero degrees forward scattering angle. The intercept at $Q^2 = 0$ projects to the weak charge of the proton. This fit incorporated all PVES measurements including proton, helium, and deuterium data. The band around the fit is the 1σ uncertainty on the fit. The dotted line represents the updated fit with theoretical estimates of the anapole form factors (from [36]).

The weak charge of the proton (Q_W^p) measurement from the Q_{weak} experiment will be extracted by repeating the global data analysis with the measured Q_{weak} asymmetry. One important issue related to this analysis is that the asymmetry measurements in this analysis may require an update with the latest radiative corrections and there are on-going discussions about this issue. Therefore, the weak charge of the proton from Wien0 is extracted using equation 2.12 after numerically estimating the hadronic contribution based on available parametrizations of proton, neutron, strange quark and axial form factors. (The second method to extract the weak charge of the proton.) Due to Wien0 limited precision, the estimation of the hadronic contribution using this technique will not hinder the Wien0 weak charge of

the proton result. The rest of this section introduces the required form factor inputs to calculate the hadronic contribution.

The Sachs form factors in the small momentum transfer region ($Q^2 < 0.1$ GeV^2) can be estimated from unpolarized electron scattering experiments to better than 1 percent by parameterizing form factors using a dipole function [37]. The dipole functions is defined as,

$$G_D^V(\tau) = \frac{1}{(1+4.97\tau)^2} \tag{2.15}$$

and the neutron electric form form factor is parametrized using the Galster function [37]. The Sachs form factors are given by,

$$\begin{aligned} G_E^p(\tau) = G_D^V(\tau), \quad G_E^n(\tau) = \frac{-\mu_n G_D^V(\tau)}{1+5.6\tau} \cdot \tau \\ G_M^p(\tau) = \mu_p G_D^V(\tau), \quad G_M^n(\tau) = \mu_n G_D^V(\tau) \end{aligned} \tag{2.16}$$

where $\mu_p = 2.79$ and $\mu_n = -1.91$ are magnetic moments of the proton and neutron, respectively. The axial-vector form factor $\tilde{G}_A^p(\tau)$ can be represented using SU(3) isovector hadronic current definition by following the reference [31] (see Appendix A.2 for more detailed derivation),

$$\tilde{G}_A^p(\tau) = \xi_A^{T=1} G_A^{(3)}(0) G_D^A(\tau), \tag{2.17}$$

where $G_A^{(3)}(0) = 1.262/2$, the dipole term $G_D^A(\tau) = (1+\lambda_D^A\tau)^{-2}$ with $\lambda_D^A = 3.32^{+0.24}_{-0.22}$, and isovector axial current coupling constant, $\xi_A^{T=1} = -2(1+R_A^{T=1})$, with the higher order radiative correction term $R_A^{T=1} = -0.34$. Based on the most precise estimation from PVES global data analysis, strange form factors ($G_{E/M}^{(s)}(\tau)$) are compatible with zero at low momentum transfer of the Q_{weak} measurement [35]. Therefore, it can be safely assumed that $G_{E/M}^{(s)}(\tau) \sim 0$ for rest of the calculations and it will not affect the less precise Wien0 result. Now using these form factor inputs and the SM prediction of $Q_W^p = 0.0705 \pm 0.0008$ [38], I have computed the SM prediction of the PV asymmetry

at $Q^2 = 0.025$ GeV^2 using equation 2.12 (see Appendix A.2 for detailed computation and error estimation). The SM calculation of the PV asymmetry is,

$$\begin{aligned} A_{LR}^{SM}(\vec{e}p) &= A_{Qwp} + A_{Had} \\ &= -0.1584 \pm 0.0018 \ + \ -0.0558 \pm 0.0024 \text{ ppm} \\ &= -0.2142 \pm 0.0030 \text{ ppm} \end{aligned} \tag{2.18}$$

where the A_{Had} result will be used to compute a preliminary measurement of the weak charge of the proton (Q_W^p) from Wien0 measured asymmetry. I will now discuss the SM results of the weak charge of the proton and the weak mixing angle used to compute the PV asymmetry.

2.1.1 Weak Charge of the Proton and Weak Mixing Angle

The weak charge of the proton in the SM at tree level is $Q_W^p(SM) = 1 - 4\sin^2\hat{\theta}_W(0)$ but electroweak radiative corrections are required in the SM as $Q^2 \to 0$ to compare with the Q_{weak} measurement of the weak charge of the proton ($Q_W^p(msr)$) which is performed at $Q^2 \sim 0.025$ GeV^2. The $Q_W^p(SM)$ (at $Q^2 = 0$) including the electroweak radiative correction is given by [39],

$$Q_W^p(SM) = [\rho_{NC} + \Delta_e][1 - 4\sin^2\hat{\theta}_W(0) + \Delta'_e] + \Box_{WW} + \Box_{ZZ} + \Box_{\gamma Z}(0) \tag{2.19}$$

where ρ_{NC} renormalizes the ratio of neutral to charged current interactions at low energies [39]. Δ_e and Δ'_e are corrections to the Zee and γee couplings at the electron vertex, respectively, $\Box_{WW}$ and $\Box_{ZZ}$ are corrections to the pure weak interaction box interactions, $\Box_{\gamma Z}(0)$ is correction to the electroweak box interaction at $Q^2 = 0$ [39] (see Figure 2.3), and $\sin^2\hat{\theta}_W(0)$ is the weak mixing angle at $Q^2 = 0$ that will be discussed in the next paragraph. Table 2.2 summarizes values for electroweak radiative corrections applied to the weak charge of the proton predicted the SM.

Table 2.2: The values of electroweak radiative corrections in equation 2.19.

Correction	Value
ρ_{NC}	1.047
Δ_{e}	-0.001
Δ'_{e}	-0.001
$\Box_{\mathrm{WW}}$	0.019
$\Box_{\mathrm{ZZ}}$	0.002
$\Box_{\gamma\mathrm{Z}}$	0.004

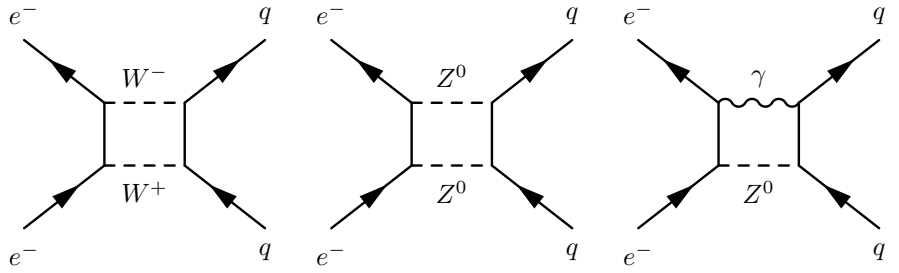

Figure 2.3: Pure weak interaction box diagrams ($\Box_{\mathrm{WW}}$ and $\Box_{\mathrm{ZZ}}$) and electroweak $\Box_{\gamma\mathrm{Z}}$ box diagram. These are the leading order box corrections to the weak charge of the proton in the SM.

The SM prediction of the weak mixing angle at $\mathrm{Q}^2 \to 0$ is based on the weak mixing angle measured precisely at the Z pole [40] ($\hat{\mathrm{s}}^2 \equiv \sin^2\hat{\theta}_{\mathrm{W}}(\mathrm{M_Z}) = 0.2312 \pm 0.0002$ at $\mathrm{Q}^2 = \mathrm{M_Z^2}$). The weak mixing angle value at $\mathrm{Q}^2 \neq \mathrm{M_Z^2}$ depends on the renormalization scheme implemented to include higher order (in α) electroweak and hadronic corrections to the tree level value. The scheme used here to apply these higher correction is called $\overline{\mathrm{MS}}$ (known as the modified minimal subtraction scheme). In this scheme the weak mixing angle has an energy (μ) dependence ($\mu^2 \equiv \mathrm{Q}^2$) where Q^2 is the momentum transfer, at which the weak mixing angle, $\sin^2\hat{\theta}_{\mathrm{W}}(\mu)$, is measured. In the $\overline{\mathrm{MS}}$ scheme, the parameter $\sin^2\hat{\theta}_{\mathrm{W}}(\mu)$ can be directly compared with the running

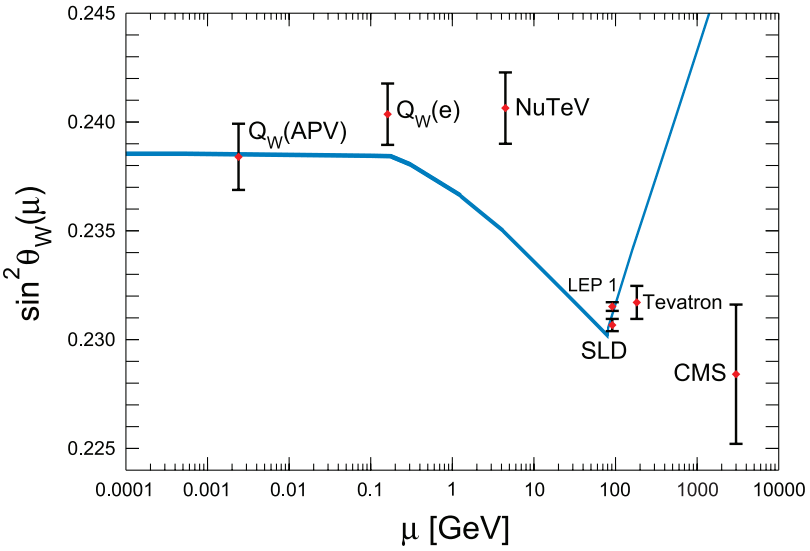

Figure 2.4: The "running of $\sin^2\theta_{\rm W}$" in the $\overline{\rm MS}$ scheme, compared with low energy measurements of the $\sin^2\hat{\theta}_{\rm W}(\mu)$ (from [40]). The $\rm Q_{weak}$ measurement is done at the same μ-scale of the Møller measurement ($\rm Q_W(e)$) from E158 [42]. The original NuTeV result [43] is included in this plot but there are on-going discussions regarding missing nuclear corrections. Once finalized, new corrections will reduce the NuTeV deviation from the SM prediction [40, pages 140-141].

of EM ($\alpha(\mu)$) and strong ($\rm g(\mu)$) couplings. Therefore μ-dependence is known as the "running of $\sin^2\theta_{\rm W}(\mu)$" (See Figure 2.4). All low energy weak mixing angle measurements so far have also used the $\overline{\rm MS}$ scheme for electroweak radiative corrections. A detailed analysis of the running of $\sin^2\theta_{\rm W}(\mu)$ and $\sin^2\hat{\theta}_{\rm W}(0)$ estimation in $\overline{\rm MS}$ scheme can be found at [39, 41]. In $\overline{\rm MS}$ scheme, the $\sin^2\hat{\theta}_{\rm W}(0)$ (at $\rm Q^2 = 0$) is given by,

$$\sin^2\hat{\theta}_{\rm W}(0) = \hat{\rm s}^2 + \Delta\kappa^{(5)}_{\rm had} + \frac{\alpha}{\pi}\left(\frac{1-4\hat{\rm s}^2}{12}\left[\sum_l \ln\left(\frac{\rm M_Z^2}{\rm m_l^2}\right)\left(1+\frac{3\alpha}{4\pi}\right)+\frac{135\alpha}{32\pi}\right] - \left[\frac{7\hat{\rm c}^2}{4}+\frac{1}{24}\right]\ln\left(\frac{\rm M_Z^2}{\rm M_W^2}\right)+\frac{\hat{\rm s}^2}{6}-\frac{7}{18}\right) \tag{2.20}$$

where α is the fine structure constant, $\hat{\rm s}^2$ is $\sin^2\theta_{\rm W}$ measured at Z pole [40], $\hat{\rm c}^2 \equiv 1-\hat{\rm s}^2$, $\Delta\kappa^{(5)}_{\rm had} = (7.90 \pm 0.05 \pm 0.06)\times 10^{-3}$ is the leading and higher order hadronic contribution to the weak mixing angle [39], and $\rm m_l$, $\rm M_W$, and $\rm M_Z$ are lepton, W-boson, and Z-boson masses, respectively. The corrections are summed over charged

leptons (l). Finally, the SM prediction of the weak mixing angle in $\overline{\text{MS}}$ scheme,

$$\sin^2\hat{\theta}_{\text{W}}(0) = 0.2387 \pm 0.0002 \tag{2.21}$$

where this results is used in the SM prediction of the weak charge of the proton (equation 2.19). The most up-to date weak charge of the proton is [38],

$$\text{Q}_{\text{W}}^{\text{p}}(\text{SM}) = 0.0705 \pm 0.0008 \tag{2.22}$$

where the SM prediction is computed using the most recent $\Box_{\gamma\text{Z}}(0)$ correction (discussed in Section 2.1.2)

2.1.1.1 A Note on NuTeV Results

The original NuTeV result [43] included in the Figure 2.4 claimed a 3σ deviation from the SM prediction. After the original publication, numerous experimental and theoretical developments outside of the NuTeV collaboration have provided better interpretation of the nuclear corrections required for the NuTeV measurement. These new developments have reduced the deviation from the SM [40, pages 140-141]. The impact of these new developments is still under investigation but NuTeV result can not be regarded as conclusive evidence for new physics beyond the SM.

2.1.2 The $\Box_{\gamma\text{Z}}$ Diagram Correction Summary

The $\Box_{\gamma\text{Z}}(0)$ correction in the equation 2.19 was assumed to be an energy independent correction ($\Box_{\gamma\text{Z}} = 0.0052 \pm 0.0005$ by Marciano et.al. [44, 45]) but based on follow-up studies [38, 46], it was found that the $\Box_{\gamma\text{Z}}$ correction contains vector and axial vector components that are energy dependent. Therefore, the energy dependent $\Box_{\gamma\text{Z}}$ contribution must be subtracted from the Q_{weak} measurement to be compared with the SM prediction of the weak charge of the proton $\text{Q}_{\text{W}}^{\text{p}}(\text{SM})$. (discussed in Section 2.1.2.1.)

The $\Box_{\gamma Z}$ contribution has two components. The electron(axial-vector) to proton(vector) interaction ($\Box^{V}_{\gamma Z}$) vanishes at small beam energy ($E \to 0$) but is non-zero at non-zero electron beam energies. The electron(vector) to proton(axial-vector) interaction ($\Box^{A}_{\gamma Z}$) is finite at all energies (zero or finite). As of Winter of 2013, there are several published results for the interpretation of $\Box_{\gamma Z}$ correction related to the Q_{weak} measurement (see Table 2.3). Figure 2.5 shows the most up-to date and detailed $\Box^{V}_{\gamma Z}$, $\Box^{A}_{\gamma Z}$, and $\Box^{V+A}_{\gamma Z}$ corrections summary [38, 46].

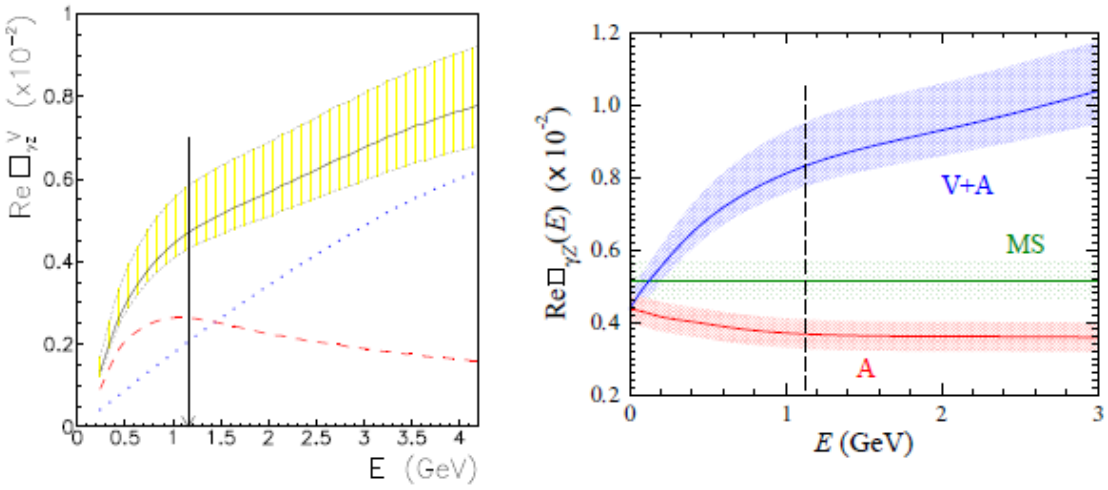

Figure 2.5: Left: As of Winter of 2013, the $\Box^{V}_{\gamma Z}$ correction to Q^{p}_{W}vs. the electron energy. The yellow-band is the total correction (from [46]), the arrow points to the Q_{weak} beam energy. Right: The old energy independent $\Box_{\gamma Z}$ correction (green-band), As of Winter of 2013, $\Box^{A}_{\gamma Z}$ correction (red-band) and total correction, $\Box^{V+A}_{\gamma Z}$ (blue-band) to Q^{p}_{W}(from [38]). The vertical dashed line shows the Q_{weak} beam energy.

Based on the recent analysis [38], $\Box_{\gamma Z}(0) = 0.0044 \pm 0.0004$ is used to compute the SM prediction of the weak charge of the proton (equation 2.19). The required correction to the Q_{weak} measurement of the weak charge of the proton is discussed in the next section.

Table 2.3: A list of available $\Box_{\gamma Z}$ corrections as of Winter of 2013. The most recent results are underlined.

Interaction	Correction at E = 1.165 GeV	References
A(e) × V(p)	0.0026 ± 0.0026	Gorchtein and Horowitz [47]
	0.0054 ± 0.0020	Gorchtein, Mikhail, Horowitz, and Ramsey-Musolf [48]
	0.0057 ± 0.0009	Rislow and Carlson [49]
	$\underline{0.0047^{+0.0011}_{-0.0004}}$	Sibirtsev, Blunden, Melnitchouk, and Thomas [46]
V(e) × A(p)	0.0052 ± 0.0005	Erler, Kurylov, and Ramsey-Musolf [39]
	$\underline{0.0037 \pm 0.0004}$	Blunden, Melnitchouk, and Thomas [38]

2.1.2.1 The $\Box_{\gamma Z}(E)$ Correction to the Q_{weak} Asymmetry

The Q_{weak} asymmetry is measured at E = 1.155 GeV[†] and the energy dependent $\Box_{\gamma Z}$ correction must be removed from the weak charge of the proton measurement ($Q_W^p(msr)$) because it is compared with $Q_W^p(SM)$, which is predicted at $Q^2 = 0$. The total $\Box_{\gamma Z}(E)$ correction (from Table 2.3) at the $E_{Qweak} = 1.155$ GeV is,

$$\Box_{\gamma Z}(E_{Qweak})^{V+A} \equiv \Box_{\gamma Z}(E_{Qweak}) = 0.0084^{+0.0011}_{-0.0006} \tag{2.23}$$

and the net $\Box_{\gamma Z}(E)$ correction to remove energy dependence from the weak charge of the proton is given by [38],

$$\begin{aligned} \Delta Q_W^p\_\Box_{\gamma Z} &= \Box_{\gamma Z}(1.155) - \Box_{\gamma Z}(0) \\ &= 0.0040^{+0.0011}_{-0.0004} \end{aligned} \tag{2.24}$$

[†]Note that the energy E = 1.165 GeV is used as the Q_{weak} electron beam energy in the original paper [38] as included in the Table 2.3 but the actual electron beam energy during the Wien0 was $E = 1.155 \pm 0.003$ GeV. This discrepancy in energy is irrelevant for the Wien0 result as seen in Figure 2.5.

where $\Box_{\gamma Z}$ correction at E = 0 is $\Box_{\gamma Z}(0) = 0.0044 \pm 0.0004$ [38]. Now this correction can be applied to the Q_{weak} result in two different ways. The correction can be subtracted after computing the weak charge of the proton from the measured asymmetry or it can be subtracted directly from the measured asymmetry. I will use the latter method to remove the energy dependent $\Box_{\gamma Z}$ contribution from the measured asymmetry. The correction to the measured asymmetry to remove the energy dependent $\Box_{\gamma Z}(E)$ contribution can now be defined using the $\Delta Q_W^p\_\Box_{\gamma Z}$,

$$\Delta A\_\Box_{\gamma Z} = -\frac{A_{LR}^0}{2} \cdot \Delta Q_W^p\_\Box_{\gamma Z} \tag{2.25}$$

where A_{LR}^0 is defined in the equation 2.7. The measured asymmetry (A^{tree}) is corrected to remove the $\Box_{\gamma Z}(E)$ correction at Q_{weak} energy E = 1.155 GeV to get,

$$A_{LR}^{msr}(\vec{e}p) = A_{Tree} - \Delta A\_\Box_{\gamma Z} \tag{2.26}$$

where A_{Tree} is the final tree-level asymmetry to be obtained from the analysis in Chapter 6. $A_{LR}^{msr}(\vec{e}p)$ is free from $E > 0$ $\Box_{\gamma Z}$ effects and it is used to extract the weak charge of the proton.

2.2 Physics Motivation

The SM prediction of the weak charge of the proton ($Q_W^p(SM)$) is a suppressed quantity. A percent level measurement of the weak charge of the proton is potentially sensitive to new physics beyond the SM. The Q_{weak} experiment will provide a 4% direct measurement of Q_W^p and 0.3% measurement of $\sin^2\hat{\theta}_W(Q)$ by measuring the PV asymmetry at a Q^2 of $0.025(GeV)^2$ which are the most precise measurements at low momentum transfer compared to results from Atomic Parity Violating (APV) experiments [50, 51] and the E158 experiment [42], respectively. Q_{weak} results will also be free from any atomic or nuclear theory calculations. The measurement is done at a comparable energy scale to the pure leptonic weak mixing angle measurement

from the E158 experiment [42] and complements the proposed Møller experiment to repeat the pure leptonic weak mixing angle measurement to the precision of the Z pole measurement [30]. As I will discuss in the next section, the semi-leptonic Q_{weak} measurement and pure leptonic Møller measurement of the weak mixing angle together will help to constrain new physics beyond the Standard Model.

The Q_{weak} measurement will provide additional constraints on the SU(3) isovector and isoscalar effective couplings $C_{1u} - C_{1d}$ and $C_{1u} + C_{1d}$, respectively (see Figure 2.6). The combined results of Q_{weak} and APV experiments [50, 51] will provide the best constraint on these effective couplings when published. These couplings test the SM prediction of the weak neutral vector-quark currents based on SU(3) isospin symmetry only using the lightest quarks (u,d, and s).

2.2.1 New Physics Beyond the Standard Model

Making a percent level measurement of the weak charge of the proton (Q_W^p) is sensitive to TeV-scale new PV physics that would couple to quarks. The possible experimental constraints from Q_{weak} will provide model independent estimates on new physics mass and coupling scales or test the credibility of proposed new physics extensions beyond the SM. The effective Lagrangian for the semi-leptonic axial(electron)-vector(quark) interaction can be written as,

$$L_{NC}^{eq} = L_{SM}^{eq} + L_{New}^{eq} \tag{2.27}$$

where the effective Lagrangian contribution from the SM is L_{SM}^{eq} and the possible new physics interactions are L_{New}^{eq}. These Lagrangians are defined using quark currents as,

$$\begin{aligned} L_{SM}^{eq} &= -\frac{G_F}{\sqrt{2}}\bar{e}\gamma_\mu\gamma_5 e \cdot \sum_q C_{1q}\bar{q}\gamma^\mu q \\ L_{New}^{eq} &= \frac{g^2}{4\Lambda^2}\bar{e}\gamma_\mu\gamma_5 e \cdot \sum_q h_V^q \bar{q}\gamma^\mu q \end{aligned} \tag{2.28}$$

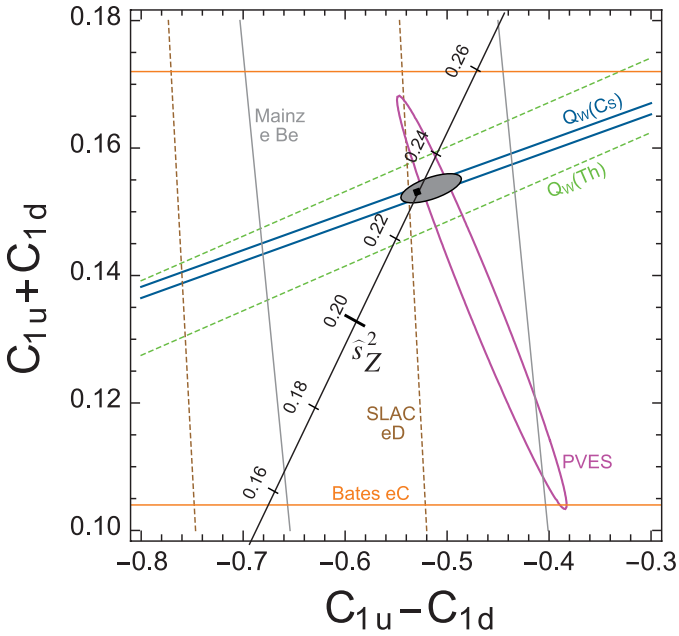

Figure 2.6: The constraints on $C_{1u} - C_{1d}$ (isovector) and $C_{1u} + C_{1d}$ (isoscalar) from parity violating electron scattering and APV experiments (no Q_{weak} results in the plot), which shows mutually orthogonal sensitivities to the isovector and isoscalar effective couplings (from [40]). The SM prediction of the coupling (black-dot) computed using $\hat{s}^2_Z = 0.2312 \pm 0.0002$ agrees within the world data best fit analysis (the Grey ellipse).

where G_F is the Fermi constant and the $g^q_V \equiv -2C_{1q}$ are effective quark couplings for q(u,d, and s quarks), g is the new physics coupling, Λ is the mass scale of the new physics, and h^q_V are new physics effective quark couplings [36]. If any experimental deviation from the SM result is observed, it could signal new physics beyond the SM. New physics deviation is defined as,

$$\delta Q^p_W(\text{New}) = Q^p_W(\text{msr}) - Q^p_W(\text{SM})$$

where $Q^p_W(\text{msr})$ is the measured weak charge of the proton and $Q^p_W(\text{SM})$ is the SM prediction. If the measured $Q^p_W(\text{msr})$ agrees with the SM prediction then the deviation is limited to the precision of the weak charge measurement, $\delta Q^p_W(\text{msr})$, then the new

physics deviation is given by,

$$\delta Q_W^p(\text{New}) \equiv \delta Q_W^p(\text{msr}) \tag{2.29}$$

If no deviation is observed, the new physics mass scale lower limit is,

$$\Lambda \sim \frac{1}{\sqrt{2\sqrt{2}G_F}} \cdot \frac{1}{\sqrt{S|\delta Q_W^p|}} \tag{2.30}$$

where the coupling g is assumed to be of order O(1) for simplification and S is the standard deviation of the final measurement that determines the confidence limit (CL) of the new physics observation. The lower limit on the new physics mass scale is related to the uncertainty of the weak charge of the proton measurement (see Figure 2.7). The Q_{weak} experiment with a 4% measurement of the Q_W^p will rule out at 95% CL new particles that generate new PV physics below 2.3 TeV, if the result agrees with the SM.

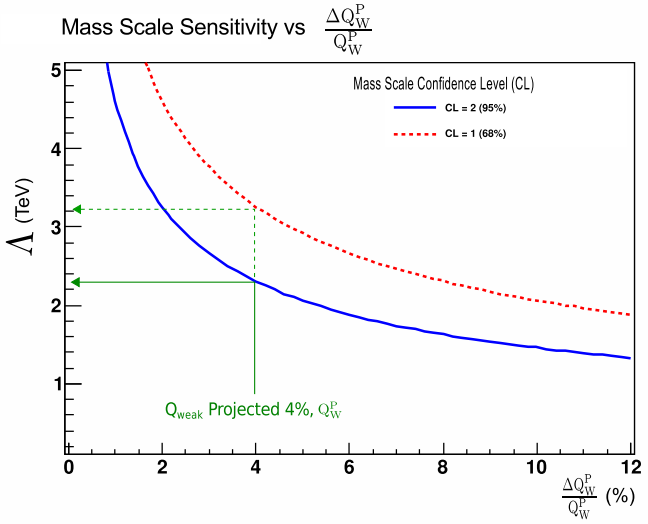

Figure 2.7: The lower bound on new physics mass scale if $Q_W^p(\text{msr})$ agrees with the SM at $\delta Q_W^p(\text{msr})$ uncertainty to rule out new particles that generate new PV physics. The solid (dashed) corresponding to 95%(68%) confidence limits (CL), respectively.

Most of the new PV physics models discussed [39] are extensions to the SM which could generate small deviation to SM quantities. Extensions include new neutral gauge bosons (Z′), leptoquarks interactions, and the extended gauge symmetry or Super Symmetry (SUSY) extension which manifests as SUSY loops or R-parity violating SUSY interactions. (see Figure 2.8.)

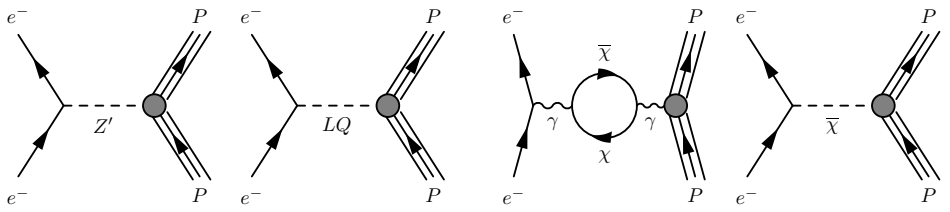

(a) (b)

Figure 2.8: Possible new physics at TeV scale. The new neutral gauge bosons (Z′) and leptoquarks interactions (Figure 2.8(a)) and SUSY loop and R-parity violating SUSY interactions (Figure 2.8(b)).

The weak charge of the proton (Q_W^p(msr)) from the Q_{weak} experiment and the weak charge of the electron (Q_W^e(msr)) measurement from E158 complement each other when constraining new physics beyond SM because the Q_{weak} measurement is a semi-leptonic measurement while the Møller measurement is a purely leptonic measurement. Different new physics interactions manifest more or less strongly in proton and electron weak charges to generate deviations from the SM (see Figure 2.9[†]). Therefore, both experimental results are helpful to interpret any observed new physics interactions.

In summary, the Q_{weak} experiment will provide a 4% measurement of Q_W^p and a 0.3% measurement of $\sin^2\hat{\theta}_W(Q)$ from the measured asymmetry at $Q^2 \sim 0.025(\mathrm{GeV})^2$.

[†]This plot was not generated using most up to date SM results for weak charge of the proton and weak mixing angle.

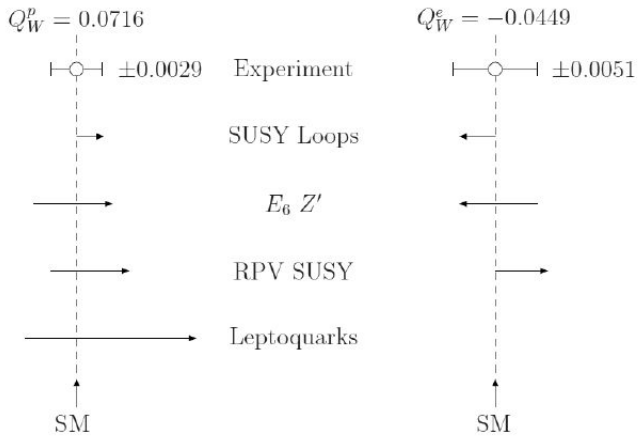

Figure 2.9: The deviations due to proposed new physics are compared with the SM results of the weak charges: Q_W^p and Q_W^e. The expected error of the Q_{weak} experiment and measured error of the E158 experiment are also included. The size of the arrow is the deviation of the weak charge allowed at 95% C.L. from each model (from [39]).

The orthogonal sensitivity between Q_{weak} and APV will provide the most stringent constraint on the effective couplings on vector hadronic currents (see Figure 2.6). These results will also provide model independent estimates on new PV physics mass and coupling scales and test the credibility of proposed new physics models beyond the SM.

3 The Q_{weak} Experiment

The Q_{weak} experiment measures the parity violating asymmetry in electron-proton elastic scattering to determine the weak charge of the proton. The expected physics asymmetry at a Q^2 of 0.025 $(GeV)^2$ is calculated to be -0.214 parts per million (ppm) (Section 2.1). The Q_{weak} experiment was designed to be an integrating experiment with a high luminosity target in order to obtain a 0.004 ppm statistical error within shortest possible time period. The important Q_{weak} experimental parameters during the Wien0 period are given in Table 3.1.

Table 3.1: Basic parameters of the Q_{weak} experiment during Wien0.

Parameter	Value
Average beam energy at vertex	1.155 GeV
Beam Polarization	88%
Beam Current (integrating Mode)	100-150 μA
Target	liquid hydrogen (LH2) at 20 K
Target thickness	35 cm
Luminosity	$1.0 - 1.5 \times 10^{39} cm^{-2} s^{-1}$
Beam current (counting Mode)	less than 1 nA
Nominal electron scattering angle	7.9^o
Angular acceptance	$\pm 3^0$
Total azimuthal (ϕ) acceptance	49% of 2π
Solid angle, $\Delta\Omega$	37 msr
Integrated cross section	4.0μb
Integrated scattering rate	5 GHz (0.6 GHz per detector)
Acceptance averaged Q^2	0.025 $(GeV)^2$
physics asymmetry	-0.214 ppm

Section 3.1 discusses the important experimental techniques used by the Q_{weak} experiment. Section 3.2 discusses the core hardware components of the Q_{weak} apparatus which include: the electron beam, the target, the collimators, the magnetic spectrometer, the Čerenkov detectors, and the Q_{weak} particle tracking system (See Figures 3.1 and 3.2).

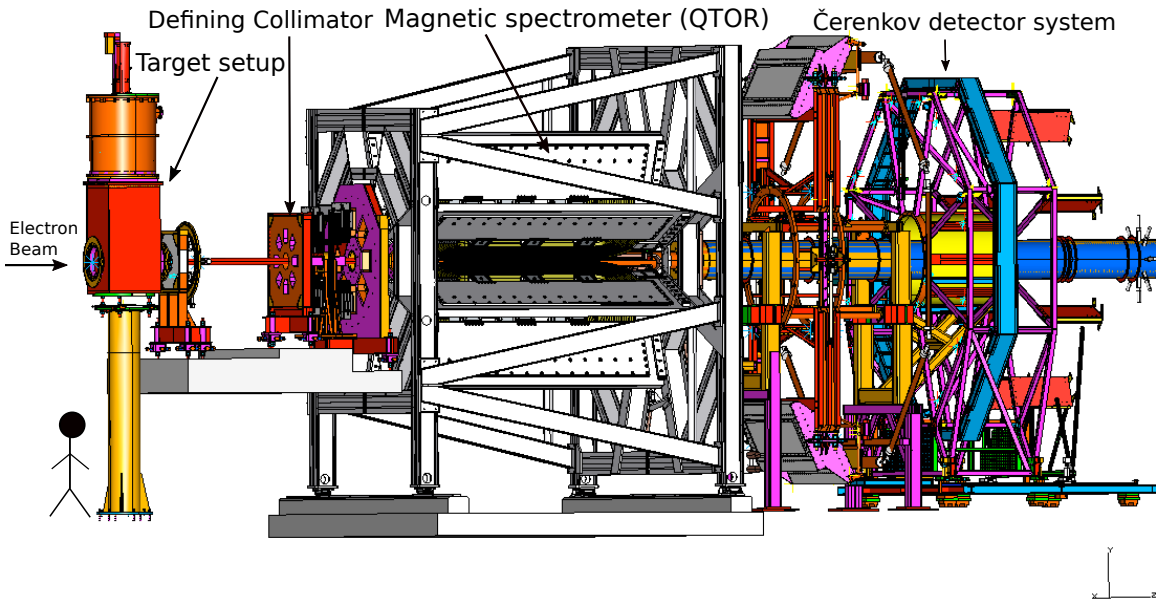

Figure 3.1: The CAD layout of the Q_{weak} experiment. The electron beam, the liquid hydrogen target, the defining collimator, the magnetic spectrometer and the ring of Čerenkov detectors are the core hardware sub-systems in the integrating mode (from [52]).

3.1 Experimental Techniques

The experimental technique used in Q_{weak} is known as Parity Violating Electron Scattering (PVES). It was first implemented by Charles Prescott in 70's and favored the electroweak coupling proposed by the SM over other models [3]. In PVES experiments, the helicity state of the longitudinally polarized electron beam is flipped

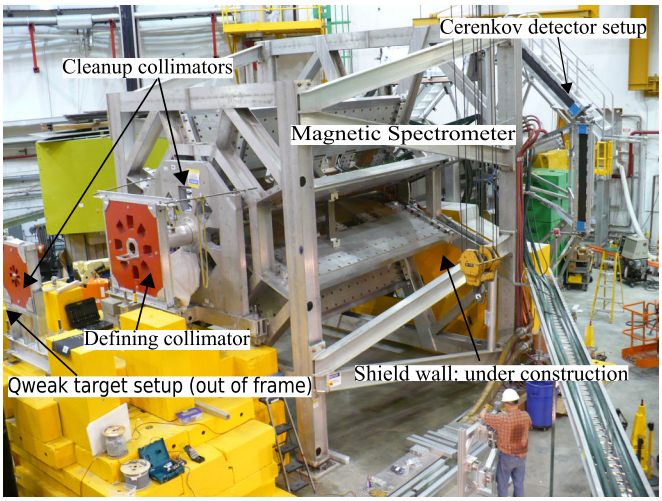

Figure 3.2: The Q_{weak} experimental setup during the installation in summer of 2010. The defining collimator, cleanup collimators, the magnetic spectrometer, and the Čerenkov detector setup were close to completion. The Q_{weak} target is out of the frame. Notice the scale of the apparatus compared to people around (from [52]).

between left and right, R/L (or +/−), and the electrons are scattered off from a fixed target which is an un-polarized proton target for Q_{weak} experiment (see Figure 3.3). The elastically scattered electron yield is measured for each helicity state, $Y^{L/R}$,† by integrating the signal from scattered electrons. The Helicity Correlated (HC) difference in scattered electron yield or the asymmetry is sensitive to parity violating quantities (equation 2.6). The raw asymmetry measured from helicity correlated yields is defined as,

$$A^{raw} = \frac{Y^R - Y^L}{Y^R + Y^L} \propto \frac{\frac{d\sigma^R}{d\Omega} - \frac{d\sigma^L}{d\Omega}}{\frac{d\sigma^R}{d\Omega} + \frac{d\sigma^L}{d\Omega}} \tag{3.1}$$

where $Y^{R/L}$ is proportional to detected scattered electrons from incident right/left (R/L) helicity electron beam. To the first order in beam current, the asymmetry

†The yield, $Y^{L/R} \propto L \int \frac{d\sigma^{L/R}}{d\Omega} d\Omega$ where L is luminosity.

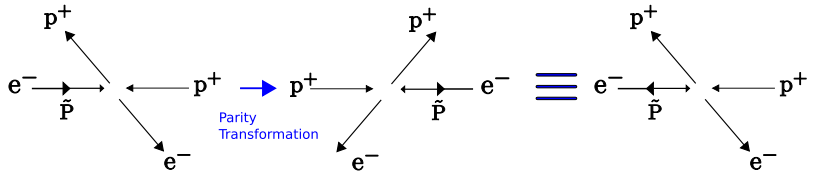

Figure 3.3: The parity transformation of the $\vec{e}^{-}p^{+}$ scattering is achieved by reversing the longitudinal polarization ($\vec{P}$) or electron helicity.

measurement is independent of beam luminosity (L). The Parity Violating (PV) asymmetry formulated in Chapter 2 (equation 2.12) is extracted from the measured raw asymmetry and this is the goal of the data analysis (Chapter 6).

The statistical uncertainty of the A^{raw} measurement is determined by the scattered total electron rate at the detector plane and how long the experiment took data. The statistical uncertainty is defined as,

$$\begin{aligned} \delta A^{raw}_{stat} &= \frac{\sigma}{\sqrt{N_{Total}}} \\ &= \frac{1}{\sqrt{(s \cdot R \cdot I) \cdot T_{total}}} \end{aligned} \tag{3.2}$$

where σ is the uncertainty of a single asymmetry measurement, N_{Total} is the total number of asymmetry measurements in the whole Q_{weak} experiment, the factor s ($= 0.89$) is the effective data read-out time at each helicity state (Section 4.1), R is the total scattered electron rate per μA at the detectors, I is the beam current/intensity, and the T_{total} is the total time required to make repeated measurements of the asymmetry. The quantity $\frac{1}{\sqrt{s \cdot R \cdot I}}$ is the statistical noise in a single asymmetry measurement (known as a quartet, to be discussed later) and it is about 200 ppm.

The scattered electron rate, R is based on the required kinematics of the Q_{weak} experiment. The electron beam current, I is limited by the capability of Continuous Electron Beam Accelerator Facility (CEBAF) and Q_{weak} apparatus. After

the scattering rate and beam currents are optimized, the final statistical uncertainty on the asymmetry (goal of 0.004 ppm) depends on T_{total} which can be parameterized as,

$$T_{total} = h_{pat} \cdot T_{int} \cdot N_{pat} \tag{3.3}$$

where the helicity pattern, $h_{pat} = 4$ is the no.of helicity states used to compute a single asymmetry measurement, T_{int} is the integration time interval or the length of a helicity state, and N_{pat} is the total no. of asymmetry measurements. The parameters h_{pat}, T_{int} (short or long helicity reversals), and N_{pat} are optimized to minimize other noise contributions.

The Q_{weak} experiment ran with integration period, $T_{int} = 1/(960\ Hz)$, which is a short reversal period compared to reversal period used in previous PVES experiments at the Jefferson Lab (1/30 Hz). The pattern size of choice is $h_{pat} = 4$ and this is known as a quartet (QRT) pattern, which consists of either R L L R or L R R L sequence of helicity states. The first helicity state of a QRT is generated pseudo-randomly using a 128 bit random generator to minimize certain periodic noise components (e.g. 60 Hz power line noise). The combination of fast helicity reversal and pseudo-random QRT patterns cancel the slow drifts in scattered electron yields, and minimizes the target density fluctuations. Under these conditions, the uncertainty of an asymmetry measurement is statistics dominated ($\sim 80\%$) for Q_{weak} experiment. The other noise contributions include resolution of the Čerenkov detectors, resolution of the Beam Charge Monitors (BCMs), and density fluctuations in the Liquid Hydrogen (LH2) target (see Table 3.2).

Helicity Correlated Beam Asymmetries (HCBAs) in beam parameters like charge, position, angle, and energy generate false asymmetries [53] that contaminate the measured asymmetry. These false asymmetries are corrected using linear regression (based on sensitivities computed using natural beam jitter or beam dithering).

Table 3.2: QRT-level noise contribution to the A^{raw} at 150 μA during Wien0.

Contribution	Noise-level (ppm)
Statistical	210 ppm
Detector resolution	90 ppm
BCM resolution	65 ppm
Target noise	55 ppm
Total	244 ppm

Combinations of active feedback and passive controls are implemented to minimize the HCBA. The false asymmetry corrections for the Q_{weak} experiment are discussed later in Chapter 6 (Data analysis). Finally, the asymmetry is corrected for the beam polarization, several background contributions, and various experimental biases to obtain the final party violating asymmetry which is defined in Chapter 2 (equation 2.12).

3.2 Experimental Apparatus

This section introduces the main subsystems of the Q_{weak} experiment: the CEBAF, the Q_{weak} target, the collimator system, the magnetic spectrometer, the main Čerenkov detector system, and the particle tracking system. A more detailed description of the Data Acquisition (DAQ) and Q_{weak} data analysis softwares can be found in Chapter 4.

3.2.1 Continuous Electron Beam Accelerator Facility

The main components of CEBAF are: the electron source, two linear accelerators and magnetic arcs, and three experimental halls (see Figure 3.4). The facility is capable of simultaneous beam delivery to all three halls at different energies, at

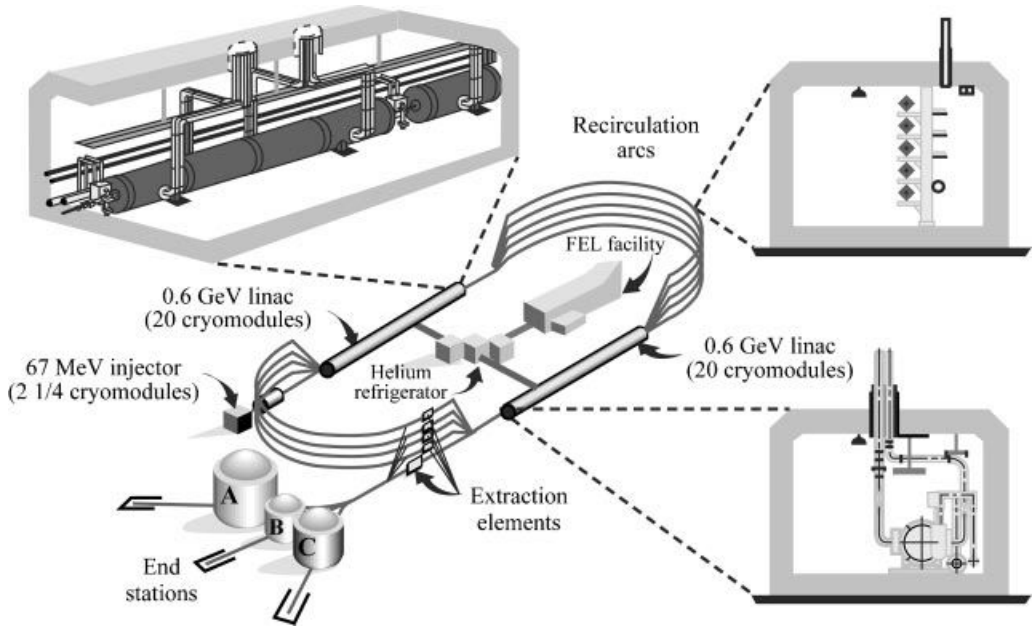

Figure 3.4: Schematic view of CEBAF in the 6 GeV configuration (from [54]).

different beam intensities, and different orientation of beam polarization. This is possible using the three independent laser sources in the injector and the five pass beam recirculation between the two linear accelerators (linacs).

Three independent circularly polarized lasers, one for each of the three experimental halls, are pulsed at 499 MHz. The lasers are incident on a common photo-cathode with a 120^{o} phase offset with respect to each other. The laser induces spin dependent electron excitation into the vacuum/free band of the strained GaAs/GaAsP photo-cathode material [55]. The spin dependent extracted electrons are then accelerated by an applied electric field to generate an electron beam. The photo-cathode and electron beam-line are housed inside an ultra-high vacuum (10^{-12} Torr) enclosure to minimize ion back-bombardment, which limits the photo-cathode life-time.

The optics setup consists of a laser source and active and passive optical elements (see Figure 3.5). The circularly polarized light is generated from linearly polarized

laser light using a Pockels cell [53], which has birefringence proportional to the applied electric field across the cell. The applied electric field is flipped to reverse the direction of the circular polarization. Due to imperfections, there is always residual linear polarization in the circularly polarized light. The residual linear polarization combined with the analyzing power on the photo-cathode generates certain classes of HCBA [53] including charge asymmetry. The Rotatable Half Wave Plate (RHWP) can be adjusted to orient the residual linear polarization vector to give equal magnitude in both circular polarization states at the photo-cathode. This technique minimizes HCBA from residual linear polarization. The Insertable Half Wave Plate (IHWP) is inserted in the laser beam before the Pockels cell to flip the direction of laser polarization. This is the primary slow reversal technique for the Q_{weak} experiment (the importance of the IHWP is discussed in Section 6.3.3).

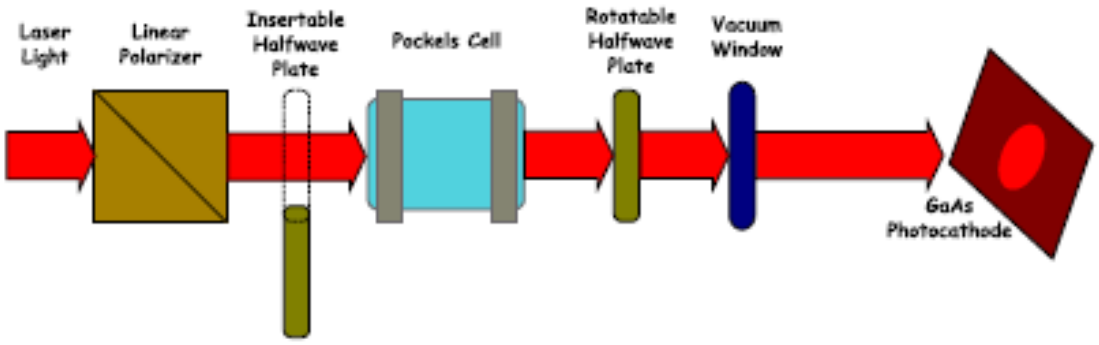

Figure 3.5: Schematic of the CEBAF laser optics setup (from [53]). The Pockels cell is the only active element shown here. The rest of optics are passive elements.

PVES experiments require the electron beam to be maximally longitudinally polarized at the target. Once electrons are extracted and partially accelerated, spin manipulating Wien filters are used to adjust the orientation of the electron spin and cancel the net spin precession of the electrons as they travel from the injector to the

experimental hall [53, 56]. A Wien filter consists of a static electric and magnetic fields in orthogonal planes. When the forces on the electrons between magnetic and electric fields cancel, the electron will go through the Wien filter without any deflection but the spin of the electron will precess around magnetic field. Two Wien filters are implemented to rotate the electron spin in horizontal and vertical planes. A pair of solenoids is integrated to Wien system to flip the spin orientation of the electron without changing the laser beam polarization (see the Figure 3.6). The Wien filters and solenoids are the basis for a slow helicity reversal to help cancel false asymmetries which might evade IHWP reversal (discussed in Section 6.3.3).

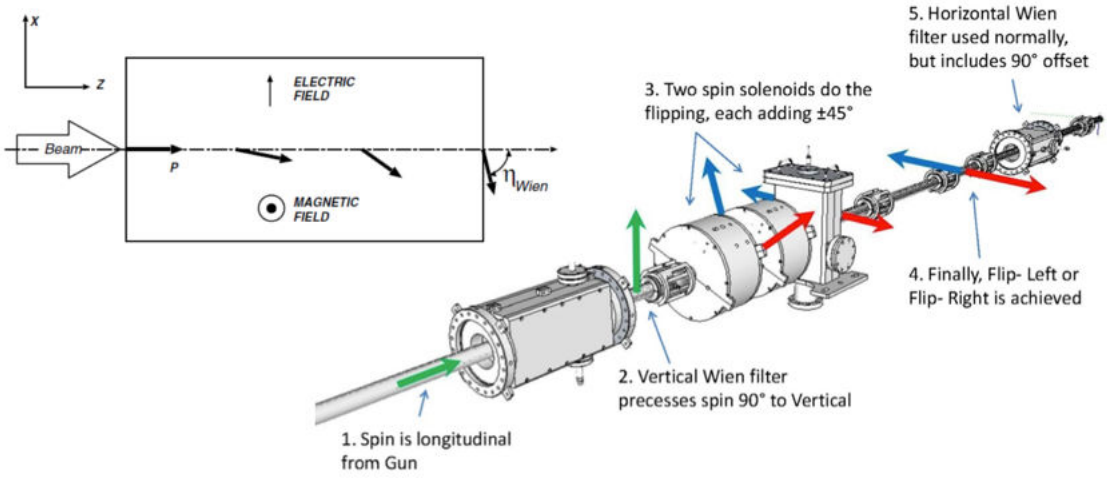

Figure 3.6: A Wien filter (inset figure) uses a combination of magnetic and electric fields to precess the electron spin without changing its direction. A double Wien setup is used to orient the electron spin to desired angle in horizontal and vertical planes, which enables the 100% longitudinal or transverse polarization in Hall C (from [57]). The two solenoids flip electron spin orientation with respect to the laser polarization at the injector.

The CEBAF main accelerator is a five pass recirculating system [54] with two superconducting radio-frequency (srf) linacs. Each linac contains a total of

20 cryomodules and is capable of accelerating electron bunches at 1497 MHz to 0.6 GeV [54]. The beam spreaders at the end of the south and north linacs spread the beam bunches with different energies to the appropriate beam-line arc specifically tuned to bend electrons of a specific beam energy. The beam recombiners reverse the process at the end of the arc (Figure 3.4). There are a total of nine arcs in the CEBAF main accelerator to have up to five passes through the linacs. Finally beam is delivered to experimental halls from the extraction region. For Q_{weak} data taking, the beam was extracted after 1-pass over the two linacs at the nominal beam energy of 1.15 GeV.

In summary, the CEBAF electron source generates electrons in bunches at 1499 MHz using three independent lasers pulsing at subharmonic 499 MHz. The beam gets accelerated up to energies ranging from 0.6 GeV to 6 GeV using a five pass recirculation between the linacs. At this bunch rate, the beam has a large duty cycle and is considered to be a continuous electron beam. During the Wien0 data taking, CEBAF delivered to the Q_{weak} target a 88% polarized electron beam at intensity up to 150 μA at parity data quality (discussed in Section 6.3) while in most cases simultaneously delivering beam to Hall A and B.

3.2.2 Beam Line Instrumentation

The beam-line starts at the photo-cathode and for Q_{weak} , it ends at the Q_{weak} target. Beam property monitors provide important measurements of the state of the electron beam. All this information is necessary to deliver a beam with minimum HC jitter[†] . The Beam Charge Monitors (BCMs) and Beam Position Monitors (BPMs) provide continuous charge and position measurements. A BCM is a cylindrical shaped cavity with an antenna inside to detect electromagnetic (EM)

[†]noise at the helicity reversal frequency.

radiation from the electron beam. The signal amplitude corresponds to the amount of beam charge passing through the device [58, pg. 40]. A BPM is a cylindrical cavity designed to resonate at the CEBAF fundamental 1497 MHz. The BPM cavities have four symmetrical antennas to pick up the radio-frequency (rf) signal generated by the passing electron beam. The amplitude of the signals from the antennas is proportional to the distance to the electron beam [59]. The BPM electronics are designed to tolerate beam current changes by adjusting the gains of the antennas. Therefore, BPMs provide beam position measurements over a wide range of beam currents (1 uA − 150 uA). In summary, the Beam-line monitoring devices provide,

- The beam charge/intensity and HC difference (Section 6.1.3),
- The beam position and angle at the target and HC differences (Section 6.1.3),
- The indirect measurement of relative beam energy and HC energy asymmetry (Section 6.1.3), and
- Indirect measurements of the beam spot size HC differences

3.2.3 Cryo-Target

The Q_{weak} target has allowed the experiment to operate up to a luminosity of about 1.5×10^{39} $s^{-1}cm^{-2}$ during Wien0 (overall up to 2×10^{39} $s^{-1}cm^{-2}$, which is the most powerful cryogenic LH2 target in the world [60]). The 35 cm long target received up to 150 μA rastered beam current during Wien0. A raster is the mechanism that spreads the electron beam on a square area (square profile) at the target uniformly. The raster completes a total cycle of motion within a helicity state to cancel the raster generated position dependence. When electrons traverse on the LH2 target cell, the system is heated by ionization and conductive heat losses in the liquid hydrogen and on the aluminum target windows. About 1800 W of power is dumped by the

150 μA beam at energy 1.155 GeV [61]. This has required an unique hybrid cooling system at JLab using refrigeration power from two sources (known as End Station Refrigerator (ESR) at 15 K and Central Helium Liquefier (CHL) at 4 K) to keep the LH2 target at required temperature of 20 K.

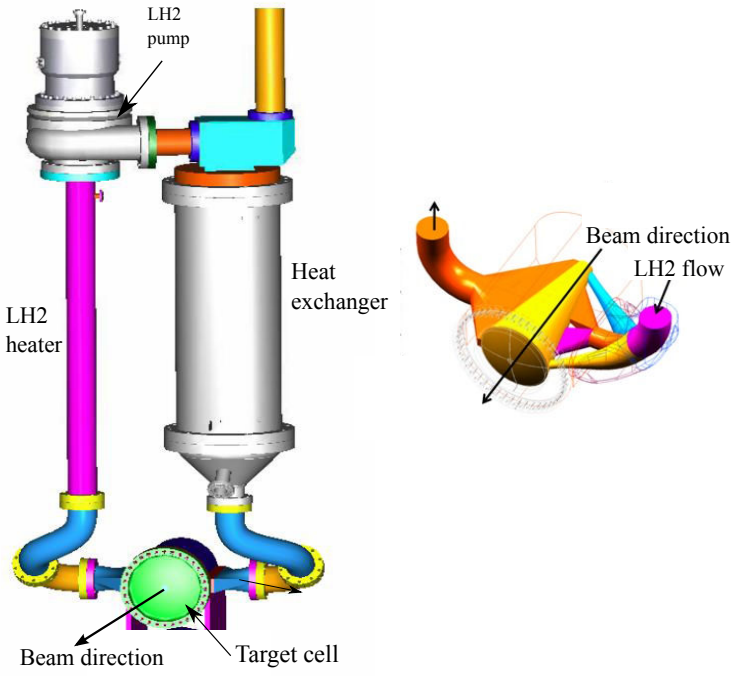

Figure 3.7: Left: Basic layout of the target cell and the liquid hydrogen loop (from [61]). Right: The conical shaped target cell where electrons are scattered (from [52]). In the target cell, there are four inlets and one broad outlet for LH2 transverse flow. Note that two of the four inlets cool the aluminum windows where a lot of heat is generated.

The Q_{weak} target (see Figure 3.7) was designed using Computational Fluid Dynamics (CFD) simulations to maintain nominal fluid density while minimizing noise from density fluctuations (Figure 3.8). Helicity Correlated (HC) noise contributions

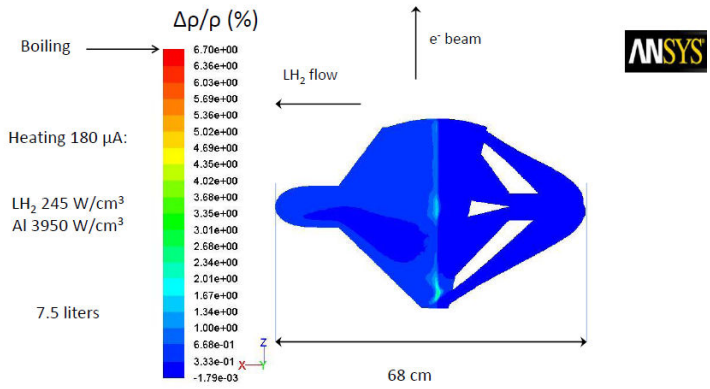

Figure 3.8: A steady state CFD simulation result with density variations across the target cell when the 180 μA electron beam is incident (from [61]).

Table 3.3: The Q_{weak} target Properties during Wien0 [62].

Parameter	Value
Target Length	35 cm
Max. Beam Current	150 μA
Luminosity	$\sim 1.5 \times 10^{39}$ s^{-1}cm^{-2}
Beam Power	1800 W
Raster size	3.5 $\times$ 3.5 mm^2
Total cooling power	2500 W
Total LH2 flow	1.1 kgs^{-1}
Density fluctuations	$\sim$ 65 ppm

at 1 KHz scale including target density fluctuations are extremely difficult to simulate due to computational constraints. Instead, dedicated measurements were taken at different LH2 flow rates (pump speeds) and helicity flip rates during the Q_{weak} data taking. During Wien0, a transverse flow of liquid hydrogen at 20 K was kept across the cell using a cryogenic pump at 30 Hz. The beam profile at target (raster) of 3.5×3.5 mm^2 was used during Wien0 but later changed to 4×4 mm^2 to further

reduce the target density fluctuation noise [63]. The azimuthally symmetric target design and target window curvature minimize false asymmetries from HC position differences and complement the azimuthally symmetric Čerenkov detector system. Table 3.3 summarizes important target performance goals achieved during the Q_{weak} experiment. Overall the Q_{weak} target performance exceeded expectation.

There were also many different types of auxiliary targets [61] implemented in the Q_{weak} target system. They were required for the detector calibrations, tracking mode optical alignment of the beam, beam centering studies, etc. The auxiliary targets were attached at the bottom of the LH2 cell. A sophisticated target ladder was implemented to move the LH2 cell out of the beam-line and move any auxiliary target in the ladder to the electron beam, and vise-versa.

The Q_{weak} target cell and all the auxiliary targets were kept inside a scattering chamber under a vacuum environment. The exit window of the scattering chamber, where the scattering electrons pass from the vacuum to the open air, is made out of aluminum alloy with thin spots to cover Q_{weak} acceptance to reduce radiative effects on the scattered electrons [61](see Figure 3.9). The target cell is made out of an aluminum alloy. The electron beam interacts with the entrance and exit windows of the target cell to generate a background contribution. A set of auxiliary thick aluminum targets were used to determine the aluminum background asymmetry and the dilution of the measured yield.

3.2.4 Q_{weak} Collimator System

The collimator system minimizes the inelastic and neutral background contribution to the detector rate. The first collimator after the Q_{weak} target and the third collimator in-front of the magnetic spectrometer act as shielding collimators from the intense radiation generated by photons and inelastic electrons. The second col-

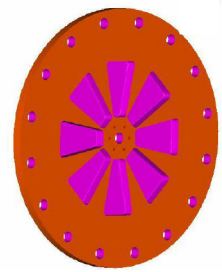

Figure 3.9: Scattering chamber exit window. The thin regions in the wagon wheel structure covers the Q_{weak} acceptance (from [52]).

limator (defining collimator) defines the angular acceptance of the experiment (see Figure 3.2). A shield wall with openings for scattered electrons was located in-front of the Čerenkov detector setup to further limit neutral background contributions (see Figure 3.10).

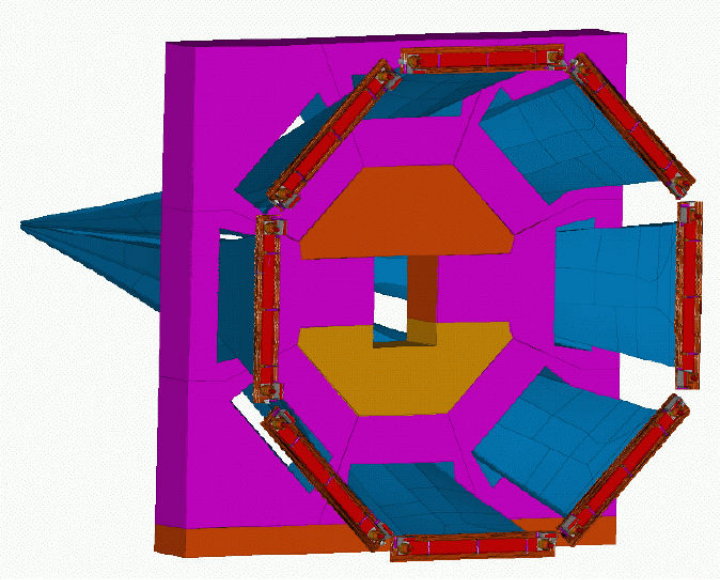

Figure 3.10: The shield wall when looked upstream of the setup. The acceptance of the scattered electrons is not reduced due to the shield wall (from [58]).

Simulation studies have shown that electrons scattered at very small angle can interact with the beam-line downstream of the target. They generate backgrounds which are difficult and costly to shield [58, pg. 54]. A water-cooled tungsten collimator (aka tungsten plug) was installed just downstream of the Q_{weak} target to block these scattered electrons while passing the rastered beam and multiple-scattered primary beam through this collimator (see Figure 3.11). There were two sources of backgrounds (mostly neutrals) that were not 100% contained using collimators and Q_{weak} TORoidal (QTOR) system (see Figure 3.12). The tungsten plug itself is a source of an intense secondary photon (and other neutral particles) beam. Also the primary elastically scattered electrons interact with the collimators and the shield walls (scraping) to generate photon backgrounds. These two background contributions were estimated using various dedicated measurements and will be discussed in the data analysis chapter. The bremsstrahlung photons (shown in the simulation result in Figure 3.12) from the elastically scattered electrons are part of the detected electrons and not a source of background.

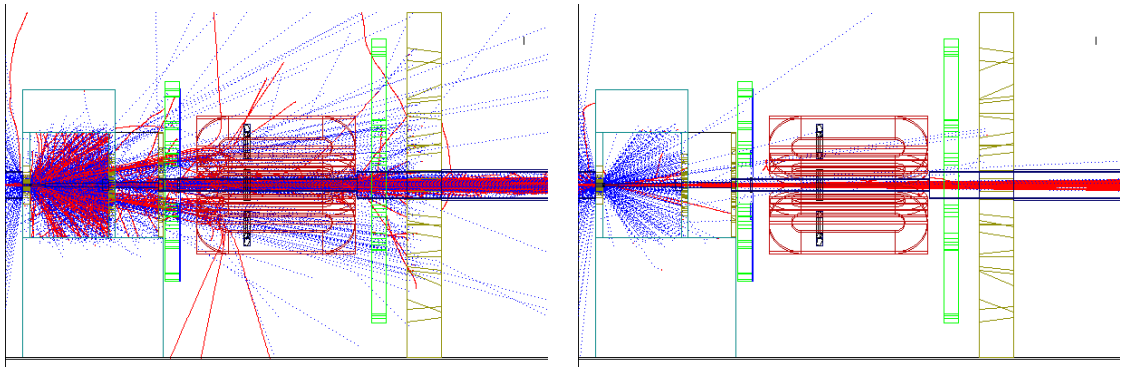

(a) Before tungsten collimator installed (b) After tungsten collimator installed

Figure 3.11: The tungsten collimator installed just downstream of the target helps to reduce certain backgrounds from small angle scattered electrons (from [58]). Notice the ratio of neutrals (photons) to electrons is significantly reduces after W-collimator is installed (right).

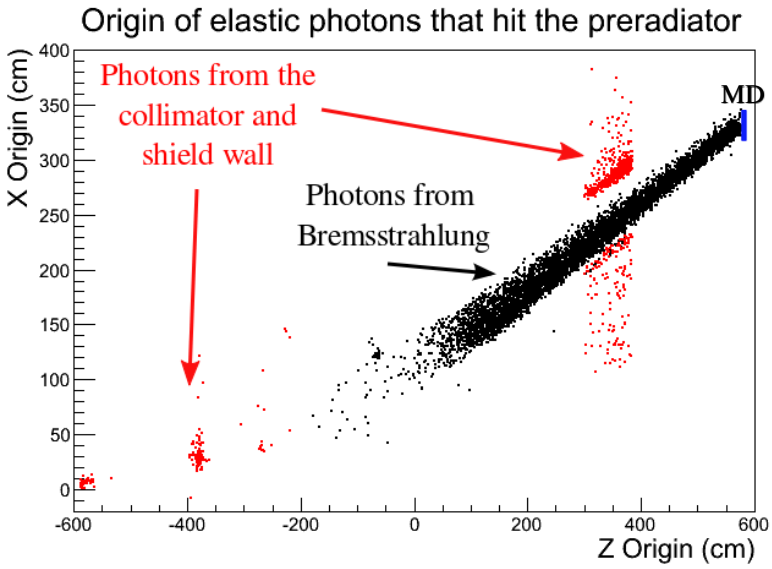

Figure 3.12: The origins of the photon generated by scattered elastic electrons include the tungsten plug, defining collimator, and the shield wall. The origins of the bremsstrahlung photons from scattered electrons are also shown (from [58, pg. 54]).

3.2.5 Q_{weak} Magnetic Spectrometer: QTOR

The spectrometer used by the Q_{weak} experiment is a magnet with eight toroidal race track type magnetic coils and it is called Q_{weak} TORoidal (QTOR) magnet (see Figure 3.13). The Q_{weak} collaboration chose a resistive toroidal magnetic system for the large azimuthal acceptance (49% of 2π), low cost, and reliability compared to a superconducting magnet. The magnetic field flux of $\int \vec{B}\cdot d\vec{l} \simeq 0.89$ Tm [60] is required to focus the scattered electrons envelope into the detector plane.[†]

The combination of collimators and QTOR minimizes background contributions and focuses elastically scattered electrons to the eight azimuthally symmetric Čerenkov detectors (Section 3.2.6) while sweeping the inelastic electrons away from the detector plane. The collimator system was optimized using Monte-

[†]We need to bend elastically scattered electrons at $\theta_{scat} \sim 8^{o}$ with momentum of 1.155 GeV by $\sim 13^{o}$

Carlo simulations to maximize elastically scattered electrons while suppressing the background contributions from photons at the detector plane [58, pg. 54].

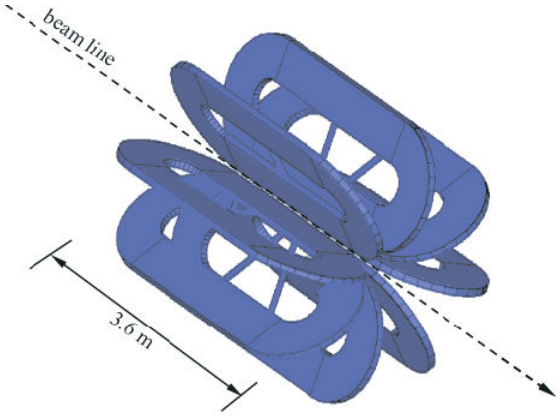

Figure 3.13: Basic layout of the QTOR spectrometer. Current flows in each coil in a racetrack path to generate the toroidal magnetic field between the coils (from [52]). Ideally, there is no magnetic field along the 0^o axis along which the beam passes to the dump.

3.2.6 Detector Systems

The Q_{weak} detector systems include the Čerenkov detectors to measure the scattered electrons and the beam luminosity monitors. First, I will discuss the Čerenkov main detectors and then provide an overview on the beam luminosity monitors.

The elastically scattered electrons are focused by QTOR into eight azimuthally symmetric envelopes 10 cm tall radially by 200 cm wide (see Figure 3.14). A fused silica Čerenkov detector sits in each of these octants. Each detector contains two optically coupled quartz bars each 100 cm long (see the Figure 3.15). The quartz material selected for the main detectors is optical polished Spectrosil 2000 [60]† .

†The actual radiator material is "artificially fused silica" a high purity glassy form of SiO_2. "Quartz" is normally a crystalline, mined material, which is not radiation hard due to contaminants.

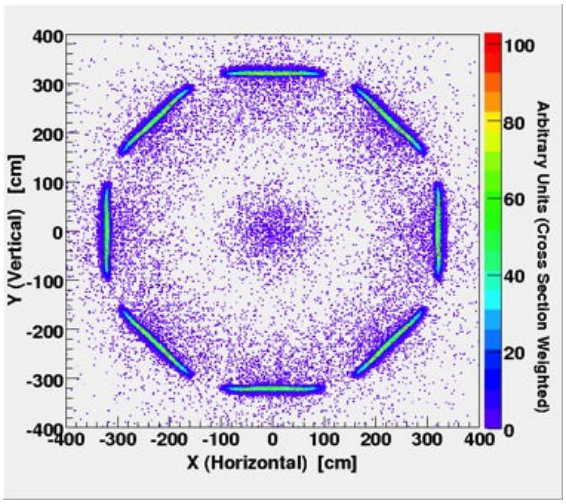

Figure 3.14: A simulation generated 2D plot where the elastic electron envelopes are focused to eight octants where Čerenkov detectors are positioned (from [52]).

This material is Ultra-Violet (UV) transparent even after a dose of 1 MRad [64] from the whole experiment when using pre-radiators. At each end of the bar, a 5 cm diameter photomultiplier tube (PMT) is glued to a quartz light-guide sitting outside of electron flux envelope. The PMTs have UV glass windows to provide a cut off at 250 nm from high energy photons. Two sets of PMT bases were used, one for the integration mode and one for the counting mode (discussed in Section 3.2.7). In the integrating mode, PMTs are configured to measure helicity correlated electron yield and in counting mode, PMTs are configured to detect individual electron tracks.

The quartz material is insensitive to photons with energies below 0.5 MeV as well as non-relativistic charged particles. Indeed, scintillation and luminescence in Spectrosil 2000 is extremely small [60]. Nevertheless, background signals in the quartz are generated from higher energy photons (> 0.5 MeV) or from neutron capture or decay. The PMTs can also detect neutral backgrounds, however in this case even low energy x-rays can contribute. These effects have been investigated during the commissioning and running of the experiment.

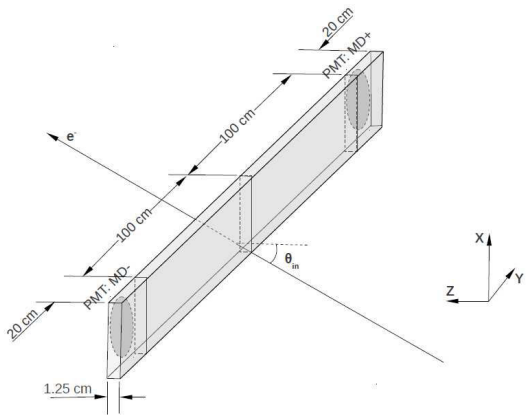

Figure 3.15: The main detector individual bar. Both ends of single bar contain PMT connected via light guides (from [65]). Dimensions are 200 $\times$ 18 $\times$ 1.25 cm^3 when light guides are excluded. The Pb pre-radiator is not shown here.

The Čerenkov detector signal only has small excess noise ($\sim 10\%$) above the counting statistics errors (detector resolution). The observed non-linearity of the detectors is about 1% at the nominal beam intensity [66]. The system was completely isolated from the helicity state reversal signals to prevent electronics cross-talks that could introduce helicity correlated noise [67]. A lead(Pb) pre-radiator was added in-front of the main detectors based on simulation studies to improve the elastic electron light yield while reducing any neutral particle contributions (improved the Signal to Noise ratio (S/N) ratio) [65].

3.2.6.1 Beam Luminosity Monitors

The beam luminosity monitors, like the main detectors were based on fused silica Čerenkov radiators [68]. There were two sets of azimuthally symmetric luminosity monitors available. One set was located at the upstream side of the primary collimator and the other set was located very close to the beam dump area. They were designed to detect electrons from small angle electron-proton and electron-electron scattering with an anticipated ppb-level (parts-per-billion) asymmetry. The intent

was to use these low statistical noise signal to check the linear regression systematics and measure target density fluctuations. In operation, they were extremely useful in estimating beam-line neutral backgrounds for Wien0 (Section 6.10.1) but did not behave as expected. First, the measured noise is high due to the high sensitivity to the electron beam position (O(100, 000 ppm/mm)) and the finite BPM resolution of about 1 μm/QRT. Secondly, the measured asymmetries from the luminosity monitors were not small as anticipated, and they were time dependent [68].

3.2.7 Particle Tracking System

The particle tracking system, which operates at 3-6 orders of magnitude smaller beam current than the parity production, is used to study acceptance and backgrounds, and to benchmark Q_{weak} simulations system to experimental biases.

In the Q_{weak} apparatus, the tracking detectors were installed in Region 2 (R2) and Region 3 (R3) (see the Figure 3.16) and covered two opposite octants simultaneously [69]. Both R2 and R3 detectors were mounted on a mechanical rotor and could be positioned in front of any pair of opposite octants.

The R2 detector (Figure 3.17) is a pair of Horizontal Drift Chambers (HDCs) positioned after the defining collimator and before the QTOR spectrometer. The chambers have about 200 μm position resolution [69]. The vertex of the electron track in the target and the scattering angle could be determined using the R2 detectors. The R3 detector (Figure 3.17) system is placed after the QTOR and in-front of the main (Čerenkov) detector system. It is a pair of Vertical Drift Chambers (VDCs) with a resolution of about 100 μm followed by a pair of plastic scintillators, one for each octant. The particle tracks generated by R3 detectors can be correlated between main Čerenkov detectors and scintillators or VDCs for kinematic and background studies. A small detector called profile scanner (see the Figure 3.17) movable across the focal

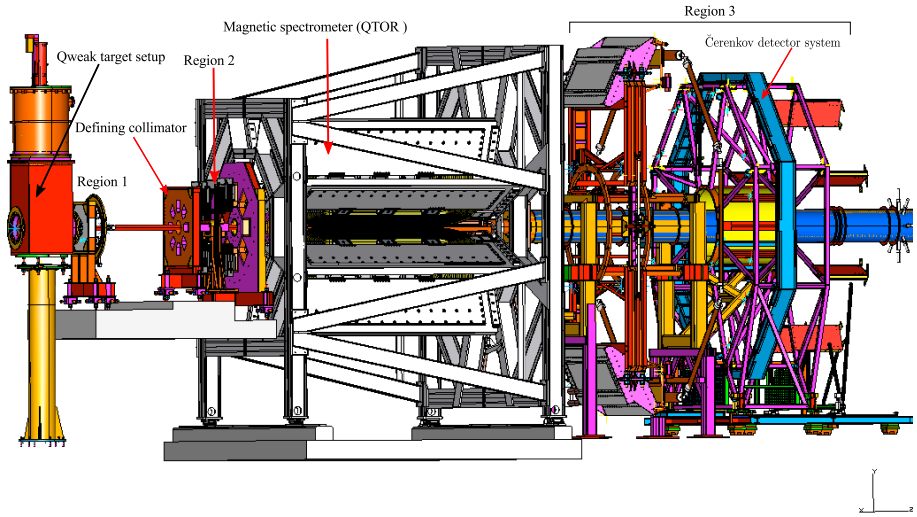

Figure 3.16: The CAD layout of the three regions of the Q_{weak} tracking system (from [52]).

plane of the bottom main detector octant was used to map the rate distribution over the focal plane during counting and integration modes of running. The results from this detector provide the important bridge between the behavior of Čerenkov detectors in counting and integrating modes.

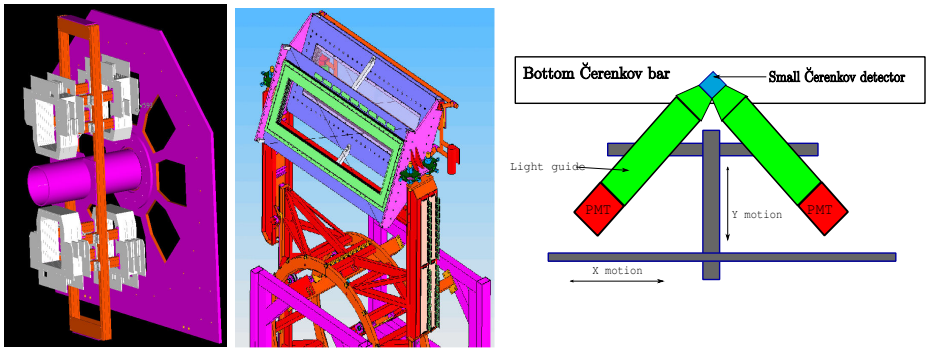

Figure 3.17: Left: The CAD layout of the pair of R2 HDCs. Middle: The CAD layout of the R3 VDCs. Both systems were mounted on the mechanical rotator. Right: The layout of the R3 profile scanner which can be moved across the focal plane to map the rate distribution in counting and integrating modes. (from [52])

4 Data Acquisition and Analysis Systems

The Q_{weak} experiment has implemented two independent Data Acquisition (DAQ) systems for integration and counting modes to acquire data for the main measurement and particle tracking based studies, respectively. The Q_{weak} DAQs were based on the CEBAF On-line Data Acquisition (CODA) framework [70–72] developed for experiments at Jefferson Lab (JLab). A custom built C++ analysis framework is used to analyze the Q_{weak} data.

I have contributed to the Q_{weak} DAQs, data analysis softwares, and related projects. I will provide an overview of the DAQ and data analysis framework and discuss projects to which I have contributed.

4.1 Integration Mode Data Acquisition System

The goal of the Q_{weak} integration mode DAQ (a.k.a. parity DAQ) was to record the integrated signals or yields from all the detectors and beam monitors. The only required trigger in the parity DAQ was the 960 Hz helicity signal (also called Macro Pulse Signal (MPS)). The MPS was generated at the CEBAF injector and a copy of the MPS was sent to the parity DAQ to generate the Analog to Digital Converter (ADC) gate signal. The gate signal was set to sample the detector and monitor signals using ADCs only during the stable period (T_{stable}) of a helicity state (see Figure 4.1). The settle period (T_{settle}) at the end of a helicity state was required to make the helicity transition and stabilize the Pockels cell (reduce the ringing effect) to reduce helicity correlated false asymmetries. For the Q_{weak} experiment, timing settings $T_{settle} = 70$ μs and $T_{stable} = 972$ μs were used. The ADCs were custom made (known as VQWK-ADC, see Section 4.1.1) for Q_{weak} and they have an internal delay before the start of data sampling (delay is 43 μs) to accommodate internal processing. The detector and monitor signals were sampled and integrated over the shaded region

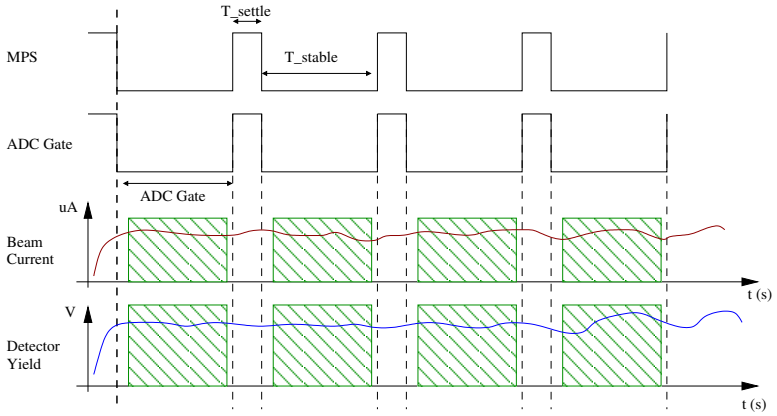

Figure 4.1: The trigger and ADC gate timing diagram. The gate is generated from the MPS. The filled area show the period of T_{stable} sampled by the VQWK-ADC where sampling starts after 43 μs into the helicity state and ends about 1 μs before the gate pulse.

in each helicity state (see Figure 4.1) by these VQWK-ADC channels. The T_{settle} and internal delay resulted in an effective data read-out period of 89% (or s=0.89) in each helicity state.

The integrated yields of certain beam monitors (for example the beam halo monitors) were recorded for diagnostic purposes using scaler (used SIS3800 series VME modules) channels through a Voltage-to-Frequency (V/F) converter which provided a less precise measurement compared to the VQWK-ADCs.

The parity DAQ required five Read-Out-Controller (ROC) crates to accommodate all the electronic read-out channels (VQWK-ADCs, Scalers, helicity, etc). The ROC crates managed the triggering and data read-out control for the electronic modules connected to it. A central VERSAModule Eurocard (VME) module called the trigger supervisor [70] was implemented to manage and synchronize triggering and data read-out processes for the five ROCs (see the Figure 4.2).

The parity DAQ produced data at about $7-8$ MBs^{-1}, and over 90% of this were generated by the integrating VQWK-ADC channels (See Appendix C.2.1).

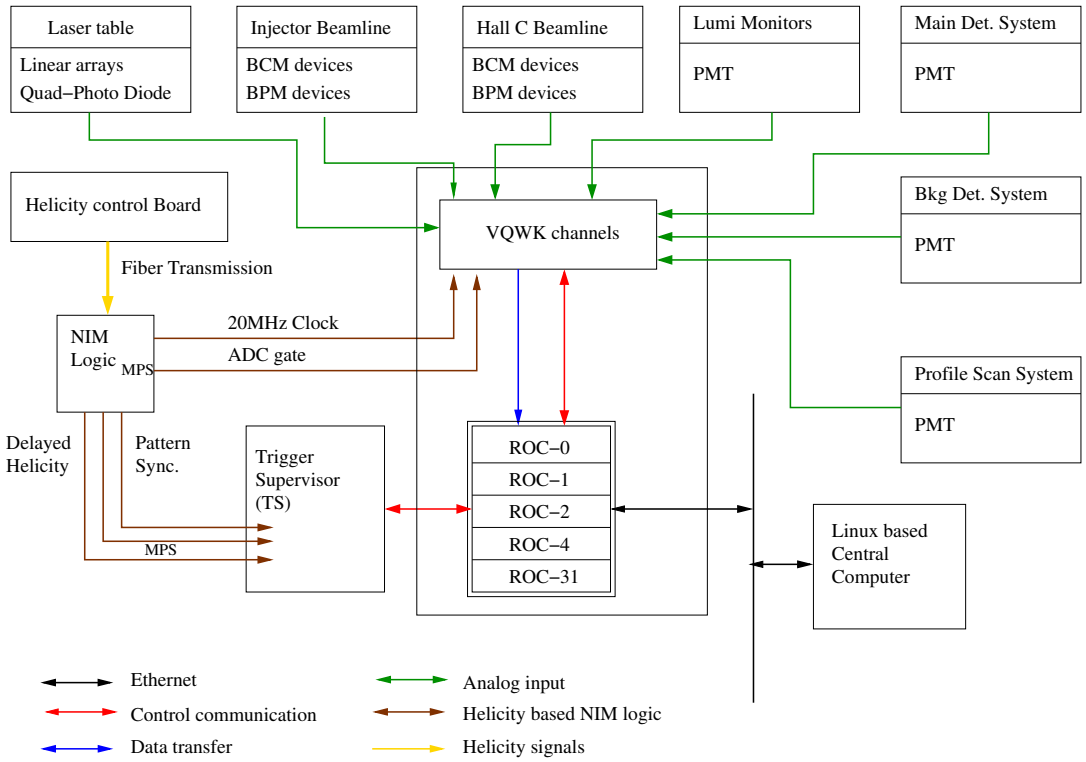

Figure 4.2: The parity DAQ layout with the MPS trigger. The VQWK-ADC modules are housed inside ROCs and analog detector signals are connected to the read-out channels in these modules. the VQWK-ADC channels are shown outside of the ROCs only for illustration purpose. Only the VQWK-ADC channels are shown here.

On average, a run lasted about $55-60$ min and each run was segmented into $1.9-2.0$ GB data files called runlets. One run has about $9-12$ runlets. Each runlet contains a succession of physics events which are triggered by the MPS, in sequential time order.

4.1.1 Front-end Electronic: VQWK-ADC Modules

The VQWK-ADC is a sampling integrating ADC, in which analog input of ± 10 V goes through a 5-pole 50 kHz low pass filter and into a 18 bit ADC. For PMT signals, the inputs go through a low noise current to voltage converter. An input signal is

sampled at 500 kHz (samples-per-sec) and each sample is read-out by the 18-bit ADC (see Figure 4.3). Then all the ADC samples are added by an internal Digital Signal Processing (DSP) chip (see user manual [73]). For the Q_{weak} experiment, samples were also summed into four sub-blocks by the DSP and made available for each helicity state. At 960 Hz read-out rate, the integrated VQWK-ADC signal has a resolution of ± 4 μV from the integrated 27 bit data word (See Appendix C.2.1). The Root Mean Square (RMS) of the noise generated from the VQWK-ADC electronics are at the level of about 3 ppm which is measured using a battery source as an input to a VQWK-ADC channel (see the Figure 4.4). This noise level is very small compared to the RMS of the measured asymmetry (about 240 ppm from Section 3.1).

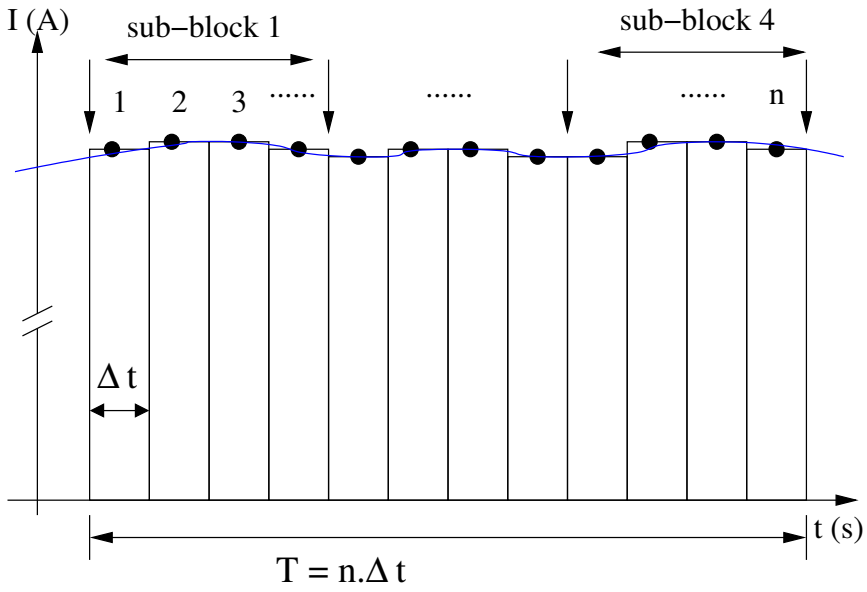

Figure 4.3: The input signal is sampled n times (with $\Delta t = 2$ μs samples) and each sample is digitized by an 18 bit ADC. All the digitized samples are summed to get integrated signal during a helicity state. Each channel also generates four sub-block sums. For illustration purposes, the input signal fluctuations are exaggerated.

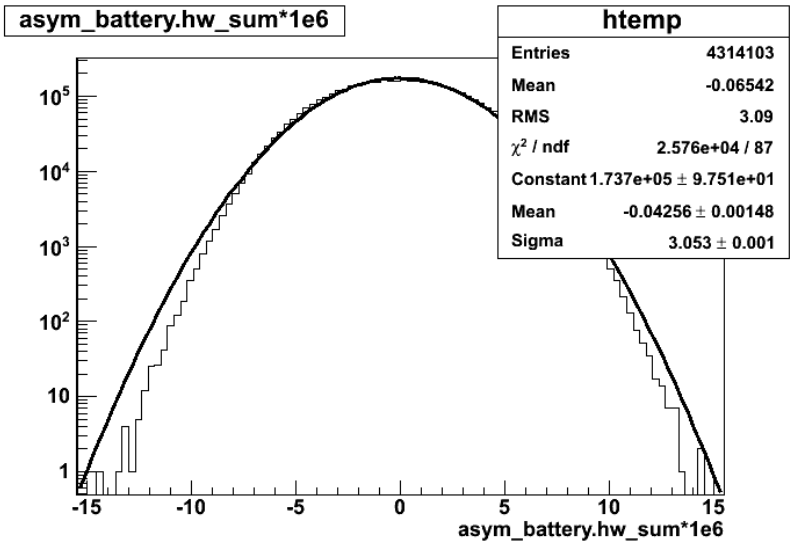

Figure 4.4: The measured asymmetry from a battery (constant current) source readout by a VQWK-ADC channel (from [74]).

A total of about 260 VQWK-ADC channels were read from the main detector photomultiplier tube (PMT) channels, Beam Charge Monitor (BCM), and Beam Position Monitor (BPM) channels (See Table C.1). The VQWK-ADC modules, each with 8 channels, were mounted into ROCs (See Figure C.3). All the VQWK-ADC modules were clocked using a 20 MHz external clock to keep them in synchronization between channels. Only the leading edge of the gate (see Figure 4.1) is used by VQWK-ADC modules to start the predefined integration period. These modules were designed by TRI-University Meson Facility (TRIUMF) [75] for the Q_{weak} experiment.

4.2 Counting Mode Data Acquisition System

The particle tracking system ran at orders of magnitude smaller beam currents to track individual particles across the Q_{weak} apparatus at minimum multiplicity. The Q_{weak} counting mode DAQ (a.k.a. tracking DAQ) recorded signals from the particle tracking detectors located in Region 2 (R2) and Region 3 (R3) of the Q_{weak} apparatus (see Section 3.2.7). The tracking DAQ was more sophisticated than the parity DAQ

because it handled multiple triggers simultaneously (see Figure 4.5 for the layout and see Appendix C.3.1 for a detail list of tracking trigger diagrams). Trigger sources include: R3 scintillator, profile scanner and Čerenkov detectors, R2 scintillator paddles, and a variable rate clock signal to replace the helicity signal (960 Hz or 10 Hz were common). A set of pre-scale factors scaled down the total input rate from trigger sources to reduce DAQ dead-time (see Appendix C.3). During nominal running, the DAQ could acquire up to about $1-2$ kHz input rate from triggers (some instances, took data at rates up to 3-4 kHz). The triggers from particle tracking detectors in R2 and R3 were used to read-out Time to Digital Converter (TDC) and charge sensitive ADC (QDC) channels.

The DAQ also recorded beam current and luminosity monitor rates using scaler channels since actual beam monitoring was not possible using integrating mode electronics at this low beam currents, the particle tracking system was operated. For scaler channel read-outs, the 960 Hz MPS signal was replaced with a $1-10$ Hz clock trigger (Fake MPS) signal to record noise discriminated detector/monitor rates. The main Čerenkov detectors were also read out using scaler channels because scaler rates were important in determining absolute scattered rates which provided first order measurement of the total scattering cross-sections.

The TDC data were used to count tracks or calculate rates and determine relative timing between tracking detectors in different regions (R2 and R3). The Horizontal Drift Chamber (HDC) and multiplexed Vertical Drift Chamber (VDC) wire signals were directly connected to TDCs. The Q_{weak} experiment used the pipeline TDC called F1TDC [76] to read multi-hits from wire chamber signals. This was necessary because the wire chamber signals were not discriminated and the first hit/signal on a wire was not always the correct hit and random hits could be generated from noise. On average 2-4 hits per wire were recorded during particle tracking studies. The F1TDC

and scaler input signals from main Čerenkov, scanner, and luminosity and beam-line detectors were discriminated to reduce random noise contribution. The Čerenkov and scintillation detectors were also read-out by charge sensitive ADCs (QDCs) to estimate the number of Photo-Electron (PE) per track. TDC and QDC data were necessary to separate charge and neutral particles, and to compare integrating mode main detector yields to counting mode yields.

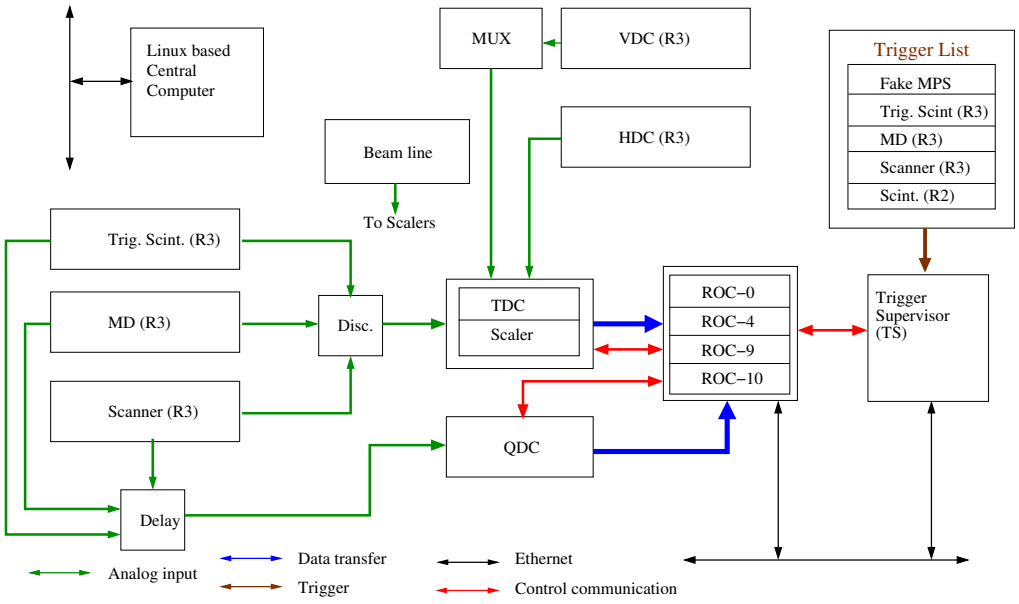

Figure 4.5: The tracking DAQ layout with multiple trigger sources. Note: the TDC, QDCs, and scalers were housed inside ROCs.

4.2.1 Front-end Electronics: F1TDC Modules

The F1TDC is a high resolution (up to 10 ps) multi-hit pipeline TDC [76, 77], and it is capable of saving up-to 7 hits within a custom hit window defined for a F1TDC channel (the hit window was set to 2000 ns, see Figure 4.6). The trigger signal initiates a scan over the hit window to save the set of TDC signals. The F1TDCs

were mainly implemented to record wire chamber signals (HDC and VDC). Even though the multi-hit capability was not an requirement, non-wire chamber detectors were also read-out by the F1TDC due to availability and consistency.

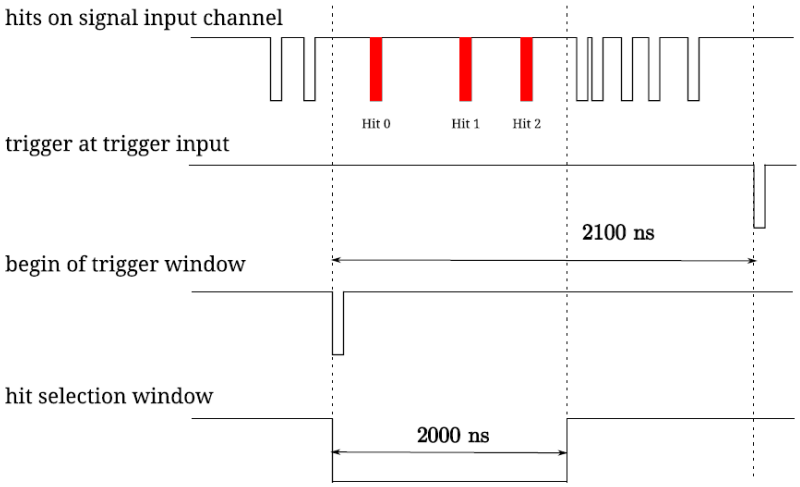

Figure 4.6: F1TDC trigger and hit selection diagram. The hits (red) within the selection window for each trigger were saved when a trigger is initiated (from [77]).

4.3 Data Analysis Framework

The analysis framework for the Q_{weak} experiment is written from scratch using the C++ object oriented language. A modular approach is used to keep the framework extendable and independent of the functionalities of the actual detectors. It is designed to decode data from the electronic channels stored in CODA data format, and to construct meaningful detector quantities (yields, asymmetries, particle tracks, etc.). The results are saved into CERN ROOT data structures (histograms and Trees) and into a MySQL database. The analysis framework can read the raw data files generated by the DAQ (off-line mode). It can also connect to the DAQ while taking data (real-time mode) and produce real-time results of the data in parallel to data saved into the disks. I have contributed to the development of this framework

and many projects related to it. In this section, I will discuss the analysis framework and projects that I have contributed to. First, the important features of the analysis framework are introduced with technical in-depth.

The abstract class, `VQwSubsystem` is the basis of all the detectors implemented in the analysis framework. The advantage of this C++ inheritance structure is the ability to define routines that all the subsystems in the base classes must use. The functionalities of the routines defined in the base class include: load configuration files, access raw data for each event, create CERN ROOT output containers (Trees/histograms), process raw data into meaningful quantities, apply data quality cuts, compute quartet (QRT) based quantities[†] , fill Trees/histograms, compute running averages[†], generate error summaries[†], and update database entries[†]. Then C++ polymorphism enables control of these functionalities for all the detectors from one main control program. Since data from tracking and integrating mode detectors are unique, two base classes are derived from the `VQwSubsystem` class (see Figure 4.7) for tracking and integrating mode detectors.

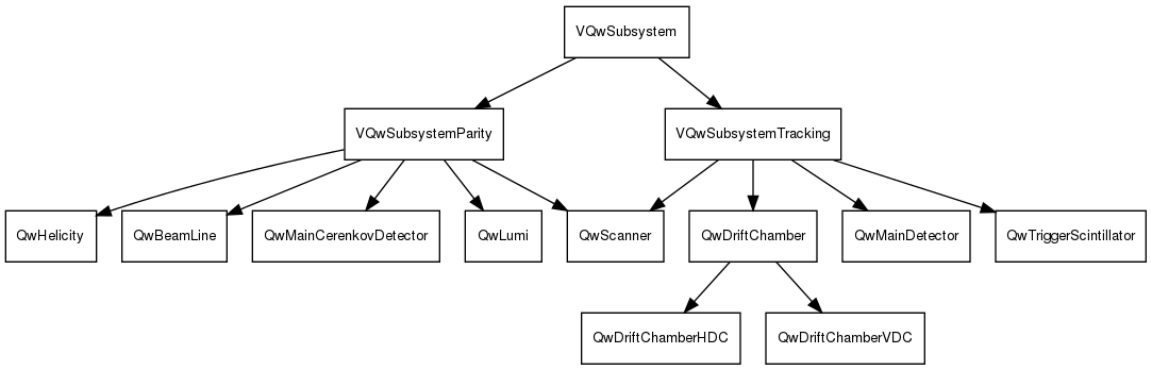

Figure 4.7: The global inheritance structure of the Q_{weak} analysis framework with parity and tracking detectors as subsystems.

[†]Only in integration mode.

The detectors in the Q_{weak} experiment are grouped into subsystems within the analysis framework and their inheritance structure is shown in the Figure 4.7. The subsystem creation is handled by a factory method design pattern, which allows any type of subsystem to be created at run time. These subsystem objects are added to an array of `VQwSubsystem` and handled collectively from the main control routine (in `QwTracking` class for tracking, and `QwParity` class for parity). This simplifies adding and managing new detectors in run-time (without recompiling the source code) which provides easy reconfiguration for analysis jobs with custom set of detectors.

All the detectors and monitors use data element classes to represent read-out electronic channels. These predefined classes are then implemented by each subsystems to handle their data (See Appendix C.4.2 for a summary diagram with available data elements). In integration mode, for example: in the beam-line subsystem (`QwBeamLine`), both BCM and BPM use VQWK-ADC data element class (`QwVQWK_Channel`) to access the beam monitor data, and main detector subsystem (`QwMainCerenkovDetector`) uses `QwVQWK_Channel` to define custom data element class for PMT channels (`QwIntegrationPMT`). In tracking mode, wire chamber subsystems (HDC and VDC) use `QwHit` class for drift chamber wire signals.

The subsystems in the analysis framework require to handle various input/output (I/O) processes and most of these processes are common to all the subsystems. A set of classes with all the common I/O processes is implemented that can be accessed by any subsystems. A list of important classes is listed here.

- The raw CODA data are partially decoded and loaded into an array of raw data words by the class `QwEventBuffer`. This class is capable of accessing raw data in real-time mode by hooking into the CODA Event Transfer (ET) component or in off-line mode by reading the raw data files. It then provides data to the subsystem array for final decoding.

- The class called `QwParameterFile` provides all the necessary tools to decode configuration text files: electronic channel maps, pedestal and calibration data, data quality cuts, histograms and tree configurations (which can be separated based on the run number to be analyzed).

- The histograms and Trees are managed by set of routines defined in the class `QwRootFile`. This enables subsystems to create and fill histograms and Trees. It also supports customization of the outputs where configuration files allow the users to selectively choose which channels are saved into the CERN ROOT Trees (known as Tree-trimming). This saves storage space and improves the data analysis rate (see Section 4.5.5).

- The class `QwOption` defines a set of routines so that subsystems can easily access the command line flags. Using this feature, many parameters related to the data analysis configurations can be set at run-time.

- The class `QwParityDB` manages accesses to the MySQL database which stores the analysis summaries from official data analysis jobs.

I have contributed to the development of the analysis framework and my major work includes: developed the tracking framework for the drift chamber classes, created a data structure to handle drift chamber data, implemented the event cut framework, developed the inter-subsystem communication, developed a method to trim ROOT Trees, and implemented parity data analysis framework for a real-time monitor, data archiver, and a charge feedback system.

4.4 Tracking Analysis Framework

The Q_{weak} tracking analysis framework provides inputs to determine the average momentum transfer or $< Q^2 >$ at the 0.5% level, to study background contributions,

and to bridge the Čerenkov detector results from counting mode to the integrating mode. The Q^2 studies are performed mainly using the drift chambers (in the R2 and R3, see Section 3.2.7) and main Čerenkov detectors (in R3). All other studies are performed using R3 detectors: the main Čerenkov detectors and Trigger Scintillators (TSs).

The important features of the tracking analysis framework include: generate output such that results from different trigger sources can be independently accessed from the output ROOT files, decode multiple signals from F1TDC channels (see Section 4.2.1), construct electron tracks from decoded wire chamber signals in R2 and R3.

The tracking data analysis procedure for each event (a trigger) can be divided into two main steps (see Figure 4.8). First, the raw data are decoded for all the tracking detectors during the Q_{weak} Track Decoder (QTD) step [78]. The decoded data from non-wire chamber detectors are saved to a regular ROOT Tree for background other systematic related studies mentioned above. Each wire chamber signal is saved as a hit (`QwHit` objects) and all the hits from the event are included in an array. The next step is the Q_{weak} Track Reconstruction (QTR) [79] in which the hit array produced in the QTD step is used to generate partial electron tracks in R2 and R3, independently. Then using a track reconstruction algorithm actual particle tracks are generated by bridging partial tracks from R2 to R3. The QTR results are saved to a special multi-hit based ROOT Tree that requires Q_{weak} libraries to access.

The HDCs and VDCs detectors are implemented in the analysis framework using two subsystems which are inherited from a drift chamber base class (`QwDriftChamber` class, see Figure 4.7). The common implementations related to track decoding are coded in this base class and the additional codes required to demultiplex the VDCs

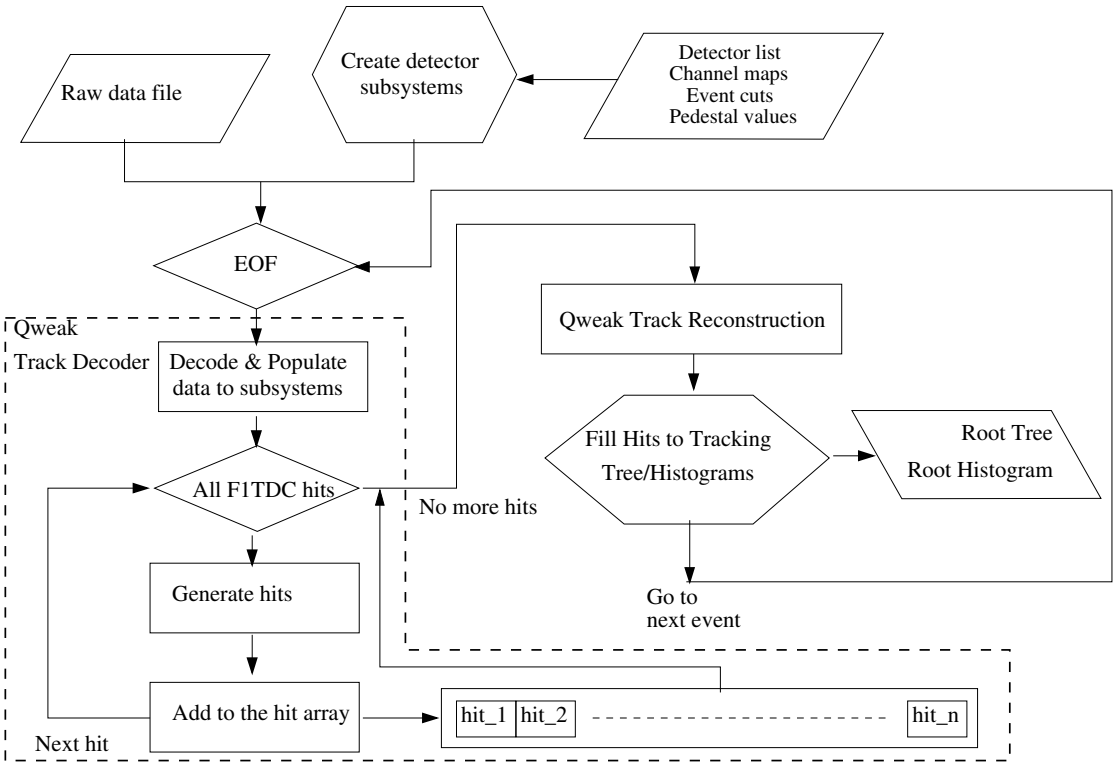

Figure 4.8: The Q_{weak} tracking analyzer framework. For each event (a trigger), a set of hits (`QwHit` objects) are generated. The array of hits is used to extract particle tracks in the region (partial tracks) and in the apparatus (tracks) during the QTR step. The hits, partial tracks and complete tracks are filled to a ROOT Tree.

signals are included in `QwDriftChamberVDC`. I have implemented the drift chamber analysis framework and data structures [80].

The basic unit of data for drift chambers is known as a hit which is a wire signal recorded in a F1TDC channel. Each decoded F1TDC signal or a hit is saved as an object of the class `QwHit` [80]. A `QwHit` object contains information about the detector region (R2/R3), the information related to the wire geometry and electronic channel, and relative and absolute time of the detected signal. The relative time is computed with respect to the time of the tracking trigger. Both subsystems produce an array of `QwHit` objects and these arrays are combined to produce one single array

with all the `QwHit` objects in a single event. This final `QwHit` array is the primary input to the Q_{weak} Track Reconstruction (QTR) procedure [79].

4.5 Parity Analysis Framework

The parity (integration mode) analysis framework decodes integration mode raw data to generate MPS and QRT based quantities in different time intervals and in different formats. It has utilized the capability of the analysis framework to read CODA events stored in raw data files (off-line) and access events directly from the parity DAQ (real-time) to provide a complete data analysis system for the Q_{weak} experiment. This section will summarize important design choices in the parity analysis framework, different implementation of the parity analysis framework, and set of post-processing analysis based on the outputs from the parity analyzer. In the end, I will comment on the performance of the parity analysis framework.

All the parity subsystems are inherited from the base class `VQwSubsystemParity` (See Figure 4.7). The main subsystems are given below,

- The helicity subsystem: for helicity information.[†]
- Main detector subsystem: PMTs from Čerenkov detectors.
- Luminosity monitor subsystem: PMTs from luminosity monitors.
- Beam-line subsystem: beam-line (BCM/ BPM) and halo monitors.

where the detectors are grouped according to the main purposes. The main steps in the parity analysis framework is shown in the Figure 4.9. Raw data file (runlet) or real-time data stream is decoded, an MPS event at a time to generate MPS yields (pedestal subtracted and calibrated) for all the detectors and monitors. The MPS yields are saved as data elements in each subsystem. For each MPS event, the subsystem array

[†]The delayed MPS state and related information to extract actual helicity state

keeps all the subsystems with data. The main steps described in the Figure 4.9 are directly applied on the subsystem array object, and analysis framework propagates these steps down to the data elements.

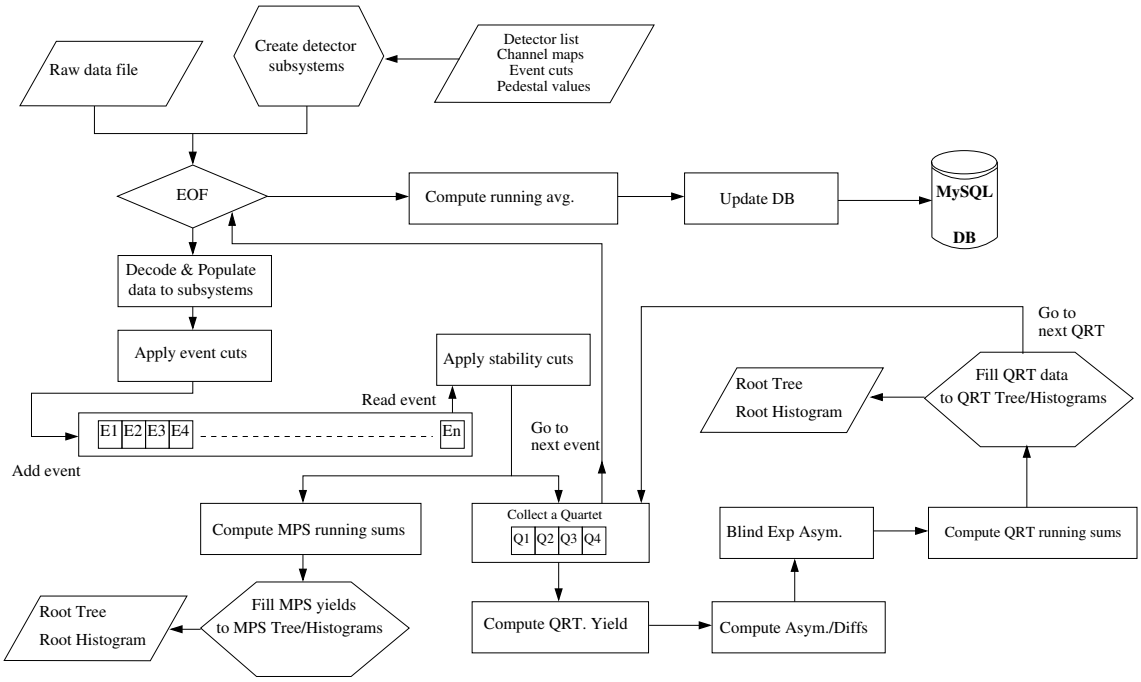

Figure 4.9: Flow chart of the off-line analysis engine where it generates MPS and QRT based ROOT files (un-regressed) as well as running averages.

The subsystem classes and their data element classes support operator overloading to define set of arithmetic operators: addition, subtraction, division, multiplication, and scaling. This feature is used in computing detector combinations and QRT quantities. For certain detectors or monitors, detector channel combinations are constructed for examples: total Čerenkov detector yield is constructed from sixteen PMT channels and beam position is constructed from combination of four data channels in each BPM.

The Helicity Correlated (HC) quantities (see Table 4.1) are computed for a QRT of events (Y^{R1}, Y^{R2} and Y^{L1}, Y^{L2}, see Section 3.1 for helicity and QRT definition) using MPS yields. The class `QwHelicityPattern` is implemented to compute all the HC quantities. The `QwHelicityPattern` object accumulates subsystem arrays (MPS events) for each QRT and applies arithmetic operations directly on these subsystem arrays to compute HC quantities in the Table 4.1.

Table 4.1: A list of QRT based quantities computed by the parity analyzer. A QRT pattern is either R1,L1,L2,R2 or L1,R1,R2,L2.

Subsystem	Quantity	Unit
Main Čerenkov detectors,	$Y_{qrt} = \frac{(Y^{R1}+Y^{R2})+(Y^{L1}+Y^{L2})}{4}$	$\frac{V}{\mu A}$
Background detectors and,	$A_{qrt} = \frac{(Y^{R1}+Y^{R2})-(Y^{L1}+Y^{L2})}{(Y^{R1}+Y^{R2})+(Y^{L1}+Y^{L2})}$	n/a
Luminosity monitors		
Beam line: BCM	$I_{qrt} = \frac{(I^{R1}+I^{R2})+(I^{L1}+I^{L2})}{4}$	μA
	$A_{Q} = \frac{(I^{R1}+I^{R2})-(I^{L1}+I^{L2})}{(I^{R1}+I^{R2})+(I^{L1}+I^{L2})}$	no units
Beam line: BPM	$X_{qrt} = \frac{(X^{R1}+X^{R2})+(X^{L1}+X^{L2})}{4}$	mm
	$D_{X} = \frac{(X^{R1}+X^{R2})-(X^{L1}+X^{L2})}{4}$	mm
Beam line: Rel. momentum	$E_{qrt} = \frac{(E^{R1}+E^{R2})+(E^{L1}+E^{L2})}{4}$	no units
	$D_{E} = \frac{(E^{R1}+E^{R2})-(E^{L1}+E^{L2})}{4}$	no units

The main Čerenkov detector asymmetries are blinded by adding an offset in the range of ± 60 ppb with the sign corrected for the absolute polarization of the beam. The blinding term is a seeded random number, where the seed is the same for all the runs in a defined "running period" (Wien0, Run 1, and Run 2). The random seed is not directly known by the experimenters but is only available internally. The blinding mechanism is implemented by using the class `QwBlinder` and integrated with the `QwHelicityPattern` class to apply the blinder to detector asymmetries.

At the end of a raw data file (a runlet), averages for yields and asymmetries are computed for all the detectors, and are uploaded into MySQL database. These averages are computed using a running average algorithm [81] integrated into subsystem and data element classes. The MPS based running averages are computed using the subsystem array itself and the QRT based running averages of HC quantities are computed using their respective subsystem arrays within the `QwHelicityPattern` class. The running averages are only computed using the data that pass the data quality cuts.

The inter-subsystem communication is a process where data from one detector is shared to many detectors within the subsystem and across the subsystems. This process is built into the subsystem array (see appendix C.4.1). It is used to normalize detector yields with beam current, compute charge asymmetry difference between two Beam Charge Monitors, and report the charge asymmetry and other beam parameters to the feedback system and data archiver (these two systems will be discussed later in a follow up sections).

So far I have given a design overview of the analysis framework. Now I will discuss the different implementations of the analysis framework. The Q_{weak} parity data analysis can be categorized into three main analysis processes based on different implementation of it. The three categories are: real-time, on-line, and off-line analysis (see Figure 4.10). The main steps from raw data to output are independent from these different implementations of parity analysis framework (see Figure 4.9 for main steps). When the experiment was running, a real-time analysis and a first 100K on-line analysis[†] were performed. Both real-time and on-line analysis were valuable to determine the data quality and to diagnose problems. They provided "immediate" data quality feedbacks both to the Q_{weak} shift crew and the beam operation experts.

[†]only the first 100×10^3 events from the raw data file were analyzed and summarized

The third category of the analysis is the off-line main parity analysis that is used to extract measured asymmetries by using all the available data. The off-line analysis can be divided into two steps. In the first step, the main analysis engine (see Figure 4.9) produces unregressed data output. The second step involves post-processing scripts for linear regressions, beam modulation analysis, and summary ROOT file generation (see Figure 4.10) which are all based on runlet based ROOT files. Each complete off-line analysis of data is know as a "data replay pass" and so far there have been four data replay passes performed on the Q_{weak} data. A text summary for each run was produced and updated a web page during the first off-line analysis (aka 1^{st} pass) when the Q_{weak} experiment was running (see Appendix E) using a post-processing script.

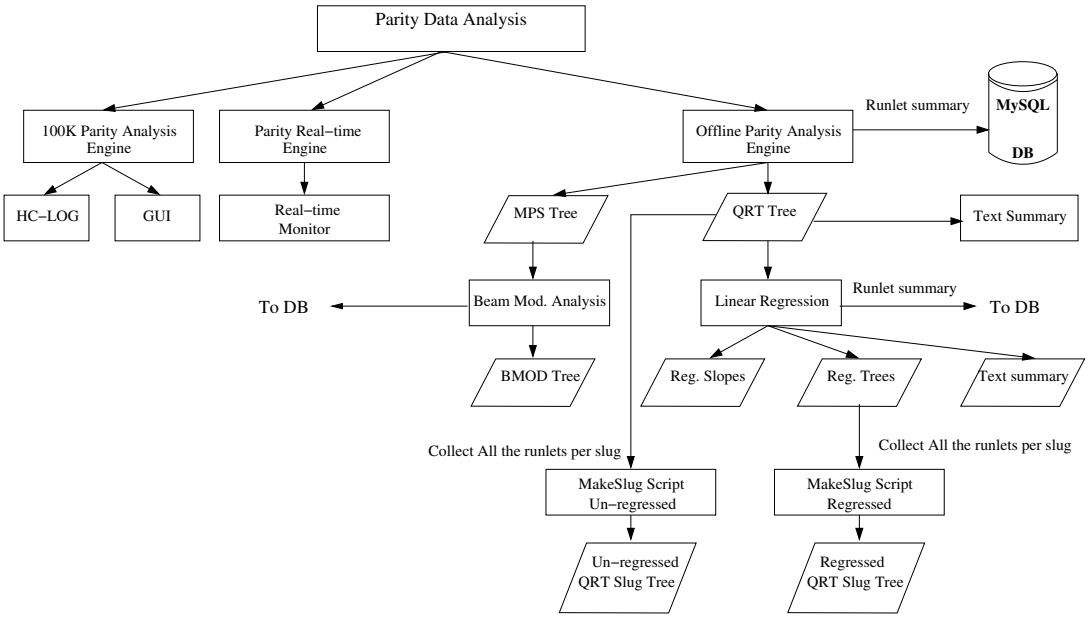

Figure 4.10: Three main Q_{weak} parity analysis categories use the same analysis framework (see Figure 4.9) with different configuration settings. The text summary, linear regression, beam modulation analysis and `MakeSlug` script are post-processing scripts.

The linear regression [82, 83] is applied by a script using the QRT based runlet ROOT files. The regression script produces linear regressed QRT based runlet root files and generate running averages to be uploaded into the MySQL database. More details on the linear regression are discussed during Chapter 6 (the data analysis chapter). For systematics studies, the linear regression is repeated with different independent beam parameters and so far there are over 10 different regression schemes implemented. For each scheme, the regression script goes through the unregressed runlet ROOT files twice, first to generate regression slopes and then to correct measured asymmetries at the QRT level.

A summary ROOT files (aka slug ROOT files) with only important beam monitor and detector asymmetries are also generated using a post processing script. Summary ROOT files are generated for each slug using raw (unregressed) and regressed QRT based runlet ROOT files. A slug has about 8 hours of data from the same state of Insertable Half Wave Plate (IHWP) setting. The Table 4.2 summarizes the accessibility of data from different data sources. The time scale for ROOT Trees can be expanded by chaining files (A CERN ROOT based technique), for example a chain of QRT based runlet Trees for a run expands the time scale from a runlet to a run.

In the parity analysis framework, I have developed the inter-subsystem communication, ROOT Tree trimming, event cut framework (see Section 4.5.1), and the text summary script. I have also deployed different implementations of the parity analysis framework: to use as a real-time diagnostic monitor, to use as an active feedback on the charge asymmetry, and to archive real-time data into Experimental Physics and Industrial Control System (EPICS) format. These parity analyzers were implemented to be used when the experiment was running (see sub-sections from 4.5.2 to 4.5.4).

Table 4.2: Q_{weak} parity data accessibility. The "Unit" is an individual entry accessible from a source and the "Time Scale" is the limit of the accessibility. It is shown with a ✓ mark. The ✓✓ shows the possibility of extending the time scales.

Source	Unit			Time Scale			
	MPS	QRT	Runlet	Runlet	Run	Slug	Wien
MPS Runlet Tree	✓			✓	✓✓		
QRT Runlet Tree		✓		✓	✓✓		
QRT Slug Tree		✓				✓	
Reg. QRT Runlet Tree		✓		✓	✓✓		
Reg. QRT Slug Tree		✓				✓	
Database			✓	✓	✓✓	✓✓	✓✓
Database (Reg.)			✓	✓	✓✓	✓✓	✓✓

4.5.1 Event Cut Framework

I have developed the event cut framework for the Q_{weak} parity data analysis which implements data quality checks on detectors allowing to reject faulty data [84]. There are three types of data quality checks applied to Q_{weak} data: the hardware error checks, single event checks, and stability checks. The hardware checks are the most basic checks, which are applied to all the electronic channels to detect and flag hardware related issues. Then single event checks are applied to calibrated MPS yields by imposing an upper and lower limits to define an acceptable yields. The hardware checks and single event checks generate an error codes for detector/monitor channels to identify failed data quality checks. Finally stability checks are applied to sequence of events in the rolling buffer that keeps an array of events up-to 5 s or 40000 events (see the buffer implementation in Figure 4.9). The stability checks monitor the amplitude of the detector signals (beam current, beam position on target, and main detector yield) to detect fluctuations related to unstable beam conditions. If the

buffer fails any stability check, then an error code is added to the detector channel for all the events in the buffer. Single event checks and stability checks are defined in text files associated with the subsystems.[†]

There are two levels of cuts available for single and stability data quality checks. A local check on a channel only applies to itself while a global check on a data channel applies to the entire event. The local/global state of a quality cut is included when the quality check is defined in the event cut file.

The effect of the data quality checks applied to unstable beam period during a sudden beam drop is shown in Figure 4.11. After the event cut framework was fully implemented during the first pass analysis, there were many improvements to the data quality. It was found that the agreement between different regression schemes has improved after stability cuts were applied on target position and main Čerenkov detector yields (see Figure 4.12). In later data analysis passes, these cuts were applied to all the data.

Only the data that have satisfied all the event checks (global and local) are used to compute the running averages and to fill histograms. The ROOT Trees contain data from all the detector channels and each channel has its own error flag that contains the error codes generated by the data quality checks. Furthermore, the global error flag which have combined all the global checks, is available for each MPS/QRT entry in the Trees. The error flags from detector channels have encoded information about the type, level and origin of the errors (See appendix C.5).

[†]can be found at Analysis_dir/Parity/prminput/qweak_*eventcuts.in

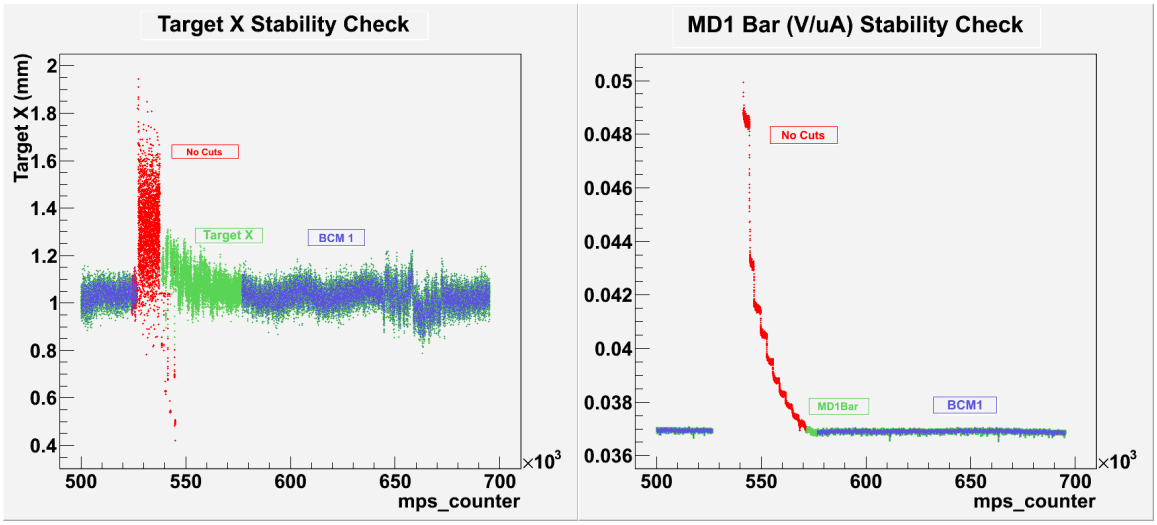

Figure 4.11: The beam position (Target X) and main detector (MD1) yield fluctuations during a sudden beam drop and recovery are removed after applying the event cuts to beam position, current, and main detector yield. The data with no cuts are shown in red, the good data are shown in blue after all the cuts are applied. Applying either beam position or main detector cut can result in data shown in green. (The x-axis is proportional to time.)

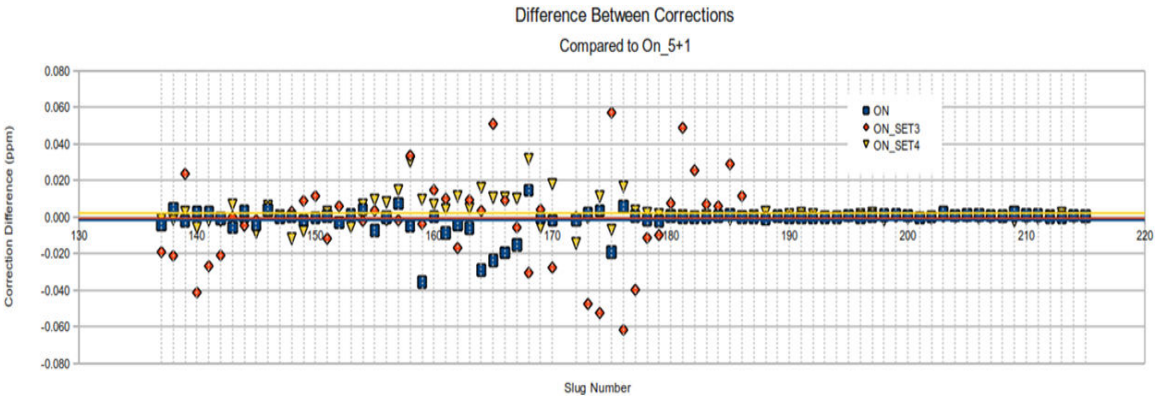

Figure 4.12: The disagreement between regression corrections from different schemes have become negligible after implementing the event cut framework with stability checks during the first pass data analysis (from [85])

4.5.2 Real-Time Parity Analyzer and Monitor

The parity analysis engine connects to the DAQ data stream (ET-Event Transfer) in real-time to decode raw data and generates a set of histograms in a Root file which is mapped to the computer memory. The real-time monitor displays the histograms (Figure 4.13). To provide a real-time diagnostic with close to 100% duty cycle during Q_{weak} experiment, the system was implemented with only the most important beam properties (charge, target position and energy) and the main detector asymmetry.

It has a plot to help detect saturation in BPM `3C12`, the BPM used for energy measurement (the sum of the BPM wires should be independent of position and proportional to beam current: see the plot in third row right column in Figure 4.13). The error summary plot in the display was used to detect certain hardware problems by reporting VQWK-ADC errors in to a histogram.

4.5.3 Active Charge Feedback System

The charge asymmetry is defined as,

$$A_Q = \frac{(I^{R1} + I^{R2}) - (I^{L1} + I^{L2})}{(I^{R1} + I^{R2}) + (I^{L1} + I^{L2})} \tag{4.1}$$

where $I^{R/L}$ is the beam current in the R/L helicity state. If the BCM and detector signal chain are perfectly linear, then a charge asymmetry leads to no false asymmetry contribution. However, if the non-linearity, f (Section 6.3.1) is non-zero then a false asymmetry of $< A_Q > \cdot f$ will be produced. Therefore, $< A_Q >$ must be kept small to keep the false asymmetry small. The main source of the A_q is imperfect circular polarization from the Pockels cell [53]. I have implemented an active charge feedback system to correct the Pockels cell high voltage to minimize the charge asymmetry. The goal of the active feedback system is to force the charge asymmetry to zero and converge at a faster rate compared to the pure statistical convergence of the charge

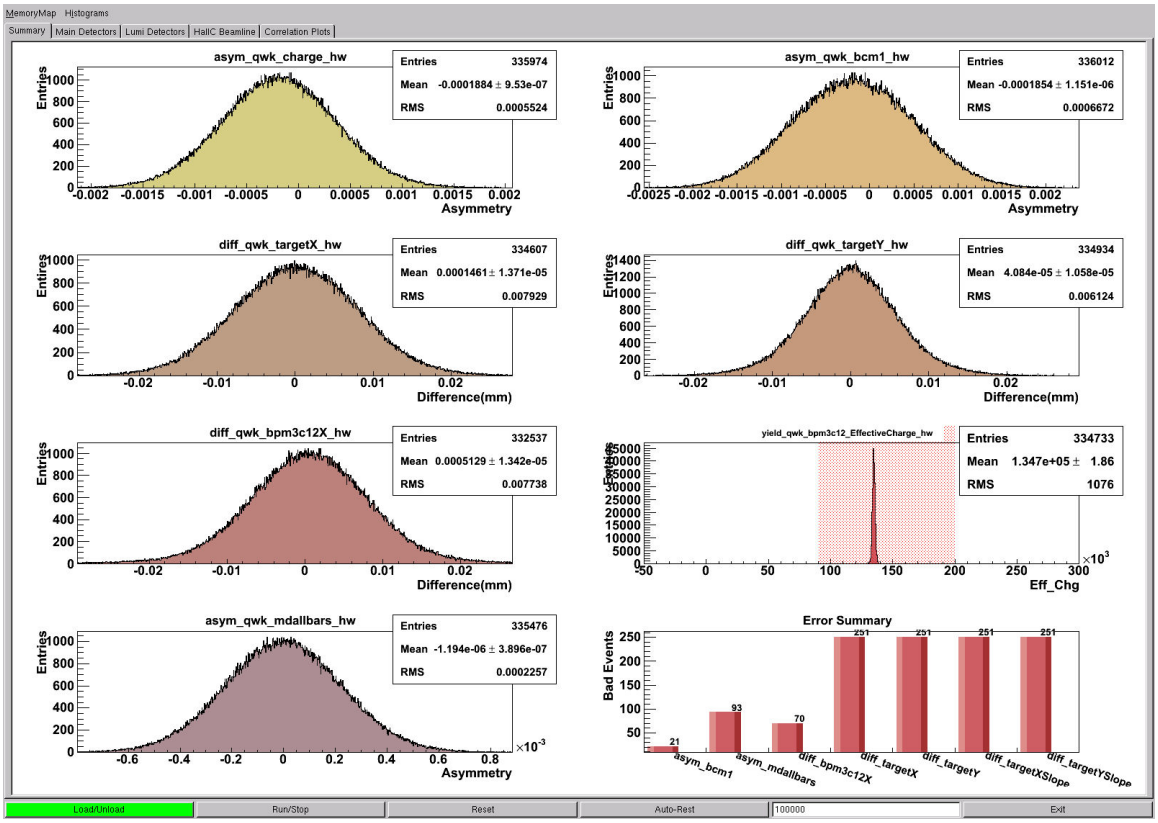

Figure 4.13: The real-time monitor plots the charge asymmetry, HC beam position differences on target, HC beam energy differences, and main detector asymmetry distribution. The bottom right plot is the summary of VQWK-ADC channel errors histogram. The monitor updates continuously or resets every N entries as specified by the user. It can also be paused to look at a snap-shot in time.

asymmetry under no assumed systematic effects. A good reference for origins of charge asymmetry and feedback principle from the SLAC experiments can be found at [86]. The charge feedback system first measures the charge asymmetry in a "2 min." time interval, calculates the Pockels cell high voltage correction based on measured asymmetry and "PITA" slope (discussed later). After n time intervals, the feedback induced asymmetry convergence is,

$$\delta \bar{A}_q \propto \frac{1}{n} \tag{4.2}$$

where the $\delta\bar{A}_q$ is the error on the average asymmetry after n time corrections (see Figure 4.14) with feedback system forcing the central value ($\bar{A}_q$) to zero. With no feedback system, the statistical jitter convergence is $\delta\bar{A}_q \propto 1/\sqrt{n}$. The simple derivation of the above claim is found at Appendix C.6.

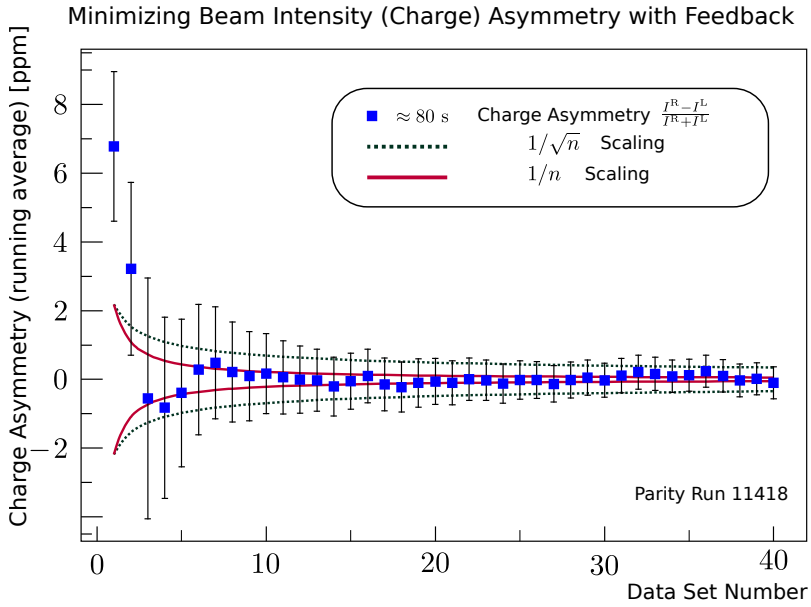

Figure 4.14: The active feedback minimizes the charge asymmetry at faster rate than statistical convergence. Each data point is the running average of data points so far. The feedback correction is done every 80 s.

The relationship between the charge asymmetry and the correction to the Pockels cell voltage is known as the "PITA slope" for historical reasons [53]. The PITA slope was measured in regular intervals (every two-three weeks, see Appendix C.6.1 for archived values) during the experiment (see the Figure 4.15).

The Q_{weak} active charge feedback is implemented using a modified version of the real-time analysis engine. Its role is to compute the charge asymmetry from a Hall C BCM and correct the Pockels cell high voltage to force the charge asymmetry to zero (see Figure 4.16). Two different high voltages ($PC^{\pm}$) are applied to get the two states

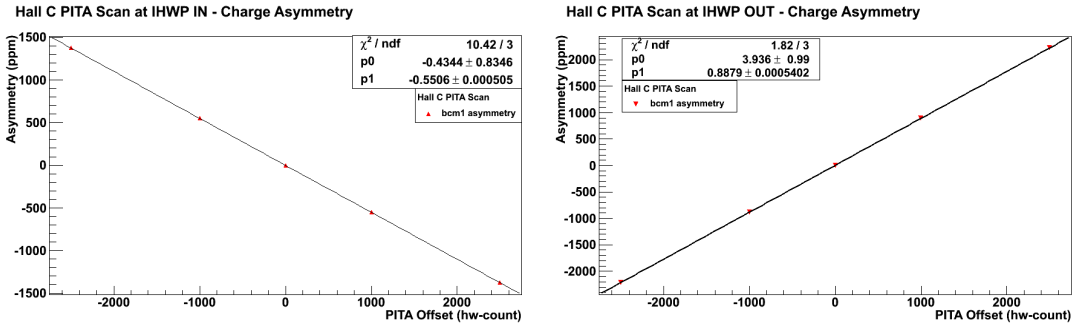

Figure 4.15: The PITA slopes for IHWP IN and OUT measured using a Hall C BCM. The x-axis is the offset to nominal Pockels cell high voltage (in arbitrary units).

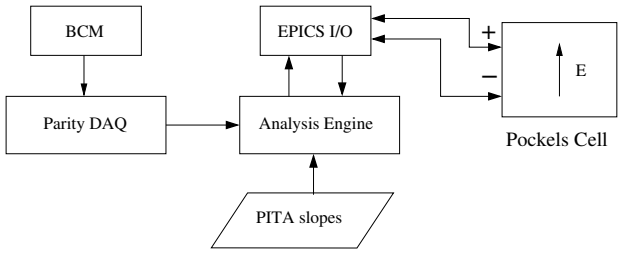

Figure 4.16: The active charge feedback flowchart. The real-time implementation of the parity analyzer is used to read the BCM data from the parity DAQ and updates the Pockels cell voltages. The EPICS I/O is used to read and set the Pockels cell high voltages ($PC^{\pm}$).

of circularly polarized light. The correction to the Pockels cell voltage is computed,

$$\Delta PC = \frac{A_q}{-1 \cdot PITA\_Slope} \tag{4.3}$$

where the PITA_Slope is the PITA slope measured using a similar plot shown in Figure 4.15. The new Pockels cell voltages ($PC^{\pm}_{new}$),

$$\begin{aligned} PC^{+}_{new} &= PC^{+}_{old} + \Delta PC \\ PC^{-}_{new} &= PC^{-}_{old} - \Delta PC \end{aligned} \tag{4.4}$$

The analysis engine computes the charge asymmetry, A_q, in real-time to update the new Pockels cell voltage set-points according to equation 4.4 (which are accessible via EPICS channels).

According to equation 4.2, the shorter the correction interval, the quicker the convergence of the charge asymmetry to zero but in practice the correction rate is limited by the dead-time of the feedback system which defines as the ratio of the QRT patterns missed by the feedback to the total QRT patterns. Larger dead-time reduces the data set accessed by the feedback system and slows down the convergence for the final data sample used to compute the measured asymmetries. Ideally the feedback system should rely on 100% of the data set but non-zero dead-time prevented it during Run 1. During the Run 1 period, the correction interval was set to 80 s (20000 patterns) with a dead-time of about 5%. The cause of the dead-time could be related to real-time data access by the analysis engine and EPICS communication in the feedback system. The real-time data access to the analysis framework was improved and EPICS communication was optimized at the beginning of the Run 2 period. This allowed to reduce the correction interval time to 40 s (10000 patterns) with about 0% dead-time.

The Pockels cell mid point $((PC^+ + PC^-)/2)$ is unique for different IHWP states obtained from the beam studies done at the laser table. When the IHWP state was changed to start a new data slug, a script (called `FlipPCValues`, available in the Q_{weak} analysis `svn` repository) was executed to set initial Pockels cell set-points (and the Rotatable Half Wave Plate (RHWP) set-point). During this transition period, the charge asymmetry always started from a large value making it unusable for main measurement. This issues was addressed during the Run 2 data taking period by feedback system regularly saving the last known good set point values (PC^+ & PC^-)

for each IHWP states. The script `FlipPCValues` uses these set points. This reduced the initial charge asymmetry from about 100 ppm to about 10 ppm (see Figure 4.17).

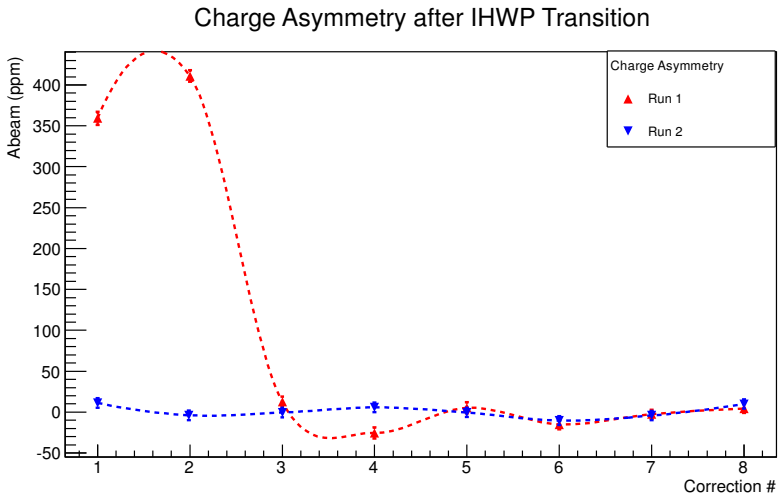

Figure 4.17: Measured charge asymmetry at the beginning of a new IHWP state for first few corrections. The Run 1 feedback system generated large charge asymmetries during IHWP transitions period and it was fixed for Run 2.

4.5.4 Real-Time Archiver

The charge feedback system has also acted as a real-time data archiver where it read detectors and monitors from the DAQ in real-time. It then computed average quantities for various beam parameters (see Table 4.3) for a period of time and updated to the EPICS archiver. The archived quantities can be plotted with time to diagnose issues and improve data quality (see Figure 4.18). These data are still available through the EPICS archiver.

Table 4.3: List of archived quantities. For each quantity, the mean, error and RMS were archived to the EPICS archiver.

Detector/Monitor	Name	Quantity (Unit)
BPM	Target	ΔX ΔY (μm)
		ΔX$'$ ΔY$'$ (nrad)
	3C12	ΔX (μm)
		A_{Eff_Q} (ppm)
BCM	BCM1,7,8	A_q (ppm)
US-Luminosity monitor	uslumi_sum	A_{lumi} (ppm)

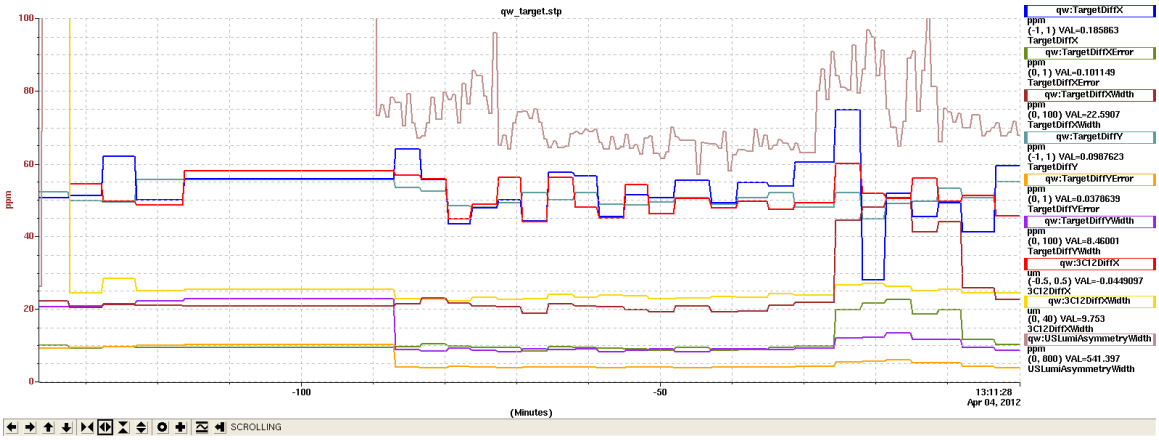

Figure 4.18: A strip chart with EPICS quantities updated by the real-time archiver. The update interval of position differences is longer to produce results with meaningful statistical errors compared to the luminosity monitor asymmetry.

4.5.5 Performance Summary

The parity analysis framework have successfully handled one major data analysis to finalize Wien0 results (this dissertation). I will summarize the parity analyzer performances and possible improvements that can be made to the framework for the final analysis and future Parity Violating experiments

The Q_{weak} data analysis framework uses the CERN ROOT libraries to generate outputs (ROOT Trees and histograms) and the input/output (I/O) related to ROOT is the main consumer of resources in the analysis framework. The data analysis rate or time it takes to process one event is completely determined by ROOT I/O processes (see Table 4.4). Highest data analysis rate (5 kHz) is observed when no ROOT I/O is accessed and rate drops to 150 Hz when all the detector channels (about 260) output to the ROOT Trees and histograms. The current off-line analyzer produces all the detector channels into ROOT Trees and it takes about 7 hours to process 1 hour of raw data. Since we use a cluster of computers (a farm) to analyze many runs in parallel, the lost time in slow analysis rate is recovered. For real-time and charge feedback analyzers, the quoted percentage is the how many events out of total parity DAQ events were analyzed in real-time (hence the duty-cycle).

Table 4.4: Parity data analysis rates. The parity DAQ event rate was 960 Hz.

Category		Rate (Hz)	Time to analyze raw data
Off-line		150	1 h raw data $\rightarrow$ 7 h
	No Tree	2000	1 h raw data $\rightarrow$ 0.5 h
	No Tree+histograms	5000	1 h raw data $\rightarrow$ 0.2 h
On-line	"first 100k analysis"	150	100 k raw data $\rightarrow$ 10 min
Real-time	Only histograms	800	80% duty-cycle
Charge feedback + Archiver	No Tree+histograms	960	100% duty-cycle

The other main concern in our parity data analysis is the storage issues. A raw data file (runlet) is about 2 GB and the ROOT Tree generated from the raw data file is 10 GB, a 5 fold increase in data volume. There are approximately 20,000 runlets with valid data in the whole experiment and saving all the ROOT files is not

practical and not necessary. Only summary ROOT files (slug-level) with essential set of detector/monitor data are generated using a post-processing script. These summary ROOT files are saved, and the regular runlet ROOT files are discarded. For future data analysis, the Tree trimming implemented in the parity framework can be used to generate trimmed ROOT files and eliminate the post-processing script. This will improve the data analysis performance.

The linear regression is implemented using a post-processing script that uses unregressed runlet ROOT Trees as inputs and generate ROOT Trees with regressed data. This is repeated for over 10 different regression schemes available in present analysis using different independent beam parameters. Therefore, post-processing linear regression takes about 7 hours to analyze 1 hour of unregressed data. There are ongoing discussions to integrate the linear regression into the parity analysis framework itself to reduce the ROOT I/O involved in the post-processing linear regression.

The Parity analysis framework is the end result of collaboration about 50 physicists and it has about 50,000 code lines. The source code is maintained using a subversion (svn) repository and can be checked out from the Q_{weak} software repository.

```
svn --no-auth-cache --username [username] checkout
    https://qweaksvn.jlab.org/repos/QwAnalysis/trunk QwAnalysis
```

5 Polarimetry

The goal of the polarimetry for the Q_{weak} experiment is to measure the longitudinal beam polarization in Hall C to about 1% precision (dP_e/P_e) and maximize the longitudinal beam polarization. The former is achieved using a combination of the Hall C Møller polarimeter [87] and the newly commissioned Compton polarimeter, while the latter is achieved with the combination of the Hall C Møller polarimeter and the Mott polarimeter [57].

I have contributed to the Møller polarimeter commissioning, data taking, and systematic studies. In this chapter, an overview of the Mott, Compton, and Møller polarimeters and my contributions to the Møller polarimeter are provided. In the end, the Wien0 Møller polarization result are documented.

5.1 Mott Polarimeter

The differential cross section for the Mott scattering of polarized electrons from a nucleus of charge Z has a beam polarization ($\vec{P}_e$) vector dependent term in the differential cross section [88, pg. 56]. The cross section is,

$$\sigma(\theta, \phi) = I(\theta)[1 + S(\theta)\vec{P}_e \cdot \hat{n}], \tag{5.1}$$

where θ is the scattering angle, $I(\theta)$ is the unpolarized Mott cross section, $S(\theta)$ is called the Sherman function which depends on Z and the electron beam energy, and $\hat{n} = \frac{\vec{k}\times\vec{k}'}{|\vec{k}\times\vec{k}'|}$ is the unit vector normal to the scattering plane where $\vec{k}(\vec{k}')$ is the electron incident (scattered) momentum. The analyzing power is generated between two helicity states and provides a measure of the incident electron beam polarization in the horizontal and vertical transverse planes. The CEBAF Mott polarimeter has a 0.1 μm gold foil target (Z=79) and a set of four detectors, two in the horizontal plane and two in the vertical plane to measure both vertical and horizontal analyzing powers. The polarimeter is located in the 5 MeV region of the injector to maximize

the Mott scattering analyzing power [57]. The Mott polarimeter can be used for Wien filter (Section 3.2.1) calibrations and to check the photo-cathode health. In the past , it has been used to cross calibrate the Hall C Møller polarimeter. Due to configuration changes and Data Acquisition (DAQ) development, the Mott polarimeter was used only to null the vertical beam polarization during Q_{weak} .

5.2 Compton Polarimeter

The underlying principle of the Hall C Compton polarimeter is the Compton scattering of the electrons from a polarized laser. The polarized Compton scattering cross section is,

$$\frac{d\sigma}{dxd\phi} = \sigma_0(1 - P^{\gamma}[P_Z^e A_Z(x,y) + P_t^e cos\phi A_t(x,y)]) \tag{5.2}$$

where the σ_0 is the unpolarized Compton cross section, ϕ is the azimuthal angle of the scattered photon, P^{γ} is the incident laser polarization, P_Z^e and P_t^e are longitudinal and transverse electron beam polarization, respectively, $A_Z(x,y)$ and $A_t(x,y)$ are longitudinal and transverse analyzing powers, respectively, and x and y are dimensionless scattering parameters [89]. The Hall C Compton polarimeter was designed to provide an uninterrupted longitudinal electron beam polarization (P_Z^e) measurements. The scattered photons and electrons are detected to provide two independent polarization measurements. It was built and commissioned for the first time during the Q_{weak} experiment. The Compton polarimeter is located in the straight-line region of a magnetic chicane where a circularly polarized laser interacts with the electron beam (see Figure 5.1). The third dipole magnet in the chicane acts as a spectrometer for the Compton scattered electrons while a photon detector detects back-scattered photons. The independent analyzing powers from the electron and photon detectors are used to compute the two independent measurements of the electron beam longi-

tudinal polarization. When the polarimeter is not in use, the straight beam line can be used to bypass the polarimeter.

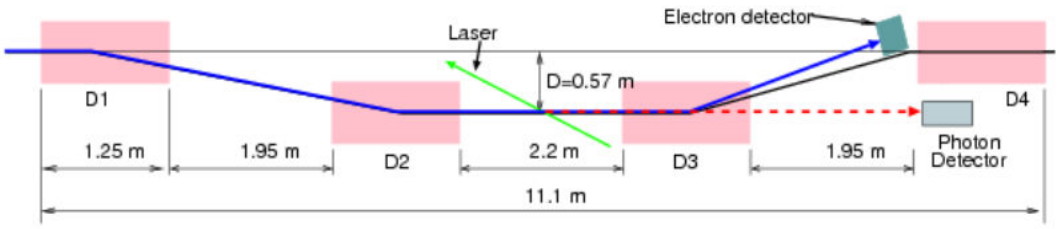

Figure 5.1: The Compton polarimeter setup in the magnetic chicane located in the Hall C beam-line. The laser interacts with the beam at the straight section of the chicane. The scattered electrons and photons are detected for each helicity (MPS) state (from [52]).

5.3 Møller Polarimeter

The Hall C Møller polarimeter uses polarized electron-electron (Møller) scattering to measure the longitudinal beam polarization [87]. The Møller (e^-e^-) scattering cross section for longitudinal polarized electrons is

$$\frac{d\sigma}{d\Omega} = \sigma_0[1 - P_{||}^b P_{||}^t A_{||}(\theta)] \tag{5.3}$$

where the σ_0 is the unpolarized Møller cross section, θ is the center of mass electron scattering angle, $P_{||}^b$ is the longitudinal electron beam polarization, $P_{||}^t$ is the longitudinal polarization of the electrons in the target. In the Møller polarimeter apparatus, the electron beam is scattered from polarized electrons in a thin foil iron target (1 μm thick), magnetically saturated along the beam axis using a 3.5 T superconducting solenoid magnetic field. The longitudinal polarized Møller scattering analyzing power is,

$$A_{||}(\theta) = \frac{(7 + \cos^2\theta)\sin^2\theta}{(3 + \cos^2\theta)^2} \leq \frac{7}{9} \tag{5.4}$$

To maximize the analyzing power, the scattered and recoiled Møller electrons at 90° center-of-mass are detected in coincidence using a pair of lead-glass calorimeters [87]. The coincidence detection minimizes the background (Mott electrons) contamination. A pair of quadrupole magnets focus the electrons to the detector plane (see Figure 5.2). Due to the insertion of the Møller target to the electron beam path, the polarization measurement interrupts the Q_{weak} measurements. Moreover, the measurement can only be performed at about 1 μA current due to high scattering rates observed at higher currents which increase random coincidence electron detection and electronic dead-time. The target heating at higher currents also results in foil depolarization that changes the analyzing power. The measured Møller polarization at low current is extrapolated to nominal Q_{weak} beam currents.

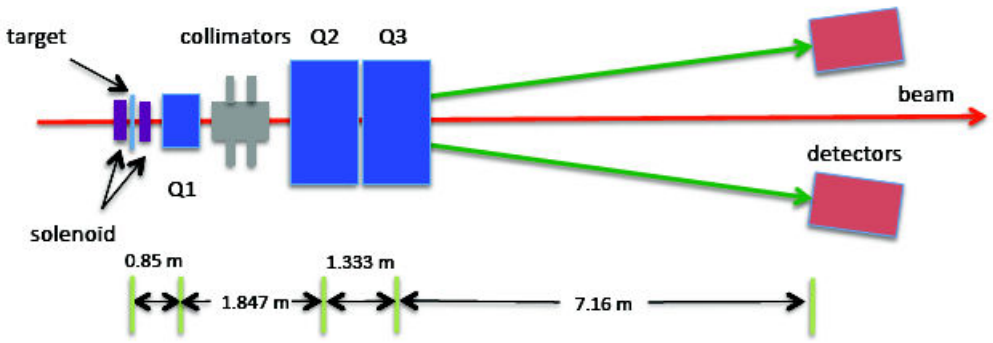

Figure 5.2: The Hall C Møller polarimeter layout. The scattered and recoiled electrons are focused to the detector plane using two quadrupole magnets (Q1 and Q3). The set of movable collimators between Q1 and Q3 are used to further reduce backgrounds. The magnet Q2 was not used during Q_{weak} experiment (from [52]).

5.3.1 Commissioning

The Møller polarimeter was recommissioned at the beginning of the Q_{weak} experiment because of modifications related to making the Møller polarimeter ready

for the 12 GeV upgrade. These included adding a new third quadrupole magnet to the setup and modifying the overall length and magnet spacing of the Møller apparatus. The changes in the geometry of the polarimeter components have modified the detector acceptance slightly. Therefore the scattered electron rates and the Møller analyzing power have changed. Also, a smaller beam-pipe and new magnetic elements placed downstream of the Q3 magnet have induced additional background contributions to the Møller detectors. Due to this additional background generated from the smaller aperture and additional material, more lead shielding blocks were added to surround these magnetic elements. As a part of the Møller polarimeter commissioning, the set of studies was performed prior to polarization measurements. The studies include, detector gains optimization, electron optics tunes using the magnets, systematics effects of Møller target electron polarization, and Møller collimators position scan.

As part of the Møller commissioning procedure, the detector gains were re-matched by adjusting high voltages. The Møller scattered electrons are focused on to the calorimeters by the magnetic fields of the two quadrupole magnets (Q1 and Q3). Two hodoscope arrays, each in-front of left and right detectors determine the horizontal positions of the electrons in the detector acceptance. The correlation observed between these left and right hodoscopes is used to adjust the quadrupole magnet currents to obtain the optimum left-right detector correlation. The ideal focus is obtained when left-right hodoscopes correlate 1-to-1 (top-right or bottom-left plot in Figure 5.3). During the Q_{weak} recommissioning, the two quadrupole magnet currents were mis-tuned up-to $\pm 3\%$ from nominal setting to test the sensitivity of the polarization measurements. The observed fluctuations are within the $\pm 0.5\%$ statistical errors of the measurements (Figure 5.4).

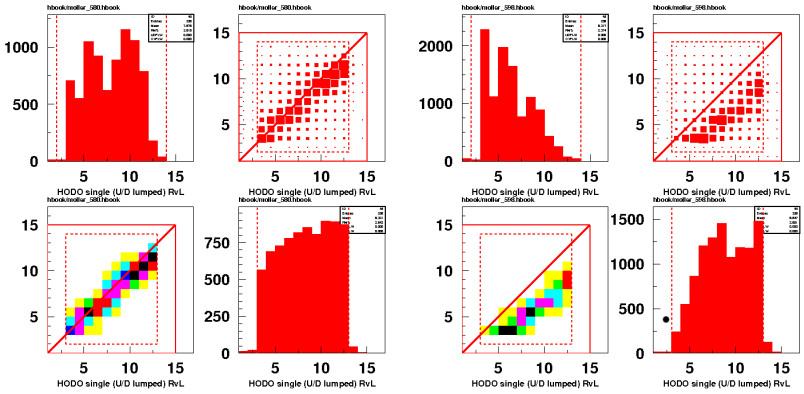

Figure 5.3: The hodoscope correlation plots for a good (left side) and a bad (right side) tune. The top-left and bottom-right are left and right hodoscope histograms for good and bad tunes. The correlation between the left and right hodoscope detectors in left and right side detector planes is shown in top-right and bottom-left plots for good and bad tunes

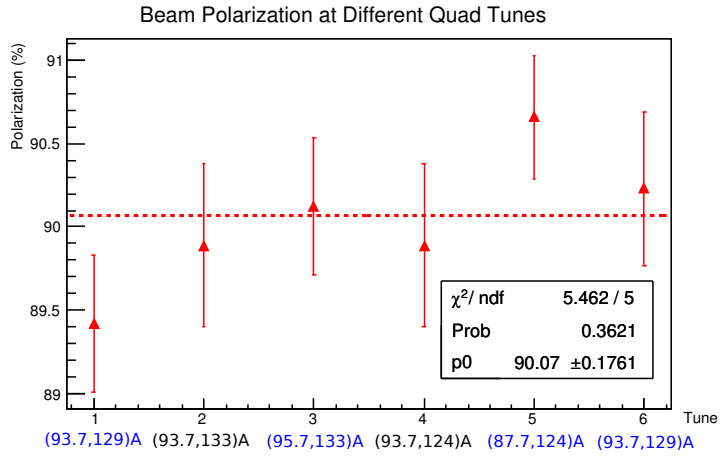

Figure 5.4: Møller polarization at different tunes of the Q1 and Q3 magnet currents. Started with the nominal magnets currents and then switched between good and bad tunes (as in Figure 5.3) by adjusting the magnet currents. The good tune set-points are shown in blue in the x-axis.

A set of movable collimators (see Figure 5.5) between Q1 and Q3 are used to reduce the background contribution (Mott electrons) into the detector acceptance. The collimators are positioned so that they have no impact on the detector acceptance and analyzing power (i.e. no coincidence events are lost). A collimator scan was performed, in which the position of the each collimator was adjusted by keeping others at optimized positions, and coincidence and random rates were observed until they impacted the acceptance (see Figure 5.6). This result was used to optimize the collimator positions.

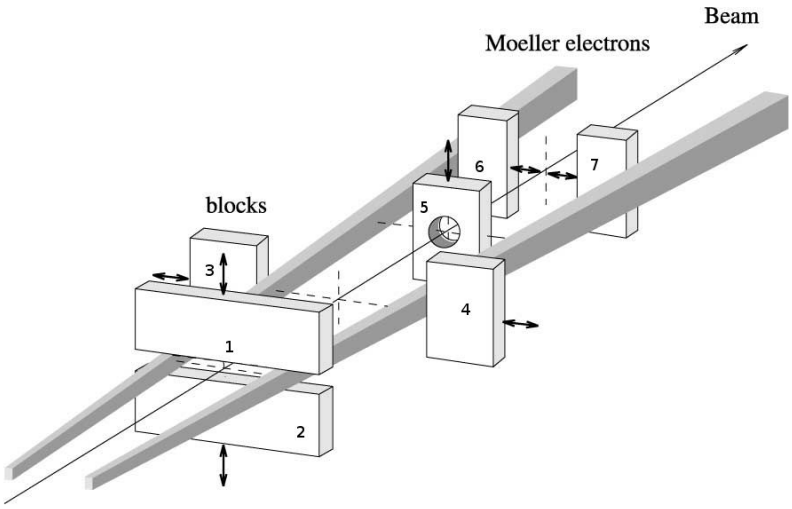

Figure 5.5: The collimator layout (from [87]). The positions of all the collimators except number 5 have been optimized to maximize the Møller coincidence rate.

The Møller target (1 μm iron foil) is magnetically saturated by using a superconducting solenoid at 3.5 T. During the commissioning, the electron beam polarization was measured as a function of the magnitude of the solenoid magnetic field to verify, that the foil was 100% saturated. An apparent deviation from the saturation is possible if the foil is tilted relative to the magnetic field axis. The absolute beam polarization was dropped down from nominal value as the solenoid

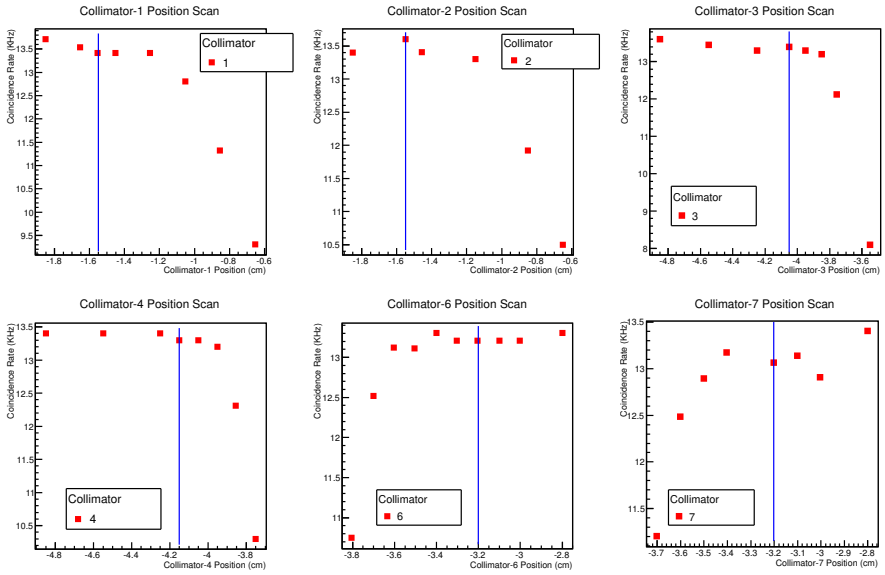

Figure 5.6: Shown in these plots are the coincidence rate vs. collimator position where each collimator position was scanned, independently to maximize the coincidence rate while minimizing random coincidences. (random coincidences not shown here.) The blue line is the set value for each collimator based on the observed coincidence rate.

magnetic filed was reduces pass the iron saturation field of 2.2 T. This change in beam polarization was compared against the original target magnetic filed studies performed in the past [90] to detect possible tilt in the target foil. These results have not indicated any tilt in the target foil (Figure 5.7), and are consistent with the full magnetic saturation of the foil.

The Møller commissioning studies have provided final configuration for the Møller polarimeter. This include, optimum beam current (about 1 μA), quadrupole magnetic current set-points (Q1=93.7 A and Q3=129 A) for ideal scattered electron tune, and optimum collimation to provide maximum coincidence detection of Møller electrons and minimum background from Mott electrons.

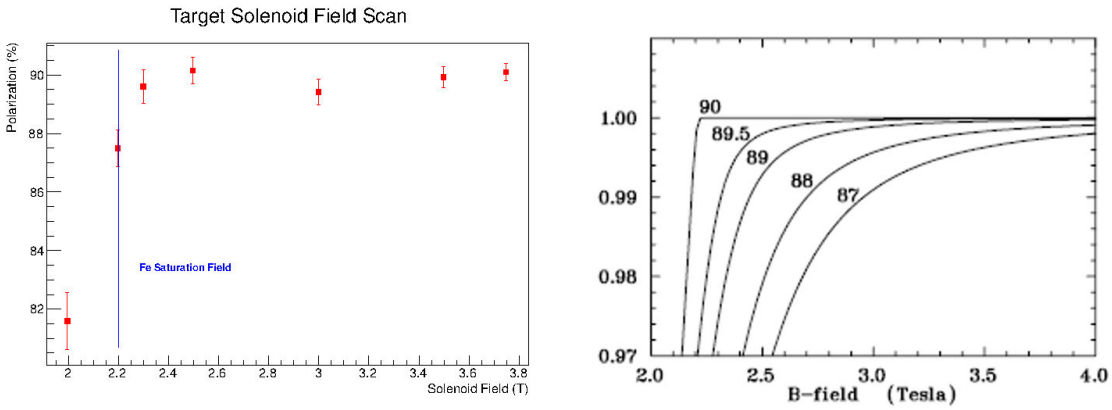

Figure 5.7: Left: The solenoid field was scanned from 2.0 T to 3.75 T to measure polarization variation. The Fe magnetic saturation field is 2.2 T. Right: The expected variation on the target polarization in absolute units with solenoid field as a function of iron foil tilt angle (from [90]). The solenoid production running setting is 3.5 T.

5.4 Møller Systematic Studies

A summary of all the systematic errors contributing to the precision of the Møller analyzing power is given in Table 5.1. The measured Møller polarization and the analyzing power have non-zero sensitivity to the beam position (see Figure 5.8) and it is the most significant systematic error contribution. The sensitivities are calculated using a Monte Carlo simulation to transport scattered electrons through collimators and magnets into the detector plane. For Wien0, a simple transport matrix was used to transport the scattered electrons through the solenoid magnet in the Møller target. The simulation result of the position sensitivities and actual beam position (x,y) during each Møller measurement are used to correct the measured polarization to get position decoupled (x=y=0) beam polarization.

It is important to note that simulation results have not agreed 100% with the measured sensitivities during the Run 1 due to quadrupole issue discussed later in this Chapter (as seen in Figure 5.8). As the next step, there have also been simulations performed using a Runge-Kutta algorithm in which electrons swim through the

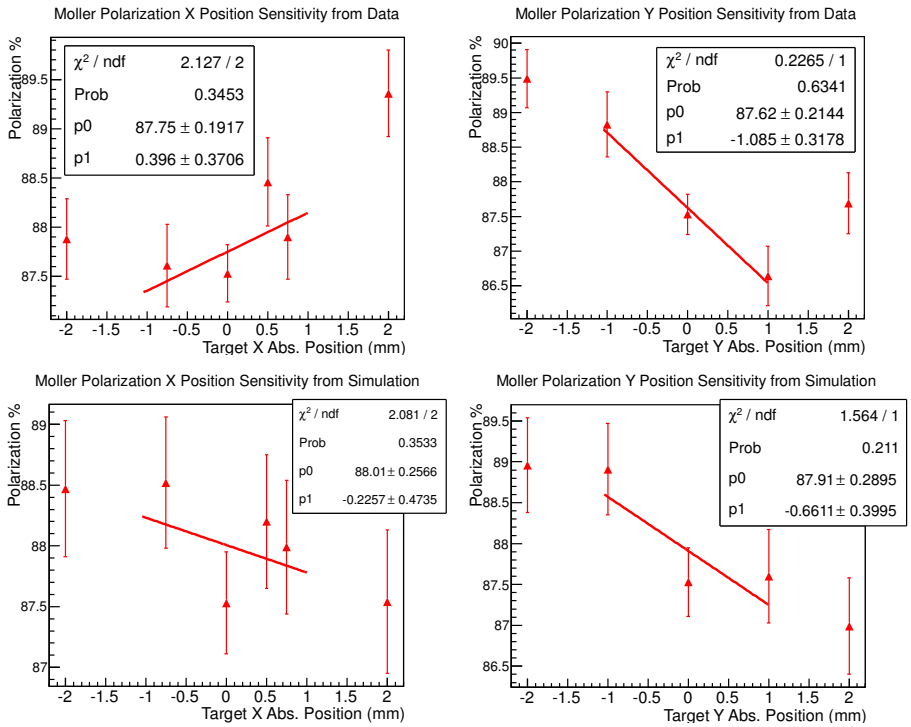

Figure 5.8: Polarization has non-zero sensitivity to position on target. The sensitivities from data taken during Run 1 (top plots) are compared with simulation results (bottom plots). The sensitivities are computed for beam positions within ±1 mm which is maximum allowed beam position range for Møller measurements used for the final results.

solenoid magnetic field of the target. Initial results from this simulation has yielded larger sensitivity (about 30% larger) to the position than predicted by the transport matrix simulation [91]. This is another issue that needs to be resolved towards final Møller analysis. Due to this discrepancy between simulation schemes, each polarization measurement was corrected using the transport matrix results but the error on the position sensitivity correction was assigned based on the Runge-Kutta algorithm results for Wien0 [91].

During Run 1, the quadrupole magnet (Q3) field was deteriorating with time and required retuning the Møller polarimeter and re-steering the beam to maintain

Table 5.1: Systematic error contributions to the Møller analyzing power. Underlined contributions are updated results from Q_{weak} running.

Source	Uncertainty	dA/A(%)
Beam position x	0.5 mm	0.25
Beam position y	0.5 mm	0.35
Beam direction x	0.15 mr	0.14
Beam direction y	0.15 mr	0.1
Q1 current	2%	0.1
Q3 current	1%	0.43
Q3 position	1 mm	0.18
Multiple Scattering	10%	0.01
Levchuk effect	10%	0.2
Collimator positions	0.5 mm	0.06
Target temperature	50%	0.14
B-field direction	2^o	0.14
B-field strength	5%	0.03
Spin polarization in Fe		0.25
Electronic D.T.	100%	0.04
Solenoid focusing	100%	0.19
Solenoid position (x,y)	0.5 mm	0.22
Point-to-point random error		0.37
High current extrapolation		0.5
Monte Carlo statistics		0.13
Total		1.04

a good orbit (no scraping beam) within the beam-line. The field deterioration would sometimes happen within a regular beam polarization measurement interval (see Figure 5.9). This issue lead to an investigation at the end of the Run 1 and a

Q3 coil short was discovered. It was determined that two of the three pancakes in one of the four coils were shorted and the effective current of Q3 was about 2/3 of the nominal current [91] during some periods of Run 1. There are on-going investigations to isolate these periods where Q3 short occurred and then apply a correction to Møller polarization measurements during these time periods. Based on the preliminary estimates for the impact of the coil short on the analyzing power, a +1% correction was applied to the final polarization (central value) and an additional $(\mathrm{dA/A})_{\mathrm{Q3}} = 1\%$ systematic error was added linearly to the total systematic error.

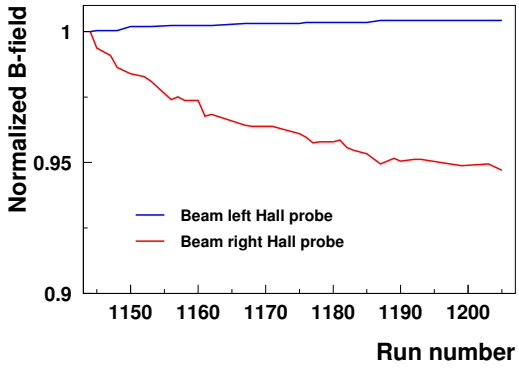

Figure 5.9: The magnetic field on the one side of the quadrupole 3 was unstable during a 6 hours of continous monitoring.

The Q3 magnet issues was fixed at the end of the Run 1 period by installing a different quadrupole magnet. Therefore, this issue was only affecting the Møller polarization measurements taken during Run 1.

5.5 Wien-0 Møller Polarization Measurement Summary

During Wien0, there have been four Møller polarization periods where in each period multiple polarization measurements were taken in two Insertable Half Wave Plate (IHWP) states. Each of the measured polarization was first corrected for beam

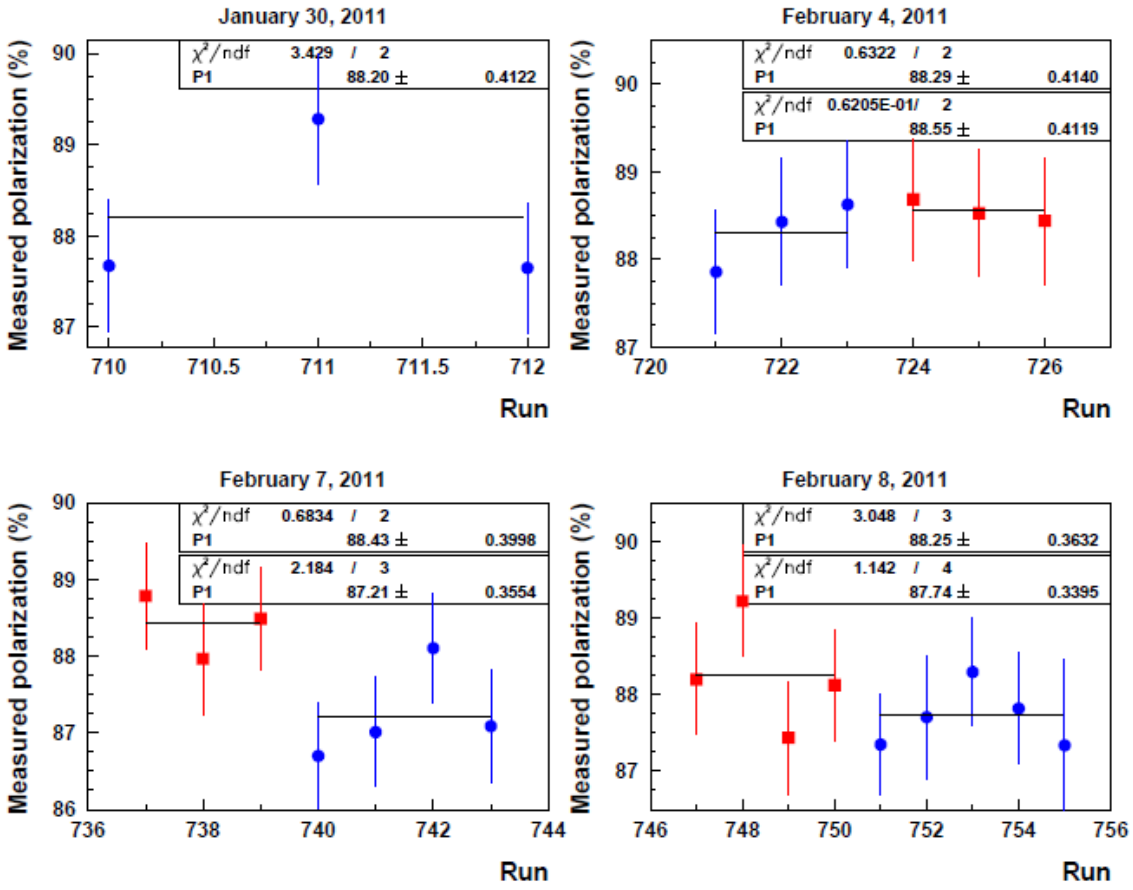

Figure 5.10: Wien0 Møller measurements. Each run based measurement is corrected for horizontal position on target (from [91]).

position dependence. Then for each day, the measurements were averaged over the IHWP state (Figure 5.10 and Table 5.2).

The set of averaged polarization measurements was then fitted to a constant to get the Wien0 Møller polarization result (see Figure 5.11). For Wien0, beam polarization was applied as a global correction because correlations with the time varying effects for example, Quantum Efficiency (QE) of the photo-cathode, etc

over the two weeks period of Wien0 was small, and they were canceled out when measurements were averaged.

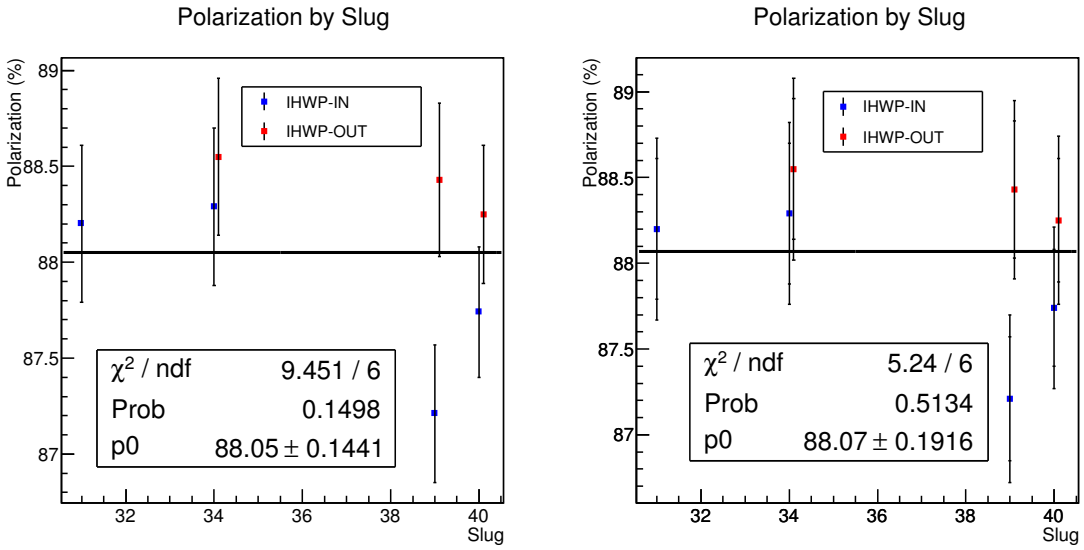

Figure 5.11: The Møller measurement summary for the Wien0. The data points on the left plot have only statistical errors. The constant fit is improved (χ^2/ndf) by quadratically adding a random error of $\Delta P/P = 0.37\%$ for each data point in the right plot.

Table 5.2: Polarization measurements are averaged over each day grouped by the IHWP (the errors are statistical only.)

Date	Slug	Wien angle (deg.)	IHWP	P (%)	$\Delta P/P(\%)$
January 30, 2011	31	-63.20	IN	-88.20	0.41
February 4,2011	34	-63.22	IN	-88.29	0.41
			OUT	88.55	0.41
February 7, 2011	39	-63.22	IN	-87.21	0.36
			OUT	88.43	0.40
February 8, 2011	39	-63.22	IN	-87.74	0.34
			OUT	88.25	0.36

For the constant fit, the χ^2 of 1.6 with the probability of about 15% has only included the statistical errors (left plot in Figure 5.11). This hints towards further investigation to identify any hidden point-to-point systematic errors that could have been unaccounted for during the analysis. For the limited data set in the Wien0, the polarization measurement is not required at the 1% precision level. Therefore an extra $\Delta P/P = 0.37\%$ error is added to each data point to get an improved constant fit to the Wien0 Møller polarization (right plot in Figure 5.11) with a $\chi^2$of 0.9 at about 50% probability. This result is then corrected for the Q3 issue (a +1% correction of the central value) to extract the final Møller polarization for the Wien0 data set:

$$\begin{aligned} P_{\text{Wien0}} &= 88.95 \pm 0.19\ (\text{stat}) \pm 0.93\ (\text{sys}) \pm 0.89\ (\text{Q3 sys})\% \\ &= 88.95 \pm 1.83\% \end{aligned} \tag{5.5}$$

where the error due to Q3 issue is linearly added to the systematic error. The relative uncertainty on the Wien0 data set is 2% (dP/P).

6 From Detector Signals to Physics Asymmetry

The goal of the physics analysis is to compute the parity violating asymmetry in electron-proton elastic scattering starting from the integrated raw detector signals. The total asymmetry is an unweighted combination of the asymmetries measured by each of the 8 Čerenkov detectors. Beam-line monitor information is used to apply data quality cuts and calculate the Helicity Correlated Beam Asymmetries (HCBAs). Linear regression is implemented to remove the HCBA induced false asymmetries from the measured asymmetry. The resulting regressed asymmetry is corrected for beam polarization and various background contributions. Then corrections for experimental bias including the radiative corrections are applied to obtain the physics asymmetry. For the Wien0 results presented here, the kinematics at which the measurement is performed is determined from simulation. Many collaborators contributed to the final results summarized in this chapter. I will provide more details on analysis projects that I contributed to.

6.1 Overview of the Q_{weak} Integration Mode Data

The main Čerenkov detector asymmetries are computed using the integrated signal (of Macro Pulse Signal (MPS) yield) measured from each of the 16 PMT channels (two per detector in each octant). The HCBAs are computed using the Beam Charge Monitors (BCMs) and the Beam Position Monitors (BPMs). Asymmetries are also computed for luminosity monitors and background detectors. The raw signals integrated over the MPS are available from the VQWK-ADCs for all the detectors and monitors. I will first provide an overview of the main detector data and different methods used to compute the final asymmetry, and then an overview of beam monitor data.

For the main detectors, beam-off offsets are removed from the raw photomultiplier tube (PMT) signals and then normalized to the beam current as follows,

$$Y^{R/L} = \frac{\frac{(Y^{R/L}_{raw} - Y_{ped}) \times g_{adc}}{N_s}}{I^{R/L}_{beam}} \tag{6.1}$$

where $Y^{R/L}_{raw}$ is the raw VQWK-ADC signal in the R/L helicity state, Y_{ped} is the measured beam-off signal or "pedestal", g_{adc} is the gain/calibration factor to convert ADC counts per sample to Volts, N_s is the number of 2 μs read-out samples per MPS state (Appendix C.2.1), and $I^{R/L}_{beam}$ is the beam current. (See Figure 6.1.) For the Čerenkov detectors and luminosity monitors, $Y^{R/L}$ is proportional to the differential scattering cross section (see Appendix D.2) hence, the $Y^{R/L}$ are used to compute the raw asymmetries from main detectors.

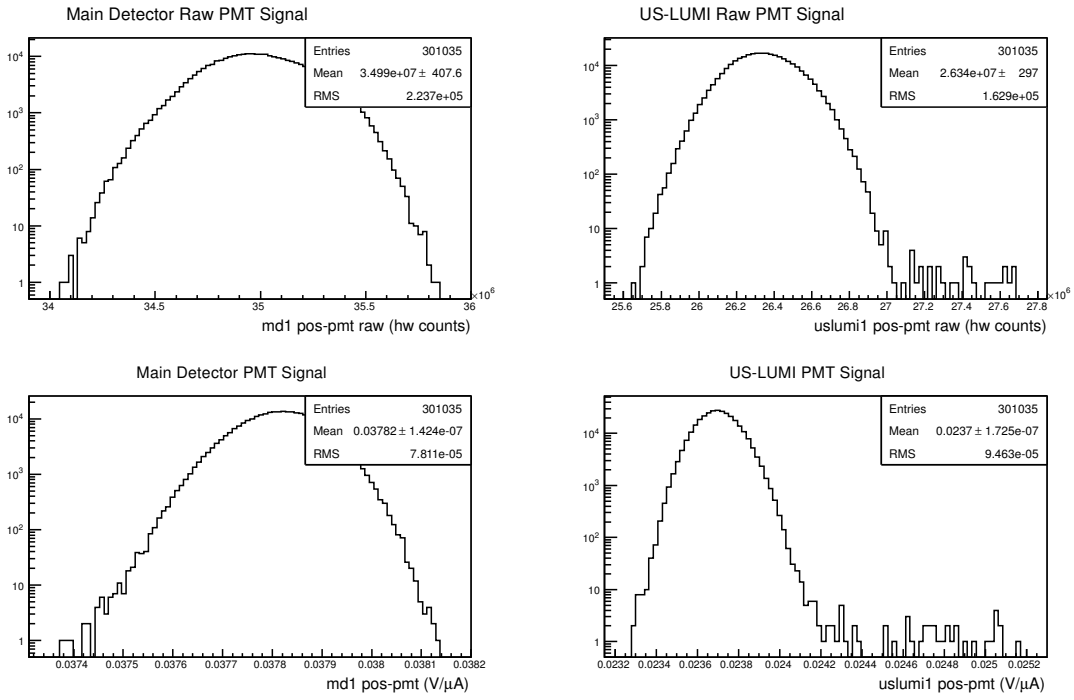

Figure 6.1: Raw MPS signals (top plots) and pedestal subtracted, normalized signals or yield (bottom plots) are compared for a main Čerenkov detector (left plots) and luminosity monitor channel (right plots).

A quartet (QRT) is defined to be one of two MPS patterns: L1,R1,R2,L2 or R1,L1,L2,R2 as discussed in Section 3.1. The raw asymmetry and average yield are computed for each QRT,

$$A^{raw} = \frac{(Y^{R1} + Y^{R2}) - (Y^{L1} + Y^{L2})}{(Y^{R1} + Y^{R2}) + (Y^{L1} + Y^{L2})} \tag{6.2}$$

$$Y = \frac{(Y^{R1} + Y^{R2}) + (Y^{L1} + Y^{L2})}{4} \tag{6.3}$$

where $Y^{L1,2}$ and $Y^{R1,2}$ are R or L MPS yields in a QRT. The A^{raw} and Y are computed for each QRT pattern for each PMT of each detector: main Čerenkov, luminosity monitors, and background detectors.

The next step is to combine asymmetries from different PMTs to obtain the whole detector asymmetry. There are 8 Čerenkov detectors with PMTs connected to either end of the Čerenkov bar. The Q_{weak} nomenclature defines the PMTs as positive (p) or negative (n) as shown in Figure 6.2.

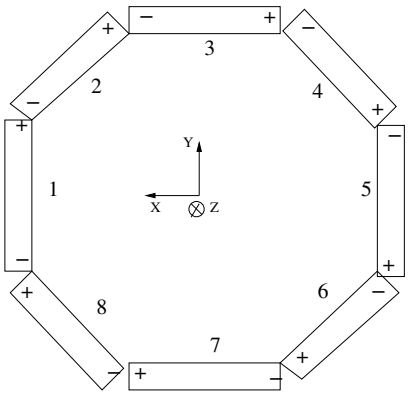

Figure 6.2: The PMT nomenclature in the main Čerenkov detector system. A Čerenkov bar is installed in each octant, and each bar has two PMTs, p (+) and n (-). The direction of the "Z" is aligned with the beam propagation.

6.1.1 Asymmetry Schemes

We used two methods to combine the asymmetries from PMTs. The first method calculates the asymmetry from a whole detector yield, while the second method calculates the average of all the PMT asymmetries.

The "yield-weighted" asymmetry is computed by combining the MPS yield of each PMT weighted by a factor to normalize the signal to remove gain and light collection variations. The weighted yield of a Čerenkov bar is

$$\mathrm{Y}^{\mathrm{R/L}}_{\mathrm{bar}} \;=\; \frac{(\mathrm{Y}^{\mathrm{R/L}}_{\mathrm{p}}\mathrm{W}_{\mathrm{p}} \;+\; \mathrm{Y}^{\mathrm{R/L}}_{\mathrm{n}}\mathrm{W}_{\mathrm{n}})}{(\mathrm{W}_{\mathrm{p}} \;+\; \mathrm{W}_{\mathrm{n}})} \tag{6.4}$$

where $\mathrm{Y}^{\mathrm{R/L}}_{\mathrm{p/n}}$ is the $\mathrm{Y}^{\mathrm{R/L}}$ for the p or n PMT in each bar. The weight, $\mathrm{W}_{\mathrm{p/n}} = 1/ < \mathrm{Y}_{\mathrm{p/n}} >$ is computed using the yields averaged over 1-2 hours, and is updated as needed to keep the weighted signals within a few percent ($\pm 4\%$) of 1 V/μA (see Figure 6.3). The yield-weighted asymmetry of a single Čerenkov bar is then computed using equation 6.2:

$$\mathrm{A}^{\mathrm{yield}}_{\mathrm{bar}} \;=\; \frac{(\mathrm{Y}^{\mathrm{R1}}_{\mathrm{bar}} + \mathrm{Y}^{\mathrm{R2}}_{\mathrm{bar}}) - (\mathrm{Y}^{\mathrm{L1}}_{\mathrm{bar}} + \mathrm{Y}^{\mathrm{L2}}_{\mathrm{bar}})}{(\mathrm{Y}^{\mathrm{R1}}_{\mathrm{bar}} + \mathrm{Y}^{\mathrm{R2}}_{\mathrm{bar}}) + (\mathrm{Y}^{\mathrm{L1}}_{\mathrm{bar}} + \mathrm{Y}^{\mathrm{L2}}_{\mathrm{bar}})} \tag{6.5}$$

The yield-weighted asymmetry for the whole Čerenkov detector is calculated using the weighted yields from Čerenkov bars in the 8 octants,

$$\mathrm{Y}^{\mathrm{L/R}}_{\mathrm{allbar}} \;=\; \frac{\sum_{\mathrm{j=1}}^{8}(\mathrm{Y}^{\mathrm{L/R}}_{\mathrm{p,j}}\mathrm{W}_{\mathrm{p,j}} \;+\; \mathrm{Y}^{\mathrm{L/R}}_{\mathrm{n,j}}\mathrm{W}_{\mathrm{n,j}})}{\sum_{\mathrm{j=1}}^{8}(\mathrm{W}_{\mathrm{p,j}} \;+\; \mathrm{W}_{\mathrm{p,j}})} \tag{6.6}$$

where the $\mathrm{Y}^{\mathrm{R/L}}_{\mathrm{p/n,j}}$ are p/n PMT yields for the j^{th} bar. The yield-weighted whole detector asymmetry is computed using equation 6.2 and given by,

$$\mathrm{A}^{\mathrm{yield}}_{\mathrm{allbar}} \;=\; \frac{(\mathrm{Y}^{\mathrm{R1}}_{\mathrm{allbar}} + \mathrm{Y}^{\mathrm{R2}}_{\mathrm{allbar}}) - (\mathrm{Y}^{\mathrm{L1}}_{\mathrm{allbar}} + \mathrm{Y}^{\mathrm{L2}}_{\mathrm{allbar}})}{(\mathrm{Y}^{\mathrm{R1}}_{\mathrm{allbar}} + \mathrm{Y}^{\mathrm{R2}}_{\mathrm{allbar}}) + (\mathrm{Y}^{\mathrm{L1}}_{\mathrm{allbar}} + \mathrm{Y}^{\mathrm{L2}}_{\mathrm{allbar}})} \tag{6.7}$$

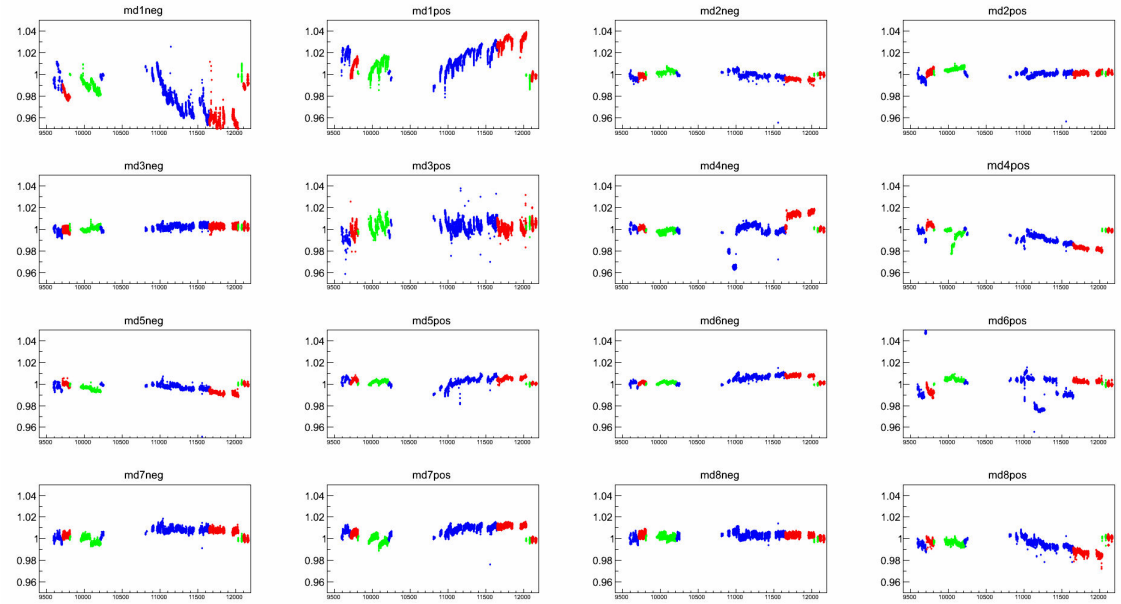

Figure 6.3: Relative weighted yields of the main detector PMTs ($\mathrm{Rel\_Y_i} = 16 \cdot \mathrm{Y_i W_i}/(\sum_{i=1}^{16} \mathrm{Y_i W_i})$) to show the yield stability during Wien0. The color corresponds to time period with new set of weights calculated to stabilize the weighted yield [92].

where the $\mathrm{Y}^{\mathrm{R1/2}}_{\mathrm{allbar}}$ and $\mathrm{Y}^{\mathrm{L1/2}}_{\mathrm{allbar}}$ are R/L MPS yields in a QRT. Similar yield-weighted asymmetries are computed for the luminosity monitors. Most background detectors only have single PMT although MD9 is the exception with a pair.

The "pmt-averaged" asymmetry for a Čerenkov bar is the average asymmetry of the positive and negative PMTs:

$$\mathrm{A}^{\mathrm{pmt}}_{\mathrm{bar}} = \frac{(\mathrm{A}^{\mathrm{raw}}_{\mathrm{p}} + \mathrm{A}^{\mathrm{raw}}_{\mathrm{n}})}{2} \tag{6.8}$$

where $\mathrm{A}^{\mathrm{raw}}_{\mathrm{p/n}}$ are asymmetries for p/n PMTs in a Čerenkov bar computed using equation 6.2. The pmt-averaged asymmetry for the whole Čerenkov detector is,

$$\mathrm{A}^{\mathrm{pmt}}_{\mathrm{allbar}} = \frac{\sum_{\mathrm{j=1}}^{8} \mathrm{A}^{\mathrm{pmt}}_{\mathrm{bar,j}}}{8} \tag{6.9}$$

where $A^{pmt}_{bar,j}$ is the pmt-averaged asymmetry for the j^{th} Čerenkov bar. Similarly pmt-averaged asymmetries are computed for luminosity monitors and the MD9 background monitor. In the next section, I discuss why A^{pmt}_{allbar} is our default whole detector asymmetry.

6.1.2 Main Čerenkov Detector Asymmetry Scheme Dependence Study

The whole Čerenkov detector asymmetry can be calculated using either equation 6.7 or 6.9 (yield-weighted or pmt-averaged asymmetries). The two schemes are sensitive to different systematic effects related to position sensitivity and PMT gain. In this section, I will derive the measured asymmetry from the two scheme, summarize an analysis that was done to compare whole Čerenkov detector asymmetries from the two schemes, and conclude with selecting the preferred whole Čerenkov detector asymmetry to be used as the final measured asymmetry.

The measured MPS yield is constructed for a PMT using first principles (Appendix D.3):

$$Y^{L/R}_{p/n} = g_{p/n} S^{L/R}(1 \pm \alpha\Delta) \tag{6.10}$$

where the Δ is the relative shift of the beam envelope of scattered electrons with respect to the center of the bar (see Figure 6.4 where $\Delta^R = -\Delta^L = \Delta$), α is the linear attenuation coefficient of the Čerenkov radiator material, $S^{R/L}$ is the ideal PMT signal when Δ equals zero and $g_{p/n}$ equals one, and the $g_{p/n}$ are the p/n PMT gains. The ideal asymmetry from a detector is given by

$$A_S = \frac{(S^{R1} + S^{R2}) - (S^{L1} + S^{L2})}{(S^{R1} + S^{R2}) + (S^{L1} + S^{L2})} \tag{6.11}$$

where the $S^{R1/2}$ and $S^{L1/2}$ are ideal PMT signals in L and R helicity states. The pmt-averaged asymmetry for a Čerenkov bar using equations 6.8 and 6.10 can be shown to be,

$$A^{pmt}_{bar} \simeq A_S + \alpha\Delta \cdot A^2_S \tag{6.12}$$

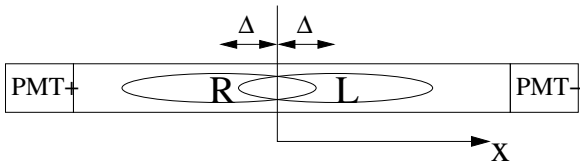

Figure 6.4: The relative shift of the beam envelope in L and R helicity states is $|\Delta|$ with respect to the center of the bar where the x-direction is parallel to the bar. The two ellipses illustrate the beam envelope during L and R helicity states.

Using equations 6.5 and 6.10, the yield-weighted asymmetry for a Čerenkov bar is,

$$A_{\rm bar}^{\rm yield} \simeq A_S + \delta\cdot\alpha\Delta + (-\delta\cdot\alpha\Delta - (\delta\cdot\alpha\Delta)^2)\cdot A_S^2 \tag{6.13}$$

where δ is the symmetry breaking gain factor

$$\delta = \frac{g_p - g_n}{g_p + g_n} \tag{6.14}$$

From equations 6.12 and 6.13, the largest discrepancy between yield-weighted and pmt-averaged asymmetries is generated by the symmetry breaking gain factor since other corrections to the measured asymmetry in the two schemes occur at higher order of A_S. The symmetry breaking gain factor (δ) is generated by the gain mismatch between the two PMT in a Čerenkovbar, and can vary from about 0% to 10%. The next to leading order effects of both schemes can be neglected since $A_S^2 \sim 10^{-11}$.

The position sensitivity in the yield-weighted scheme will be larger if the PMT gains are not balanced. If the gains are carefully balanced, we expect the two schemes to be similar. To test this, pmt-averaged and yield-weighted octant asymmetries are compared after the linear regression is applied.[†] The comparison of the regressed asymmetry measurements (see Table 6.1 and Figure 6.5) using 8 hours of data shows that yield-weighted and pmt-averaged asymmetries agree at the level of ±2 ppb. The yield-weighted asymmetry can have higher position sensitivity if the PMT gains are

[†]Linear regression will be discussed in section 6.4.

Table 6.1: Comparison of A_{bar}^{yield} and A_{bar}^{pmt} for approximately 8 hours of data (slug 69) using the "5+1" regression scheme.

Octant	A_{bar}^{yield} (ppm)	A_{bar}^{pmt} (ppm)	$(A^{yield} - A^{pmt})$ (ppb)
1	0.0597 ± 0.3573	0.0619 ± 0.3573	-2
2	0.3884 ± 0.3586	0.3884 ± 0.3586	0
3	-0.4514 ± 0.3606	-0.4514 ± 0.3606	0
4	0.4516 ± 0.3637	0.4520 ± 0.3637	0
5	0.0010 ± 0.3630	0.0008 ± 0.3630	0
6	0.4424 ± 0.3603	0.4426 ± 0.3603	-1
7	0.4242 ± 0.3575	0.4247 ± 0.3575	-1
8	-0.2756 ± 0.3560	-0.2762 ± 0.3560	0
All-octants	0.1295 ± 0.1339	0.1305 ± 0.1339	-1

poorly matched. However regression will in principle correct for this resulting in $A^{yield} = A^{pmt}$. The fact that this is not exactly the case is probably due to transverse leakage when gains are mismatched. The 1 ppb discrepancy is the expected order of magnitude to be explained by leakage of transverse asymmetry due to the percent level imperfections in weights used in A^{yield} [93]. Therefore, to avoid any potential symmetry breaking effects in gains into the final results, A_{allbar}^{pmt} is used to obtain the whole Čerenkov detector asymmetry.

6.1.3 Beam-line Monitors

This section provides an overview of the data from beam-line monitors which are used to apply main data quality cuts. The Helicity Correlated (HC) beam differences generated by beam charge, position, and energy monitors are commonly known as HCBAs, and they are used by the linear regression to remove false asymmetries from

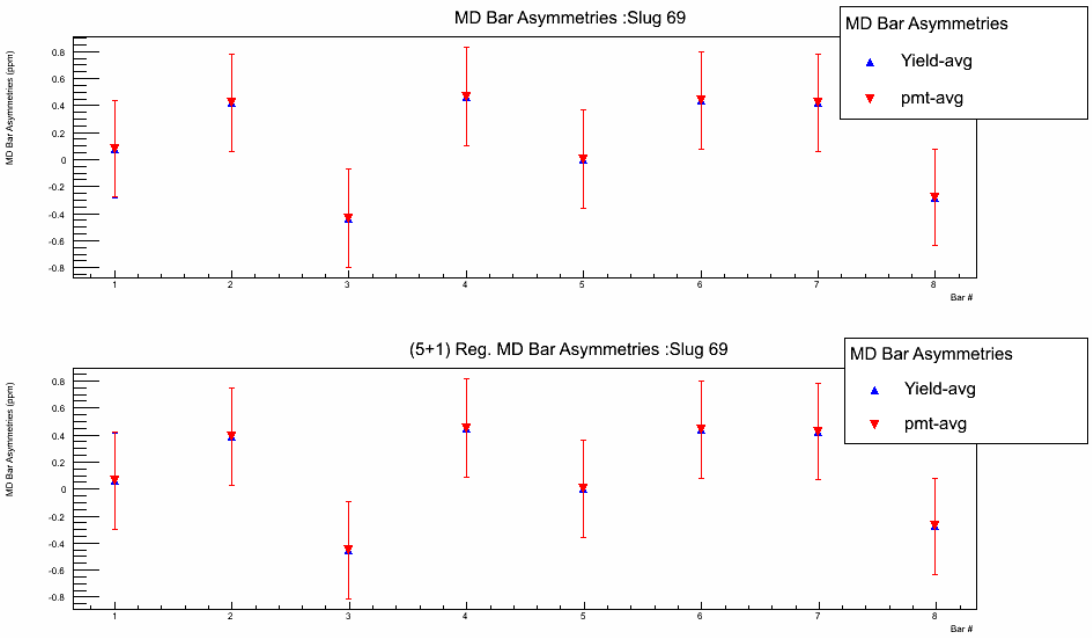

Figure 6.5: Comparison of yield-weighted (A_{bar}^{yield}) and pmt-averaged (A_{bar}^{pmt}) asymmetries for Čerenkov bar (octant-level). The raw asymmetries (top) and "5+1" regressed asymmetries (bottom) are compared using data from Table 6.1 (Slug 69 was taken after Wien0)

the measured asymmetry. The most important types of beam-line monitors are the BPMs and the BCMs. The BCMs provide the total charge accumulated during each MPS state. The charge accumulated in a MPS state is used to normalize the detector signal yields before computing asymmetries (see equation 6.1). The BPMs provide beam position measurements at various locations along the beam-line. A combination of BPMs is used to determine the beam position, angle, and relative energy at the Q_{weak} target during each MPS state. At least 3 BPMs are needed to span the beam phase space in position, angle, and energy [59]. The HC beam differences in beam position and angle, and HC beam asymmetry in charge and energy, are calculated for each QRT.

6.1.3.1 Beam Current Monitors

For Wien0, the average of two BCMs (BCM1 and BCM2) is used to normalize the detector yields (in equation 6.1). This average reduces BCM noise contribution to the measured asymmetry [94]. The beam current is determined for each MPS using,

$$\mathrm{I}^{\mathrm{L/R}}_{\mathrm{BCM}} \;=\; \frac{(\mathrm{I}^{\mathrm{L/R}}_{\mathrm{raw}} \;-\; \mathrm{I}_{\mathrm{ped}}) \times \mathrm{g}_{\mathrm{bcm}}}{\mathrm{N}_{\mathrm{s}}} \tag{6.15}$$

where $\mathrm{I}_{\mathrm{ped}}$ is the pedestal (beam off) and $\mathrm{g}_{\mathrm{bcm}}$ converts pedestal corrected raw ADC counts in to μA. $\mathrm{I}_{\mathrm{ped}}$ can in principle be adjusted to minimize the average non-linearity (discussed later in Section 6.3.1) in the main Čerenkov detectors. Two sets of optimized pedestals are used for Wien0: one value for Wien0 high beam current (145 μA) and another value for low beam current ($20 - 45$ μA) [58, pg. 145]. The HC beam current (charge) asymmetry is defined as,

$$\mathrm{A_Q} = \frac{(\mathrm{I}^{\mathrm{R1}}_{\mathrm{BCM}} + \mathrm{I}^{\mathrm{R2}}_{\mathrm{BCM}}) - (\mathrm{I}^{\mathrm{L1}}_{\mathrm{BCM}} + \mathrm{I}^{\mathrm{L2}}_{\mathrm{BCM}})}{(\mathrm{I}^{\mathrm{R1}}_{\mathrm{BCM}} + \mathrm{I}^{\mathrm{R2}}_{\mathrm{BCM}}) + (\mathrm{I}^{\mathrm{L1}}_{\mathrm{BCM}} + \mathrm{I}^{\mathrm{L2}}_{\mathrm{BCM}})} \tag{6.16}$$

where the $\mathrm{I}^{\mathrm{R/L}}_{\mathrm{BCM,i}}$ are MPS yields (equation 6.15) for R/L pairs of states in QRT.

6.1.3.2 Beam Position Monitors

The absolute beam position for each R/L MPS state is calculated using the raw signals from four antennas for each BPM(section 3.2.2),

$$\begin{aligned}
\mathrm{X}^{\mathrm{L/R}}_{\mathrm{rel}} &= \kappa[\frac{(\mathrm{XP}^{\mathrm{L/R}} - \mathrm{XP}_{\mathrm{ped}}) - \alpha_{\mathrm{X}}(\mathrm{XM}^{\mathrm{L/R}} - \mathrm{XM}_{\mathrm{ped}})}{(\mathrm{XP}^{\mathrm{L/R}} - \mathrm{XP}_{\mathrm{ped}}) + \alpha_{\mathrm{X}}(\mathrm{XM}^{\mathrm{L/R}} - \mathrm{XM}_{\mathrm{ped}})}] \\
\mathrm{Y}^{\mathrm{L/R}}_{\mathrm{rel}} &= \kappa[\frac{(\mathrm{YP}^{\mathrm{L/R}} - \mathrm{YP}_{\mathrm{ped}}) - \alpha_{\mathrm{Y}}(\mathrm{YM}^{\mathrm{L/R}} - \mathrm{YM}_{\mathrm{ped}})}{(\mathrm{YP}^{\mathrm{L/R}} - \mathrm{YP}_{\mathrm{ped}}) + \alpha_{\mathrm{Y}}(\mathrm{YM}^{\mathrm{L/R}} - \mathrm{YM}_{\mathrm{ped}})}] \\
\mathrm{X}^{\mathrm{L/R}}_{\mathrm{abs}} &= \cos(\phi) \cdot \mathrm{X}^{\mathrm{L/R}}_{\mathrm{rel}} - \sin(\phi) \cdot \mathrm{Y}^{\mathrm{L/R}}_{\mathrm{rel}} + \mathrm{X}_{\mathrm{offset}} \\
\mathrm{Y}^{\mathrm{L/R}}_{\mathrm{abs}} &= \sin(\phi) \cdot \mathrm{X}^{\mathrm{L/R}}_{\mathrm{rel}} + \cos(\phi) \cdot \mathrm{Y}^{\mathrm{L/R}}_{\mathrm{rel}} + \mathrm{Y}_{\mathrm{offset}}
\end{aligned} \tag{6.17}$$

where $XP^{L/R}$, $XM^{L/R}$, $YP^{L/R}$, $YM^{L/R}$ are the four antenna signals, XP_{ped}, XM_{ped}, YM_{ped}, YP_{ped} are linearly fitted pedestals[†] for the four antennas, α_X/α_Y are relative gains, κ is the calibration factor that converts arbitrary position readings to correct position units (mm), ϕ is the BPM rotation angle, and X_{offset}/Y_{offset} are surveyed offsets that converts the $X^{L/R}_{abs}/Y^{L/R}_{abs}$ into the accelerator coordinate system which is the default coordinate system used during the experiment [59]. The BPMs are typically rotated by $\phi = 45^o$ to shield the antennas from synchrotron radiation [59].

The electron beam position at the Q_{weak} target is obtained using a set of BPMs in the drift region (free of beam correctors) in front of the target. The beam position and angle are determined for each helicity state using a linear least squares fit of the absolute beam positions from set of BPMs [59]:`3H07a, 3H07b, 3H07c, 3H09 and, 3H09B`. A virtual BPM is available to access beam position and angle at the Q_{weak} target (know as the `qwk_target`) [59]. A relative measurement of the electron beam momentum (know as `qwk_energy`) is determined by using the horizontal beam position and angle at the Q_{weak} target and the horizontal beam position from the BPM `3C12` at the highest dispersion region in the Hall C arc [74]. The relative momentum at Q_{weak} target is computed using,

$$\frac{dp_T}{p_T} = \frac{X_{3C12} - X_T M_{11} - M_{12} X'_T}{M_{15}} \tag{6.18}$$

where M_{ij} are transport matrix elements that transform electron position, angle, and momentum from the highest dispersion region to the Q_{weak} target, X_{3C12} is horizontal beam position at BPM `3C12`, and X_T/X'_T are horizontal position/angle at Q_{weak} target.

[†]The pedestal can be determined using two different methods. For linear devices this is simply the beam off signal. For significantly nonlinear devices, the pedestal is determined from a linear fit to data close to production conditions.

The QRT averaged yields for beam position and angle, and relative beam momentum/energy are calculated using,

$$X_{BPM} = \frac{(X^{R1}_{BPM} + X^{R2}_{BPM}) + (X^{L1}_{BPM} + X^{L2}_{BPM})}{4} \tag{6.19}$$

where the $X^{R1/2}_{BPM}$ and $X^{L1/2}_{BPM}$ are MPS quantities (beam position, angle, and relative momentum) and HC beam differences for beam position and angle, and HC beam energy asymmetry, are calculated using,

$$D_{BPM} = \frac{(X^{R1}_{BPM} + X^{R2}_{BPM}) - (X^{L1}_{BPM} + X^{L2}_{BPM})}{4} \tag{6.20}$$

where X_{BPM} and D_{BPM} are computed for beam position, angle, and relative momentum.[†]

Now that an overview of the Čerenkov detector asymmetry, beam position/angle/relative energy, and HC differences are given, the next section will discuss the data quality cuts applied in the analysis using the absolute yields of Čerenkov detectors and beam-line monitors.

6.2 Data Quality Cuts

The goal of data quality cuts is to remove data with read-out errors, low beam current, and unusual fluctuations in the beam parameters (beam excursions and trips). These conditions are defined using a set of criteria that applies to the detector/monitor MPS based yields. They ultimately decide which data are used to extract the final asymmetry. The overview of the data quality cut framework, which I have implemented for Q_{weak} , was given the section 4.5.1. This section summarizes the data quality cuts applied in the Q_{weak} analyzer.

[†]With this definition, the HC BPM values are $X_{BPM} \pm D_{BPM}$ and the difference between different helicity states is $2 \cdot D_{BPM}$.

6.2.1 Beam Position Related Cuts

Two main data quality cuts are applied to BPM data. First, cuts are applied to remove BPM signal saturations. Then cuts are applied to absolute beam positions to remove excursions and diversion from nominal values. These excursions (see Figure 6.6 for an example) can induce an additional background contribution to the measured asymmetry because the beam may then interact with the beam pipe. Therefore, they must be removed from the final data set.

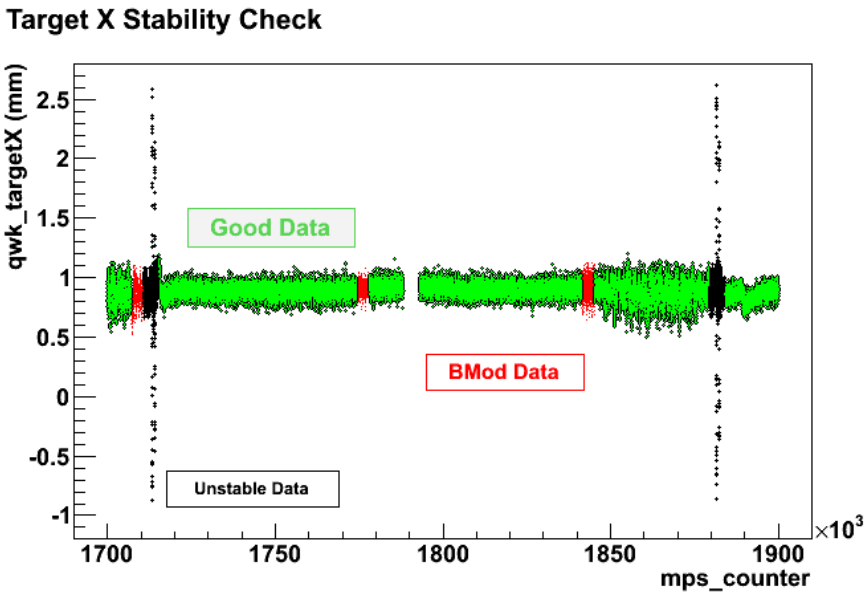

Figure 6.6: The data quality cut removes **unstable beam** and beam modulation periods. Only good data periods are included in the final analysis

6.2.2 Beam Current Related Cuts

Data quality cuts are applied to BCM signals to remove low beam currents and unstable beam periods. Unstable beam periods are mainly caused by sudden loss of beam known as beam trips (see Figure 6.7). On average, we got 5 beam trips per hour

during Q_{weak} experiment running. After a beam trip, it takes about 30-60 seconds to recover back to nominal beam current. The recovery period is knows as the beam ramp. I will discuss an analysis that I have done to determine the low beam current limit for the final data set in the remainder of this section.

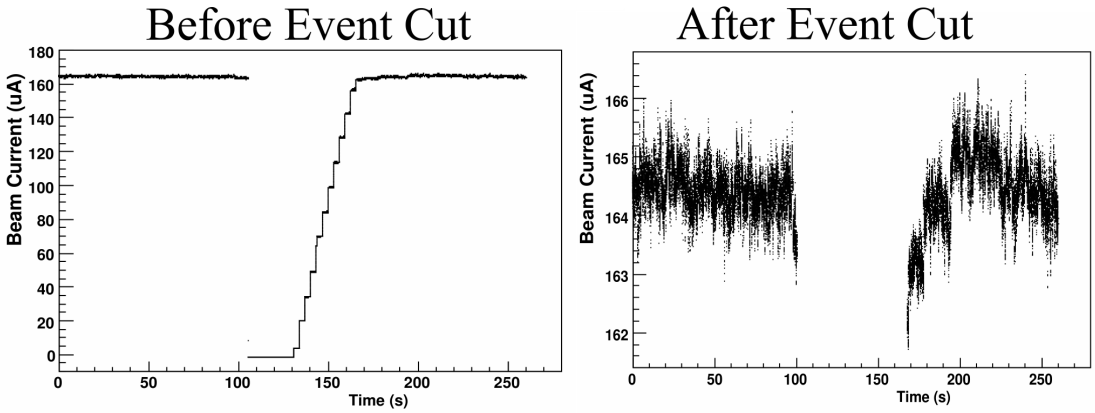

Figure 6.7: The data quality cut on beam current removes unstable beam periods (mostly beam trips). At the usual beam ramp rate of about 5 μAs^{-1} it takes about 30-60 seconds to restore beam current back. (This example was taken from a different Wien during Run 1.) Note the different vertical scales in both plots.

In certain beam ramps after a beam trip, an unusually stable period of low beam current ($I_{BCM} \sim 10$ μA) data passes the previous data quality cuts. (see Figure 6.8.) These low beam current data generate a shift in the average asymmetry beyond the expected statistical shift when 1% of data is removed. (see Table 6.2 and see Appendix D.1 for statistical shift definition.) Further investigation revealed that both the charge asymmetry (Figure 6.9) and the BCM non-linearity are large (about 44%) for the low beam current data which can generate large false asymmetry. The large non-linearity at low beam current occurs due to operation far from where the BCM pedestals are optimized (optimized for currents over 140 μA). Therefore, the BCM data cut is updated to remove data with I_{BCM} less than 100 μA.

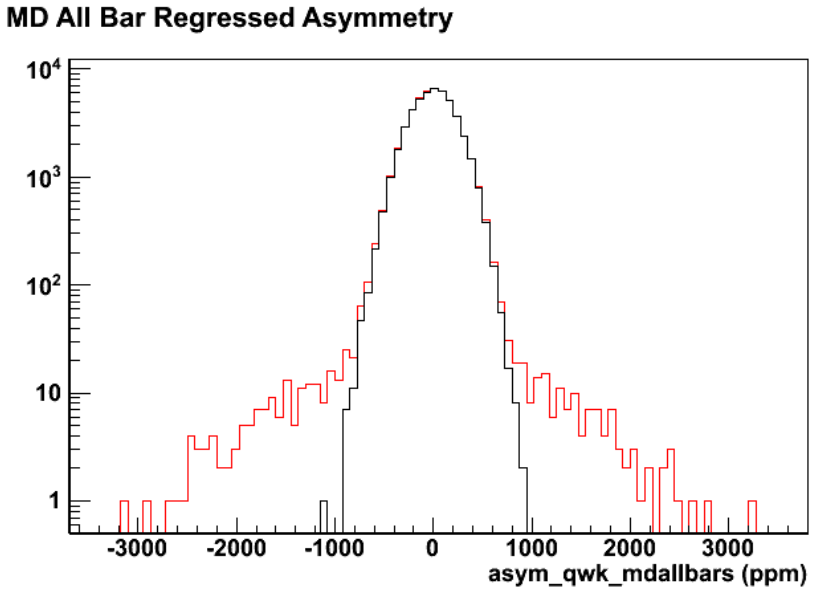

Figure 6.8: The regressed main Čerenkov detector asymmetry (red: $I_{BCM} > 1$ μA , black: $I_{BCM} > 10$ μA). Note: The RMS width of the Čerenkov detector asymmetry is large at small beam currents ($\sim$1000 ppm at $I_{BCM} \sim 10$ μA vs. $\sim$220 ppm at $I_{BCM} \sim 180$ μA) generating tails in the distribution. (This analysis was done using data after Wien0.)

Table 6.2: The effect of low beam current contamination on the standard regressed asymmetry. The error is RMS/$\sqrt{N_{QRT}}$.

		Asymmetry	
Data Cut	Entries (N_{QRT})	Average (ppm)	RMS (ppm)
$I_{BCM} > 1$ μA cut	49879	-2.198 ± 1.146	256
$I_{BCM} > 10$ μA cut	49152	-0.955 ± 1.010	224
Observed shift		1.243	
Statistical shift expected [58, pg. 148]		0.136	

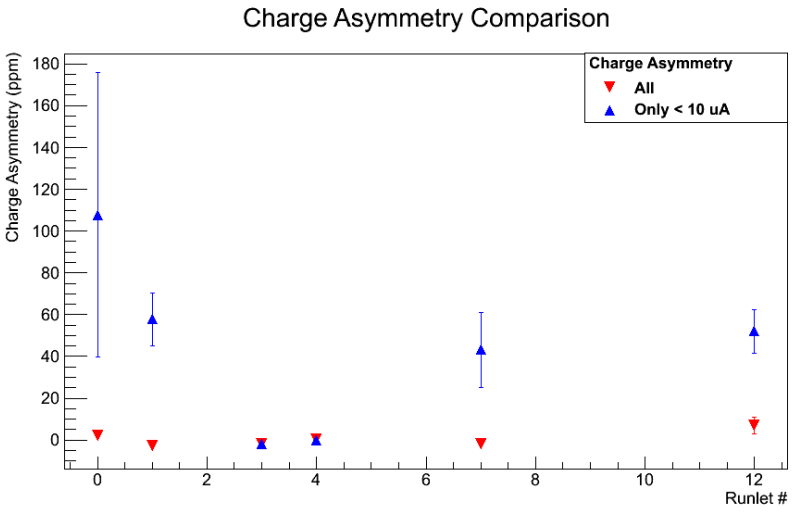

Figure 6.9: The charge asymmetry vs. runlet (red: all beam currents, blue: $I_{BCM} < 10\ \mu A$). Note that for runlets 5,6,8,9,10, and 11 are missing in the analysis due to no beam availability. Also during runlets 3 and 4, no low beam current data exists.

6.2.3 Other Data Quality Cuts

All the VQWK-ADC channels have hardware error checks implemented to detect any issues that require data to be removed from the final analysis (Section 4.5.1). Then, an event cut also removes beam modulation (a special set of events with induced dithering to the beam properties) periods from the final data analysis. Data quality cuts are also applied to the yields of two Čerenkov detectors with highest sensitivity to the horizontal and vertical beam motion (detectors at octants 1 and 7: MD1 and MD7) to prevent yield fluctuations due to beam excursions and other effects. The main detector yield cuts are mostly benign cuts because 99.9% of the time yield fluctuations are caused by beam excursions and data quality cuts applied to BPM can detect beam excursions effectively. Finally, there is a set of data quality cuts applied to keep the integrity of the blinding factor. These cuts are related to

Q_{weak} target type and status, beam current, and QTOR current. A summary of all the data quality cuts applied for Wien0 is given in Table 6.3.

Table 6.3: A list of data quality cuts and loss of data from each cut. Note: X_{ant} is signals from BPM antennas defined in equation 6.17

Detector/Monitor	Data Cut	Stability/Extended Cut	Data loss (%)
VQWK-ADCs	Hardware errors	none	~ 1.0
BPM Pedestal cut	$X_{ant} < 10000$ counts	none	~ 1.0
BPM Saturation cut	$X_{ant} >$ custom_limit	BPM dependent limit	
X/Y at target	10 mm $>$ |Y/X|	RMS(X/Y) > 0.15 mm	~ 0.1
MD1/MD7 octant	$Y > 0.05 V\mu A^{-1}$	RMS(Y) > 0.0001 $V\mu A^{-1}$	< 0.1
BCM (charge)	$I_{BCM} < 100$ μA	RMS(I_{BCM}) > 2 μA	~ 3.0
Blinder-related			~ 3.0

6.3 False Asymmetries

HC beam differences from beam position and angle, and HC beam asymmetries from beam charge and energy generate false asymmetries in the measured Čerenkov detector asymmetry. The HC beam differences are computed for each QRT and are used to correct the false asymmetries by applying linear regression (see Section 6.4).

During Wien0, the Insertable Half Wave Plate (IHWP) state is changed roughly every 8 hours (a slow helicity reversal) to help cancel HC beam differences. This section summarizes the HC beam differences/asymmetries, introduces the slow helicity reversal techniques, and discusses the levels of cancellation of HC beam differences in Wien0 data.

6.3.1 Charge Asymmetry

The measured main detector signals are normalized to the beam charge (equation 6.1). Due to target density changes, PMT and electronic non-linearity, VQWK-ADC non-linearity, and BCM electronic chain non-linearity (see Appendix D.4), the measured detector yields are non-linear with respect to charge. This non-linearity (f) distorts the physics asymmetry ($f \cdot A_{PV}$) and generates a false asymmetry by coupling the measured asymmetry to the charge asymmetry [66]. The false asymmetry generated by charge is given by,

$$A^{false}_{non-lin} \propto f \cdot A_Q, \text{ and } A_{msr} = A_{PV} + A^{false}_{non-lin} \tag{6.21}$$

where A_{msr} is the measured asymmetry, A_{PV} is the Parity Violating physics asymmetry, and A_Q is defined in equation 6.16. The physics asymmetry distortion will be discussed further in Section 6.5.3. Therefore, the non-linearity and charge asymmetry must be minimized to reduce these effects. The charge asymmetry was converged to zero using an active feedback system (see section 4.5.3) running continuously during data taking. The non-linearity can be estimated from the correlation between the measured asymmetry and the charge asymmetry (see Figure 6.10[†]).

We need to minimize the false asymmetry from charge to satisfy the condition $f \cdot A_Q << \delta A_{msr}$ where δA_{msr} is the uncertainty of the Čerenkov detector measured asymmetry. In the Wien0 data set, the average charge asymmetry during a runlet is about 0.04 ppm (see Figure 6.11) and the maximum observed non-linearity of about 2%, therefore, the false asymmetry is about 0.0008 ppm which is smaller than the uncertainty on the Čerenkov detector asymmetry during a runlet (about $\pm$0.8 ppm).

[†]The Čerenkov detector asymmetry is regressed using the Standard regression scheme to be discussed in Section 6.4.

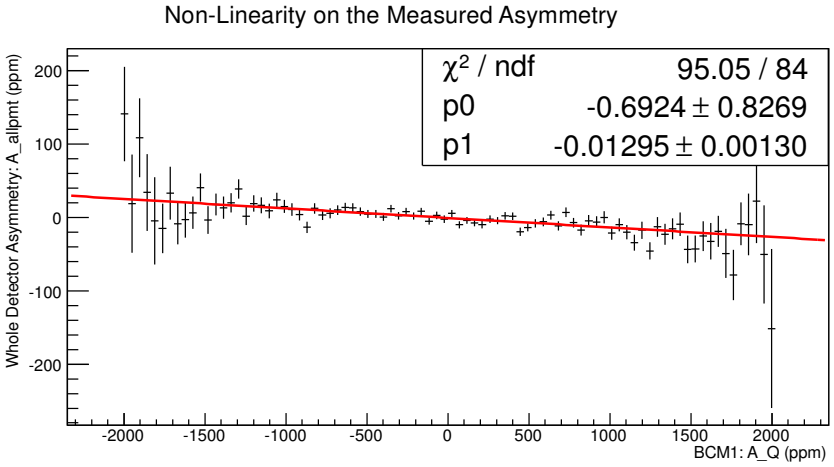

Figure 6.10: The non-linearity appears as a correlation between the main detector asymmetry and charge asymmetry. This particular measurement is from a regular production runlet (7-8 min of data) at 145 μA and the non-linearity, f = -0.013.

Therefore, the false asymmetry due to charge asymmetry can be neglected. The distortion of the physics asymmetry due to the non-linearity can only be minimized by minimizing the non-linearity itself. Furthermore, it could be removed or minimized by using linear regression (discussed in Section 6.5.3)

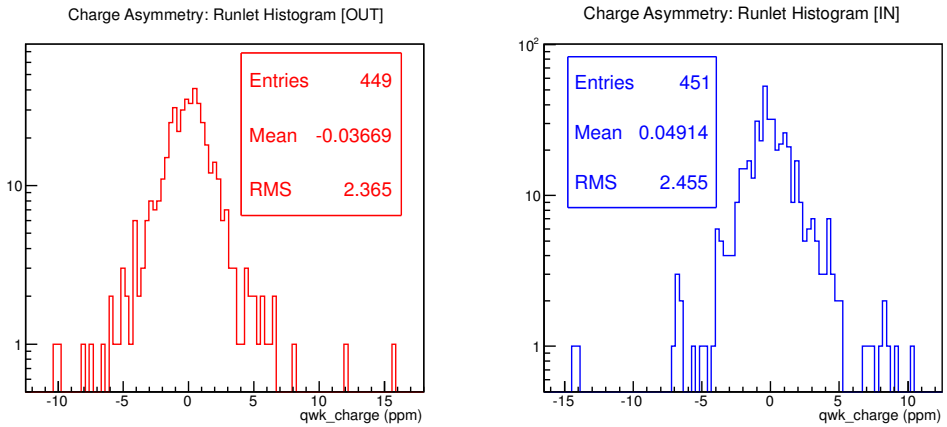

Figure 6.11: Runlet level charge asymmetry distribution for IHWP IN and OUT in Wien0.

6.3.2 HC Beam Parameters

The Helicity Correlated (HC) position differences are minimized by optimizing the Pockels cell alignment and voltages and by using adiabatic damping during beam transport from the source to the Q_{weak} target. For longer time scales (5-8 hours or slug scale), slow helicity reversals (see section 6.3.3 for the general discussion) may reduce the average HC beam parameter differences. The measured runlet level distributions of HC position differences are shown in Figures 6.12 and 6.13. A good reference for the stability of beam positions during Wien0 is [95]. The HC energy asymmetry, $D(\frac{dp}{p})$ is a measure of the HC energy/momentum fluctuations at the Q_{weak} target (see Figure 6.14).

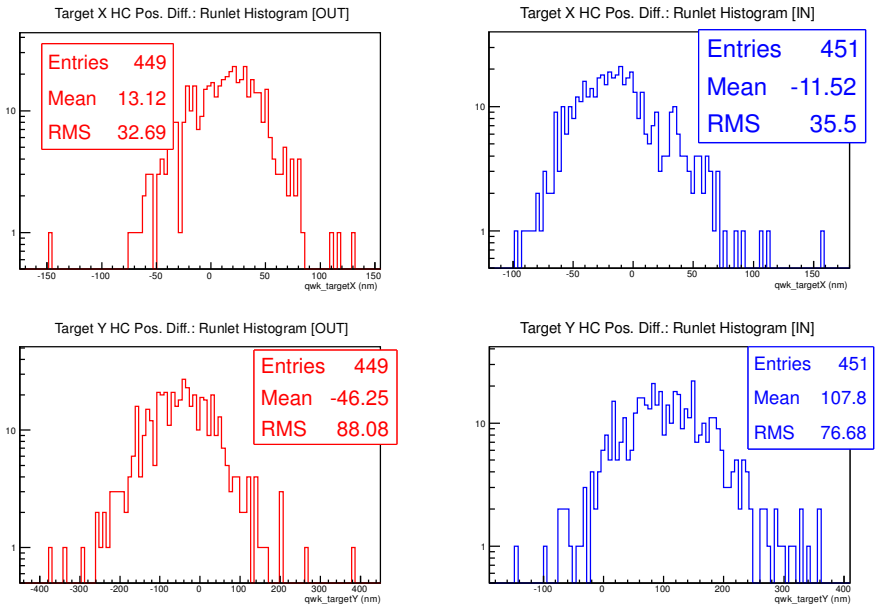

Figure 6.12: The runlet level HC position differences at the Q_{weak} target for Wien0.

So far, Sections 6.3.1 and 6.3.2 summarized un-weighted average HC asymmetries/differences. The errors included in plots are statistical fluctuations in measurements. Since these measurements are used to correct the false asymmetries in the

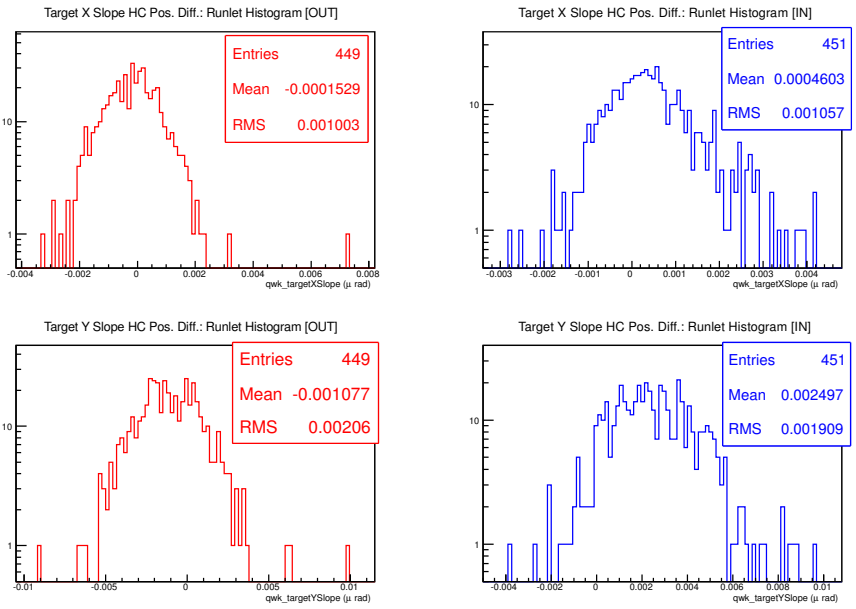

Figure 6.13: The runlet level HC angle (direction) differences at the Q_{weak} target for Wien0.

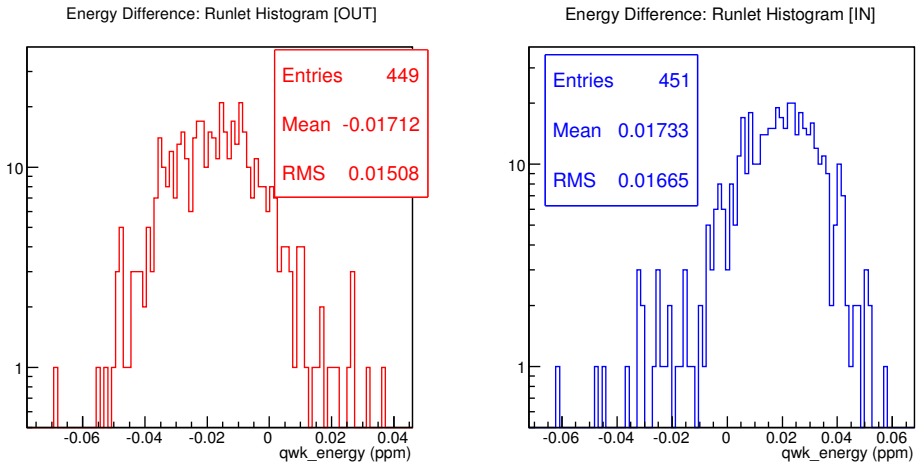

Figure 6.14: The runlet level HC energy (qwk_energy) differences at the Q_{weak} target for Wien0.

measure main detector asymmetry, I have included the main detector asymmetry error weighted HC asymmetries/differences during Wien0 in Table 6.4. (See reference [96]

for more details.) The errors are computed based on monitor resolutions instead of statistical fluctuations. The monitor resolution is the limit of a measurement by a beam monitor at quartet level and statistical fluctuations are greater than monitor resolutions due to random noise. The monitor resolutions ultimately determine the limit of the linear regression to correct false asymmetries at QRT scale [93].

The BCM resolution is about 60 ppm/$\sqrt{\mathrm{N_{QRT}}}$ where the $\mathrm{N_{QRT}}$ is the total number of quartets (QRTs).[†] The BPM position resolution is 1 μm/$\sqrt{\mathrm{N_{QRT}}}$ and angle resolution is 0.13 μrad/$\sqrt{\mathrm{N_{QRT}}}$ [59]. The energy resolution is 0.3 ppm/$\sqrt{\mathrm{N_{QRT}}}$ which estimated by using the BPM resolution and the length of the dispersive region in Hall C arc where the beam is bended.

Table 6.4: Average HCBAs in Wien0. Errors for a runlet are based on monitor resolutions, $\delta \mathrm{X} = \frac{\sigma_{\mathrm{X}}}{\sqrt{\mathrm{N_{QRT}}}}$, then averaged to whole Wien0. Results are weighted by $\frac{1}{\sigma_{\mathrm{A}}^2}$ where σ_{A} is the main detector asymmetry RMS for the runlet.

Qty	IHWP-OUT	IHWP-IN	AVG(OUT,-IN)
Dx (nm)	14.43 ± 0.25	-13.60 ± 0.25	14.02 ± 0.18
Dy (nm)	-50.41 ± 0.25	108.44 ± 0.25	-79.03 ± 0.18
Dxp (nrad)	-0.13 ± 0.05	0.43 ± 0.05	-0.28 ± 0.04
Dyp (nrad)	-1.16 ± 0.05	2.51 ± 0.05	-1.84 ± 0.04
$\mathrm{A_E}$ (ppm)	-0.02 ± 0.0001	0.02 ± 0.0001	-0.02 ± 0.00004
$\mathrm{A_Q}$ (ppm)	-0.039 ± 0.007	-0.036 ± 0.007	-0.002 ± 0.005

6.3.3 Slow Helicity Reversals

The IHWP state is changed roughly every 8 hours to help cancel HCBAs. The IHWP reversal flips the sign of the physics asymmetry due to reversal of the polarization vector (see Section 3.2.1), while if aligned properly, most HCBAs do

[†]BCM resolution is determined from BCM double difference distribution

not. The IHWP IN and OUT data sets are averaged after correcting the sign of the asymmetry (AVG(OUT, −IN)), helping to cancel any false asymmetries which are independent of the IHWP state. HCBAs that do not change sign under the IHWP reversal include Pockels cell optical effects and leakage of helicity reversal signals into the detector/monitor yields. If the two data sets are combined as (OUT + IN)/2, then the resultant asymmetry is a measure of the residual false asymmetry.

There are also HCBA effects for example, due to Pockels cell polarization effects, that change sign with the IHWP reversal. These effects require an additional slow reversal technique to minimize false asymmetries. The Wien state reversal is one such technique where the spin of the electrons are flipped magnetically instead of optically (see section 3.2.1). However, this was not available for the Wien0 data set but during the rest of Q_{weak} data taking, the Wien state was flipped at slower time scale compared to IHWP reversal to improve the false asymmetry cancellation. Unfortunately, HCBAs from position/angle and beam energy during Wien0 were changing sign with the IHWP reversal and we did not have a Wien reversal, so cancellation was poor for AVG(OUT,-IN). (See Table 6.4.)

6.4 Linear Regression

Linear regression is applied to the measured raw Čerenkov detector asymmetry (A^{raw}) to remove false asymmetries generated from HCBAs. The measured asymmetry (A_{msr}) after linear regression is

$$\begin{aligned} A_{msr} &= A^{raw} - \sum_{i=1}^{5} \frac{\partial A^{raw}}{\partial x_i} \cdot \Delta x_i \\ &= A^{raw} - \sum_{i=1}^{5} A_{false\_i} \end{aligned} \tag{6.22}$$

where Δx_i is the HCBA from i^{th} beam parameter (see Table 6.5), $\frac{\partial A^{raw}}{\partial x_i}$ is the sensitivity or slope of the measured raw asymmetry to the i^{th} beam parameter, and A_{false_i} is the false asymmetry contribution from the i^{th} beam parameter. For the Wien0 analysis, the sensitivities ($\frac{\partial A^{raw}}{\partial x_i}$) are determined for each runlet by performing a multidimensional linear regression based on the set of beam parameters (x_i) and correction to A^{raw} is applied on a QRT basis [82, 83].

Table 6.5: The beam parameter list used in the standard regression scheme

Beam Qty	Description
Dx (nm)	HC X position differences at target
Dy (nm)	HC Y position differences at target
Dxp (nrad)	HC X angle differences at target
Dyp (nrad)	HC Y angle differences at target
DE (ppm)	Relative Energy/momentum differences at target

In the next section, I will summarize measured sensitivities and address certain issues related to the correlations between beam parameters. Then I introduce different regression schemes available, present the standard linear regression results, discuss the size of the regression correction, and summarize the systematic errors for the measured asymmetry due to linear regression.

6.4.1 Measured Sensitivities

I have done an analysis related to the sensitivity variation between yield-weighted (A_{bar}^{yield}) and pmt-averaged (A_{bar}^{pmt}) main Čerenkov asymmetries based on Run 1 data taken after the Wien0. The goal of this analysis is to investigate the sensitivity variation in detector octants. The sensitivities of yield-weighted and pmt-averaged octant level asymmetries are compared for all 8 octants averaged over a slug. (see

Figures 6.15 - 6.17.) If $A_{bar}^{yield} \simeq A_{bar}^{pmt}$ is satisfied according to equations 6.12 and 6.13, then the measured sensitivities are,

$$\frac{\partial A_{bar}^{yield}}{\partial X_i} \simeq \frac{\frac{\partial A_p}{\partial X_i} + \frac{\partial A_n}{\partial X_i}}{2} \tag{6.23}$$

where $\frac{\partial A_{bar}^{yield}}{\partial X_i}$ is the measured sensitivity of the yield-weighted asymmetry and $\frac{\partial A_{p/n}}{\partial X_i}$ is the measured sensitivities of the p/n PMT asymmetries in each octant.

The variation of the sensitivities for HC X/Y differences vs. the octant (see Figures 6.15 and 6.16) arises from the azimuthal angle of the octants. Note that the X sensitivities of the p/n PMTs are same for octant 1 and 5 which are the left and right octant detectors (see Figure 6.2). The X (horizontal) variation in these two octants is perpendicular to the detector and therefore the sensitivities are same for both PMTs of the detector. Similarly the difference in sensitivities for p/n PMTs is maximized at octant 3 and 7 where the X variation is parallel to the bar. The same argument can be made about the top and bottom octant for Y (vertical) position sensitivities[†] . In general, when averaged over the whole detector, the sensitivities are minimized compared to individual octants due to the symmetry of the detector system (see Table 6.6 for X sensitivity numbers) which is a design specification of the detector system.

Ideally, energy sensitivity is expected to behave as a monopole that is independent of the octant but this is not observed (see Figure 6.17). One can conclude that the position coupling with energy has created a hybrid of a monopole dipole combination. The octant dependence of the energy/momentum fluctuations

[†]One of the interesting observation about the individual PMT position sensitivities is that they change sign when going from the top octant to the bottom octant for X sensitivity and going from left to right for Y sensitivity. This is related to the convention that defines the p and n PMTs for each octant (see Figure 6.2) where the two azimuthally opposed octants have p and n PMTs on opposite sides.

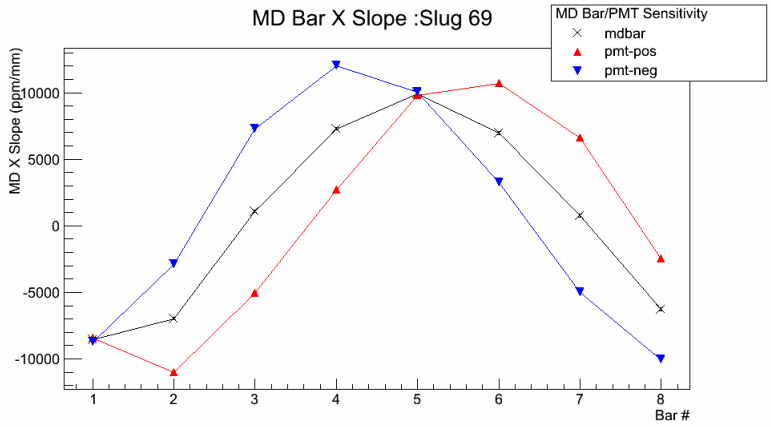

Figure 6.15: Octant variation of the vertical position (X) sensitivities, $\frac{\partial A_{bar}^{yield}}{\partial X}$, $\frac{\partial A_p}{\partial X}$, and $\frac{\partial A_n}{\partial X}$ for p/n PMTs.

Table 6.6: Comparison of horizontal beam position sensitivities of yield weighted and PMT averaged asymmetries. Last row has sensitivity of the all Čerenkov detectors yield weighted asymmetry (data from slug 69).

Octant	$\frac{\partial A_{bar}}{\partial X}$ (ppm/mm)	$\frac{\frac{\partial A_p}{\partial X} + \frac{\partial A_n}{\partial X}}{2}$ (ppm/mm)
1	-8571 ± 101	-8570 ± 82
2	-6965 ± 101	-6968 ± 77
3	1099 ± 101	1108 ± 78
4	7297 ± 102	7361 ± 80
5	9918 ± 102	9918 ± 79
6	6957 ± 101	6959 ± 77
7	782 ± 101	795 ± 77
8	-6262 ± 100	-6253 ± 77
Octant average	532 ± 36	543 ± 28
yield weighted all bar	505 ± 38	

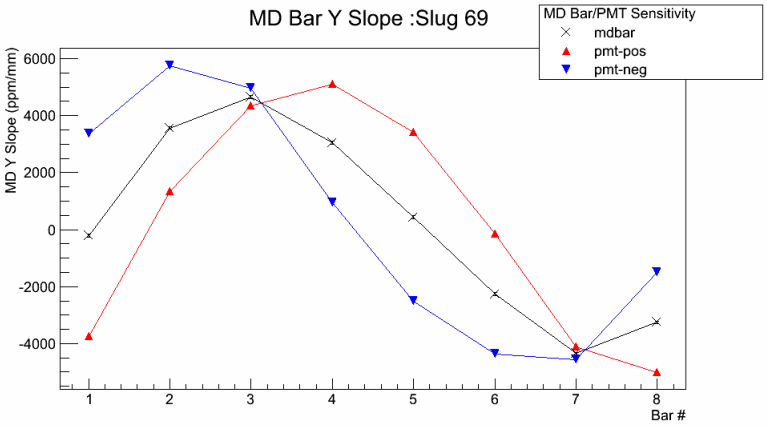

Figure 6.16: Octant variation of the vertical position (Y) sensitivities, $\frac{\partial A_{bar}^{yield}}{\partial Y}$, $\frac{\partial A_p}{\partial Y}$, and $\frac{\partial A_n}{\partial Y}$.

(HCBA from relative energy) can be attributed to the correlation with horizontal beam position in the energy measurement. The octant variation shows similarities to horizontal position sensitivity.

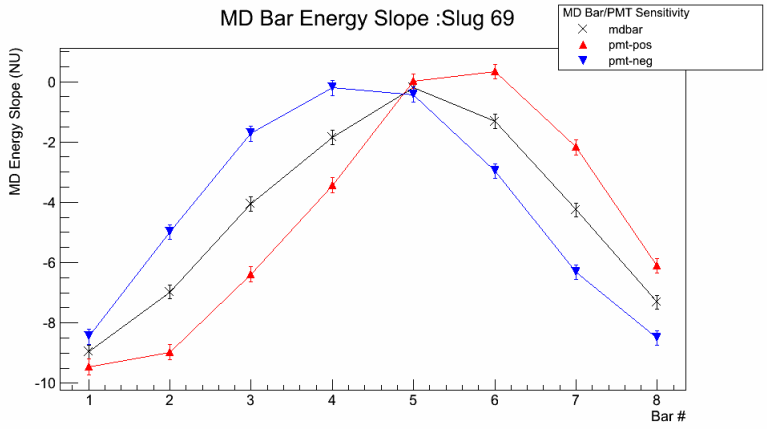

Figure 6.17: Octant variation of the energy sensitivities, $\frac{\partial A_{bar}^{yield}}{\partial E}$, $\frac{\partial A_p}{\partial E}$, and $\frac{\partial A_n}{\partial E}$.

Similarly, there is no reason to expect an azimuthal variation of charge asymmetry sensitivity. But the charge asymmetry sensitivity (from the regression

scheme we call, "5+1") also has an octant dependence (see Figure 6.18) very similar to a dipole and it can be related to the correlation of the charge asymmetry and the HC position differences. This dipole behavior is not typical during Wien0 but seen during Run 1. The correlation of charge asymmetry to the HC position differences is observed (see Figure 6.19) in an analysis I have done using large charge asymmetry induced by adjusting the Pockels cell high voltage (A PITA scan [97, 98]). Further analysis will be followed to investigate the effects of the correlation in linear regression for the final data set.

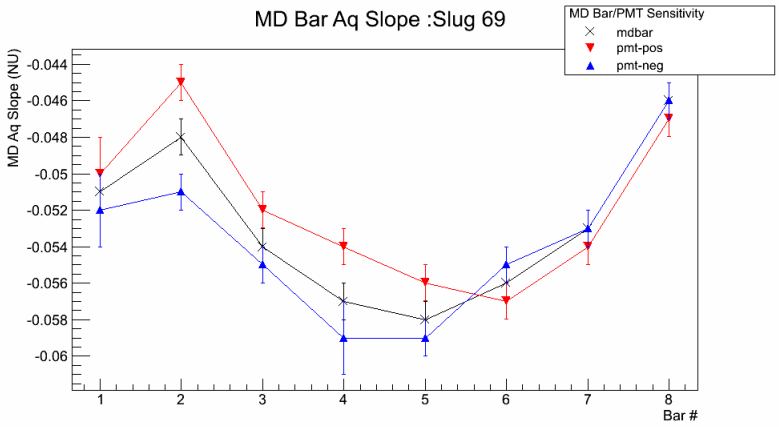

Figure 6.18: Octant variation of the charge sensitivities, $\frac{\partial A_{bar}^{yield}}{\partial A_q}$, $\frac{\partial A_p}{\partial A_q}$, and $\frac{\partial A_n}{\partial A_q}$.

In summary, charge asymmetry and energy differences are coupled to each other and they are both coupled strongly to the HC position differences. This correlation between beam parameters (aka strength sharing) is not an issue for false asymmetry correction as long as the regression beam parameters include all the sources of HCBAs into account. But it is important to have further investigation into these correlations to identify any HCBAs from hidden parameters and include it into the linear regression to regressed against.

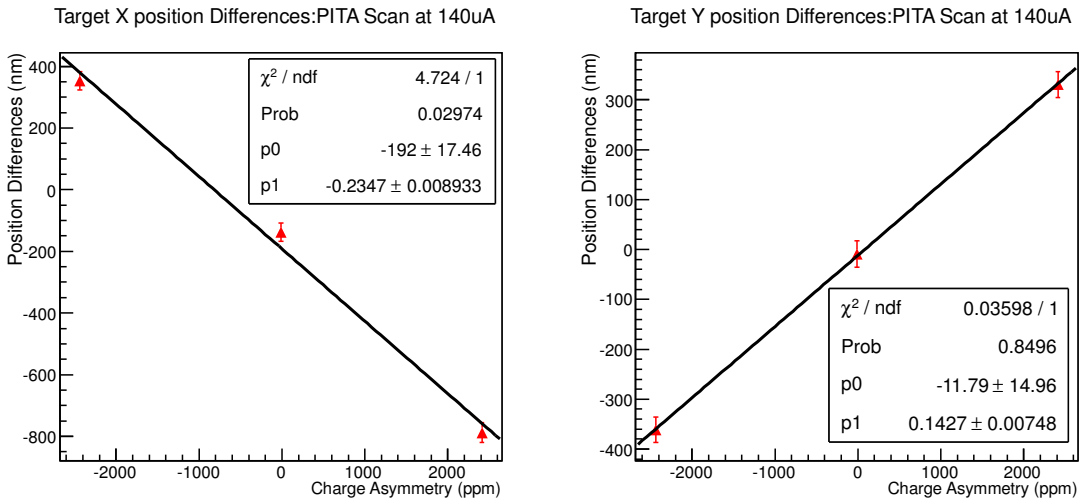

Figure 6.19: The HC position differences and charge asymmetry correlation during the PITA scan (from [98]).

6.4.2 Linear Regression Schemes

The Standard linear regression scheme discussed so far is one of many different schemes available. We have many different schemes with different set of independent variables or IVs (see Table 6.7). These schemes differ in,

- Charge vs. no-charge (5+1, set3, set4, set6, set8, set10 vs. std, set5, set7)
- Target-BPM vs. individual-BPM pair (std, 5+1, set3, set4, set9 vs. set5, set6, set7, set8, set10)
- energy-monitor vs. BPM-3C12 (std, 5+1, set9 vs. set3, set4, set5, set6, set7, set8, set10)

The quartets (QRTs) used by each scheme must be identical so that results from different schemes can be compared for systematic studies. Therefore, a common set of event cuts are applied to all regression schemes. Ideally, the regression results from all the schemes must agree but during Wien0 they have not agreed with each other.

Table 6.7: Regression schemes and their beam parameters or independent variables (IV).

Regression Scheme	Position and Angle IVs	Energy IV	Charge IV	Other IV
std	qwk_target	qwk_energy	—	—
5+1	qwk_target	qwk_energy	qwk_charge	—
set3	qwk_target	bpm_3c12X	qwk_charge	—
set4	qwk_target	bpm_3c12X	qwk_bcm5	—
set5	BPMs 9b+4	bpm_3c12X	—	—
set6	BPMs 9b+4	bpm_3c12X	qwk_charge	—
set7	BPMs 9+4	bpm_3c12X	—	—
set8	BPMs 9+4	bpm_3c12X	qwk_charge	—
set9	qwk_target	qwk_energy	qwk_charge	qwk_uslumi
set10	BPMs 9b+4y	bpm_3c12X	qwk_bcm6	—

Therefore, the goal of many different regression schemes is to understand the causes of scheme dependence and fix any regression issues that generate these differences. For Wien0, we have not able to resolve scheme dependence issue and therefore a systematic error is assigned to final results.

The scheme dependent error is set by comparing the regressed Čerenkov detector asymmetry from different regression schemes (see Figure 6.20). The regression scheme dependent error is defined as the largest difference between the Standard regression scheme to any other scheme [99] and the current estimate is ± 0.007 ppm.

Based on the scheme dependent regression results, the largest discrepancy exists between charge vs. no charge regression. For Wien0, charge regression is not applied

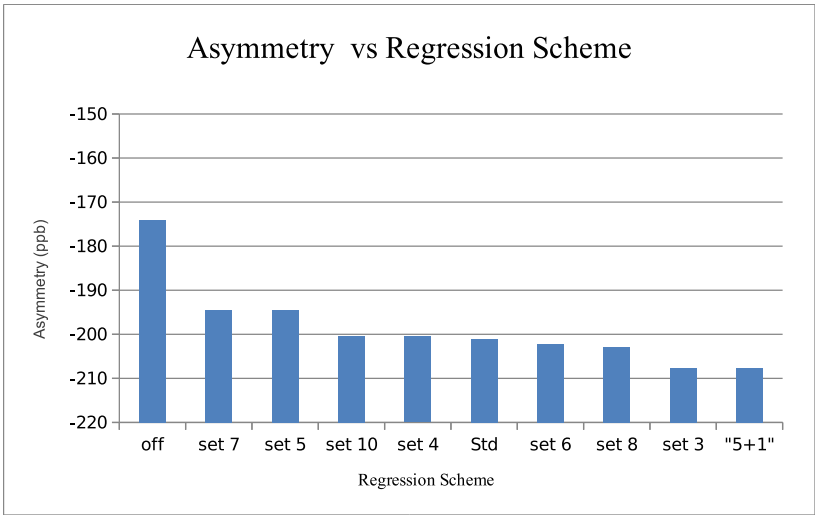

Figure 6.20: The raw asymmetry (off) and final regressed main detector asymmetries from different regression schemes (from [99]).

due to non-linearity related issues discussed in Section 6.5.3. Therefore, the Standard linear regression scheme is used for the Wien0 final results.

6.5 Standard Linear Regression Results

The Standard linear regression scheme was chosen to remove the false asymmetries generated by HC beam differences in the Wien0 data analysis. The unregressed asymmetry (A^{raw}) and Standard regressed asymmetry (A_{msr}) are given in Tables 6.8 and 6.9, and plotted in Figure 6.21.

The measured asymmetry reverses the sign when the IHWP is flipped as expected from anticipated physics asymmetry. The integrity or goodness of the average Wien0 asymmetry for each IHWP could be evaluated using the reduced χ^2 (χ^2/ndf) value. The reduced χ^2 is consistent with 1 for IHWP-OUT state before and after the linear regression. In IHWP-IN state, the reduced χ^2 is not consistent with 1 but improves slightly after the linear regression. This is mainly related to slug-39 asymmetry being an outlier by about 2σ. Since there is no basis for excluding slug-39, its outlier result

could be a statistical fluctuation or some unknown effect unaccounted in the analysis. Overall, the reduced χ^2 has improved slightly after regression.

The results from the two IHWPs are combined by computing the weighted average of OUT and the opposite of the IN results, Avg(IN,-OUT). This computation allows taking into account the trivial change of physics asymmetry sign due to the insertion and removal of the IHWP. The Wien0 measured asymmetry using Standard regression is,

$$\mathrm{A_{msr}} \;=\; -0.205 \pm 0.031(\mathrm{stat}) \pm 0.012(\mathrm{syst.})\ \mathrm{ppm} \tag{6.24}$$

where the total systematic error will be summarized in Section 6.5.3.

The $(\mathrm{OUT}+\mathrm{IN})/2$ or the residual false asymmetry before applying the linear regression is 2.5 σ away from zero. After the standard linear regression is applied, the $(\mathrm{OUT}+\mathrm{IN})/2$ is 2.2 σ away from zero which shows only a small improvement from the linear regression. Ideally, the residual false asymmetry should to be zero after applying the linear regression. Large $(\mathrm{OUT}+\mathrm{IN})/2$ for Wien0 points to effects of worst HC beam differences during Wien0 and underlying issues related to the linear regression as seen in the cut dependence study (see Section 6.5.2) that require more understanding.

Table 6.8: The raw main detector asymmetry ($\mathrm{A^{raw}}$) at slug-scale for Wien0.

Slug OUT	Asymmetry (ppm)	Slug IN	Asymmetry (ppm)	$(\mathrm{OUT}+\mathrm{IN})/2$ (ppm)	$\mathrm{AVG}(\mathrm{OUT},-\mathrm{IN})$ (ppm)
32	-0.029 ± 0.117				
34	-0.174 ± 0.084	33	0.110 ± 0.078	-0.032 ± 0.057	-0.139 ± 0.057
36	-0.045 ± 0.089	35	0.215 ± 0.088	0.085 ± 0.062	-0.131 ± 0.062
38	-0.082 ± 0.096	37	0.259 ± 0.087	0.089 ± 0.065	-0.179 ± 0.064
40	-0.072 ± 0.118	39	0.476 ± 0.094	0.202 ± 0.075	-0.319 ± 0.073
AVG	-0.089 ± 0.044	AVG	0.248 ± 0.043	0.079 ± 0.031	-0.170 ± 0.031

Table 6.9: The Standard regressed main detector asymmetry (A_{msr}) at slug-scale for Wien0.

Slug OUT	Asymmetry (ppm)	Slug IN	Asymmetry (ppm)	(OUT + IN)/2 (ppm)	AVG(OUT, −IN) (ppm)
32	-0.070 ± 0.117				
34	-0.202 ± 0.084	33	0.139 ± 0.077	-0.032 ± 0.057	-0.168 ± 0.057
36	-0.097 ± 0.089	35	0.249 ± 0.088	0.076 ± 0.062	-0.174 ± 0.062
38	-0.139 ± 0.096	37	0.283 ± 0.087	0.072 ± 0.065	-0.219 ± 0.064
40	-0.130 ± 0.118	39	0.479 ± 0.093	0.174 ± 0.075	-0.344 ± 0.073
AVG	-0.135 ± 0.044	AVG	0.272 ± 0.043	0.068 ± 0.031	-0.205 ± 0.031

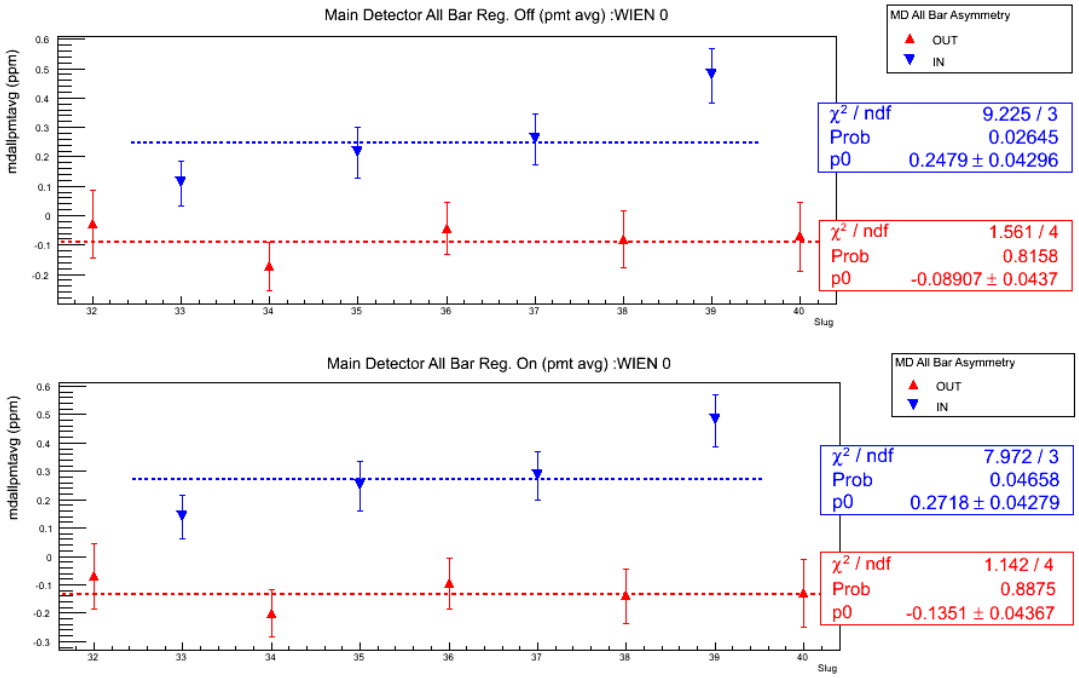

Figure 6.21: Top: Raw main detector asymmetry before regression. Bottom: The Standard regressed main detector asymmetry.

6.5.1 Regression Corrections Summary

The linear regression correction (false asymmetry) to the measured raw asymmetry is defined as (from equation 6.22),

$$\Delta A_{x_i} = \frac{\partial A^{raw}}{\partial x_i} \cdot \Delta x_i \tag{6.25}$$

where the average HCBAs (Δx_i) obtained during Wien0 are summarized in Table 6.10. The Standard regression average sensitivities ($\frac{\partial A^{raw}}{\partial x_i}$) during Wien0 are shown in the Table 6.11. The Standard regression correction averages (ΔA_{x_i}) are shown in the Table 6.12. The largest individual correction originates from the HC asymmetry in the relative beam energy.

Table 6.10: Average HCBAs in Wien0. Errors for a runlet are based on monitor resolutions, $\delta X = \frac{\sigma_X}{\sqrt{N_{QRT}}}$, then averaged to whole Wien0. Results are weighted by $\frac{1}{\sigma_A^2}$ where σ_A is the main detector asymmetry RMS for the runlet.

Qty	IHWP-OUT	IHWP-IN	AVG(OUT,-IN)
Dx (nm)	14.43 ± 0.25	-13.60 ± 0.25	14.02 ± 0.18
Dy (nm)	-50.41 ± 0.25	108.44 ± 0.25	-79.03 ± 0.18
Dxp (nrad)	-0.13 ± 0.05	0.43 ± 0.05	-0.28 ± 0.04
Dyp (nrad)	-1.16 ± 0.05	2.51 ± 0.05	-1.84 ± 0.04
A_E (ppm)	-0.02 ± 0.0001	0.02 ± 0.0001	-0.02 ± 0.00004
A_Q (ppm)	-0.039 ± 0.007	-0.036 ± 0.007	-0.002 ± 0.005

6.5.2 Cut Dependence Study

The goal of a cut dependence study is to see whether the linear regressed asymmetry is stable within statistical expectations. If linear regression is working properly, large false asymmetries in runlets with large HCBAs should be removed

Table 6.11: Standard regression average sensitivities during Wien0.

Sensitivity	Average value
$\frac{\partial A^{raw}}{\partial x}$ (ppm/mm)	-1000 ± 10
$\frac{\partial A^{raw}}{\partial y}$ (ppm/mm)	300 ± 10
$\frac{\partial A^{raw}}{\partial xp}$ (ppm/μrad)	38.0 ± 0.3
$\frac{\partial A^{raw}}{\partial yp}$ (ppm/μrad)	-3.0 ± 0.3
$\frac{\partial A^{raw}}{\partial A_E}$ (ppm/ppm)	-6.0 ± 0.2

Table 6.12: Average False Asymmetries or Regression Corrections for Wien0.

IV	IHWP-OUT Correction (ppm)	IHWP-IN Correction (ppm)
Dx	-0.012 ± 0.0003	0.013 ± 0.0003
Dy	-0.019 ± 0.0003	0.037 ± 0.001
Dxp	-0.005 ± 0.002	0.018 ± 0.002
Dyp	0.004 ± 0.0003	-0.006 ± 0.001
A_E	0.096 ± 0.0005	-0.107 ± 0.0005

from the measured asymmetry after linear regression is applied. In this study, an inclusive cut is applied to all HCBAs (beam position/angle and energy) to remove only a small subset of runlets with large false asymmetries and the shift observed in the measured asymmetry is compared with the expected statistical shift when a small subset of data is removed (see Appendix D.1).

During the study, inclusive cuts 7,6,5, and 4 σ are applied to all HCBAs where the σ is the Root Mean Square (RMS) of each HCBA. The observed shift in the measured asymmetry from these cuts are larger than the expected statistical shift (see Figure 6.22 and Table 6.13).

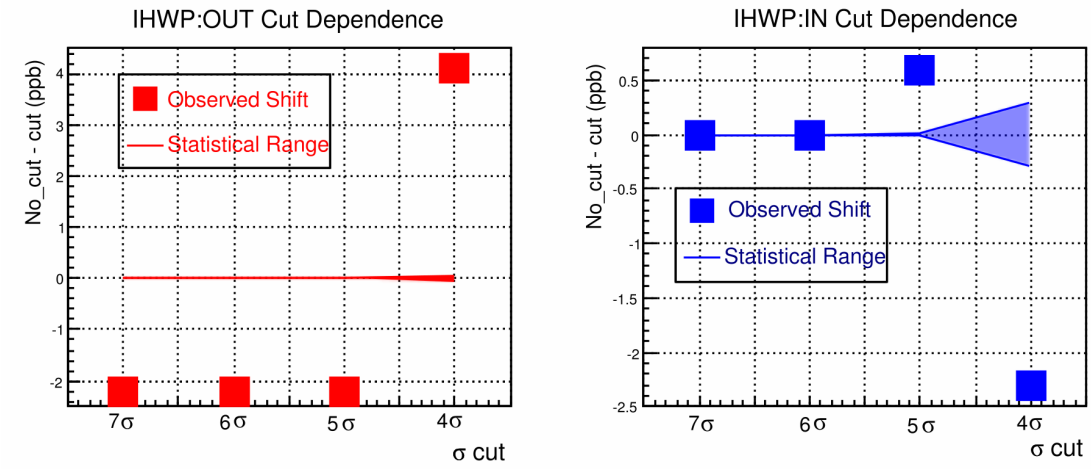

Figure 6.22: LH2 cut dependence study. At each level of inclusive cut, runlets with central values that failed the cut are removed and shift in the central value of the Čerenkov detector regressed asymmetry is plotted. The band in each plot is the expected range of statistical shift when small percentage of data is removed. A cut dependence systematic error is assigned based on the shift observed at the 5σ cut.

Table 6.13: Comparison of the observed and expected range of statistical shift of main detector asymmetry when a cut is applied to remove runlets with large HC differences. (The analysis is done using runlet distribution of data.)

	IHWP	OUT		IHWP	IN	
Cut	Data Lost (%)	Stat. Range (ppb)	no_cut - cut (ppb)	Data Lost (%)	Stat. Range (ppb)	no_cut - cut (ppb)
7 σ	0.021	$\pm$0.005	-2.200	0.000	$\pm$0.000	0.000
6 σ	0.021	$\pm$0.005	-2.200	0.000	$\pm$0.000	0.000
5 σ	0.021	$\pm$0.005	-2.200	0.033	$\pm$0.008	0.600
4 σ	0.276	$\pm$0.067	4.100	1.162	$\pm$0.294	-2.300

If the linear regression had worked properly, the observed shift on the main detector asymmetry would have been consistent with the expected statistical shift when a small subset of data is removed. The non-statistical shifts observed in cut dependence study point to a systematic effect in linear regression when correcting large false asymmetries (or outliers). The next steps in the cut dependence study are to investigate causes of non-statistical shifts, and to improve the linear regression. (See references [100, 101] for on-going analysis) For the Wien0 results, a systematic error based on the observed shift at 5 σ cut is assigned and it is ± 0.0014 ppm (See Figure 6.23). The error is assigned based on 5 σ cut because cuts smaller than 5 σ start to remove non-outliers. No data were cut based on this analysis but only a systematic error was assigned.

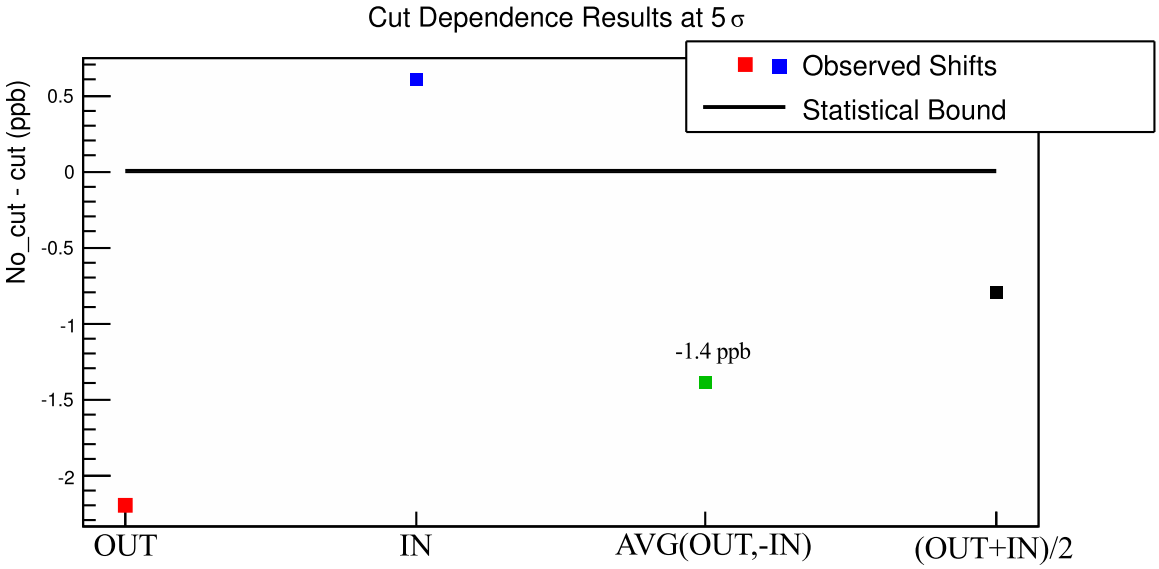

Figure 6.23: Observed shift in measured asymmetry at 5σ cut on Standard regression beam parameters. A systematic error is assigned based on the average shift from AVG(OUT,-IN) (green data point). The cut dependent shift on residual asymmetry ((OUT+IN)/2) is also shown (black data point). The width of the band at zero is the 1 σ limit of statistically allowed shift.

An analysis based on a previous data replay was used to estimate the official Wien0 systematic error for cut dependence [58, pg. 148] and it was ± 0.0042 ppm. The improvement in the systematic error can be attributed to proper Čerenkov detector weightings (see Section 6.1.1) and improved data quality cuts in the newer data replay.

6.5.3 Regressed Asymmetry Systematic Error Summary

Systematic errors are assigned to certain issues related to linear regression that generate uncertainties in the final measured asymmetry. The regression issues include: differences in the final measured asymmetry between different linear regression schemes (discussed in Section 6.4.1), the cut dependence uncertainty in the measured asymmetry (discussed in Section 6.5.2), non-linear correction to HC horizontal position differences, and distortion of the physics asymmetry due to non-linearity. In this section, remaining linear regression issues and associated systematic errors are summarized.

The quartet (QRT) level correlation between the regressed Čerenkov detector asymmetry and the HC horizontal beam position differences have revealed a non-linearity in the correlation. There exists two different horizontal position sensitivities at the core and the tail of the HC position differences distribution (see Figure 6.24). The present hypothesis assumes the cause to be double peaking in HC horizontal beam position differences originated from harmonic instrumental noise. The overlap of two distributions with slightly different mean values is known as the double peaking and it generates the non-linear correlation observed in data [102] and this proposed model estimates an error of ± 0.008 ppm [103].

The false asymmetry from the charge asymmetry is not regressed out in the Standard linear regression. This is related to the observed discrepancy in the difference between the Standard and "5+1" regression corrections ($|A_{\rm std} - A_{5+1}|$)

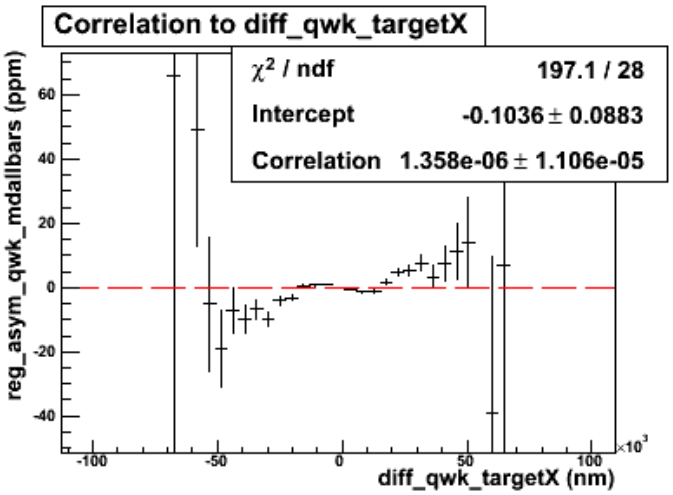

Figure 6.24: The QRT level correlation between the regression corrected main Čerenkov detector asymmetry and the HC horizontal beam position differences, where the core and the wing areas have two different correlations (from [102]).

and the distortion to the physics asymmetry from the detector non-linearity [66] (see Table 6.14). Looking forward to the full Q_{weak} analysis, there is also evidence for effects that are not understood in the charge regression as observed in an ongoing analysis work where the Standard and the "5+1" regression schemes are tested using large charge asymmetry induced data [104]. These discrepancies must be resolved before starting to use the "5+1" regression scheme where the charge asymmetry is also regressed out. For the less precise Wien0 results this effect is small compared to the statistical error of the final asymmetry. Since the charge asymmetry is not regressed to remove non-linearity from the measured asymmetry (see Figure 6.10 in Section 6.3.1), a systematic error is assigned based on the physics asymmetry distortion due to non-linearity [105, 106]. The systematic error is $dA_{msr\_nonlin} = \pm|f \cdot A_{msr}| = \pm 0.004$ ppm. (see Table 6.14.)

Table 6.14: "5+1" regression and non-linearity corrections discrepancy, ($|f \cdot A_{msr}| \neq |A_{std} - A_{5+1}|$.

Scheme	Asymmetry
off	-0.170 ± 0.003 ppm
std	-0.205 ± 0.003 ppm
5+1	-0.212 ± 0.003 ppm
$\lvert A_{std} - A_{5+1} \rvert$	0.007 ppm
non-lin,f	$\sim 2\%$ [105]
$\lvert f \cdot A_{msr} \rvert$	~ 0.004 ppm

6.6 Transverse Polarization Leakage

Transversely polarized electrons generate a parity conserving transverse beam spin asymmetry [107] and it is given by,

$$A^T = B_n |P_T| \cdot \sin(\phi_{det} - \phi_s) \tag{6.26}$$

where B_n is the vector analyzing power, P_T is the transverse beam polarization, and ϕ_{det} and ϕ_s are as shown in Figure 6.25.

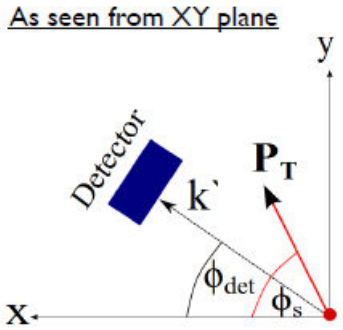

Figure 6.25: The Čerenkov detector and transverse polarization direction guide. ϕ_{det} is the location of the detector in the azimuthal plane. ϕ_s is the location of the polarization vector in the azimuthal plane (from [74]).

During Wien0, the estimated residual transverse polarization in the electron beam is, $-3.8 \pm 0.9\%$ from horizontal and $4.2 \pm 0.9\%$ from vertical transverse polarizations [108]. Due to the symmetry of the Čerenkov detector system, the transverse contribution is suppressed by a factor of ~ 100. Using the dedicated Q_{weak} transverse measurements, the transverse leakage into the measured parity violating asymmetry is estimated to be $\sim 0.5 \pm 4$ ppb [108]. The effects from non-zero transverse beam polarization [74] is treated as a systematic error in the Wien0 data. The uncertainty due to transverse leakage in wien0 is $dA_{msr\_trans} = \pm 0.004$ ppm [108].

So far I have discussed all the systematic errors related to regressed asymmetry (A_{msr}) and they are summarized in the Table 6.15.

Table 6.15: The systematic errors on A_{msr}.

Source	Error	Estimate (ppm)
Regression	Scheme dependence	± 0.007
	Double peaking	± 0.008
	Cut dependence	± 0.001
Regression	Total	± 0.011
Non-linearity		± 0.004
Transverse leakage		± 0.004
Total Systematic		± 0.012

6.7 From the Regressed to Physics Asymmetry

The measured asymmetry (A_{msr}) originates mainly from the elastic electron proton scattering but also has several other different processes known as backgrounds. It is expressed as,

$$\frac{A_{msr}}{P_e} = (1 - f_{Total}) \cdot A_{\tilde{e}p} \; + \; \sum_{i=1}^{4} f_{bi} \cdot A_{bi} \tag{6.27}$$

where $A_{\tilde{e}p}$ is the electron proton scattering asymmetry with experimental biases uncorrected, A_{msr} is the measured asymmetry, P_e is the electron beam polarization, f_{bi} is the background dilution, A_{bi} is the background asymmetry, and $f_{Total} = \sum_{i=1}^{4} f_{bi}$ is the total dilution. The electron proton scattering asymmetry after correction for experimental bias is known as the tree-level asymmetry,

$$A_{Tree}(< Q^2 >_{Tree}) = R_{other} \times \frac{\{\frac{A_{msr}}{P_e} \; - f_{b1} \cdot A_{b1} \; - f_{b2} \cdot A_{b2} \; - f_{b3} \cdot A_{b3} \; - f_{b4} \cdot A_{b4} \; \}}{(1 \; - \; f_{Total})} \tag{6.28}$$

where R_{other} is the remaining set of corrections related to radiative and other experimental bias corrections (detector and momentum transfer), and $< Q^2 >_{Tree}$ is the average elastic electron proton scattering momentum transfer after correcting for experimental bias corrections. Using equation 6.28, the error derivatives are computed as,

$$
\begin{aligned}
dA_{Tree}|_{A_{msr}} &= R_{other} \times \frac{1}{P_e} \cdot \frac{1}{(1 - f_{Total})} \cdot dA_{msr} \\
dA_{Tree}|_{P_e} &= R_{other} \times \ -1 \cdot \frac{1}{(1 - f_{Total})} \cdot A_{msr} \cdot \frac{dP_e}{P_e^2} \\
dA_{Tree}|_{A_{b_i}} &= R_{other} \times \ -1 \cdot \frac{f_{b_i}}{(1 - f_{Total})} \cdot dA_{b_i} \\
dA_{Tree}|_{R_{Det}} &= dR_{other} \times \ \frac{\{\frac{A_{msr}}{P} \ - f_{b1} \cdot A_{b1} \ - f_{b2} \cdot A_{b2} \ - f_{b3} \cdot A_{b3} \ - f_{b4} \cdot A_{b4} \ \}}{(1 \ - \ f_{Total})} \\
dA_{Tree}|_{f_{b_1}} &= R_{other} \times \{\frac{A_{msr}}{P_e} \ + \ (-1 \ + \ f_{b_2} \ + \ f_{b_3} \ + \ f_{b_4}) A_{b_1} \\
&\quad - \ A_{b_2} f_{b_2} \ - \ A_{b_3} f_{b_3} \ - \ A_{b_4} f_{b_4}\} \cdot \frac{df_{b_1}}{(1 - f_{Total})^2}
\end{aligned}
\tag{6.29}
$$

For $dA_{Tree}|_{f_{b_1}}$, permutation of $1 \rightarrow 2$, $2 \rightarrow 3$, $3 \rightarrow 4$ and, $4 \rightarrow 1$ will give all the background dilution errors. Using error derivatives in equation 6.29, the final error on the $A_{Tree}(< Q^2 >)$ is,

$$
dA_{Tree} \ = \ \sqrt{dA_{Tree}|^2_{A_{msr}} + dA_{Tree}|^2_{A_{P_e}} + dA_{Tree}|^2_{A_{b_i}} + dA_{Tree}|^2_{R_{Det}} + dA_{Tree}|^2_{f_{b_i}}} \tag{6.30}
$$

I have written a program (Appendix B.1) to compute the $A_{Tree}(< Q^2 >_{Tree})$ and related errors using the results from many different analysis work done by other collaborators and myself. The remaining sections will discuss the blinded analysis, polarization correction, background corrections, and experimental bias corrections. I will provide additional details on my neutral background analysis in the background section. At the end of this section, the final tree-level electron proton scattering asymmetry and Q_{weak} kinematics results are documented.

6.7.1 Blinded Analysis Overview

The Q_{weak} asymmetry analysis is performed using blinded results where the measured asymmetry has an offset added to it to prevent any analysis bias towards a particular central value. Only the asymmetries computed from the Čerenkov

detectors for the Liquid Hydrogen (LH2) target are blinded. For all other asymmetry measurements, using different targets and/or different QTOR currents, are not blinded. The blinding mechanism is incorporated into the Q_{weak} analysis framework where the blinding offset is applied for the asymmetry computed from each QRT. The blinder value is randomly generated from the range ± 0.06ppm and it is always added to the raw asymmetry after the sign is corrected according to the expected physics asymmetry at the IHWP. For the entire Q_{weak} data set, there were three different blinders applied. Separate blinder values exist for: Wien0, remaining Run 1 data (Wien1-5), and Run 2 data. The un-blinding, or the removing of the hidden offset is done when all the corrections to the measured asymmetry are finalized. Wien0 data was unblinded after the main analysis was completed. For Wien0, the asymmetry was blinded using the following method.

$$\begin{aligned} A^{raw}(OUT) &= A^{raw\_unblinded}(OUT) \ + B_{offset} \\ A^{raw}(IN) &= A^{raw\_unblinded}(IN) \ - B_{offset} \end{aligned} \tag{6.31}$$

After computing the physics asymmetry ($A^{blinded}_{msr} = AVG(A^{blinded}_{msr}(OUT), -A^{blinded}_{msr}(IN))$) for the Wien0 data set, the asymmetry was unblinded using [109],

$$A_{msr} = A^{blinded}_{msr} - B_{offset} \tag{6.32}$$

where the $A^{blinded}_{msr}$ is the blinded regressed asymmetry and A_{msr} is the unblinded regressed asymmetry used in equation 6.28.

6.8 Polarization Correction

The measured asymmetry (A_{msr}) needs to be corrected for the $< 100\%$ electron beam polarization because the parity violating asymmetry is only originating from polarized electron scattering. The measured asymmetry in terms of the total

scattering cross section can be expressed as,

$$A_{msr} = \frac{\sigma^R - \sigma^L}{\sigma^R + \sigma^L} \tag{6.33}$$

where $\sigma^{R/L} = \sigma_{PC} + P_e \cdot \sigma_{PV}^{R/L}$, σ_{PC} is the parity conserving cross section and $\sigma_{PV}^{R/L}$ is the parity violating cross section. The polarization correction is defined as,

$$A_{msr} = P_e \cdot A_{PV} \tag{6.34}$$

where the parity violating asymmetry, $A_{PV} = \frac{\sigma_{PV}^R - \sigma_{PV}^L}{\sigma^R + \sigma^L}$ is the physics asymmetry of interest to us. The electron beam polarization for the Wien0 data set was measured to be

$$P_e \ = \ 88.95 \pm 1.83\%$$

using the Hall C Møller polarimeter, and was discussed in detail in Chapter 5. The correction to the measured asymmetry from the beam polarization is the third largest correction after the aluminum background correction and Standard linear regression correction. It is estimated to be about 0.026 ppm.

6.9 Background Corrections

The measured main Čerenkov detector yield consists of mainly of elastically scattered electrons from the LH2 target but some fraction of inelastic electrons also exist in the yield. In addition, electrons scattered from the Al windows of the LH2 target, a small fraction of neutral particles (photons, neutrons, and pions) from the beam-line and shield wall interactions also exist in the measured Čerenkov detector yield. These additional contributions are known as backgrounds and they contribute to the measured asymmetry. Therefore, the measured asymmetry needs to be corrected for these background contributions. It can be shown that, when the measured yield consists of individual yields from different processes,

the measured asymmetry consists of main elastic electron proton asymmetry and individual asymmetries from background processes.

$$\begin{aligned} Y_{total} &= Y_{\tilde{e}p} + \sum_{i=1}^{N} y_{bi} \\ \frac{A_{msr}}{P_e} &= (1 - f_{Total})A_{\tilde{e}p} + \sum_{i=1}^{N} \frac{y_{bi}}{Y_{total}} \cdot A(y_{bi}) \end{aligned} \tag{6.35}$$

where y_{bi} are individual yields from background process bi, $A(y_{bi})$ are corresponding background asymmetries, and the measured $\tilde{e}p$ asymmetry is $A_{\tilde{e}p}$. $f_{bi} = \frac{y_{bi}}{Y_{total}}$ is defined as the dilution of the background, bi. The various background contributions are summarized in Table 6.16. In the following sub-sections, I will provide more details on these background processes.

Table 6.16: The List of Q_{weak} Backgrounds.

Background	Dilution, f_{bi}	Asymmetry, A_{bi} (ppm)
Al window background, b1	0.0323 ± 0.0021	1.7581 ± 0.2582
QTOR transport channel, b2	0.0019 ± 0.0019	0.0000 ± 0.2000
Beam-line background, b3	0.0019 ± 0.0006	-5.5000 ± 11.5000
$N \rightarrow \Delta$ inelastic, b4	0.0002 ± 0.0002	-3.0200 ± 0.9700

6.9.1 Aluminum Background

The largest background contribution to the measured asymmetry comes from the LH2 target aluminum windows. The Al background dilution is about 3% but due to the large aluminum asymmetry, this becomes the largest correction (about 0.060 ppm) to the measured asymmetry. Therefore, dedicated aluminum data were taken for about 8 hours, twice a week using a 4% radiation length aluminum-alloy target (4% DS Al) located at the same z location as the down-stream (DS) target window. The goal of the aluminum data analysis is to extract the background

asymmetry and dilution from Al target windows [58]. The Al data are slug averaged to get Wien0 Al asymmetry from the 4% DS target (see Figure 6.26). The Standard regression is applied to remove false asymmetries [110] and the regressed asymmetries are corrected for the electron beam polarization and background contributions to get the electron aluminum scattering asymmetry [111]. The electron beam polarization for the Al results is averaged over the Møller polarization measurements taken during periods closest to the Al data periods. The background contributions to the Al measurement comes from the beam-line and Q_{weak} TORoidal (QTOR) transport channel backgrounds. Finally radiative corrections are applied to the electron aluminum scattering asymmetry to get the final result for the aluminum background (b1) asymmetry [112] (see the reference [58] for the current status of radiative correction model calculation). The final aluminum asymmetry measurement from Wien0 data is

$$A_{b1} = 1.7581 \pm 0.1818(\text{stat.}) \pm 0.1795(\text{syst.}) \pm 0.0376(\text{model}) \text{ ppm} \qquad (6.36)$$

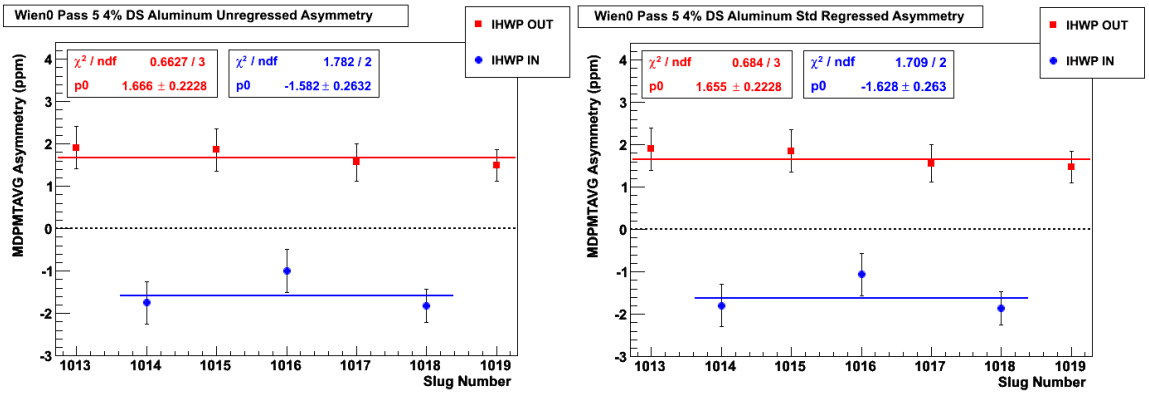

Figure 6.26: The comparison of un-regressed and standard regressed 4% DS aluminum asymmetry using PMT averages (from [110]).

The aluminum background dilution is calculated by measuring the electron scattering rate from the evacuated LH2 target where electrons are scattered directly from the aluminum windows. The dilution is then computed by taking the ratio of the scattered electrons rate from the evacuated and normal Q_{weak} targets [58, pg. 111]. The radiative corrections applied final aluminum dilution result is [113],

$$f_{b1} = 0.03226 \pm 0.0001(\text{stat.}) \pm 0.0004(\text{syst.}) \pm 0.0021(\text{model}) \tag{6.37}$$

where f_{b1} is the aluminum background (b1) dilution required for calculation of the asymmetry equation 6.28.

6.9.2 Inelastic Background

The inelastic background (b4) originates from the nucleon transition to the $\Delta(1232)$ resonance state that generates a parity violating asymmetry [68]. The $N \rightarrow \Delta$ asymmetry was measured using the LH2 target and setting the QTOR magnet current to 6700 A, where the inelastic $N \rightarrow \Delta$ rate is maximum (left plot in the Figure 6.27). The scattering rate and the $N \rightarrow \Delta$ inelastic dilution were estimated using simulation analysis [114]. The background asymmetry from inelastic was estimated for Wien0 data using dedicated inelastic measurements that were taken after Wien0 time period. The regression applied measured asymmetry is shown in Figure 6.27. This asymmetry is corrected for background contribution from beam-line, aluminum and elastic electrons to get the inelastic background asymmetry (b4) given by,

$$A_{b4} = -3.020 \pm 0.970 \text{ ppm} \tag{6.38}$$

and the dilution [114],

$$f_{b4} = 0.0002 \pm 0.0002 \text{ ppm} \tag{6.39}$$

where the dilution error is set to 100% pending further analysis [93].

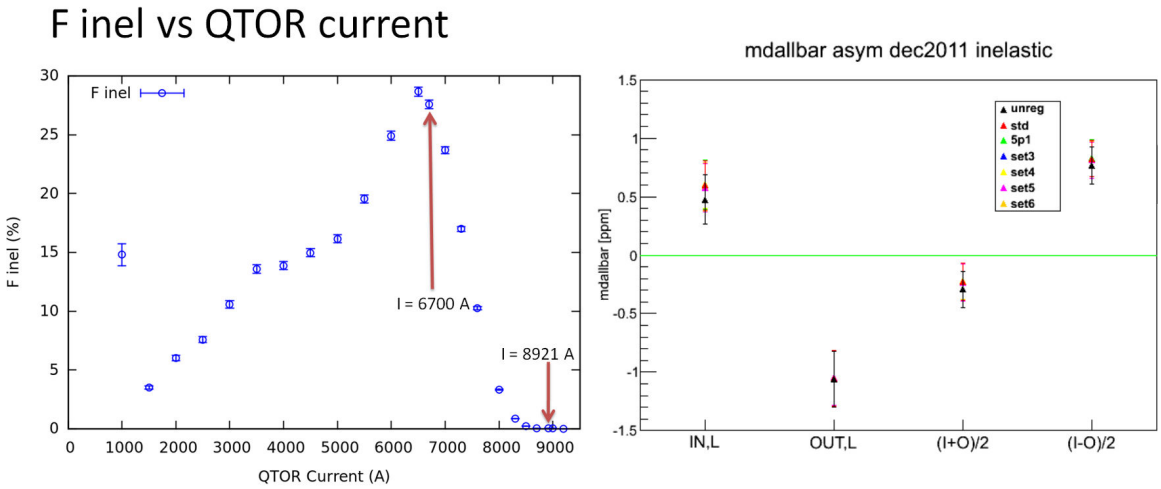

Figure 6.27: $N \rightarrow \Delta$ results, left: Dilution estimates from simulations and right: Measured inelastic asymmetry from LH2 target for each IHWP state, residual false asymmetry or $(IN + OUT)/2$, and physics asymmetry are shown [68, pg. 128]. The asymmetry results are compared for all the available regression schemes where each colored data point represent a regression scheme.

6.10 Total Neutral Background Fraction

The goal of this analysis was to determine the total neutral fraction (total neutral background dilution) in the measured main detector yield and to estimate the QTOR transport channel background dilution [115, 116]. I have developed the run plans to collect all the necessary data and then performed their analysis to extract the neutral background dilution. The neutral backgrounds originating from the tungsten plug and beam-line (from Q_{weak} target to the beam dump) are called *beam-line backgrounds* while the secondary photons generated by primary elastic electrons scraping in the collimator and shield wall edges are known as the *QTOR transport channel neutral background*. Photons are the main contributor of the neutral background but it is expected that a small percentage of pions and neutrons contribute to the neutral fraction as well. As the Q_{weak} analysis progress beyond the Wien0 results, there are future analysis plans to include a neutron transport model into the Q_{weak} simulation in

order to understand the neutron contribution. An estimation of the pion contribution at the detector plane is expected from the data collected from the pion detector setup installed during the Q_{weak} experiment to determine the pion neutral contribution.

The total neutral fraction is estimated from counting mode data taken at beam currents ranging from 10 to 100 nA, so that individual particles can be detected in the Region 3 (R3) detectors. The R3 has a pair of scintillators known as Trigger Scintillator (TS) and the main Čerenkov detectors (MD). The pair of TS detectors cover two Čerenkov detectors in opposite octants. Only particles that register signals in the main Čerenkov detectors (the trigger is MD) are used to estimate the neutral yield fraction (see Figure 6.28). The scintillation and Čerenkov detectors are highly insensitive to neutral particles but neutrals can generate light in the main Čerenkov detectors in the following types of interactions while producing no scintillation in the TS,

- A neutron decay or capture on the radiator or light guide.
- Photons incident on the detector entering the PMT.
- Compton scattering in the bar or light guide or air.

A neutral particle is identified when it produces no scintillation in the TS while producing a signal in the Čerenkov detector. Using this definition, each detected particle can be categorized into either charge or neutral particle based on the amount of energy deposited (light) on TS and Čerenkov detectors. These light signals are read-out using Time to Digital Converter (TDC) and Analog to Digital Converter (ADC) to determine the scattering rates and the light deposited by each particle, respectively. They are used to determine the integrated yield from all the particles detected as,

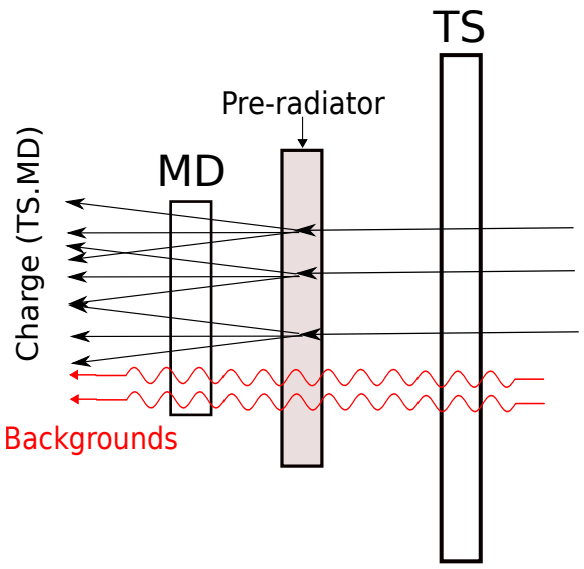

Figure 6.28: Neutral particles only generate light in the main Čerenkov detector (MD). Charge particles generate light in TS and MD.

$$\text{Yield} \propto \text{PE/track} \times \text{Rate}_{\text{TDC}} \tag{6.40}$$

where PE/track is number of Photo-Electron (PE) generated by a particle (obtained from the ADC data) and Rate_{TDC} is the scattered particle rate determined from TDC data. Both the TS and Čerenkov detectors have two PMTs connected in either ends to collect the generated light. The TDC signals from the two PMTs are averaged to get the meantime (MT) using the following equation,

$$\text{T}_{\text{MT}} = (\text{T}_{\text{PMT\_L}} + \text{T}_{\text{PMT\_R}})/2 \tag{6.41}$$

where T_{MT} is the meantime, $\text{T}_{\text{PMT\_L/R}}$ is TDC time of hit from PMT L/R. A cut is applied to only select particles within the geometry of the detector,

$$\text{X(T)} \propto (\text{T}_{\text{PMT\_L}} - \text{T}_{\text{PMT\_R}}) \tag{6.42}$$

where X(T) is proportional to the position on the detector, the particle is detected. The peak in the MT spectrum (see Figure 6.29) corresponds to the particles detected

and by applying a time range cut, number of particles detected are counted (the continuous background spectrum is subtracted from the total counts). The ADC signal is used to estimate the number of PE collected for each particle detected. The Čerenkov detector MT cut select all the particles detected and a cut is applied to the ADC spectrum of the TS to only include particles with no scintillation light in the TS Figure 6.30). The black ADC spectrum shown in the plot on the right in Figure 6.30 corresponds to the neutral particles.

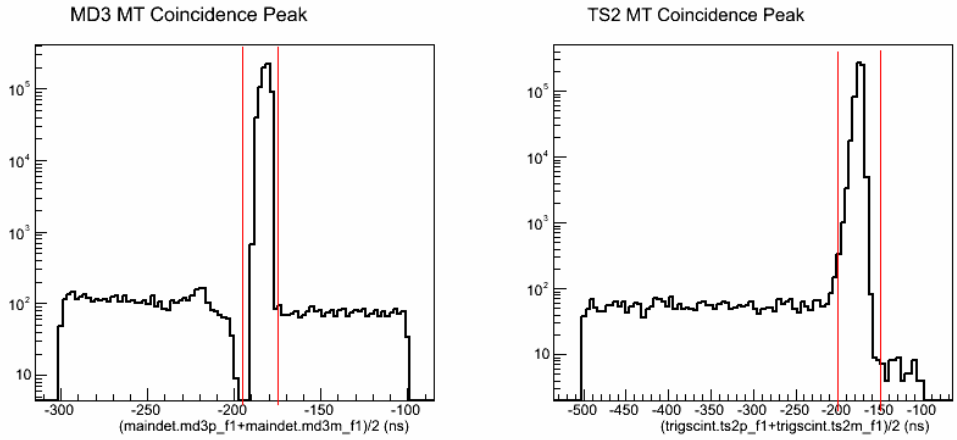

Figure 6.29: The meantime distribution (MT in octant 3 main detector and the trigger scintillator. A particle registers a coincidence peak in the TDC for Čerenkov and scintillation detectors. The applied time range cut (red lines) is used to count detected particles.

The neutral fraction (n_f) or the total neutral background dilution is determined for each octant independently as,

$$n_f = \frac{\text{MD\_neutral\_tracks} \times \text{Light\_neutral\_track}}{\text{MD\_any\_tracks} \times \text{Light\_any\_track}} \tag{6.43}$$

where MD_neutral_tracks is the total neutral particles detected in the Čerenkov detector from the MT peak, Light_neutral_track is the average ADC channels detected for a neutral particle in the Čerenkov detector, MD_any_tracks is all the particles

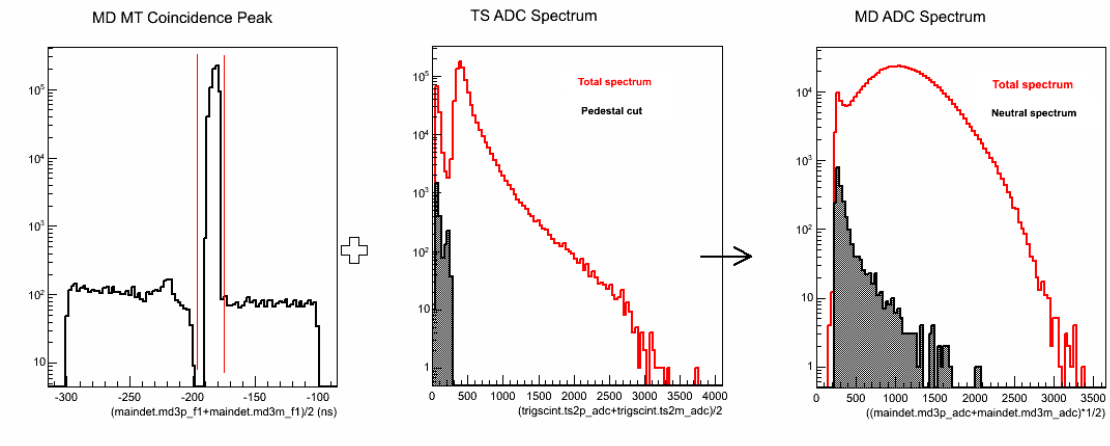

Figure 6.30: Left: MD MT peak. Center: TS ADC spectrum for any particle detected and the shaded area is the pedestal cut to select particles with no scintillation. Right: MD ADC spectrum for any and **neutral** particles. Combination of MT cut on MD and pedestal cut on TS extract the ADC spectrum of neutral particles.

observed in the Čerenkov detector, and Light_any_track is the average ADC channels detected for any particle in the Čerenkov detector (The ADC channels are pedestal subtracted).

This unique analysis does not require any absolute measurement of PE and TDC rates. Thus, it is independent of any dead time corrections associated with regular event mode analysis [115]. The neutral fraction measurement is done for all the octants at the nominal QTOR current (8920 A) for LH2 target (see Table 6.17 [115]). The error on the total dilution background measurements is based on the standard deviation of the measurements performed at each octant at different beam currents.

The neutral fraction is also measured as a function of the QTOR current, 9200 to 1000 A, (see Figure 6.31). The measurement at 6700 A is used for the $N \rightarrow \Delta$ inelastic asymmetry analysis. The measured variation in neutral fraction vs. the QTOR current is expected, as the QTOR current is reduced the elastic electron yield (charged particle yield) incident on the detector plane is reduced,

Table 6.17: All the LH2 neutral fraction measurements. For each octant the measurements are repeated multiple times and the errors are standard deviation (S.D.) of these repeated measurements in each octant.

Octant	n_f (%)
1	0.25 ± 0.01
2	0.23 ± 0.01
3	0.64 ± 0.20
4	0.37 ± 0.02
5	0.38 ± 0.03
6	0.33 ± 0.01
7	0.50 ± 0.12
8	0.30 ± 0.03

increasing the measured neutral fraction. As the QTOR current is reduced further, at around 2000 A, the Møller scattered electrons contribute to the charged particle yield reducing the neutral fraction. Based on these observations, it is assumed that the neutral background is independent of the QTOR current, ie the origin of the neutrals is independent of the scattered electron energy. This observation is important for developing a neutral particle transport model from simulation.

Figure 6.31 reveals a consistent offset in the neutral background fraction between octant 1 and 5. Indeed, I have used universal pedestal cut to select no scintillation on the TS to extract neutral particles for all the measurements done. This pedestal cut can be optimized for single measurements to improve the results by a better selection of neutral particles. For present analysis, I have assigned a systematic error of ± 0.0011 for the variation in the dilution when the pedestal cut is varied around the optimal value [115]. The final neutral background dilution for the LH2 target

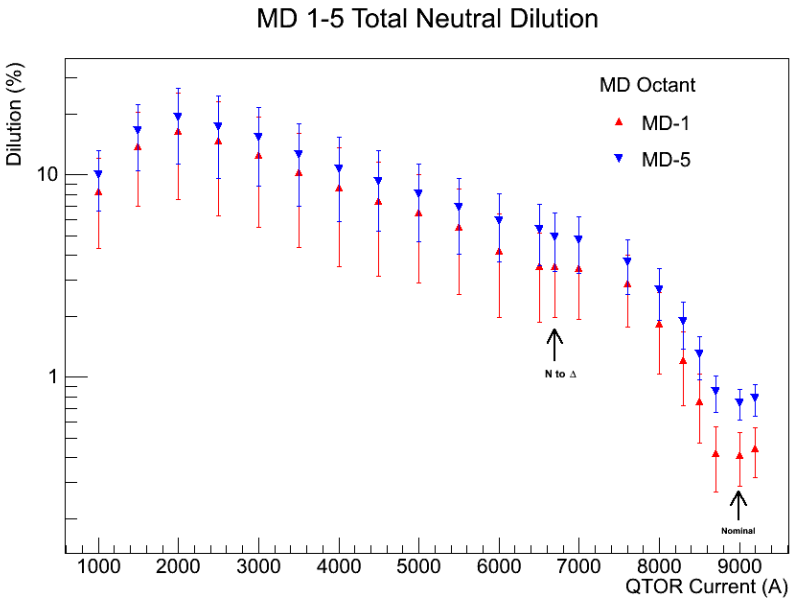

Figure 6.31: QTOR scan of the total neutral fraction (dilution) in Čerenkov detectors located at octant 1 and 5.

using the results in Table 6.17 is,

$$f_{\text{total\_neutral}} = 0.0038 \pm 0.0014 \text{ (std.dev.)} \pm 0.0011 \text{ (syst.)} \tag{6.44}$$

6.10.1 Neutral Background Correction

The background correction to the measured asymmetry requires the dilution and the asymmetry of each background contribution. This section discusses the estimation of QTOR transport channel background (b2) and beam-line neutral background (b3). The estimation of neutral asymmetry (b2) from QTOR transport channel electrons is based on two assumptions. If the QTOR transport channel neutral asymmetry is dominated by elastic electron interactions with the shield walls and collimator edges then the expected asymmetry is of the same order as the elastic electron asymmetry (~ 0.2 ppm). If the primary electron interaction at scraping is dominated by Møller scattering then the expected neutral asymmetry is about 0 ppm [93]. There is an

ongoing simulation effort to estimate the neutral background asymmetry but for Wien0, a conservative estimate is made using above assumptions,

$$A_{b2} \;=\; 0.00 \pm 0.200(\text{assumption})\ \text{ppm} \tag{6.45}$$

On the other hand, the beam-line neutral background asymmetry (b3) is estimated using the background measurements acquired with the blocked-octant study. The blocked-octant study was done by blocking two opposite octants (octant 1 and 5) at the first clean-up collimator (after the Q_{weak} target) using two tungsten shutters [117]. (See Section 3.2.4 for collimator view.) The blocked-octant study was performed during Wien9 data taking. To make things even more complicated, during the blocked-octant study, the background detectors were placed in different locations compared to Wien0 locations. Therefore, a simple-minded estimation of the background asymmetry (b3) is performed by using the up-stream (US) luminosity monitors, which were located at the same place during the Wien0 and Wien9 data sets [118]. Details of steps used to obtain the beam-line background asymmetry are given in Appendix D.7. The final estimated beam-line background asymmetry (b3) for Wien0 data set is [118],

$$A_{b3} \;=\; -5.500 \pm 11.500(\text{model})\ \text{ppm} \tag{6.46}$$

and the beam-line background dilution (b3) estimated from the blocked-octant study [119] is,

$$f_{b3} \;=\; 0.00193 \pm 0.00064 \tag{6.47}$$

The final error on the A_{b3} includes an uncertainty to account for the fact that not all eight octants are used to estimate the A_{b3} and another uncertainty on beam-line background amplitude due to beam halo fluctuations [118]. The dilution for the b2 background can not be determined directly. It is calculated indirectly using the total

neutral background dilution results presented in the previous section and given by,

$$f_{b2} = f_{total\_neutral} - f_{b3}$$
$$f_{b2} = 0.0019 \pm 0.0019 \quad (6.48)$$

6.11 Experimental Bias Corrections to the Measured Asymmetry

The goal of these remaining corrections is to remove all the experimental bias from the measured asymmetry. The measured $\vec{e}p$ Parity Violating (PV) asymmetry is corrected for the electromagnetic (EM) radiative corrections, light weighting on the Čerenkov detector, and detector acceptance bias from momentum-transfer square, Q^2. These corrections are treated as independent factors and are applied to the final measured $\vec{e}p$ PV asymmetry [120]. The experimental bias removed asymmetry is called the tree-level asymmetry.

The EM radiative effects cause depolarization of the incident electron, energy loss and angle change that result in modification of the measured asymmetry and momentum transfer. The leading order EM radiative effects include real bremsstrahlung photon emissions and virtual photon loops. The interactions can either occur in the field of the scattering nucleus (internal) or the field outside of the scattering nucleus (external) as shown in Figure 6.32. Internal radiative corrections include real internal bremsstrahlung photons and virtual photon loops (see Figure 6.33). The external radiative corrections are real bremsstrahlung photon emissions (see Figures 6.34). The GEANT3 simulation developed for the Q_{weak} experiment is used to determine the asymmetry with radiative corrections (A_{RC}^{sim}) and the momentum transfer square ($< Q^2 >_{RC}^{sim}$) [121]. Using the same set of events, the tree-level asymmetry (A_{tree}^{sim}) and momentum transfer square ($< Q^2 >_{tree}^{sim}$) are determined by removing higher order contributions [121]. The EM radiative correction factor, which removes the EM radiative effects from the measured

asymmetry, is defined as,

$$R_{RC} = \frac{A_{tree}^{sim}}{A_{RC}^{sim}} \tag{6.49}$$

$$= 1.010 \pm 0.005 \tag{6.50}$$

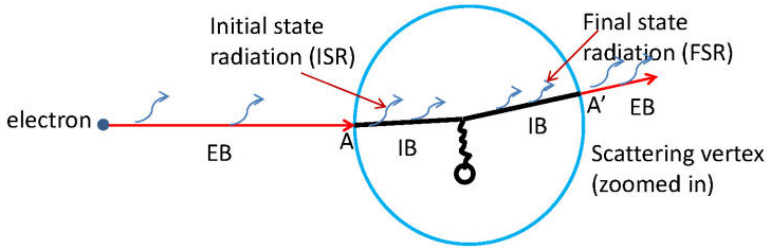

Figure 6.32: EM radiative corrections. The scattering vertex is zoomed in to the blue circle (from [121]). The internal effects are shown inside the zoomed blue circle.

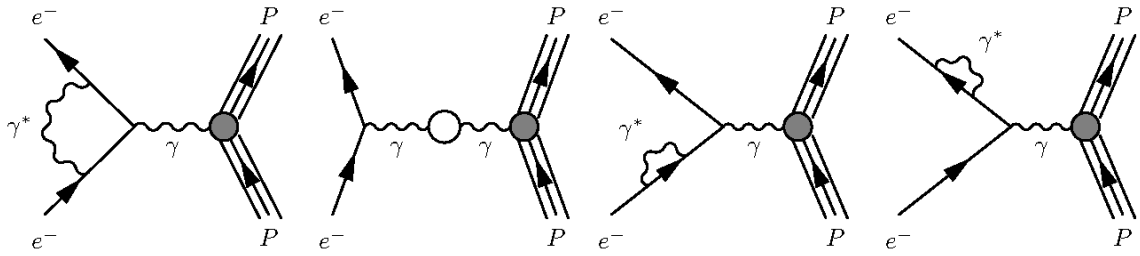

Figure 6.33: The Feynman diagrams for emission of a virtual photon, which is later reabsorbed, and for a virtual loop effect.

The experimental asymmetry is computed using the Čerenkov light collected in the detectors. The collected light varies spatially over the radiator area [122] and a "light weighting" corrections is required measured asymmetry and kinematic parameters. In the simulation, the asymmetry can be determined either with (A_{bias}^{sim}) or without ($A_{no\_bias}^{sim}$) the light collection weighting applied (detector bias) from the

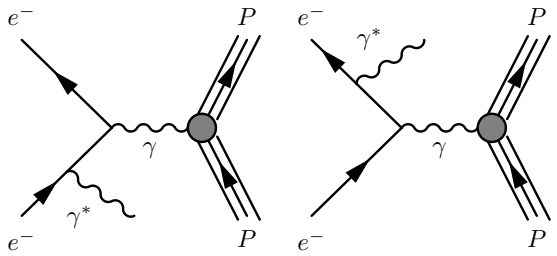

Figure 6.34: The Feynman diagrams for a bremsstrahlung photon emission.

same set of events. The detector bias correction factor is defined as,

$$\begin{aligned} \mathrm{R_{Det}} &= \frac{\mathrm{A^{sim}_{no\_bias}}}{\mathrm{A^{sim}_{bias}}} \times \delta \mathrm{Q}^2 \\ &= 0.9870 \pm 0.0065 \end{aligned} \tag{6.51}$$

where $\delta \mathrm{Q}^2$ is applied to $\mathrm{R_{Det}}$ as an additional correction (see an explanation in a Appendix D.8).

The remaining correction to the measured asymmetry is related to the detector acceptance averaged momentum transfer square, $< \mathrm{Q}^2 >$. The measured asymmetry, $< \mathrm{A_{Tree}}(\mathrm{Q}^2) >$ is averaged over the range of Q^2 defined by the $\mathrm{Q_{weak}}$ experimental acceptance. It is important to quote the $\mathrm{Q_{weak}}$ results at an average momentum transfer square, $< \mathrm{Q}^2 >$ to be able to compare to theoretical calculations. The acceptance correction is done using the factor,

$$\mathrm{A_{Tree}}(< \mathrm{Q}^2 >) \;=\; \mathrm{R_{eff\_acc}} \;< \mathrm{A_{Tree}}(\mathrm{Q}^2) > \tag{6.52}$$

where $\mathrm{R_{eff\_acc}}$ factor is computed using simulation results [123] and was found to be,

$$\mathrm{R_{eff\_acc}} = 0.980 \pm 0.01 \tag{6.53}$$

where $\mathrm{R_{other}}$ can now be defined as,

$$\mathrm{R_{other}} = \mathrm{R_{RC}} \times \mathrm{R_{Det}} \times \mathrm{R_{eff\_acc}} = 0.9769 \pm 0.0082 \tag{6.54}$$

6.12 Q_{weak} Kinematics

The effective kinematics for the Q_{weak} experiment is quoted following the HAPPEX prescription [124]. The average electron beam energy is calculated by correcting for ionization energy loss in the Q_{weak} LH2 target [121],

$$\begin{aligned} E_s &= \langle E_{beam} - \frac{dE}{dx} \cdot t \rangle \\ &= 1155 \pm 3 \text{ MeV} \end{aligned} \tag{6.55}$$

where E_{beam} is the incident beam energy, $\frac{dE}{dx}$ is the ionization energy loss, and t is the distance traveled by an electron before the primary interaction. The acceptance averaged effective momentum transfer square at tree level is determined from a GEANT4 simulation benchmarked by the tracking mode Q_{weak} experiment data [121] to represent the geometry of the experimental setup, collimation, and magnetic spectrometer. The Wien0 results quoted here is a preliminary result from an on-going simulation and analysis of the tracking data taken during the Q_{weak} experiment. The tree-level momentum transfer square is,

$$< Q^2 >_{tree} \equiv < Q^2 >^{sim}_{tree} = \ 0.0250 \pm 0.0006 \ (\text{GeV/c})^2 \tag{6.56}$$

the values E_s and $< Q^2 >_{tree}$ are used to compute the effective scattering angle using the following equation [124],

$$\cos(\theta_{eff}) = \frac{1 - \frac{< Q^2 >_{tree}}{2E_s^2}(1 + \frac{E_s}{M})}{1 - \frac{< Q^2 >_{tree} \cdot E_s}{2E_s^2 \cdot M}} \tag{6.57}$$

$$< \theta_{eff} > = 7.90 \pm 0.30^o$$

where M is the proton rest mass and other parameters were defined in equations 6.55 and 6.56.

6.13 Results and Discussions

This section will summarize all the corrections and errors discussed so far and present the tree level asymmetry at Q_{weak} effective kinematics. The final asymmetry $A_{Tree}(< Q^2 >_{Tree})$ will be used to extract the weak charge of the proton in the next chapter. The raw asymmetry was linearly regressed to remove false asymmetries (equation 6.24) to get A_{msr}, the main input asymmetry of equation 6.28. The raw, regressed corrections, and measured asymmetries are

$$A_{raw} = -0.170 \pm 0.031 \text{ (stat.)} \quad \text{ppm}$$

$$\Delta A_{std.reg} = -0.035 \pm 0.011 \text{ (stat.)} \quad \text{ppm (regression correction)}$$

$$A_{msr} = -0.205 \pm 0.031 \text{ (stat.)} \pm 0.012 \text{ (syst.) ppm}$$

The tree-level asymmetry is extracted using equation 6.28. The breakdown of all the corrections to the A_{msr} are summarized in Table 6.18. Figure 6.35 shows the corrections steps in order, starting from A_{raw} to get the final tree-level asymmetry.

Table 6.18: The breakdown of Corrections to A_{msr} for Wien0 data. (The correction definitions can be found in Appendix D.6.)

Source	Correction to A_{msr} (ppm)
Polarization, ΔA_P	-0.0257
Aluminum windows, ΔA_{b1}	-0.0576
QTOR transport channel, ΔA_{b2}	0.0000
Beam-line, ΔA_{b3}	+0.0108
$N \rightarrow \Delta$, ΔA_{b4}	+0.0006
R_{Other}	-0.0028
Total	-0.0747

The final errors are computed using equations 6.30 (see Table 6.19).

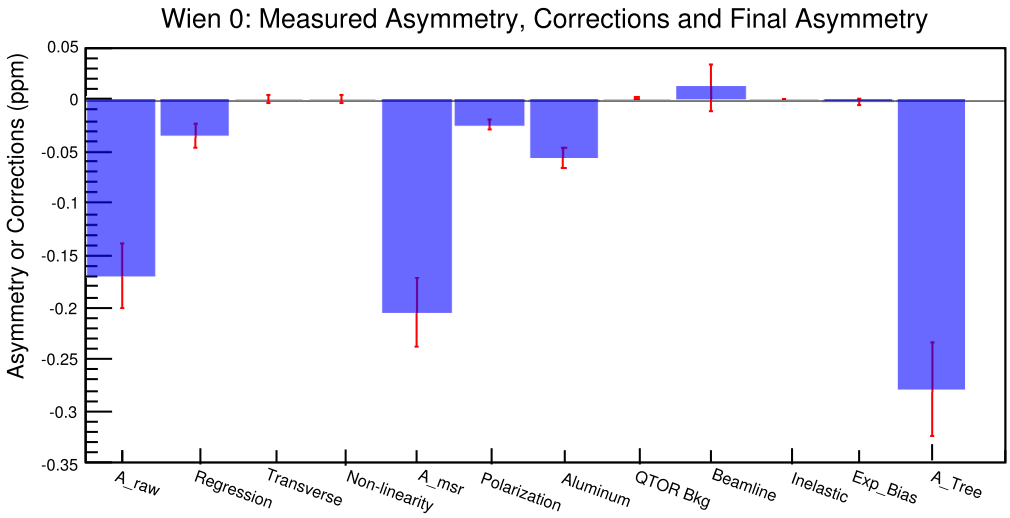

Figure 6.35: The breakdown of the asymmetry corrections which transform A_{raw} into A_{msr} (equation 6.22) and then transform into $A_{Tree}(< Q^2 >_{Tree})$ (equation 6.28).

Table 6.19: The Breakdown of A_{Tree} errors. The statistical and systematic errors on A_{msr} are properly scaled using the equations 6.29 to reflect the errors on A_{Tree}.

Source	Contribution to dA_{Tree} (ppm)
A_{msr} **statistical (Scaled)**	**0.0348**
A_{msr} systematic (Scaled)	0.0140
Polarization	0.0048
Al window asymmetry (b1)	0.0085
Al window dilution (b1)	0.0044
QTOR transport neutral asymmetry (b2)	0.0004
QTOR transport neutral dilution (b2)	0.0005
Beamline neutral asymmetry (b3)	0.0225
Beamline neutral dilution (b3)	0.0034
$N \rightarrow \Delta$ asymmetry (b4)	0.0002
$N \rightarrow \Delta$ dilution (b4)	0.0006
Det. bias correction	0.0018
EM radiative correction	0.0014
Acceptance correction	0.0028
Total Systematic error	**0.0290**
Total Error	**0.0453 (16%)**

The blinding factor was released after all the corrections to the A_{msr} were finalized [109] and the value is,

$$B_{offset} = -0.0005079 \text{ ppm} \tag{6.58}$$

The unblinded tree-level asymmetry from the Q_{weak} Wien0 data set is computed based on equation 6.28 and the asymmetry is,

$$A_{Tree}(< Q^2 >_{Tree}) = -0.2788 \pm 0.0348 \text{ (stat.)} \pm 0.0290 \text{ (syst.) ppm,}$$

where the $A_{Tree}(< Q^2 >_{Tree})$ is the PV electron-proton scattering asymmetry corrected for EM radiative effects and other extended experimental biases and this asymmetry is measured at these effective Q_{weak} kinematics,

Acceptance averaged incident beam energy, $< E_s >$	1.155 ± 0.003 GeV
Acceptance averaged $< Q^2 >_{Tree}$	0.0250 ± 0.0006 (GeV/c)^2
Effective scattering angle, $< \theta_{eff} >$	7.90 ± 0.30^o

7 Results and Discussions

A 16% measurement of the Parity Violating (PV) asymmetry of elastic electron-proton scattering was obtained from the Wien0 data set (Chapter 6). Based on this result, this chapter will provide a preliminary measurement of the weak charge of the proton, and a constraint on the isoscalar and isovector quark couplings predicted by the Standard Model (SM). I will also discuss issues related to the Wien0 results and provide an outline of future work needed to perform the full Q_{weak} analysis based on the Wien0 data analysis experience.

7.1 Weak Charge of the Proton and Weak Mixing Angle

The weak charge of the proton ($Q_W^p(msr)$) is extracted using the measured asymmetry, and then weak mixing angle ($\sin^2\hat{\theta}_W(msr)$) is extracted using $Q_W^p(msr)$. I have written a program to compute the weak charge and mixing angle (see Appendix B.2) and the results are presented here as well as the important steps in the analysis. The measured asymmetry is first corrected for the beam energy dependent part of the electroweak radiative correction, $\Box_{\gamma Z}(E)$ (see Section 2.1.2). Then the hadronic contribution in the measured asymmetry is removed to obtain the measured asymmetry contribution from the weak charge of the proton hence the weak charge of the proton can be computed (equation 2.13). Finally the weak mixing angle is extracted after applying necessary SM based electroweak radiative corrections to the weak charge of the proton (equation 2.19).

From Chapter 6, the tree-level PV asymmetry measured at $< Q^2 >_{Tree} = 0.0250 \pm 0.0006$ (GeV)^2 is,

$$A_{Tree} = -0.2788 \pm 0.0348 \text{ (stat.)} \pm 0.0290 \text{ (syst.) ppm} \tag{7.1}$$

First, the $\Box_{\gamma Z}(E)$ contribution (Section 2.1.2.1) is corrected from the measured asymmetry. The correction is applied using,

$$\begin{aligned} A_{LR}^{msr}(\tilde{e}p) &= A_{Tree} - \Delta A\_\Box_{\gamma Z} \\ &= -0.2698 \pm 0.0348(\text{stat.}) \pm 0.0290(\text{syst.}) \pm 0.0025(\text{theory}) \text{ ppm} \end{aligned} \quad (7.2)$$

where $\Delta A\_\Box_{\gamma Z} = -0.009 \pm 0.0025$ ppm (equation 2.26 in Section 2.1.2.1) which is a 3% correction to the measured asymmetry and negligible compared to the uncertainty on the Wien0 measured asymmetry. The error on the $\Delta A\_\Box_{\gamma Z}$ is added to the corrected asymmetry as a theory uncertainty. This choice of correcting the energy dependent electroweak radiative correction from the measured asymmetry is consistent with separating energy dependent and independent contribution in the SM prediction of the PV electron-proton scattering asymmetry. Also looking forward to the full Q_{weak} analysis, the collaboration intends to combine the worldwide data set at various Q^2 (including the Q_{weak} results) to extrapolate the weak charge at $Q^2 = 0$ GeV^2 (See Figure 2.2). Every one of these world data were taken at a different beam energy. Therefore, the choice of $\Delta A\_\Box_{\gamma Z}$ correction to the measured asymmetry is the sensible way to do it. Now the result can be compared to the SM prediction at $Q^2 = 0.025$ GeV^2 (equation 2.18 in Section 2.1):

$$\begin{aligned} A_{LR}^{msr}(\tilde{e}p) &= -0.2698 \pm 0.0348(\text{stat.}) \pm 0.0290(\text{syst.}) \pm 0.0025(\text{theory}) \text{ ppm} \\ A_{LR}^{SM}(\tilde{e}p) &= -0.2142 \pm 0.0030 \text{ ppm} \end{aligned}$$

As discussed in Section 2.1, the weak charge can be extracted using a global fit to world Parity Violating Electron Scattering (PVES) asymmetries. This analysis is still in its preliminary stages because there are discrepancies regarding the treatment of the energy dependent $\Box_{\gamma Z}$ contributions in this analysis. Therefore, for the Wien0 data set, the weak charge of the proton is extracted by correcting the hadronic contribution

estimated in Section 2.1 (equation 2.18) without Q^2 extrapolation or strange form factor contributions. In that case, the measured asymmetry only from the $Q_W^p$is given by,

$$A_{Qwp}^{msr} = A_{LR}^{msr}(\tilde{e}p) - A_{Had} \tag{7.3}$$

where $A_{Had} = -0.0558 \pm 0.0024$ ppm (from equation 2.18) and $A_{LR}^{msr}(\vec{e}p)$ is the final measured asymmetry from Wien0 (equation 7.2). Eventually, the world PVES data fit will be used to extract the weak charge of the proton from Wien0 and final Q_{weak} data set once remaining issues related to world data fit are resolved. It will be a better extraction of the weak charge of the proton compared to the result in my dissertation because the hadronic contributions will be bounded by precise experimental data providing a realistic measurement of the hadronic contribution. Using these inputs, the weak charge of the proton from the Wien0 data set is computed as

$$Q_w^p(msr) = -2 \cdot \frac{A_{Qwp}^{msr}}{A_{LR}^0} = \frac{-4\pi\alpha\sqrt{2}}{G_F|Q^2|} \cdot A_{Qwp}^{msr} \tag{7.4}$$

I have added the errors on the hadronic term and $\Box_{\gamma Z}(E)$ corrections as the theory uncertainty into the final weak charge of the proton error. The SM prediction of Q_W^p including the electroweak radiative correction is given by [39, 41],

$$Q_W^p = [\rho_{NC} + \Delta_e][1 - 4\sin^2\hat{\theta}_W(0) + \Delta_e'] + \Box_{WW} + \Box_{ZZ} + \Box_{\gamma Z} \tag{7.5}$$

where ρ_{NC} re-normalizes the ratio of neutral to charged current interaction at low energies [39]. Δ_e and Δ_e' are corrections to the Zee and γee couplings at electron vertex, respectively, and remaining corrections are from box contributions [39] (see Section 2.1 for detailed discussion). This relationship is used to apply electroweak radiative corrections (see Table 2.2 in Chapter 2) and extract the weak mixing angle. Equation 7.5 with electroweak radiative corrections substituted is given by,

$$Q_W^p(msr) = [1.045][1 - 4 \cdot \sin^2\hat{\theta}_W(msr) - 0.001] + 0.025 \tag{7.6}$$

and using this results, the weak mixing angle is extracted. The extracted weak charge of the proton ($Q_W^p(msr)$) and weak mixing angle ($\sin^2\hat{\theta}_W(msr)$) are given below,

$Q_w^p(msr)$	=	$+0.0952 \pm 0.0155(stat.) \pm 0.0131(syst.) \pm 0.0015(theory)$
$Q_w^p(SM)$	=	$+0.0705 \pm 0.0008$
$\sin^2\hat{\theta}_W(msr)$	=	$+0.2328 \pm 0.0039(stat.) \pm 0.0033(syst.) \pm 0.0004(theory)$
$\sin^2\hat{\theta}_W(SM)$	=	$+0.2387 \pm 0.0002$

and Wien0 results are 1-standard deviation (1σ) away from the SM prediction. The running of the weak mixing angle plot is generated with Wien0 measurement placed (see Figure 7.1).

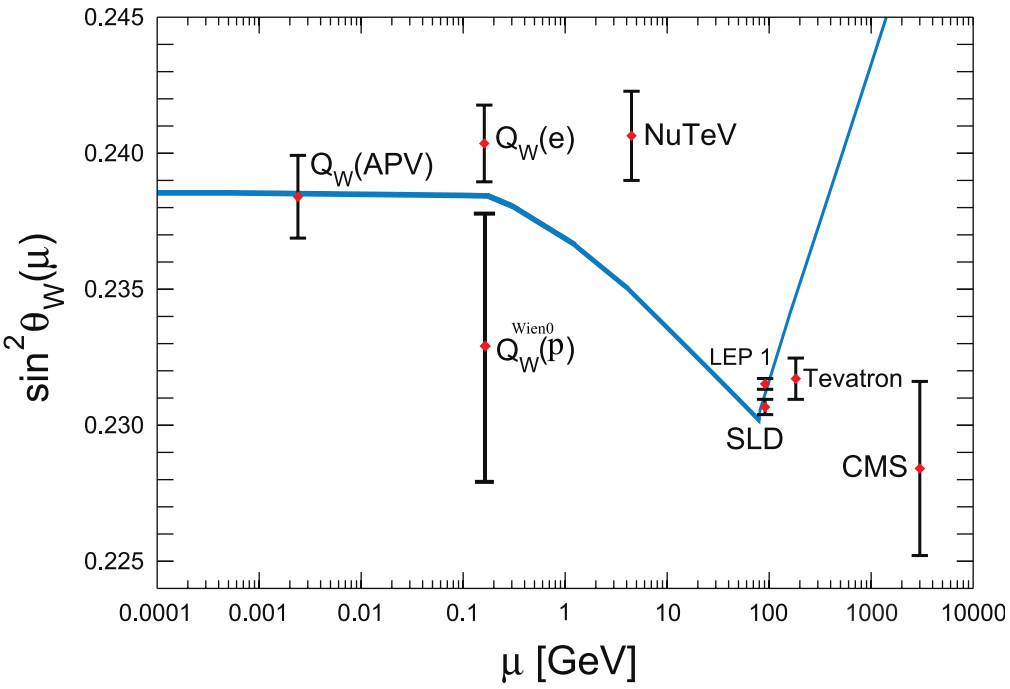

Figure 7.1: The "running of $\sin^2\theta_W$" in the $\overline{MS}$ with low energy measurements of the $\sin^2\hat{\theta}_W(\mu)$ including the Wien0 result ($Q_W^{Wien0}(p)$), which is at the same μ-scale of the Møller measurement ($Q_W(e)$) from E158 (original figure from [40]).

The extracted value of Q_W^p(msr) is also used to constrain the couplings for weak neutral hadronic currents in the SM, which are built out of the SU(3) octet and singlet currents using only lightest quarks (u,d, and s). The couplings for the weak isoscalar (T=0) and isovector (T=1) hadronic vector currents are defined as,

$$\xi_V^{T=0} = -2 \cdot \sqrt{3}(C_{1u} + C_{1d})$$
$$\xi_V^{T=1} = -2 \cdot (C_{1u} - C_{1d}) \tag{7.7}$$

where $g_V^{u/d} = -2C_{1u/d}$ were defined in Table 2.1 and $Q_w^p = -2(2C_{1u} + C_{1d})$ (equation 2.11). Therefore, the measurement of the weak charge of the proton (Q_w^p(msr)) can be used to bound the weak isoscalar and isovector couplings (see Figure 7.2).

The Wien0 results deviate from the SM prediction by 1 standard deviation (1σ). The upper limit of the new PV physics mass reach from Wien0 results is about 1 TeV (see Section 2.2.1). A 1σ deviation does not signify any discrepancy from the SM but the final Q_{weak} result will be approximately 7 times more precise. A similar central value for the final Q_{weak} results would give a 8σ deviation from the SM prediction which would be a signal for new physics beyond the Standard Model. Already with the limited Wien0 results, the Q_{weak} constraint on the effective quark couplings is the next best single measurement after the Atomic Parity Violating (APV)-Cs (Q_W(Cs)) measurement (see Figure 7.2). When combined, the effective quark couplings from Wien0 and the APV-Cs results will provide the best experimental bound on couplings so far.

7.2 Discussion: Wien0 Data Analysis

The Wien0 result is based on a statistically limited data set with experimental conditions not exactly matching the full Q_{weak} experiment. Therefore for this

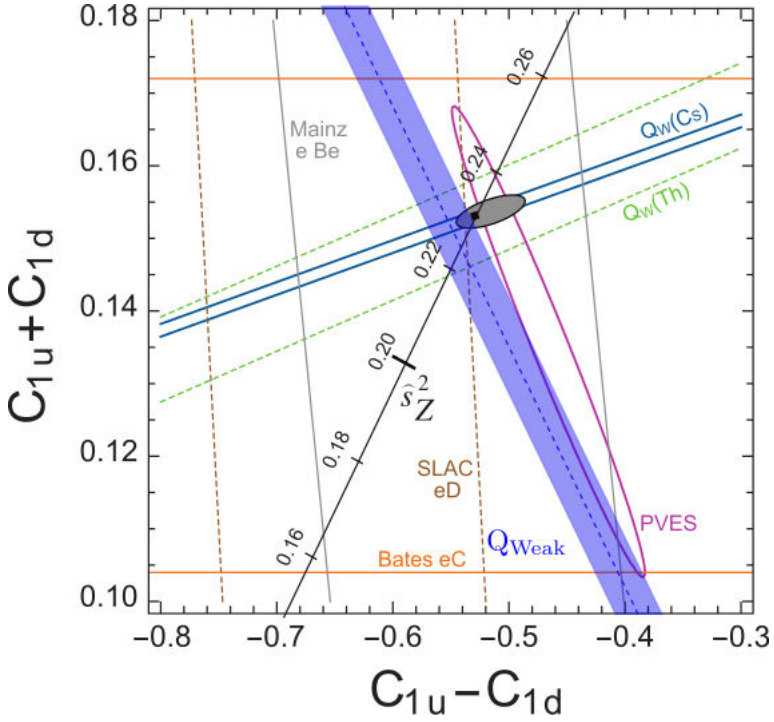

Figure 7.2: The constraints on $C_{1u} - C_{1d}$ (isovector) and $C_{1u} + C_{1d}$ (isoscalar) from parity violating electron scattering, atomic parity violating experiments, and Q_{weak} Wien0 data set (blue-band). The PVES and APV experiments have mutually orthogonal sensitivities to the isovector and isoscalar effective quark couplings. The SM estimation of the quark couplings using $\hat{s}^2_Z = 0.2311 \pm 0.00026$ agrees with the world data best fit analysis (the Grey ellipse with no Q_{weak}) (original figure from [40]). The Wien0 Q_{weak} estimation is 1σ away from the SM prediction when it intersects with the APV-Cs results.

analysis, certain issues with the data were bounded by large systematic errors. These issues will need to be better understood for the full Q_{weak} results but they have not hindered Wien0 results because of the large statistical error (± 0.0348(stat.) vs. $\pm\, 0.0290$(syst.) ppm). The Wien0 analysis is a proof of concept analysis which tested the analysis procedures and tools to be used for the final full data analysis and in doing so, it has provided a 21% measurement of the weak charge of the proton. In this section, I will provide a summary of Wien0 limitations and issues that need further attention.

The Wien0 data set was taken during the last two weeks of the commissioning period at the beginning of the Q_{weak} experiment. During this period, certain experimental parameters were not settled as initial studies were still on-going. For example, the electron beam profile (Section 3.2.3) on the target was 3.5×3.5 mm^2 for the Wien0 data set but changed to 4×4 mm^2 after the end of Wien0 in order to minimize the target noise contribution to the measured asymmetry. The beam current used during Wien0 was up to 150 μA but was increased to about 180 μA after Wien0 ended. Both of these measures were taken to increase the statistical precision of the overall measurement by reducing noise and increasing scattering rates.

One of the main issues in the Wien0 data set was that, after the Standard linear regression was applied, the final measured asymmetry has a large residual false asymmetry (a 2σ $A_{msr}(IN + OUT)/2$: see Section 6.5). This was partially related to the large and imperfect Helicity Correlated (HC) beam differences during the Wien0 data set. (The sign of HC beam differences reversed with the Insertable Half Wave Plate (IHWP) state: see Section 6.3.) Beam-line background studies performed on the Wien0 data set have also proved inconclusive as the cause of the large residual false asymmetry. For the Wien0 data set, the charge asymmetry was not regressed out due to unresolved issues related to non-linearity and charge regression (Section 6.5.3). Instead, a conservative systematic error was assigned to bound false asymmetry from non-linearity but the charge regression alone could not be attributed to the residual false asymmetry in the final result.

Another conservative error was assumed when correcting for neutral background contributions. Indeed, the neutral background generated by the electron beam halo and low angle scattered electron interactions with the beam-line shielding was constrained using the blocked octant preliminary analysis. The large conservative error (200%) was assigned to the measured neutral asymmetry to cover the time-

varying amplitude. Moreover, the neutral background from Q_{weak} TORoidal (QTOR) transport channel is the least known component in the Wien0 data analysis where only the dilution was estimated based on the event mode analysis. See Section 6.10.1 for more details on neutral background issues.

In conclusion, the most problematic issues related to the Wien0 data analysis are related to residual false asymmetry and neutral background contaminations. The residual false asymmetry issue is related to imperfect HC beam differences and unresolved linear regression problems. For Wien0, linear regression woes are concealed as systematics errors. They include cut dependence, non-linearity, and double peaking errors discussed in Section 6.5.3. The Wien0 neutral beam-line background contaminations are only constrained from measurements done from different data sets and based on preliminary analysis also resulting in larger systematic errors.

7.3 Future Work

Looking ahead to the analysis of the full Q_{weak} data set, and comparing the Wien0 errors to the Q_{weak} final error goals (see Table 7.1), the backgrounds and Helicity Correlated Beam Asymmetry (HCBA) corrections require significant reduction in systematic errors. Therefore, the future analysis of the full Q_{weak} data set will be mainly focused on the following two main issues.

First, understanding issues related to the residual false asymmetry (IN+OUT) and discrepancies related to linear regression are important. Therefore, it is useful to utilize the two independent systems implemented to measure and correct false asymmetries: the linear regression based on natural beam motion (Section 6.4) and beam dithering (modulation). The two systems will be used for the remaining Q_{weak} data analysis for false asymmetry corrections. They will provide better understanding of linear regression related issues.

Table 7.1: Comparison of the precision on the measured Wien0 asymmetry to the precision goal of the full Q_{weak} measurement. The systematic error shown here covers errors from linear regression, non-linearity, and transverse leakage.

Source	Wien0		Proposed	
	Results (ppm)	(%)	Goal (ppm)	(%)
Statistics	0.035	12.5	0.006	2.1
Systematics (HCBA+Transverse)	0.015	5.3	0.001	0.5
Backgrounds	0.025	8.9	0.002	0.7
Q^2 (Exp. bias Corrections)	0.004	1.3	0.001	0.5
Polarization	0.005	1.7	0.003	1.0
Total Error	**0.046**	**16.3**	**0.007**	**2.5**

The second issue is related to the time varying beam-line background asymmetry and dilution which will require estimation at Wien or Slug time scales[†] to remove the beam-line background asymmetry. As a minor issue a better estimation of neutral background asymmetry in QTOR transport channel (Section 6.10.1) is also required and this can only be achieved by simulation using a transport model for neutral particles generated within the elastic transport channel.

The remaining issues are related to electron beam polarimetry. The goal of a 1% relative precision measurement of the beam polarization will require on the one hand, rigorous studies to understand the effects of the broken Møller quadrupole magnet during Run 1, and on the other hand, it will be necessary to combine polarimetry results from Compton and Møller polarimeters (see Chapter 5). The preliminary transverse leakage analysis points towards bounding with a systematic error for the final Q_{weak} results but a case can be built to apply a correction at the finer time

[†]A Wien period corresponding approximately to 8 to 10 slugs while a slug period corresponds to approximately 8 hours of data.

scale (slug) or a global correction based on the estimated transverse-beam leakage (see Section 6.6).

7.4 Q_{weak} Experiment and PVES Outlook

It has been a wonderful journey to start my graduate research work as a software developer for the Q_{weak} experiment and to finish with an important physics result that will pave the way to the final goal of the experiment. The future looks bright for the on-going Q_{weak} data analysis as it gears towards the final analysis to obtain weak charge of the proton using all the data accumulated. The auxiliary data taken during the Q_{weak} experiment provide many different physics results: electron-proton elastic transverse-beam asymmetry (2-photon exchange) [74], first measurement of the PV asymmetry in electron-aluminum scattering (preliminary results [58]), electron-nuclei elastic scattering transverse-beam asymmetries (for the understanding of the nuclear Coulomb distortion) from carbon and aluminum, $N \rightarrow \Delta$ PV asymmetry measurements at 2 beam energies [68], and PV asymmetry and transverse-beam asymmetry measurements from non-resonant inelastic electron-proton scattering that will help to understand $\Box_{\gamma Z}(E)$ contributions to neutral current interactions. The polarimetry for Q_{weak} has resulted in successful commissioning of the Compton polarimeter which will provide real-time polarimetry measurements for future Hall C experiments. The first official Compton polarimetry results are soon to be published.

The Q_{weak} experiment will provide the first direct determination of the weak charge of the proton, a precise semi-leptonic determination of the weak mixing angle well below the Z-pole, and the most stringent constraints on the effective quark vector couplings (C_{1q}) predicted in the SM. Beyond this important result, two ambitious PVES experiments have proposed to utilize the Jefferson Lab 12 GeV upgraded beam. These experiments will provide precision measurements related to electroweak

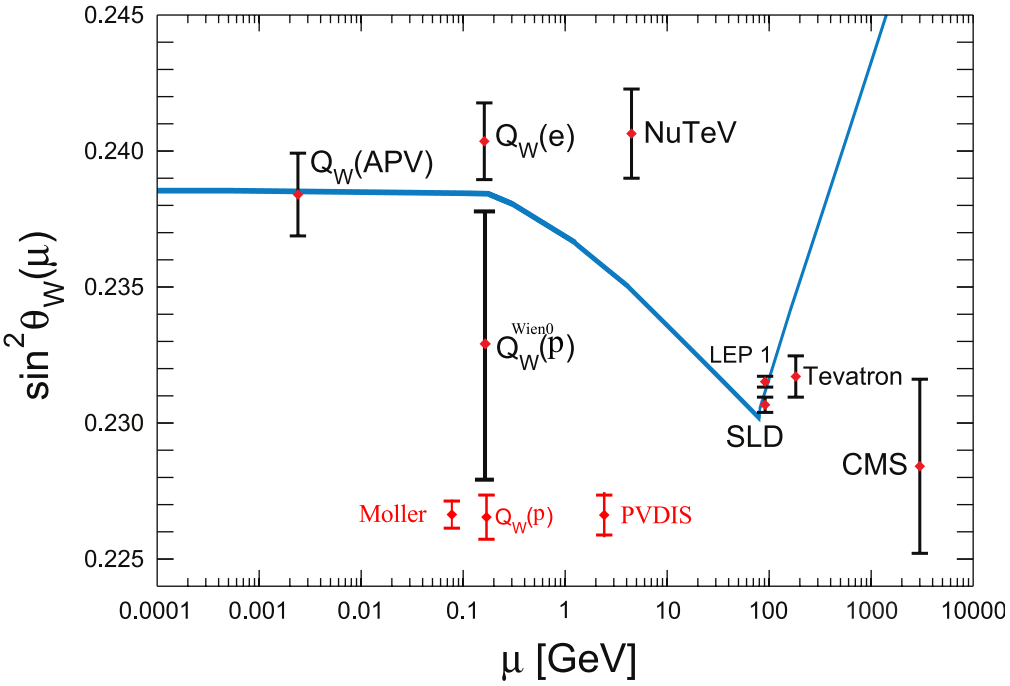

Figure 7.3: The "running of $\sin^2\theta_W$" in the $\overline{\text{MS}}$ with proposed (or on-going) and completed low energy measurements of the $\sin^2\hat{\theta}_W(\mu)$. Original figure taken from [40].

interactions of leptons and quarks. The importance of the Q_{weak} experiment and of these future PVES experiments was also outlined in the National Science Advisory Committee (NSAC) long range plan [125]. First, the proposed next generation Møller experiment will provide a pure leptonic measurement of the weak mixing angle with precision comparable to the ones achieved by the Z-pole measurements [30]. The other experiment (PVDIS) proposes to measure the effective quark axial-vector couplings (C_{2q}) by measuring parity violation in the Deep-Inelastic Scattering (DIS) sector [126]. Figure 7.3 shows the impact of these two measurements on running of weak mixing angle. Q_{weak} and these proposed experiments in search of the complete Standard Model will advance our understanding of the universe.

References

[1] F.J. Hasert et al. Observation of Neutrino Like Interactions Without Muon Or Electron in the Gargamelle Neutrino Experiment. *Phys.Lett.*, B46:138–140, 1973.

[2] Francis Halzen and Alan D. Martin. *Quarks and Leptons: An Introductory Course in Modern Particle Physics*. John Wiley and Sons, Inc., 1984.

[3] C.Y. Prescott et al. Parity Nonconservation in Inelastic Electron Scattering. *Phys.Lett.*, B77:347–352, 1978.

[4] S. Schael et al. Precision electroweak measurements on the Z resonance. *Phys.Rept.*, 427:257–454, 2006.

[5] G.W. Bennett et al. Measurement of the negative muon anomalous magnetic moment to 0.7 ppm. *Phys.Rev.Lett.*, 92:161802, 2004.

[6] D. Denegri. The discovery of the W and Z. *Phys.Rept.*, 403-404:107–145, 2004.

[7] G. Aad et al. Combined search for the Standard Model Higgs boson in pp collisions at $\sqrt{s}$=7 TeV with the ATLAS detector. *Phys. Rev. D*, 86:032003, Aug 2012.

[8] S. Chatrchyan et al. Combined results of searches for the Standard Model Higgs boson in pp collisions at $\sqrt{s} = 7\ TeV$. *Physics Letters B*, 710(1):26 – 48, 2012.

[9] F. Abe et al. Observation of Top Quark Production in $\overline{p}p$ Collisions with the Collider Detector at Fermilab. *Phys. Rev. Lett.*, 74:2626–2631, Apr 1995.

[10] S. Abachi et al. Observation of the top quark. *Phys. Rev. Lett.*, 74:2632–2637, Apr 1995.

[11] D. Hanneke, S. Fogwell, and G. Gabrielse. New measurement of the electron magnetic moment and the fine structure constant. *Phys. Rev. Lett.*, 100:120801, Mar 2008.

[12] F. P. An et al. Observation of electron-antineutrino disappearance at daya bay. *Phys. Rev. Lett.*, 108:171803, Apr 2012.

[13] M. V. Romalis, W. C. Griffith, J. P. Jacobs, and E. N. Fortson. New limit on the permanent electric dipole moment of ^{199}Hg. *Phys. Rev. Lett.*, 86:2505–2508, Mar 2001.

[14] P. Belli et al. Search for 2β decays of ^{96}Ru and ^{104}Ru by ultra-low background HPGe gamma spectrometry at LNGS: final results. *ARXIV:1302.7134*, 2013.

[15] Alex Geringer-Sameth. The VERITAS Dark Matter Program. *ARXIV:1303.1406*, 2013.

[16] Monica Pepe Altarelli. CP violation in charm and beauty decays at LHCb. *ARXIV:1301.3082*, 2013.

[17] Rui-zhi Yang, Emma de Oa Wilhelmi, and Felix Aharonian. Probing Cosmic Rays in Nearby Giant Molecular Clouds with the Fermi Large Area Telescope. *ARXIV:1303.7323*, 2013.

[18] C.L. Bennett et al. Nine-Year Wilkinson Microwave Anisotropy Probe (WMAP) Observations: Final Maps and Results. *ARXIV:1212.5225*, 2012.

[19] G. Hinshaw et al. Nine-Year Wilkinson Microwave Anisotropy Probe (WMAP) Observations: Cosmological Parameter Results. *ARXIV:1212.5226*, 2012.

[20] P. Astone. Recent results for the search of continuous waves with the LIGO and Virgo detectors. *Class.Quant.Grav.*, 29:124011, 2012.

[21] James R. Boyce. An overview of dark matter experiments at Jefferson Lab. *J.Phys.Conf.Ser.*, 384:012008, 2012.

[22] Thomas Kirn. The AMS-02 TRD on the international space station. *Nucl.Instrum.Meth.*, A706:43–47, 2013.

[23] D. Armstrong et al. The Qweak Experiment: A Search for New Physics at the TeV Scale via a Measurement of the Proton's Weak Charge. *ArXiv e-prints*, 1202.1255, February 2012.

[24] T.M. Ito et al. Parity violating electron deuteron scattering and the proton's neutral weak axial vector form-factor. *Phys.Rev.Lett.*, 92:102003, 2004.

[25] F.E. Maas et al. Measurement of strange quark contributions to the nucleon's form-factors at Q**2 = 0.230-(GeV/c)**2. *Phys.Rev.Lett.*, 93:022002, 2004.

[26] F.E. Maas et al. Evidence for strange quark contributions to the nucleon's form-factors at q**2 = 0.108 (GeV/c)**2. *Phys.Rev.Lett.*, 94:152001, 2005.

[27] K.A. Aniol et al. Parity-violating electron scattering from He-4 and the strange electric form-factor of the nucleon. *Phys.Rev.Lett.*, 96:022003, 2006.

[28] K.A. Aniol et al. Constraints on the nucleon strange form factors at. *Physics Letters B*, 635(56):275 – 279, 2006.

[29] D. Armstrong et al. Strange quark contributions to parity-violating asymmetries in the forward G0 electron-proton scattering experiment. *Phys.Rev.Lett.*, 95:092001, 2005.

[30] Juliette Mammei. The MOLLER Experiment. *Nuovo Cim.*, C035N04:203–208, 2012.

[31] M.J. Musolf et al. Intermediate-energy semileptonic probes of the hadronic neutral current. *Physics Reports*, 239(12):1 – 178, 1994.

[32] T. W. Donnelly, J. Dubach, and Ingo Sick. Determination of the neutron electric form factor from ^{1}H($\vec{e}$,e)^{1}H. *Phys. Rev. C*, 37:2320–2325, Jun 1988.

[33] D.T Spayde et al. The strange quark contribution to the proton's magnetic moment. *Physics Letters B*, 583(12):79 – 86, 2004.

[34] A. Acha et al. Precision Measurements of the Nucleon Strange Form Factors at Q**2 0.1-GeV**2. *Phys.Rev.Lett.*, 98:032301, 2007.

[35] Ross Young et al. Extracting nucleon strange and anapole form factors from world data. *Phys.Rev.Lett.*, 97:102002, 2006.

[36] Ross Young et al. Testing the Standard Model by precision measurement of the weak charges of quarks. *Phys.Rev.Lett.*, 99:122003, 2007.

[37] S. Galster et al. Elastic electron-deuteron scattering and the electric neutron form factor at four-momentum transfers $5fm^{-2} < q^2 < 14fm^{-2}$. *Nuclear Physics B*, 32(1):221 – 237, 1971.

[38] P.G. Blunden, W. Melnitchouk, and A.W. Thomas. New formulation of gamma-Z box corrections to the weak charge of the proton. *Phys.Rev.Lett.*, 107:081801, 2011.

[39] Jens Erler, Andriy Kurylov, and Michael J Ramsey-Musolf. The Weak charge of the proton and new physics. *Phys.Rev.*, D68:016006, 2003.

[40] J. Beringer et al. Review of particle physics. *Phys. Rev. D*, 86:010001, Jul 2012.

[41] Jens Erler and Michael J. Ramsey-Musolf. Weak mixing angle at low energies. *Phys. Rev. D*, 72:073003, Oct 2005.

[42] P.L. Anthony et al. Precision measurement of the weak mixing angle in Moller scattering. *Phys.Rev.Lett.*, 95:081601, 2005.

[43] G.P. Zeller et al. A Precise Determination of Electroweak Parameters in Neutrino Nucleon Scattering. *Phys.Rev.Lett.*, 88:091802, 2002.

[44] W. J. Marciano and A. Sirlin. Radiative corrections to atomic parity violation. *Phys. Rev. D*, 27:552–556, Feb 1983.

[45] W. J. Marciano and A. Sirlin. Some general properties of the $o(\alpha)$ corrections to parity violation in atoms. *Phys. Rev. D*, 29:75–88, Jan 1984.

[46] A. Sibirtsev et al. gamma-Z corrections to forward-angle parity-violating e-p scattering. *Phys.Rev.*, D82:013011, 2010.

[47] M. Gorchtein and C.J. Horowitz. Dispersion gamma Z-box correction to the weak charge of the proton. *Phys.Rev.Lett.*, 102:091806, 2009.

[48] Mikhail Gorchtein, C.J. Horowitz, and Michael J. Ramsey-Musolf. Model-dependence of the γZ dispersion correction to the parity-violating asymmetry in elastic *ep* scattering. *Phys.Rev.*, C84:015502, 2011.

[49] Benjamin C. Rislow and Carl E. Carlson. Contributions from γZ box diagrams to parity violating elastic *ep* scattering. *Phys.Rev.*, D83:113007, 2011.

[50] S.C. Bennett and Carl E. Wieman. Measurement of the 6S $\rightarrow$ 7S transition polarizability in atomic cesium and an improved test of the Standard Model. *Phys.Rev.Lett.*, 82:2484–2487, 1999.

[51] S.G. Porsev, K. Beloy, and A. Derevianko. Precision determination of weak charge of ^{133}Cs from atomic parity violation. *Phys.Rev.*, D82:036008, 2010.

[52] Qweak Collaboration. Qweak Image Repository. https://qweak.jlab.org/private/gallery/index.html, 2012.

[53] K. Paschke. Controlling helicity-correlated beam asymmetries in a polarized electron source. *The European Physical Journal A - Hadrons and Nuclei*, 32:549–553, 2007.

[54] Christoph W. Leemann et al. THE CONTINUOUS ELECTRON BEAM ACCELERATOR FACILITY: CEBAF at the Jefferson Laboratory. *Annual Review of Nuclear and Particle Science*, 51(1):413–450, 2001.

[55] Y. C. Chao et al. CEBAF accelerator achievements. *J. Phys. Conf. Ser.*, 299:012015, 2011.

[56] P.A. Adderley et al. Two Wien Filter Spin Flipper. *Conf.Proc.*, C110328:862–864, 2011.

[57] J. M. Grames et al. Unique electron polarimeter analyzing power comparison and precision spin-based energy measurement. *Phys. Rev. ST Accel. Beams*, 7(4):042802, Apr 2004.

[58] Katherine Myers. *The First Determination of the Proton's Weak Charge Through Parity-Violating Asymmetry Measurements in Elastic e+p and e+Al Scattering.* PhD thesis, The George Washington University, 2012.

[59] Buddhini Waidyawansa. Beam Position and Angle Determination in Qweak. *Qweak Document Database*, (Qweak-doc-1772-v2), 2012.

[60] D. Armstrong et al. Qweak Jeopardy Proposal: E05-008. *Qweak Document Database*, (Qweak-doc-190-v1), 2004.

[61] Gregory Smith et al. Qweak Liquid Hydrogen Target: Preliminary Design and Safety Document. *Qweak Document Database*, (Qweak-doc-1041-v2), 2009.

[62] Gregory Smith. Qweak Target Measured Performance. *Qweak Document Database*, (Qweak-doc-1679-v1), 2012.

[63] Jiawei Mei. Target Boiling. *Qweak Document Database*, (Qweak-doc-1407-v2), 2011.

[64] David Mack. A Quartz Cerenkov Detector: How Complicated Could That Be. *Qweak Document Database*, (Qweak-doc-0006-v1), 2002.

[65] Peiqing Wang. *A Measurement Of The Proton's Weak Charge Using An Integration Cerenkov Detector System.* PhD thesis, University of Manitoba, 2012.

[66] David Mack. Non-linearity Specification for the Qweak Detector Chain. *Qweak Document Database*, (Qweak-doc-172-v1), 2005.

[67] Buddhini Waidyawansa. Studying the Effects of Delayed Helicity. *Qweak Document Database*, (Qweak-doc-1180-v1), 2010.

[68] John D. Leacock II. *Measuring the Weak Charge of the Proton and the Hadronic Parity Violation of the* $N \rightarrow \Delta$ *Transition.* PhD thesis, Virginia Polytechnic Institute and State University, 2012.

[69] Klaus H. Grimm. The Qweak tracking system. *The European Physical Journal A - Hadrons and Nuclei*, 24:159–160, 2005.

[70] Jlab DAQ Group. CODA Manual. https://coda.jlab.org/wiki/index.php/Main_Page, 2012.

[71] P. Banta et al. The Front end readout control software for the CODA data acquisition toolkit. *INSPIRE-445926*, 1997.

[72] W.G. Heyes et al. A distributed object-oriented control system for the CODA data acquisition system. 1997.

[73] Bill Roberts. Users' manual for the TRIUMF 8-channel VME digital integrator. *Qweak Document Database*, (Qweak-doc-693-v1), 2007.

[74] Buddhini Waidyawansa. *to-be published*. PhD thesis, Ohio University, 2013.

[75] Des Ramsey. Current Mode Electronics for the Qweak Experiment. *Qweak Document Database*, (Qweak-doc-552-v1), 2006.

[76] G. Braun et al. F1: An Eight channel time to digital converter chip for high rate experiments. 1999.

[77] Jeong Han Lee. F1TDC and its Multihit Histograms. *Qweak Document Database*, (Qweak-doc-1604-v2), 2012.

[78] Rakitha Beminiwattha. Qweak Software Framework; Track Decoding Framework. *Qweak Document Database*, (Qweak-doc-1124-v1), 2009.

[79] Wouter Deconinck. Qweak Tracking Software. *Qweak Document Database*, (Qweak-doc-1094-v2), 2009.

[80] Rakitha Beminiwattha. Qweak Track Decoder Framework. *Qweak Document Database*, (Qweak-doc-951-v2), 2009.

[81] Philippe Pebay. Formulas for robust, one-pass parallel computation of covariances and arbitrary-order statistical moments. Technical report, SAND2008-6212, Sandia National Laboratories: http://infoserve.sandia.gov/sand_doc/2008/086212.pdf, 2008.

[82] Jan Balewski. Toy model of 6 dimensional linear regression. *Qweak Document Database*, (Qweak-doc-1294-v2), 2010.

[83] Jan Balewski. Complete set of formulas for the linear regression analysis. *Qweak Document Database*, (Qweak-doc-1317-v2), 2010.

[84] Rakitha Beminiwattha. Qweak Event Cut Framework. *Qweak Document Database*, (Qweak-doc-1682-v1), 2012.

[85] Scott MacEwan. Run2Pass1 Dependence on Regression Schemes. *Qweak Document Database*, (Qweak-doc-1584-v1), 2012.

[86] T. B. Humensky et al. SLAC's polarized electron source laser system and minimization of electron beam helicity correlations for the E-158 parity violation experiment. *Nucl. Instrum. Meth.*, A521:261–298, 2004.

[87] M. Hauger et al. A High precision polarimeter. *Nucl.Instrum.Meth.*, A462:382–392, 2001.

[88] Joseph Michael Grames. *Measurement of A Weak Polarization Sensitivity to the Beam Orbit of the CEBAF Accelerator*. PhD thesis, University of Illinois at Urbana-Champaign, 2000.

[89] Morris L. Swartz. PHYSICS WITH POLARIZED ELECTRON BEAMS. *Conf.Proc.*, C8708101:83–131, 1987.

[90] Loppacher, M. *Møller Polarimetry for CEBAF Hall C*. PhD thesis, University of Basel, 1996.

[91] David Gaskell. Moller measurement and beam polarization for Qweak Wien-0. *Qweak Electronic Logbook*, (moller-109), 2012.

[92] Scott MacEvan. Using a modified root script written by author.

[93] David Mack. Private communication. During Wien0 analysis.

[94] David Mack. Beam Current Normalization Issues, Part I. *Qweak Document Database*, (Qweak-doc-1354-v1), 2011.

[95] Manolis Kargiantoulakis. 25% data quality checks: BPMs . *Qweak Electronic Logbook*, (analysis-635), 2012.

[96] Donald Jones. Official wien 0 (slugs 32-40) charge and position asymmetries (weighted by 1/mdallbarserror^2). *Qweak Electronic Logbook*, (analysis-741), 2012.

[97] Rakitha Beminiwattha. PITA/IA Scan - Charge Asymmetry and MD Non-linearity . *Qweak Electronic Logbook*, (analysis-360), 2011.

[98] Rakitha Beminiwattha. PITA/IA Scan - Helicity Correlated Position Differences. *Qweak Electronic Logbook*, (analysis-361), 2011.

[99] David Mack. Pass 5 Wien 0 Regression Systematics. *Qweak Document Database*, (Qweak-doc-1718-v1), 2012.

[100] Donald Jones. Asymmetry dependence on monitor cuts. *Qweak Electronic Logbook*, (analysis-805), 2012.

[101] David Mack. Thoughts on Don's and Martin's cut dependence studies. *Qweak Electronic Logbook*, (analysis-831), 2012.

[102] Kent Paschke. Beam Corrections. *Qweak Document Database*, (Qweak-doc-1718-v1), 2012.

[103] Kent Paschke. regression error. *Qweak Electronic Logbook*, (analysis-772), 2012.

[104] Manolis Kargiantoulakis. Effect of regression on large Aq runs . *Qweak Electronic Logbook*, (analysis-623), 2012.

[105] Wade Duvall. [Wien 0] Charge asymmetry sensitivites by runlet . *Qweak Electronic Logbook*, (analysis-637), 2012.

[106] Wade Duvall. [Wien 0] Charge slopes vs current . *Qweak Electronic Logbook*, (analysis-644), 2012.

[107] Buddhini Waidyawansa. Preliminary results from the transverse measurement done on February 2011. *Qweak Document Database*, (Qweak-doc-1401-v4), 2012.

[108] Buddhini Waidyawansa. Transverse uncertainty for 25% Qweak. *Qweak Electronic Logbook*, (analysis-758), 2012.

[109] Paul King. Blinding offset as used for Wien0. *Qweak Electronic Logbook*, (analysis-795), 2012.

[110] Katherine Myers. [Aluminum] Pass5 Round1 Asymmetry for Wien 0 Aluminum Including Systematics . *Qweak Electronic Logbook*, (analysis-743), 2012.

[111] David Mack. Input file v3(frozen!) for Wien0 4is BEFORE radiative corrections) . *Qweak Electronic Logbook*, (analysis-753), 2012.

[112] Katherine Myers. [Aluminum] Radiatively Corrected Asymmetry for Wien0 Pass5 Aluminum. *Qweak Electronic Logbook*, (analysis-748), 2012.

[113] Josh Magee. Corrected 25% Aluminum Dilution . *Qweak Electronic Logbook*, (analysis-748), 2012.

[114] Adesh Subedi. QWGEANT 3 simulations of rates & inelastic dilution factor. *Qweak Electronic Logbook*, (analysis-451), 2011.

[115] Rakitha Beminiwattha. The Total Neutral Background Dilution Results. *Qweak Document Database*, (Qweak-doc-1741-v1), 2012.

[116] Rakitha Beminiwattha. Main Detector Neutral Background Contribution. *Qweak Document Database*, (Qweak-doc-1549-v1), 2012.

[117] Wade S Duvall. W-shutter studies in run 2. *Qweak Document Database*, (Qweak-doc-1748-v1), 2012.

[118] Kent Paschke. proposed Wien0 neutral beamline background correction. *Qweak Electronic Logbook*, (analysis-782), 2012.

[119] David Mack. Wien0 Beamline Background Dilution Central Value and Uncertainty. *Qweak Electronic Logbook*, (analysis-784), 2012.

[120] Mark Pitt. Suggested Prescription for Quoting EM RadCorr/Light Weighting/Q2. *Qweak Document Database*, (Qweak-doc-1724-v1), 2012.

[121] Adesh Subedi. Official EM radiative correction for the Wien0 Hydrogen elastic asymmetry . *Qweak Electronic Logbook*, (analysis-769), 2012.

[122] Valerie Gray and Wouter Deconinck. Light-yield weighting effects on asymmetry . *Qweak Electronic Logbook*, (analysis-765), 2012.

[123] Mark Pitt. "Effective Kinematics" and Acceptance Correction for Wien 0 Hydrogen Result . *Qweak Electronic Logbook*, (analysis-794), 2012.

[124] K.A. Aniol et al. Parity violating electroweak asymmetry in polarized-e p scattering. *Phys.Rev.*, C69:065501, 2004.

[125] NSAC. The Frontiers of Nuclear Science, A Long Range Plan. *arXiv:0809.3137*, 2008.

[126] P. Bosted et al. Precision measurement of parity-violation in deep inelastic scattering over a broad kinematic range. Technical report, Jefferson-Lab proposal PR-09-012 (http://hallaweb.jlab.org/collab/PAC/PAC34/PR-09-012-pvdis), 2009.

[127] J. Alcorn et al. Basic Instrumentation for Hall A at Jefferson Lab. *Nucl.Instrum.Meth.*, A522:294–346, 2004.

[128] Buddhini Waidyawansa. Noise Levels of Battery sources Using the Qweak Cable Runs and Parity DAQ. *Qweak Document Database*, (Qweak-doc-1192-v2), 2010.

[129] Paul King. TRIUMF Integrators. *Qweak Document Database*, (Qweak-doc-727-v1), 2008.

[130] Rakitha Beminiwattha. DAQ Dead-time Correction to the Neutral Background Fraction, N_f . *Qweak Electronic Logbook*, (analysis-543), 2012.

[131] Rakitha Beminiwattha. Qweak Tracking DAQ Implementation. *Qweak Document Database*, (Qweak-doc-1328-v1), 2010.

[132] Mark Pitt and Wade Duvall. Beamline background asymmetry for Wien 0 analysis - followup. *Qweak Electronic Logbook*, (analysis-782), 2012.

[133] Wade Duvall. [W-shutter] Fractional yields in blocked MD's in 'good' halo conditions. *Qweak Electronic Logbook*, (analysis-779), 2012.

[134] Valerie Gray. Light weighting: a Quick look. *Qweak Electronic Logbook*, (tracking-125), 2012.

Appendix A: Physics Derivations Supplemental

This appendix will discuss more details related to SM derivations and computations.

A.1 A Supplement to the Physics Formalism

The hadronic states of the proton are dominated by lightest quarks (u,d, and s quarks) at the energies Q_{weak} experiment is carried out. Therefore heavier quarks are neglected and hadronic current are represented using SU(3) octet and singlet currents [31]. With the assumed SU(3) isospin symmetry, the hadronic current operators are decomposed using SU(3) octet and singlet operators:

$$\hat{V}_{\mu}^{(a)} \equiv \bar{q}\frac{1}{2}\lambda^{a}\gamma_{\mu}q, \quad q \equiv \begin{pmatrix} u \\ d \\ s \end{pmatrix} \tag{A.1}$$

where λ^{a} are the Gell-Mann matrices. The 3^{rd} and 8^{8th} matrices are related to the electromagnetic (EM) isoscalar($T = 0$) and isovector currents ($T = 1$) [31]. The currents are defined as,

$$\hat{J}_{\mu}^{EM}(T = 1) = \hat{V}_{\mu}^{(3)}, \quad \hat{J}_{\mu}^{EM}(T = 0) = \frac{1}{\sqrt{3}}\hat{V}_{\mu}^{(0)} \tag{A.2}$$

where,

$$\hat{V}_{\mu}^{(3)} = \frac{1}{2}(\bar{u}\gamma_{\mu}u - \bar{d}\gamma_{\mu}d), \quad \hat{V}_{\mu}^{(8)} = \frac{1}{2\sqrt{3}}(\bar{u}\gamma_{\mu}u + \bar{d}\gamma_{\mu}d - 2\bar{s}\gamma_{\mu}s) \tag{A.3}$$

The hadronic electroweak currents can be represented using EM isoscalar($T = 0$) and isovector currents ($T = 1$). The neutral vector hadronic current (using equation 2.5 and equation A.2),

$$\hat{J}_{\mu}^{NC} = \xi_{V}^{T=1}\hat{J}_{\mu}^{EM}(T = 1) \; + \; \sqrt{3}\xi_{V}^{T=0}\hat{J}_{\mu}^{EM}(T = 0) \; + \xi_{V}^{(0)}\bar{s}\gamma_{\mu}s \tag{A.4}$$

where the iso-scalar charge are defined(Table A.1),

$$\xi_{\rm V}^{\rm T=1} = ({\rm g_v^u} - {\rm g_v^d}), \quad \xi_{\rm V}^{\rm T=0} = \sqrt{3}({\rm g_v^u} + {\rm g_v^d}), \quad \xi_{\rm V}^{(0)} = ({\rm g_v^u} + {\rm g_v^d} + {\rm g_v^s}) \tag{A.5}$$

Table A.1: Hadronic weak neutral coupling (charges)

Coupling	Standard Model (tree-level)
$\xi_{\rm V}^{(0)}$	-1
$\sqrt{3}\xi_{\rm V}^{\rm T=0}$	$-4\sin^2\theta_{\rm w}$
$\xi_{\rm V}^{\rm T=1}$	$2(1-2\sin^2\theta_{\rm w})$

The lepton-nucleons scattering PV asymmetry is dominated by the interferences of $\rm M^{EM}$ and $\rm M^{PV}$ amplitudes defined in equations 2.1 and 2.3. The asymmetry is defined as,

$$\begin{aligned} {\rm A_{LR}} &\propto \frac{{\rm M^{EM}} \cdot {\rm M^{PV}}}{|({\rm M^{EM}})^2|} \\ &= \frac{\dfrac{{\rm d}\sigma^{\rm R}}{{\rm d}\Omega} - \dfrac{{\rm d}\sigma^{\rm L}}{{\rm d}\Omega}}{\dfrac{{\rm d}\sigma^{\rm R}}{{\rm d}\Omega} + \dfrac{{\rm d}\sigma^{\rm L}}{{\rm d}\Omega}} \\ &\equiv {\rm A_{LR}^0} \frac{{\rm W^{(PV)}}({\rm q},\theta)}{{\rm F_p^2}({\rm q},\theta)} \end{aligned} \tag{A.6}$$

where $\frac{{\rm d}\sigma^{\rm R/L}}{{\rm d}\Omega}$ are the total differential cross sections, $\rm W^{(PV)}(q,\theta)$ is the PV response of the scattering amplitude [31], $\rm F_p^2(q,\theta)$ is the total EM response of the scattering amplitude [31], and $\rm A_{LR}^0$ is defined below,

$$\rm A_{LR}^0 = \frac{G_f|Q^2|}{2\pi\alpha\sqrt{2}} \tag{A.7}$$

where the $\rm G_F$ is the Fermi constant and α is the fine structure constant. The angle θ is replaced with the quantity ε,

$$\varepsilon \equiv \frac{1}{1+2(1+\tau)\tan^2\frac{\theta}{2}} \tag{A.8}$$

where $\tau = \mathrm{Q}^2/4\mathrm{M}^2$. The elastic electron-proton scattering PV asymmetry can be defined [31] in terms of the quantities ε and τ,

$$\mathrm{A_{LR}}(\vec{\mathrm{e}}\mathrm{p}) = \mathrm{A^0_{LR}}\frac{\mathrm{W^{(PV)}}(\tau,\varepsilon)}{\mathrm{F^2_p}(\tau,\varepsilon)} \tag{A.9}$$

The $\mathrm{F^2_p}$ and $\mathrm{W^{(PV)}}$ are expressed using electric and magnetic Sachs form factors which are only functions of τ [31] [32],

$$\mathrm{F^2_p}(\tau,\varepsilon) = \frac{\varepsilon \mathrm{G^p_E}(\tau)^2 + \tau \mathrm{G^p_M}(\tau)^2}{\varepsilon(1+\tau)} \tag{A.10}$$

$$\mathrm{W^{(PV)}}(\tau,\varepsilon) = \frac{-[\mathrm{g^e_A}(\varepsilon \mathrm{G^p_E}(\tau)\tilde{\mathrm{G}}^{\mathrm{p}}_{\mathrm{E}}(\tau) + \tau \mathrm{G^p_M}(\tau)\tilde{\mathrm{G}}^{\mathrm{p}}_{\mathrm{M}}(\tau)) + \mathrm{g^e_V}\sqrt{1-\varepsilon^2}\sqrt{\tau(1+\tau)}\mathrm{G^p_M}(\tau)\tilde{\mathrm{G}}^{\mathrm{p}}_{\mathrm{A}}(\tau)]}{2\varepsilon(1+\tau)} \tag{A.11}$$

where $\mathrm{G^P_E}(\tau)/\mathrm{G^P_M}(\tau)$ are proton form factors of the electromagnetic hadronic current, $\tilde{\mathrm{G}}^{\mathrm{P}}_{\mathrm{E}}(\tau)/\tilde{\mathrm{G}}^{\mathrm{P}}_{\mathrm{M}}(\tau)$ are proton form factors of the weak neutral hadronic vector current, $\tilde{\mathrm{G}}^{\mathrm{P}}_{\mathrm{A}}(\tau)$ is the proton form factor of the weak neutral hadronic axial-vector current.

By following the neutral vector hadronic current definition (equation A.4), the form factors for the weak neutral hadronic vector current can be defined,

$$\begin{aligned}
\tilde{\mathrm{G}}^{\mathrm{P}}_{\mathrm{E}}(\tau) &= \xi_{\mathrm{V}}^{\mathrm{T}=1}\mathrm{G}_{\mathrm{E}}^{(\mathrm{T}=1)}(\tau) \;+\; \sqrt{3}\xi_{\mathrm{V}}^{\mathrm{T}=0}\mathrm{G}_{\mathrm{E}}^{(\mathrm{T}=0)}(\tau) + \xi_{\mathrm{V}}^{(0)}\mathrm{G}_{\mathrm{E}}^{(\mathrm{s})}(\tau) \\
\tilde{\mathrm{G}}^{\mathrm{P}}_{\mathrm{M}}(\tau) &= \xi_{\mathrm{V}}^{\mathrm{T}=1}\mathrm{G}_{\mathrm{M}}^{(\mathrm{T}=1)}(\tau) \;+\; \sqrt{3}\xi_{\mathrm{V}}^{\mathrm{T}=0}\mathrm{G}_{\mathrm{M}}^{(\mathrm{T}=0)}(\tau) + \xi_{\mathrm{V}}^{(0)}\mathrm{G}_{\mathrm{M}}^{(\mathrm{s})}(\tau)
\end{aligned} \tag{A.12}$$

Now the isoscalar and isovector form factors can be represented using nucleon form factors assuming nucleons are eigenstates of isospin [31],

$$G_E^{(T=1)}(\tau) = \frac{1}{2}(G_E^p(\tau) - G_E^n(\tau)), \quad G_E^{(T=0)}(\tau) = \frac{1}{2}(G_E^p(\tau) + G_E^n(\tau))$$
$$G_M^{(T=1)}(\tau) = \frac{1}{2}(G_M^p(\tau) - G_M^n(\tau)), \quad G_M^{(T=0)}(\tau) = \frac{1}{2}(G_M^p(\tau) + G_M^n(\tau)) \tag{A.13}$$

where $\mathrm{G_E^p}(\tau)/\mathrm{G_M^p}(\tau)$ are EM Sachs form factors of the proton and $\mathrm{G_E^n}(\tau)/\mathrm{G_M^n}(\tau)$ are EM Sachs form factors of the neutron. The weak charges of the proton and neutron can be defined using the SM predictions for weak vector, and weak axial-vector charges (coupling constants) quarks (defined in Table 2.1),

$$\mathrm{Q_W^p} = 2\mathrm{g_V^u} + \mathrm{g_V^d}, \quad \mathrm{Q_W^n} = 2\mathrm{g_V^d} + \mathrm{g_V^u} \tag{A.14}$$

Now the $\xi_{\mathrm{V}}^{\mathrm{T=1}}$ and $\xi_{\mathrm{V}}^{\mathrm{T=0}}$ charges can be represented using $\mathrm{Q_W^p}$ and $\mathrm{Q_W^n}$,

$$\xi_{\mathrm{V}}^{\mathrm{T=1}} = (\mathrm{Q_W^p} - \mathrm{Q_W^n}), \quad \sqrt{3}\xi_{\mathrm{V}}^{\mathrm{T=0}} = (\mathrm{Q_W^p} + \mathrm{Q_W^n}) \tag{A.15}$$

using the result obtained in equations A.15 and A.12, the $\mathrm{W^{(PV)}}$ (equation A.11) is rewritten in terms of EM Sachs form factors of the proton and neutron, and weak charges of proton and neutron.

$$\mathrm{W^{(PV)}}(\tau,\varepsilon) =$$
$$-\frac{1}{2\varepsilon(1+\tau)}\Big[\mathrm{g_A^e}\big(\ \mathrm{Q_W^p}[\varepsilon \mathrm{G_E^p}(\tau)^2 + \tau \mathrm{G_M^p}(\tau)^2] + \varepsilon \mathrm{G_E^p}(\tau)[\mathrm{Q_W^n G_E^n}(\tau) + \xi_{\mathrm{V}}^{(0)}\mathrm{G_E^{(s)}}(\tau)] +$$
$$\tau \mathrm{G_M^p}(\tau)[\mathrm{Q_W^n G_M^n}(\tau) + \xi_{\mathrm{V}}^{(0)}\mathrm{G_M^{(s)}}(\tau)]\ \big)\ + \mathrm{g_V^e}\sqrt{1-\varepsilon^2}\sqrt{\tau(1+\tau)}\mathrm{G_M^p}(\tau)\tilde{\mathrm{G}}_{\mathrm{A}}^{\mathrm{p}}(\tau)\Big] \tag{A.16}$$

The PV asymmetry (equation A.9) can be represented in terms of EM Sachs form factors of the proton and neutron, and axial-vector weak form factors ($G_{E/M}^{(s)}$)

$$A_{LR}(\tilde{e}p) = -\frac{1}{2}A_{LR}^{0}\Bigg[Q_{W}^{p} + \frac{\varepsilon G_{E}^{p}(\tau)[Q_{W}^{n}G_{E}^{n}(\tau) + \xi_{V}^{(0)}G_{E}^{(s)}(\tau)] + \tau G_{M}^{p}(\tau)[Q_{W}^{n}G_{M}^{n}(\tau) + \xi_{V}^{(0)}G_{M}^{(s)}(\tau)]}{\varepsilon G_{E}^{p}(\tau)^{2} + \tau G_{M}^{p}(\tau)^{2}} - (1 - 4\sin^{2}\theta_{W})\frac{\sqrt{1-\varepsilon^{2}}\sqrt{\tau(1+\tau)}G_{M}^{p}(\tau)\tilde{G}_{A}^{p}(\tau)}{\varepsilon G_{E}^{p}(\tau)^{2} + \tau G_{M}^{p}(\tau)^{2}}\Bigg] \tag{A.17}$$

For the forward angle scattering ($\theta \to 0$) and as $Q^2 \to 0$, the $\varepsilon \to 1$ and $\tau << 1$. Under these constraints, the axial-vector contribution has become negligible and the leading contribution of the PV asymmetry is the weak charge of the proton ($Q_{W}^{p} = 1 - \sin^{2}\theta_{W}$ at tree level) and remaining contribution is related to proton, neutron, and strange quark EM form factors.

$$A_{LR}(\tilde{e}p) = -\frac{1}{2}A_{LR}^{0}\Bigg[Q_{W}^{p} + \frac{G_{E}^{p}(\tau)[Q_{W}^{n}G_{E}^{n}(\tau) + \xi_{V}^{(0)}G_{E}^{(s)}(\tau)] + \tau G_{M}^{p}(\tau)[Q_{W}^{n}G_{M}^{n}(\tau) + \xi_{V}^{(0)}G_{M}^{(s)}(\tau)]}{G_{E}^{p}(\tau)^{2} + \tau G_{M}^{p}(\tau)^{2}}\Bigg] \tag{A.18}$$

The Q^2 dependence of the Sachs form factors are known from unpolarized electron scattering experiments [37].

A.2 Elastic ep Asymmetry SM Prediction at $Q^2 \sim 0.03$ Gev^2

SM prediction of the PV asymmetry can be represented in terms of EM Sachs form factors of the proton and neutron, and axial-vector weak form factors ($G_{E/M}^{(s)}$),

$$A_{LR}(\tilde{e}p) = -\frac{1}{2}A^0_{LR}\Bigg[Q^p_W + \frac{Q^n_W[\varepsilon G^p_E(\tau)G^n_E(\tau) + \tau G^p_M(\tau)G^n_M(\tau)]}{\varepsilon G^p_E(\tau)^2 + \tau G^p_M(\tau)^2} + \frac{\xi^{(0)}_V[\varepsilon G^p_E(\tau)G^{(s)}_E(\tau) + \tau G^p_M(\tau)G^{(s)}_M(\tau)]}{\varepsilon G^p_E(\tau)^2 + \tau G^p_M(\tau)^2} + Q^e_W\frac{\sqrt{1-\varepsilon^2}\sqrt{\tau(1+\tau)}G^p_M(\tau)\tilde{G}^p_A(\tau)}{\varepsilon G^p_E(\tau)^2 + \tau G^p_M(\tau)^2}\Bigg] \tag{A.19}$$

where $Q^e_W = -(1 - 4\sin^2\theta_W)$ at tree-level. For the forward angle scattering ($\theta \to 0$) and as $Q^2 \to 0$, the $\varepsilon \to 1$ and $\tau << 1$. Assume $G^{(s)}_{E/M}(\tau) \sim 0$

$$A_{LR}(\tilde{e}p) = -\frac{1}{2}A^0_{LR}\Bigg[Q^p_W + \frac{Q^n_W[\varepsilon G^p_E(\tau)G^n_E(\tau) + \tau G^p_M(\tau)G^n_M(\tau)]}{\varepsilon G^p_E(\tau)^2 + \tau G^p_M(\tau)^2} + Q^e_W\frac{\sqrt{1-\varepsilon^2}\sqrt{\tau(1+\tau)}G^p_M(\tau)\tilde{G}^p_A(\tau)}{\varepsilon G^p_E(\tau)^2 + \tau G^p_M(\tau)^2}\Bigg] \tag{A.20}$$

The Q^2 dependance of the Sachs form factors are known from unpolarized electron scattering experiments [37].

$$G^p_E(\tau) = G^V_D(\tau), \quad G^n_E(\tau) = \frac{-\mu_n G^V_D(\tau)}{1 + 5.6\tau}\cdot\tau$$
$$G^p_M(\tau) = \mu_p G^V_D(\tau), \quad G^n_M(\tau) = \mu_n G^V_D(\tau) \tag{A.21}$$

where $\mu_p = 2.79$ and $\mu_n = -1.91$ are magnetic moments of the proton and neutron, respectively. The form factors are described by a dipole function,

$$G^V_D(\tau) = \frac{1}{(1 + 4.97\tau)^2} \tag{A.22}$$

The axial-vector current form factor $\tilde{G}^p_A(\tau)$ can be represented using SU(3) hadronic current definition (Following equation 3.17 and 3.31b in [31])

$$\tilde{G}^p_A(\tau) = \xi^{T=1}_A G^{(3)}_A(\tau) + \xi^{T=0}_A G^{(8)}_A(\tau) + \xi^{(0)}_A G^{(s)}_A(\tau) \tag{A.23}$$

and coupling coefficients (Table 3.2 [31])

$$\xi_{\rm A}^{\rm T=1} = -2(1 + {\rm R_A^{T=1}}) \tag{A.24}$$

where ${\rm R_A^{T=1}} = -0.34$ is higher order radiative correction term, at tree level this is zero (Table 3.3 [31])

$$\xi_{\rm A}^{\rm T=0} = \sqrt{3}{\rm R_A^{T=0}} \tag{A.25}$$

where $\sqrt{3}{\rm R_A^{T=0}} = -0.62$ is higher order radiative correction term , at tree level this is zero (Table 3.3 [31])

$$\xi_{\rm A}^{(0)} = 1 + {\rm R_A^{(0)}} \tag{A.26}$$

where ${\rm R_A^{(0)}}$ is higher order electroweak correction term , at tree level this is zero (equation 3.19c [31]). Assume ${\rm G_A^{(s)}}(\tau) \sim 0$ and ${\rm G_A^{(8)}}(\tau) \sim 0$ and parameterize using a dipole form factor term (equation 3.43, 3.44, and 3.45 [31]),

$$\tilde{\rm G}_{\rm A}^{\rm p}(\tau) = \xi_{\rm A}^{\rm T=1}{\rm G_A^{(3)}}(0){\rm G_D^A}(\tau) \tag{A.27}$$

where ${\rm G_A^{(3)}}(0) = 1.262/2$ (From equation3.43a [31]) and the dipole term ${\rm G_D^A}(\tau) = (1 + \lambda_{\rm D}^{\rm A}\tau)^{-2}$ and $\lambda_{\rm D}^{\rm A} = 3.32^{+0.24}_{-0.22}$ (From equation3.45 [31]). Now using the eqaution A.20, the SM prediction for the ${\rm A_{LR}}(\tilde{\rm e}{\rm p})$ is calculated. All the necessary inputs for this calculation are discussed so far and the following results is based on the ${\rm Q_W^p} = 0.0705 \pm 0.0008$ (see Section A.3). The SM prediction for the ${\rm A_{LR}}(\tilde{\rm e}{\rm p})$ contains weak charge and hadronic contributions,

$${\rm A_{LR}}(\tilde{\rm e}{\rm p}) = {\rm A_{Qwp}} \ + \ {\rm A_{Total\_Hadronic}} \tag{A.28}$$

where ${\rm A_{Qwp}}$ is the contribution from the weak charge of the proton and ${\rm A_{Total\_Hadronic}}$ is the contribution from EM and axial form factors.

$$\begin{aligned} A_{Qwp} &= -\frac{1}{2}A^0_{LR} \cdot Q^p_W \\ &= -0.1584 \pm 0.0018 \text{ ppm} \end{aligned} \tag{A.29}$$

and

$$\begin{aligned} A_{Total\_Hadronic} = -\frac{1}{2}A^0_{LR}\Bigg[&\frac{Q^n_W[\varepsilon G^p_E(\tau)G^n_E(\tau) + \tau G^p_M(\tau)G^n_M(\tau)]}{\varepsilon G^p_E(\tau)^2 + \tau G^p_M(\tau)^2} + \\ &Q^e_W \frac{\sqrt{1-\varepsilon^2}\sqrt{\tau(1+\tau)}G^p_M(\tau)\tilde{G}^p_A(\tau)}{\varepsilon G^p_E(\tau)^2 + \tau G^p_M(\tau)^2}\Bigg] \\ = -0.0558 \pm 0.0024 \text{ ppm} \end{aligned} \tag{A.30}$$

Finally the SM prediction is,

$$A_{LR}(\tilde{e}p) = -0.2142 \pm 0.0030 \text{ ppm} \tag{A.31}$$

A.2.1 Error Estimation for the $A_{LR}(\tilde{e}p)$

The expected relative error on the hadronic contribution ($A_{Total\_Hadronic}$) from the Q_{weak} latest specifications is 1.5%.

$$\left.\frac{\delta A_{LR}(\tilde{e}p)}{A_{LR}(\tilde{e}p)}\right|_{A_{Total\_Hadronic}} = \frac{\delta A_{Total\_Hadronic}}{A_{LR}(\tilde{e}p)} = 1.5\% \tag{A.32}$$

and I assigned a scaled Q^p_W error bar to the A_{Qwp}.

A.3 Update on Weak Charge of the Proton

The Q^p_W from [41] has no up-to date $\Box_{\gamma Z}(0)$ correction

$$Q^p_W = 0.0713 \pm 0.0008 \tag{A.33}$$

This result is an update to the $Q^p_W = 0.0716 \pm 0.0008$ from the reference [39]. The change in the results is related to the weak mixing angle value in the updated analysis.

The $\Box_{\gamma Z}(E)$ correction in the updated result (equation A.36) is the $\Box_{\gamma Z}(E = 0)$ value obtained by following the Marciano formulation [38]. This correction is assumed to be energy independent.

$$\Box_{\gamma Z}(E = 0) = 0.0052 \pm 0.0005 \tag{A.34}$$

A.4 Update on the $\Box_{\gamma Z}(E)$

The most upto date calculation on the $\Box_{\gamma Z}(E = 0)$ is found at [38] and the new $\Box_{\gamma Z}(E = 0)$ results is,

$$\Box_{\gamma Z}(E = 0) = 0.0044 \pm 0.0004 \tag{A.35}$$

To update the Q_W^p the old $\Box_{\gamma Z}(E = 0)$ results is removed and new value is added to it [38]. This is the most recent result of the Q_W^p.

$$\begin{aligned} Q_W^p &= 0.0713 \pm 0.0008 \ - 0.0052 \ + 0.0044 \\ &= 0.0705 \pm 0.0008 \end{aligned} \tag{A.36}$$

Appendix B: Tree-level Asymmetry Code

B.1 A Code to Calculate the Acceptance Corrected Tree-level Asymmetry

I have written a code to calculate the acceptance corrected tree-level asymmetry using raw asymmetry measured from the experiment. It is available in the Q_{weak} software repository.

```
svn --no-auth-cache --username [your JLab username] checkout
    https://qweaksvn.jlab.org/repos/QwAnalysis/trunk ~/QwAnalysis
```

After check out, the code can be found at
`Analysis_dir/Extensions/Macro/Parity/compute_LH2_asym.cc`.

B.2 A Code to Calculate the Weak Charge of the Proton

This code can compute the SM prediction of the PV asymmetry and the weak charge of the proton. The hadronic contribution is estimated using the Sachs form factors. References are given in the code to show where values and formula were taken.

I have written a code to calculate the SM prediction of the PV asymmetry and the weak charge of the proton. The hadronic contribution is estimated using the Sachs form factors. References are given in the code to show where values and formular werer taken. It is available in the Q_{weak} software repository.

```
svn --no-auth-cache --username [your JLab username] checkout
    https://qweaksvn.jlab.org/repos/QwAnalysis/trunk ~/QwAnalysis
```

After check out, the code can be found at
`Analysis_dir/Extensions/Macro/Parity/compute_SM_ep_asym.cc`.

Appendix C: DAQ and Software

C.1 Qweak Data Acquisition Framework

The layout of the integration (parity) Data Acquisition (DAQ) is shown in the Figure C.1 to introduce a CEBAF On-line Data Acquisition (CODA) based DAQ deployed over the network. Additional information about CODA based implementations can be found at the reference [127]

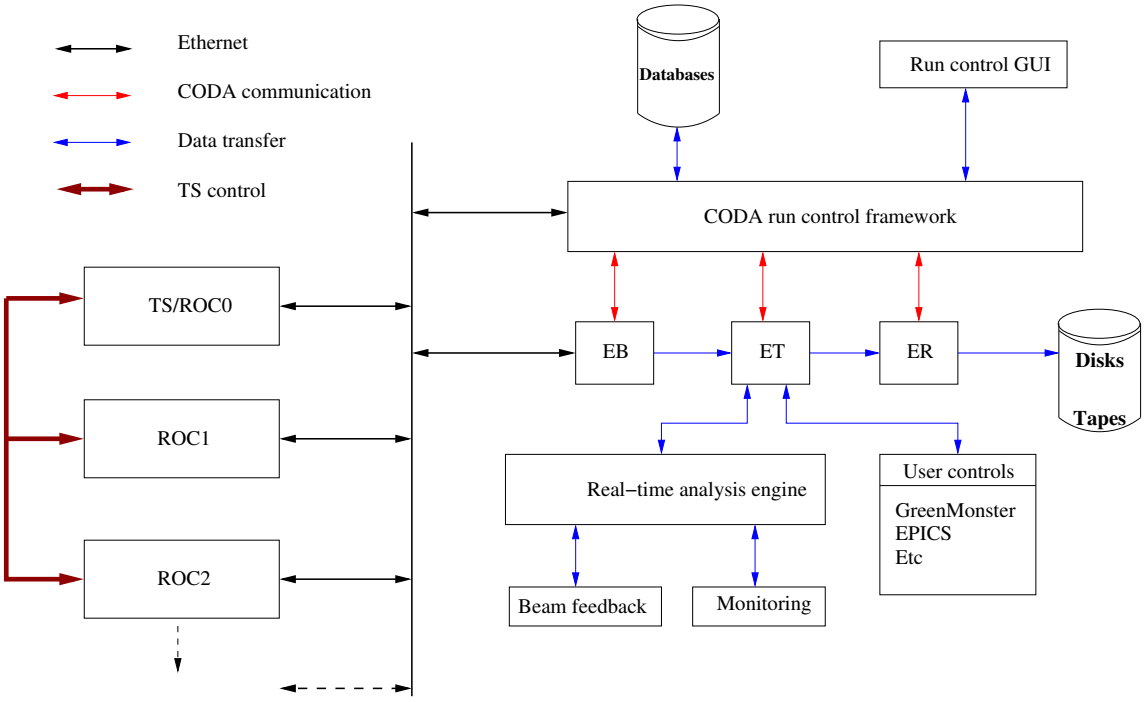

Figure C.1: The basic layout the Qweak The CODA system. This will be the layout for the Qweak integration mode and counting mode DAQ systems

A DAQ system reads data available at the front-end electronic modules based on a trigger signal. Then the system will prepare an event consisting of all the detector signals and trigger signals in a well defined structure. This procedure is then repeated for all the triggers the system receives. Any trigger signal originate directly from a detector is called a level-1 trigger. Higher trigger levels corresponds to more post-

processing done to constrain the physics events to be recorded. The Q_{weak} DAQ will be an extension of this system with many detectors and many level-1 triggers. In practice the DAQ takes finite time to read and process fragments of data to generates an event and store it. This introduces a dead time to the system. If the trigger interval is smaller than the DAQ process time, the system starts loosing triggers and hence value physics events. The processing time of the DAQ have to be smaller than trigger interval to keep the dead time at zero. Any successful experiment must reduce the DAQ dead time and design the DAQ system to loose minimum events of physics interest. The Figure C.2 has a simplified DAQ system to explain the basic DAQ. The Q_{weak} DAQ system has following essential components,

1. Front-end electronics modules
2. VERSAModule Eurocard (VME) Read-Out-Controller (ROC)s
3. Trigger Supervisor (TS)
4. Ethernet support
5. Linux/Unix based computer
6. CODA software framework
7. Software drivers/libraries for front-end electronics and ROCs

Front-end electronics modules are mounted to VME ROCs. The VME ROC is an electronic module with a single Central Processing Unit (CPU), an trigger interface module and many module slots to connect front-end modules that supports VME protocol, see Figure C.3. The ROC collects fragments of data from all the front-end modules based on the input trigger to the ROC and sends them over the Ethernet to

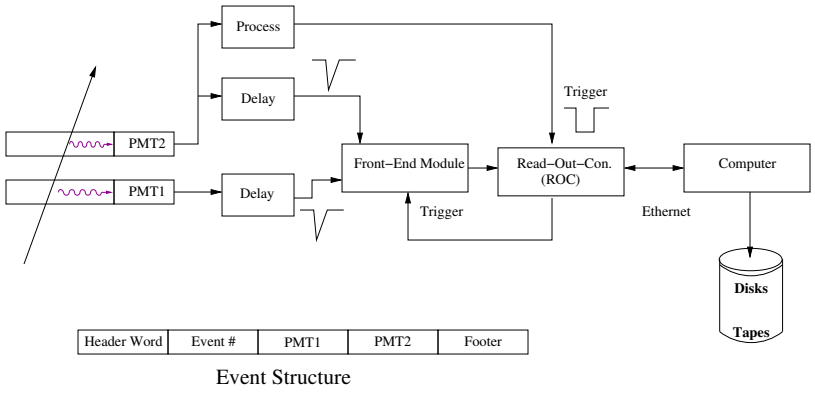

Figure C.2: Simple DAQ with single trigger, two detector signals and a read out system similar to the Qweak design. The event structure is what stored for each trigger. Each fragment in the this structure is a data word.

a central computer. The Q_{weak} experiment has implemented many ROCs and support multiple triggers to acquire data, therefore a special ROC called TS is dedicated to handle all the triggers and manage multiple ROCs. A dedicated connections between all the ROCs and TS provide the central control to the TS. All ROCs and front-end modules were programmed using VME software drivers/libraries developed in the Jefferson Lab (JLab) and provided by vendors.

The Qweak CODA framework provides modules to read, control, monitor and store data from the detectors. The ROCs host front-end electronics for detector signals. The Event Builder (EB) system to generate complete event from fragments of data read from ROCs. the Event Transfer (ET) system provides central access to data events for multiple clients at real-time. The application called the GreenMonster allows the users to add additional data useful for diagnostic purposes and, this application access the data through the ET system. The real time analysis engine accesses data from the ET system to provide charge feedback system and real time data monitoring system. Slow control parameters read through the Experimental

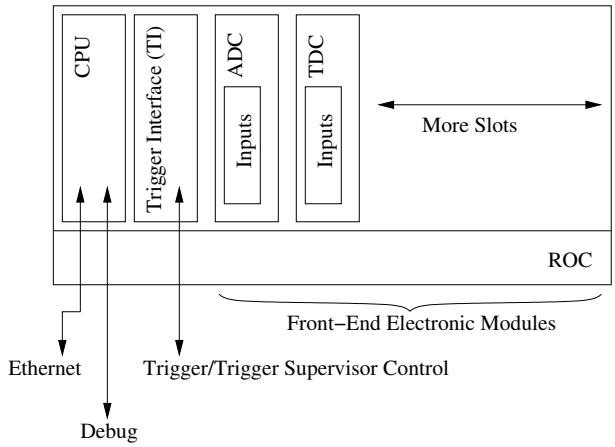

Figure C.3: A standard components of a ROC. The trigger interface handles trigger input or TS controls. The on board CPU comes in handy to handle many front-end module and data flow related processes. The debug is used to upgrade, reset firmware and driver software in the ROC.

Physics and Industrial Control System (EPICS) system are added to the event using the ET system. The Event Recorder (ER) system stores data into a local disk. The Q_{weak} DAQ framework is shown in the Figure C.1. The CODA run control framework controls the DAQ system. The ROCs are physical modules conveniently located at many place in the experiment setup and accessed through the Ethernet and rest of the components shown in the Figure C.1 are implemented on a Linux/Unix based computer. All the ROCs are connected to the TS using a dedicated connection to handle the triggering and the CODA run control framework can access them over the Ethernet to monitor the state of the system. The users can start, monitor the DAQ state, raw data state and stop data acquisition by interacting with the run control Graphical User Interface (GUI). A screen capture of the GUI is shown in the Figure C.4. The real-time access of the DAQ to real-time analyzer and the charge feedback is controlled using the analysis control tool GUI shown in the Figure C.5

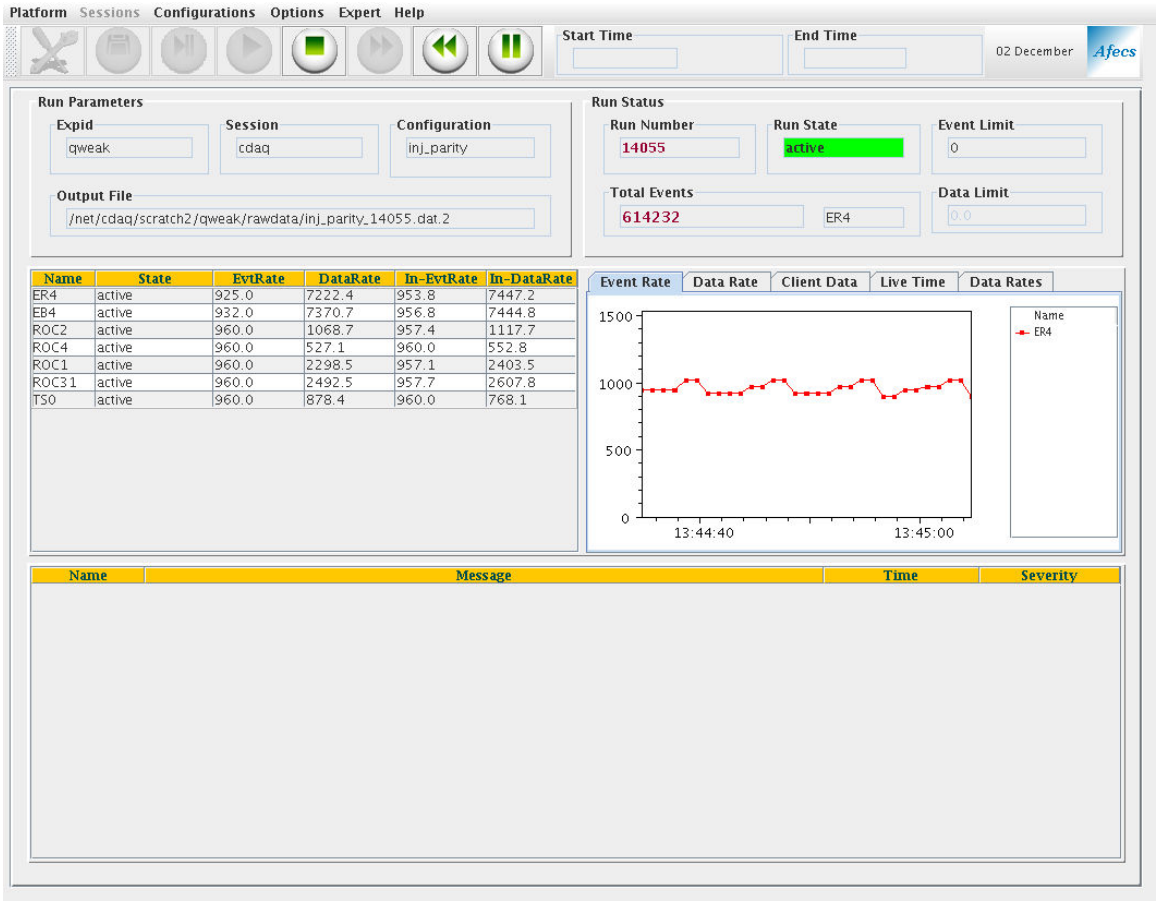

Figure C.4: The run control GUI when activated and taking data

C.1.1 Sub-bank Structure of CODA Data

In each physics event (see the Figure C.6), data are organized into ROC crates. Within each ROC, the different types of read-out electronic modules are grouped in to sub-banks. Each sub-bank contains headers and data words from read-out electronic channels. Data from multiple read-out modules are sequentially added under the sub-bank (Figure C.6). The complexity of the sub-bank structure depends on the read-out modules. Scalers are straight forward with each read-out channel only contains one data word and a header word is repeated to identify a scaler module. The VQWK modules have a complex sub bank structure with each channel containing

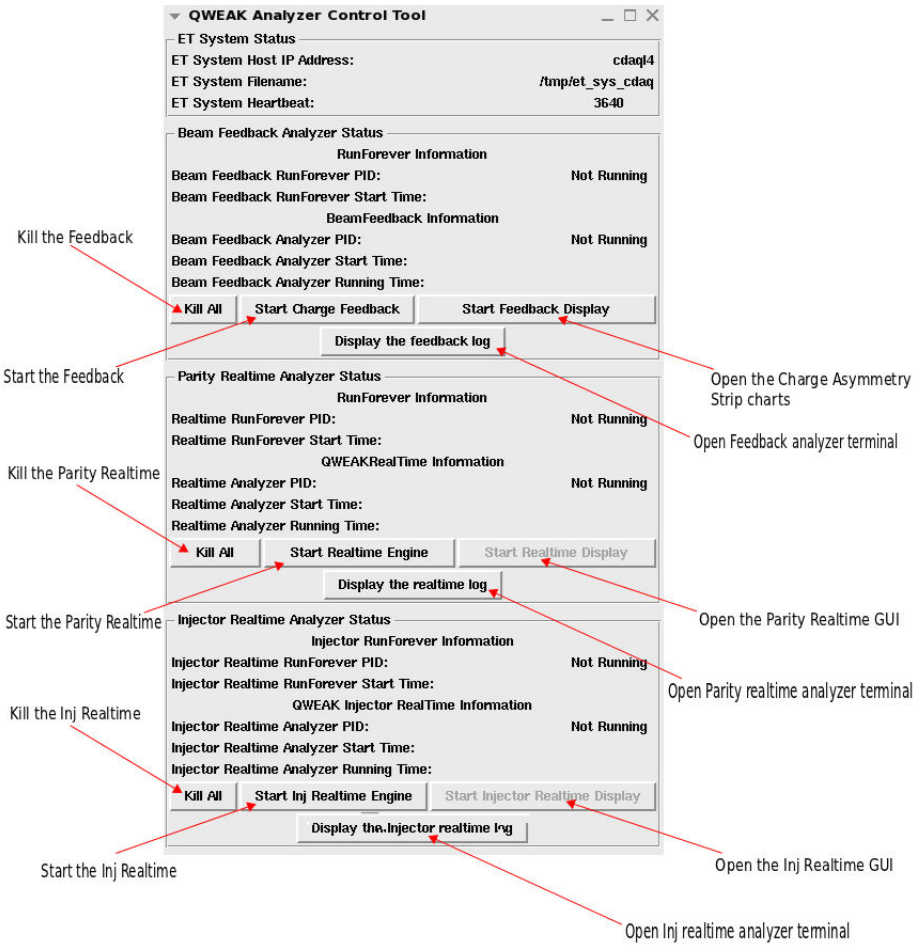

Figure C.5: The analysis control tool is used to monitor the real-time and charge feedback systems health

multiple data words and headers related to different configuration flags and etc.

C.2 Integration Mode Data Acquisition System

The measured scattered electron rate is about 800 MHz per main detector. A counting mode experiment would require sophisticated electronics to read at this rate with less dead time and achieve the statistical goal within the given beam time. Therefore the scattered electron rate is integrated over the helicity window to measure

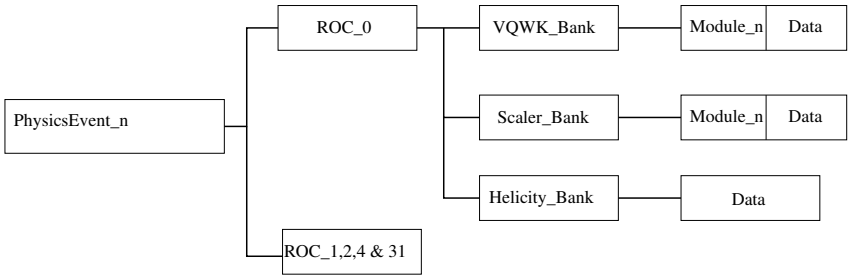

Figure C.6: The general CODA data structure where data are grouped by data bank (VQWK_Bank or scaler or etc.).

the flux. The integration mode requires less complicated DAQ systems. Basically the DAQ needs only single trigger to identify the helicity state and customized Analog to Digital Converter (ADC) called TRI-University Meson Facility (TRIUMF) ADC modules (front-end electronics module) to read out the detector yields. These ADC modules are introduces in the section C.2.1.

The Qweak integration mode DAQ aka Parity DAQ have to accommodate detector signals from eight main Čerenkov bars, background Čerenkov bars and photomultiplier tube (PMT) devices, two sets luminosity monitors and large number of beam line monitoring devices including manyBeam Charge Monitor (BCM) and Beam Position Monitor (BPM) devices. The Table C.1 has a summary of required front-end electronics channels, the Parity ADC must accommodate. The signals related to Helicity state are generated by the custom built Helicity control board that will eventually generate the trigger signal.

Note of Beam Monitor Read-out

The radio-frequency signals from BCMs and BPMs are down-converted to lower frequencies, filtered for better Signal to Noise ratio (S/N), and converted to DC voltage with ~ 25 KHz bandwidth to be digitized by custom 18 bit ADC, which

Table C.1: A summary of electronics channels the Parity DAQ needs to read out.

Detector System	Front-end Module	Required Channels
Main Čerenkov detectors	TRIUMF ADC	16
Background detectors	TRIUMF ADC	8
Luminosity detectors	TRIUMF ADC	16
Hall C Beam position monitors	TRIUMF ADC	94
Hall C Beam charge monitors	TRIUMF ADC	6
Injector Beam position monitors	TRIUMF ADC	84
Injector Beam charge monitors	TRIUMF ADC	1
Injector batteries	TRIUMF ADC	4
Injector QPD	TRIUMF ADC	4
Injector Phase monitor	TRIUMF ADC	1
Injector empty channel	TRIUMF ADC	2
Beam halo monitors	VME Scalers	8
Helicity signals	Flex IO	4
Other signals	VME Scalers	8
Required total:		
TRIUMF ADC	n/a	265
VME Scalers	n/a	8

samples at 500 KHz and integrates for 1/960 s period. Each BCM requires single ADC channel while a BPM requires four channels.

C.2.1 TRIUMF Qweak ADC module and Implementation

Some additional references related to VWQK modules are given below,

- See reference [128] for VQWK noise study.
- For VQWK board design and images, see reference [129]

- VQWK list of specification and noise tests see reference [75]

The VQWK input range is ± 10 V and frequency is band width limited to 50 KHz. Each VQWK has 18 bit ADC and the VQWK integrates 500 K ADC samples per sec. The DAQ read-out rate is 960 Hz. This gives an effective 27 bit precision on the mean value of the integrated signal over Macro Pulse Signal (MPS). Each 18 bit sample read by the ADC has a single bit error of $20\text{V}/2^{18} = \pm 76.29\ \mu\text{V}$. The sample size is determined using,

$$(\text{VQWK\_sample} \times 4 + \text{vqwkdelay} + 1.25) \times \text{st} = \text{T}_{\text{stable}} \tag{C.1}$$

where vqwkdelay = 20 is the no of samples to be skipped and will accommodate the internal processing requirements of the VQWK between MPS triggers. The 1.25 is an internal synchronization delay for a channel. The $\text{T}_{\text{stable}} = 972\ \mu$s and st = 2 μs is the VQWK sample period. This results in sample size, VQWK_sample = 463.5 but to makes it even, this is set to 464.

At MPS the VQWK can integrate 464 samples.

Error on the integrated signal per MPS is $76.29\ \mu\text{V}/\sqrt{464} = \pm 3.54\ \mu\text{V}$

Now in Q_{weak} we needed total of 34 vqwk modules each with 8 channels. In Roc 1: 13, ROC2: 8, ROC0: 1 and ROC31: 12 If each data word from a VQWK channel is read as 64 bit word, Then total data rate from VQWK channels,

$$64\ \text{bit} \times 8 \times\ 32 \times 960\ \text{s}^{-1} = 15728640\ \text{bits}^{-1} = 1.875\ \text{MB} \cdot \text{s}^{-1} \tag{C.2}$$

If all the scaler channels are added,

$$64\ \text{bit} \times 8 \times\ 40 \times 960\ \text{s}^{-1} = 19660800\ \text{bits}^{-1} = 2.34\ \text{MB} \cdot \text{s}^{-1} \tag{C.3}$$

add over-sampline from 4 sub-blocks,

$$64\ \text{bit} \times 8 \times\ (32 \times 5) \times 960\ \text{s}^{-1} = 78643200\ \text{bits}^{-1} = 9.375\ \text{MB} \cdot \text{s}^{-1} \tag{C.4}$$

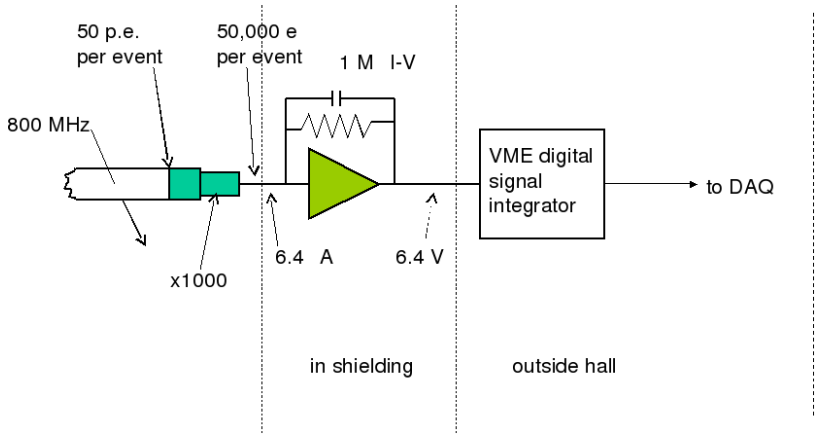

Figure C.7: The VQWK electronic diagram

from looking at raw data files, The parity DAQ produced data at about $7 - 8$ MBs^{-1} and reading each crate took about 600μs per event.

C.2.2 Parity DAQ Performance and Issues

One of the important factor of using an integration mode DAQ is to keep 0% dead time. The system have to process and distribute the trigger and read out front end modules from all the ROC within the integration period and ready to accept the next helicity trigger. This could get disrupted due to various factor to loose triggers. We have understood that following factors are the most contributors to the dead time,

- ROC under-performing due to memory issues in the CPU. Upgrading to latest model rectified the issue
- ROC communication with the CODA lags due to high traffic in the Ethernet. Running the CODA system on a dedicated computer resolved the issue.

The dead time is monitored real time to make sure the system missing physics event. Missing an single event throws away four consecutive events in the quartet pattern.

C.3 Counting Mode Data Acquisition System

The Qweak experiment includes a small percentage of beam time to measure the Q^2 to 0.5% accuracy at low beam counting mode by employing the tracking system. The tracking system will provide a map of light response of Cerenkov detectors, a sanity check on collimators and toroidal fields, and also a limited diagnostic on backgrounds and radiative corrections. This will involve triggering the DAQ read-out using various detector responses as the trigger sources that provide inputs to the Trigger Supervisor to generates the master trigger. Inputs to the Trigger Supervisor can be pre-scaled to produce acceptable trigger rates. The DAQ system accommodates multiple triggers from multiple detector signals (such triggers are called LeVel 1 (LV1) triggers). The end-user can select the triggers to record data and can set pre-scales on the triggers to reduce the trigger rate. This is required due to the limited capability of the DAQ to acquire data at large event rates increasing the dead time.

C.3.0.1 DAQ Dead-time: Naive Model

I have tried to built a simply DAQ dead-time model to find the event mode DAQ dead-time based on Time to Digital Converter (TDC) and scaler data [130].

In this module, the DAQ trigger is formed from the sum of two MD bar signals (see Figure C.8). The trigger rate, $\mathrm{R_{Trigger}}$ can be written as,

$$\mathrm{R_{Trigger}} = \frac{\mathrm{n_{Total\_Triggers}}}{\mathrm{T_{DAQ}}} \times \mathrm{prescale} \tag{C.5}$$

where the $\mathrm{n_{Total\_Triggers}}$ is the no.of MD bar triggers acquired by the DAQ, $\mathrm{T_{DAQ}}$ is the DAQ ON live time and prescale > 0 is set to adjust the read-out rate of the DAQ to 1-2KHz range. For the Neutral background studies, the DAQ was triggered by MD bar triggers from two octants. The Md bar rates are recorded by the scalers. The scaler

rates are independent of the DAQ dead-time and electronic dead-time corrections are easily applied to extract the true MD bar rates from scalers. Therefore the sum of actual MD rates from two octants can be written as,

$$R_{\text{true}} = R_{\text{sca\_true\_MD3}} + R_{\text{sca\_true\_MD7}} \tag{C.6}$$

where $R_{\text{sca\_true\_MD3}}$ and $R_{\text{sca\_true\_MD7}}$ are electronic dead-time corrected scaler rates for MD3 and MD7 respectively. If the DAQ dead-time is τ_{DAQ},

$$R_{\text{true}} = \frac{R_{\text{Trigger}}}{(1 - R_{\text{Trigger}} \times \tau_{\text{DAQ}})} \tag{C.7}$$

Since the parameters $n_{\text{Total\_Triggers}}$, T_{DAQ}, prescale, $R_{\text{sca\_true\_MD3}}$ and $R_{\text{sca\_true\_MD7}}$ are known for given MD triggered run, the τ_{DAQ} can be calculated.

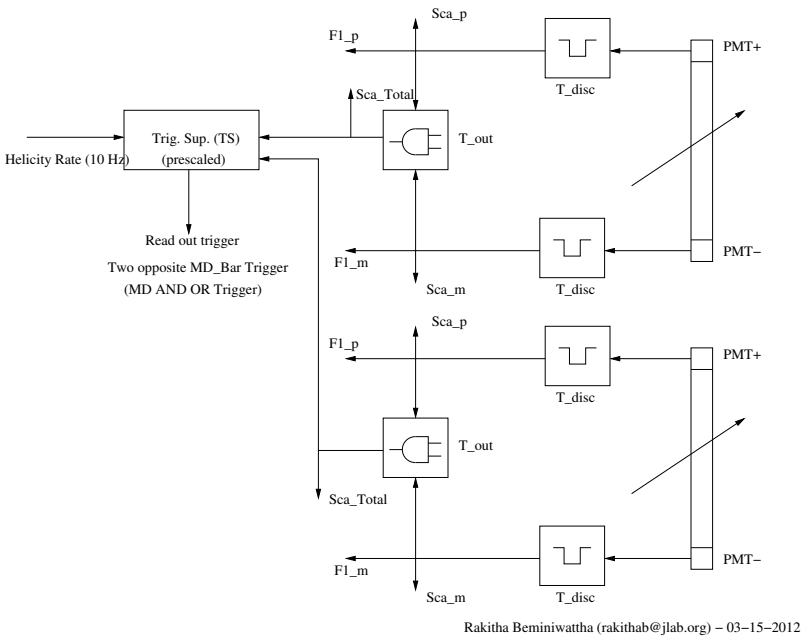

Figure C.8: A simple DAQ setup with multiple triggers and read-outs using scalers and TDC channels.

C.3.1 Trigger/DAQ Diagrams

Following diagrams are taken from [131]. The complete tracking trigger system is summarized in the FIG C.9. I have included event mode trigger diagrams for Trigger Scintillator (Region 3) (Figure C.10), Main detectors (Figure C.11), Quartz Scanner (Figure C.12) and Region 2 Scintillators (Figure C.13). These trigger diagrams were generated while they were setup in the Qweak cage. So they can be used as a guidance during any debugging sessions. The basic tracking trigger system is summarized into the trigger/DAQ diagrams for each detector system.

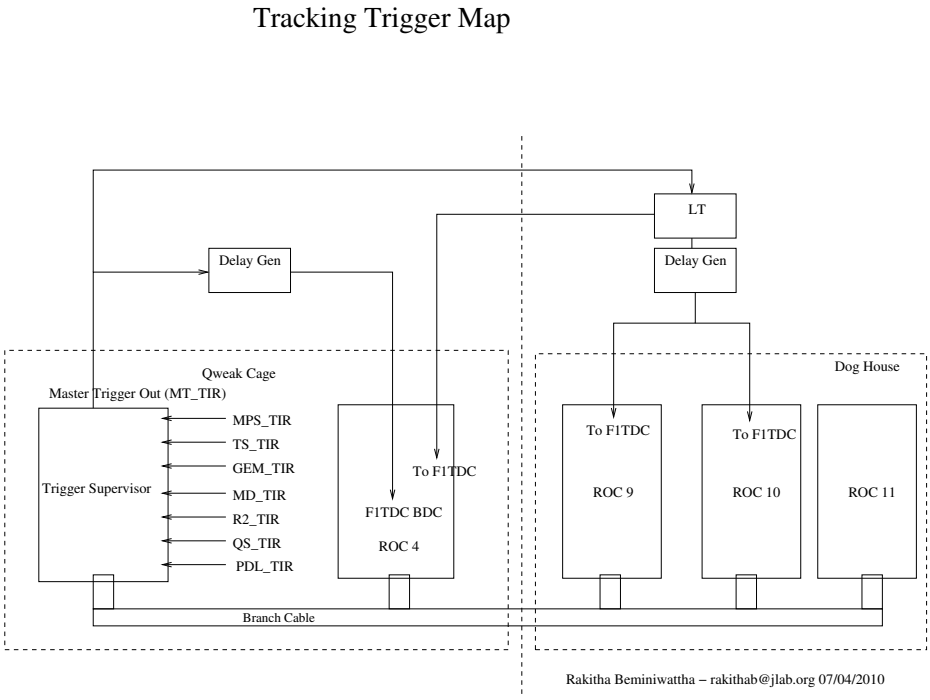

Figure C.9: Complete Qweak Tracking Trigger System

The layout of the Q_{weak} electronic cage is shown in the Figure C.14 and the layout of the Hall C dog house is shown in the Figure C.15

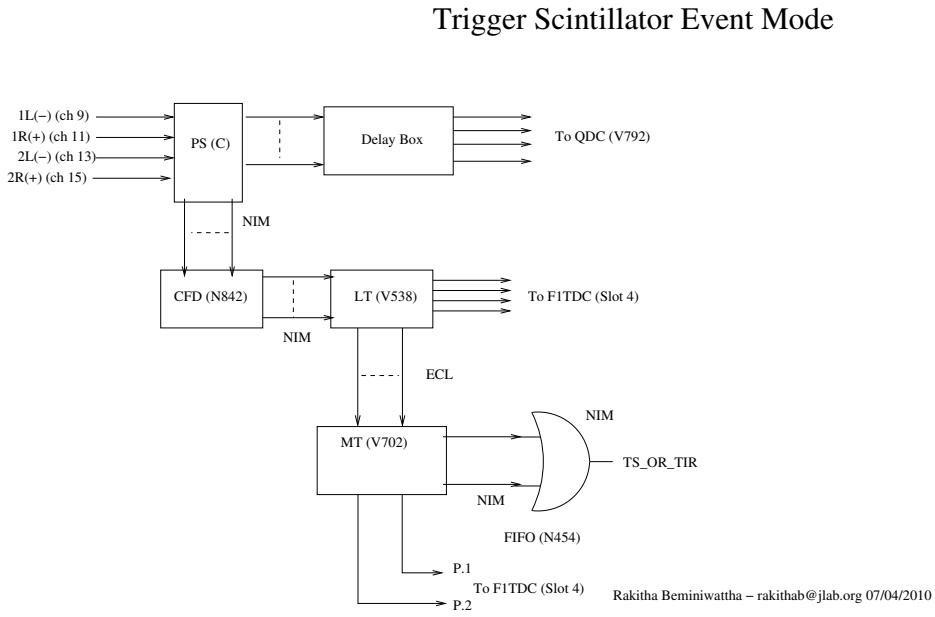

Figure C.10: Qweak trigger scintillator event mode trigger diagram

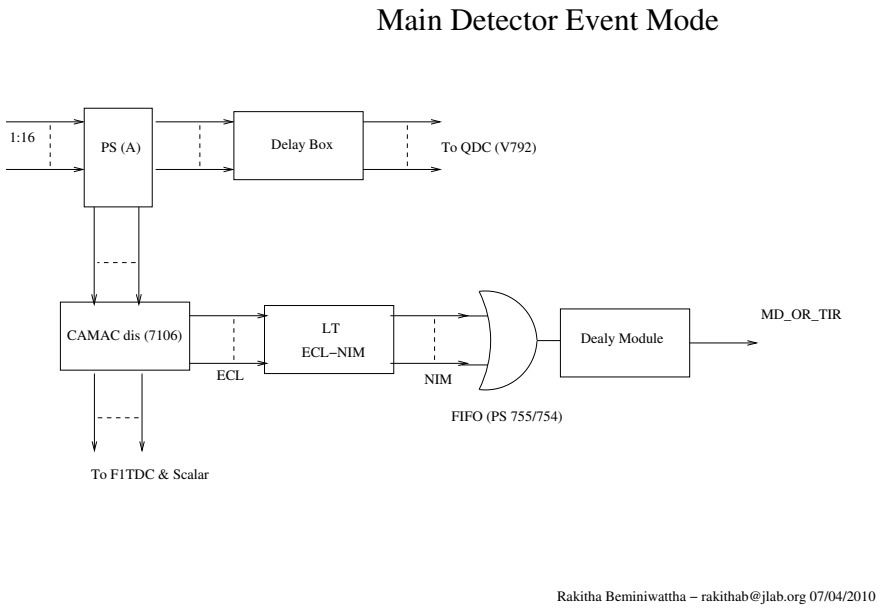

Figure C.11: Qweak main detector event mode trigger diagram

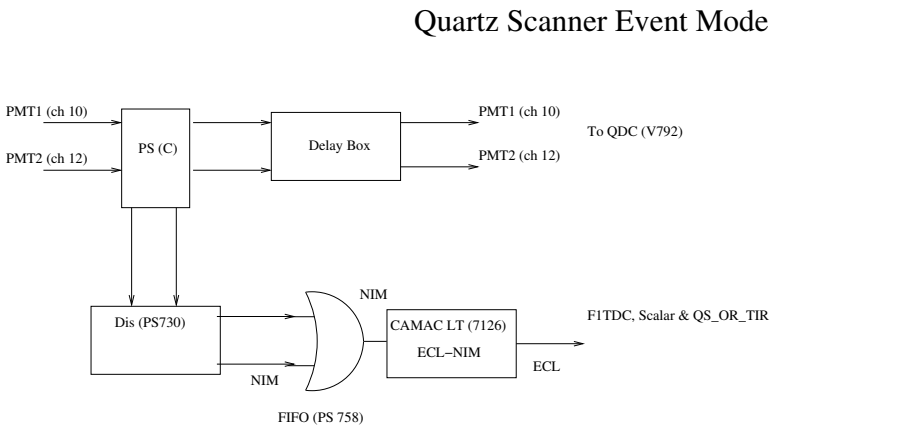

Figure C.12: Qweak scanner event mode trigger diagram

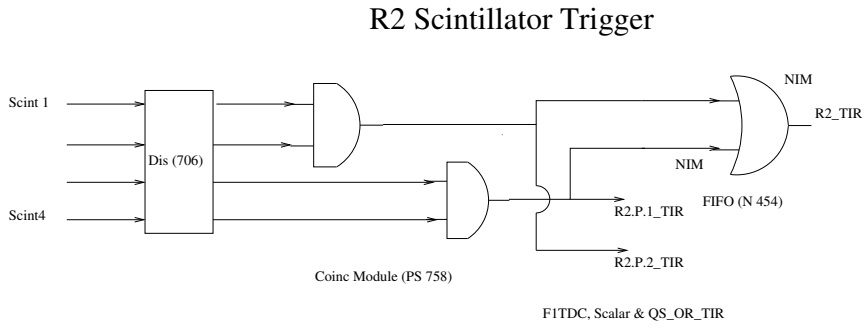

Figure C.13: Qweak R2 scintillator event mode trigger diagram

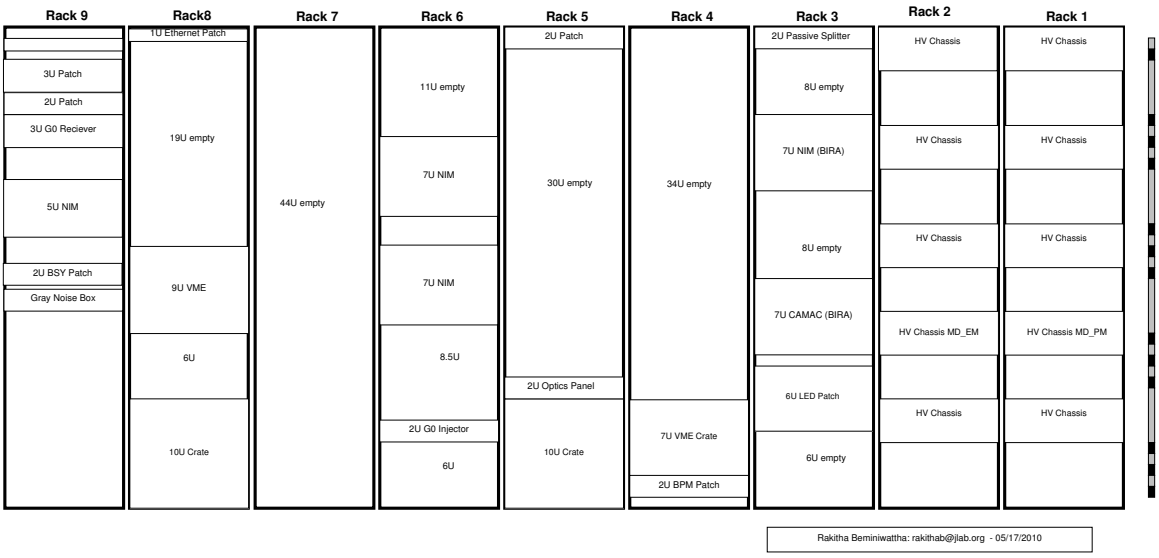

Figure C.14: The layout of the electronic modules in the Q_{weak} electronic cage

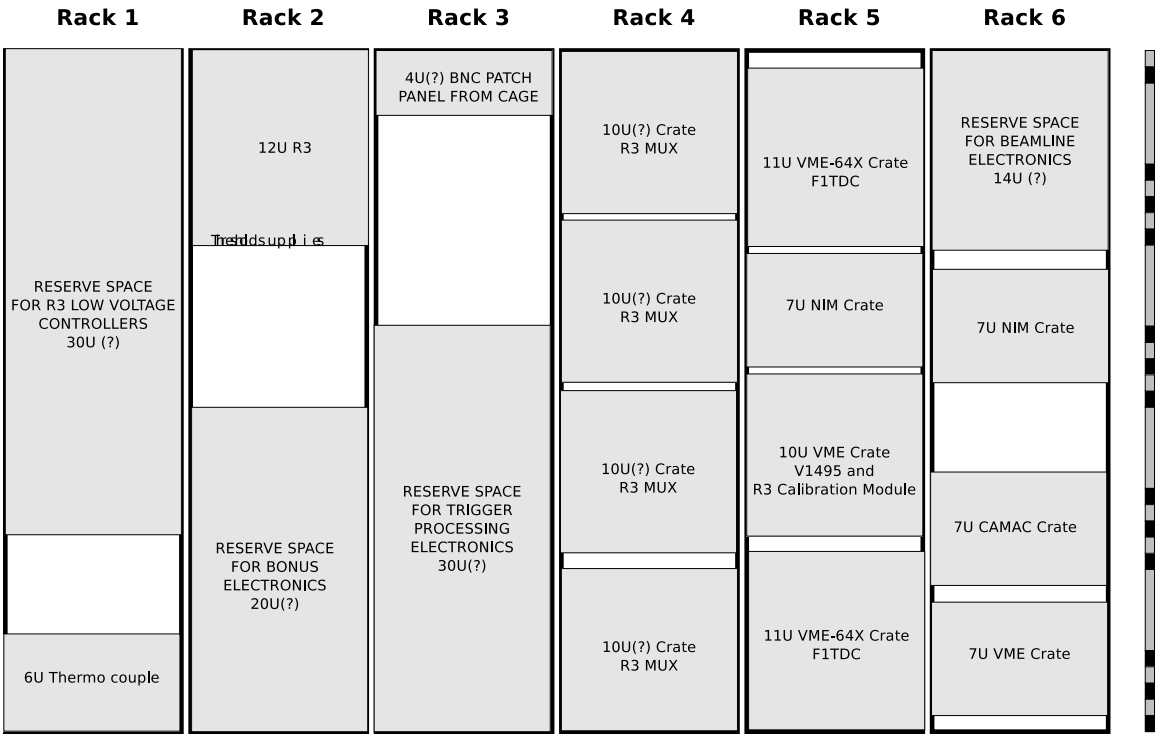

Figure C.15: The layout of the electronic modules in the hall C dog house

C.4 Data Analysis Framework

The Q_{weak} data analysis framework repository is available at https://qweaksvn.jlab.org/repos/QwAnalysis/ and can be checked out using,

```
svn --no-auth-cache --username [your JLab username] checkout
    https://qweaksvn.jlab.org/repos/QwAnalysis/trunk ~/QwAnalysis
```

C.4.1 Inter-Subsystem Communication

This enables to communicate with subsystems defined within a `QwSubsystemArray`. A subsystem class can successfully publish values that can be requested by any other subsystem. Under this mechanism any `VQWK_Channel` data elements (I have only implemented in the `QwBeamLine class`) can be successfully published and can be accessed from anywhere within the subsystem array. Currently, `QwMainCerenkovDetector` class is setup to properly request published variables. The detector quantities which included in the channel map file under "[PUBLISH]" are published

C.4.2 Q_{weak} Data Elements Summary

A list of detectors/monitors implemented for the parity subsystems is shown in the Figure C.18

C.5 Event Cut Framework: Addtional Details

The Table C.2 summarizes all the error codes used by the event cut framework.

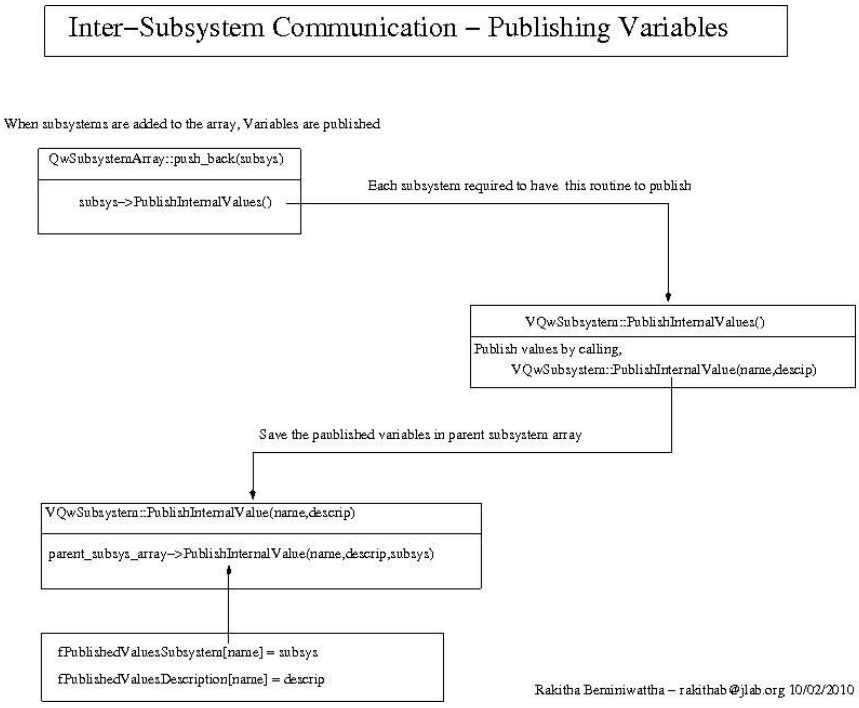

Figure C.16: Detector quantities are published from the subsystem

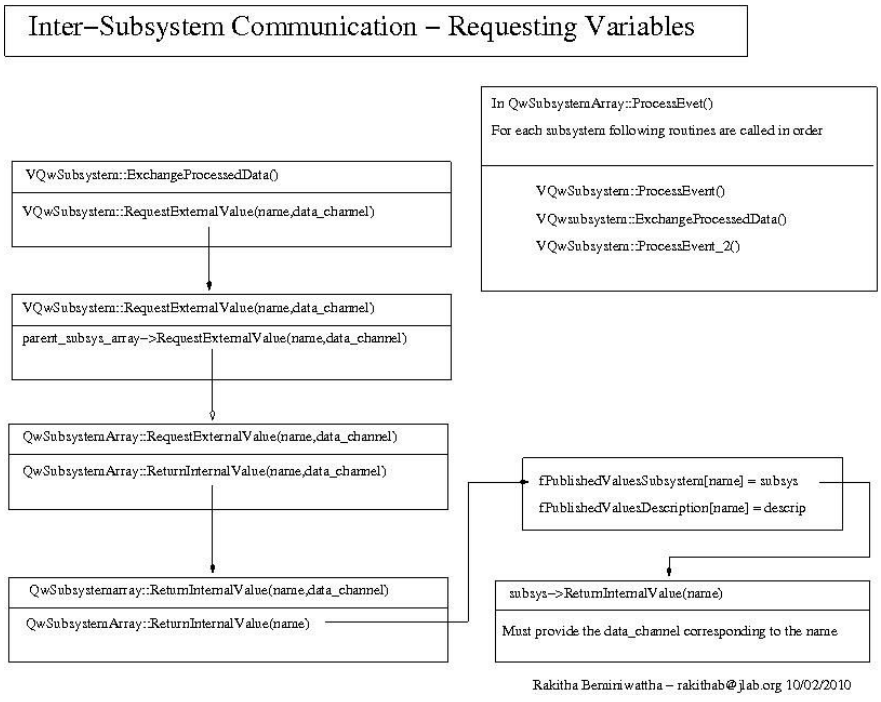

Figure C.17: Detector quantities are accessed by a subsystem

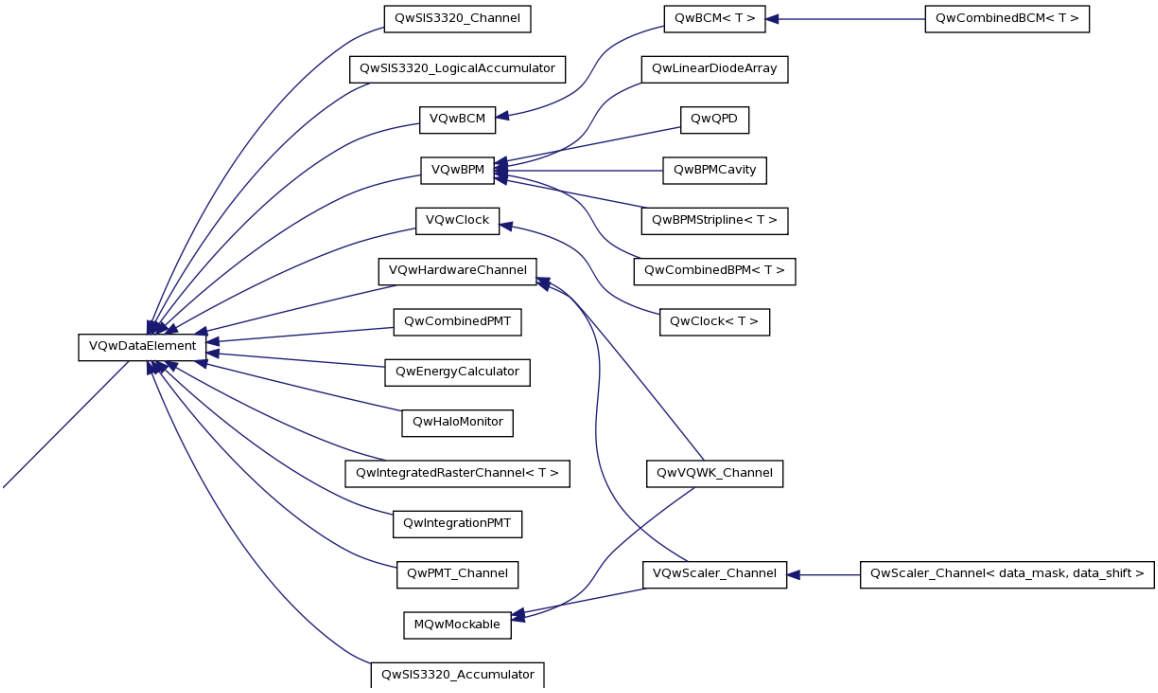

Figure C.18: The inheritance structure of the Q_{weak} data elements (scalers and VQWK) used in the parity subsystems

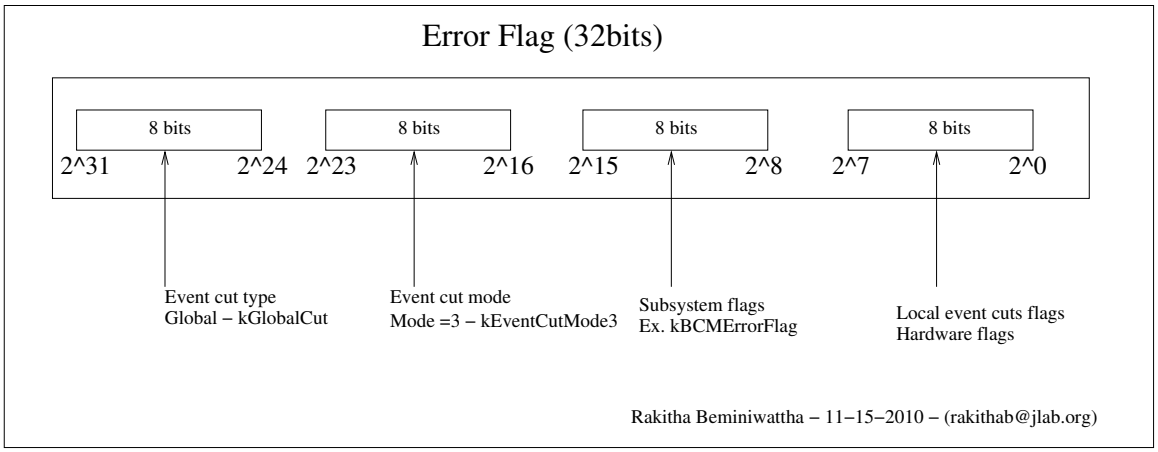

Figure C.19: The universal format of the error codes used in the analysis framework

Table C.2: Error Code Names and their Values

Name	Numerical value (HEX)	Type	Description
kErrorFlag_VQWK_Sat	0x01	Hardware error error (HW Error)	VQWK Saturation Cut. Currently saturation limit is set to ± 8.5 V
kErrorFlag_sample	0x02	HW Error	If sample size mis-matches with the default value in the map file.
kErrorFlag_SW_HW	0x04	Hardware error	If software sum and hardware sum are not equal.
kErrorFlag_Sequence	0x08	HW Error	If the ADC sequence number is not incrementing properly
kErrorFlag_SameHW	0x10	HW Error	If ADC value keep returning the same value
kErrorFlag_ZeroHW	0x20	HW Error	Check to see ADC is returning zero
kErrorFlag_EventCut_L	0x40	Single event cut error	Flagged if lower limit of the event cut has failed
kErrorFlag_EventCut_U	0x80	Single event cut error	Flagged if upper limit of the event cut has failed
kBCMErrorFlag	0x00100	Config. Error flag	Identify the single event cut is failed for a BCM (regular or combo)
kErrorFlag_BlinderFail	0x00200	Config. Error	Identify the blinder fail flag
kBPMErrorFlag	0x00400	Config. Error	Identify the single event cut is failed for a BPM (Stripline or cavity or comboBPM)
kPMTErrorFlag	0x00800	Config. Error	in Decimal 2018 to identify PMT based cuts
kBModFFBErrorFlag	0x01000	Config. Error	Identify the energy modulation pause period cut
kBModErrorFlag	0x08000	Config. Error	Identify the beam modulation cut
kEventCutMode3	0x10000	Config. Error	Identify the mode 3 where we only flag event cut failed events
kLocalCut	0x02000000	Config. Error	Identify the single event cut is a local cut
kGlobalCut	0x04000000	Config. Error	Identify the single event cut is a global cut
kStabilityCutError	0x10000000	Config. Error	Identify the stability cut failure

C.6 Active Charge Feedback System

The charge asymmetry,

$$A_{beam} = A_{feedback} + A_{false} + A_{stat} \tag{C.8}$$

where the $A_{feedback}$ is the feedback induces charge asymmetry, the A_{false} is the inherent charge asymmetry and the A^1_{stat} is the statistical jitter in the system.

$$A^1_{feedback} = 0 \tag{C.9}$$

and the active feedback relationship,

$$A^n_{feedback} = A^{n-1}_{feedback} + g \cdot A^{n-1}_{beam} \tag{C.10}$$

is used to correct the charge asymmetry in the feedback loop. We set the gain of the loop,$g = 1$ and assume A_{false} is constant. Equations C.11, C.12, C.13 C.14, C.15, C.16

$$A^1_{feedback} = 0 \tag{C.11}$$

$$A^2_{feedback} = A^1_{feedback} - A^1_{beam}$$
$$= A^1_{feedback} - A^1_{feedback} - A_{false} - A^1_{stat}$$
$$= -A_{false} - A^1_{stat} \tag{C.12}$$

$$\vdots$$

$$A^N_{feedback} = A^{N-1}_{feedback} - A^{N-1}_{beam}$$
$$= -A_{false} - A^N_{stat} \tag{C.13}$$

$$A^1_{beam} = A^1_{feedback} + A_{false} + A^1_{stat} \tag{C.14}$$

$$A^2_{beam} = A^2_{feedback} + A_{false} + A^2_{stat}$$
$$= -A_{false} - A^1_{stat} + A_{false} - A^2_{stat}$$
$$= -A^1_{stat} - A^2_{stat} \tag{C.15}$$

$$\vdots$$

$$A^N_{beam} = A^N_{feedback} + A_{false} + A^N_{stat}$$
$$= -A^{N-1}_{stat} - A^N_{stat} \tag{C.16}$$

$$\bar{\mathrm{A}} = \frac{1}{\mathrm{N}}\Sigma_{\mathrm{n}=1}^{\mathrm{N}} A_{beam}^{n} \tag{C.17}$$

$$= \frac{1}{\mathrm{N}}(\mathrm{A}_{\mathrm{beam}}^{1} + \mathrm{A}_{\mathrm{beam}}^{2} + \cdots + \mathrm{A}_{\mathrm{beam}}^{\mathrm{N}}) \tag{C.18}$$

$$= \frac{1}{\mathrm{N}}(\mathrm{A}_{\mathrm{false}} + \mathrm{A}_{\mathrm{stat}}^{1} + (-\mathrm{A}_{\mathrm{stat}}^{1} + \mathrm{A}_{\mathrm{stat}}^{2}) + \cdots + (-\mathrm{A}_{\mathrm{stat}}^{\mathrm{N}-1} + \mathrm{A}_{\mathrm{stat}}^{\mathrm{N}})) \tag{C.19}$$

$$\bar{\mathrm{A}} = \frac{1}{\mathrm{N}}(\mathrm{A}_{\mathrm{false}} + \mathrm{A}_{\mathrm{stat}}^{\mathrm{N}}) \tag{C.20}$$

$$\bar{\mathrm{A}} \propto \frac{1}{\mathrm{N}} \tag{C.21}$$

C.6.1 Set of PITA Slope Results

The Table C.3 summarizes all the PITA slopes used during the $\mathrm{Q}_{\mathrm{weak}}$ experiment.

Table C.3: Set of PITA slopes used for the charge feedback system

PITA Slope (ppm/dac-tick)				
IN	OUT	OUT_IN	Date applied	Reference
−0.73	+0.73		23 oct 2010	
−0.554	+0.554		Dec. 03, 2010	
+0.996	−0.996		Dec. 19. 2010	
+0.859	−0.859		Jan. 06, 2011	
+1.145	+1.145		Feb. 04, 2011	HCLog 218348
+0.7192	+0.775		Mar. 17, 2011	HCLog 224296
+0.979	+0.956		Apr. 07, 2011	HCLog 227091
+1.079	+0.870		Apr. 12, 2011	HCLog 227952
+0.834	+0.772		Apr. 23, 2011	HCLog 229730
+0.834	−0.96		Nov, 2011	
+0.551	−0.888	−0.888	Dec. 02, 2011	HCLog 241985
+0.808	−1.228	+0.600	Feb. 05, 2012	HCLOG 252279
+1.060	+0.530	+0.570	Feb. 15, 2012	Beam E-log 250

Appendix D: Asymmetry Analysis

This appendix will include additional details related to data analysis.

D.1 Statistical Shift Explained

The statistical shift of the central value when a subset of data is removed from a sample is used to study the non-statistical effects in normal asymmetry distributions (Figure D.1).

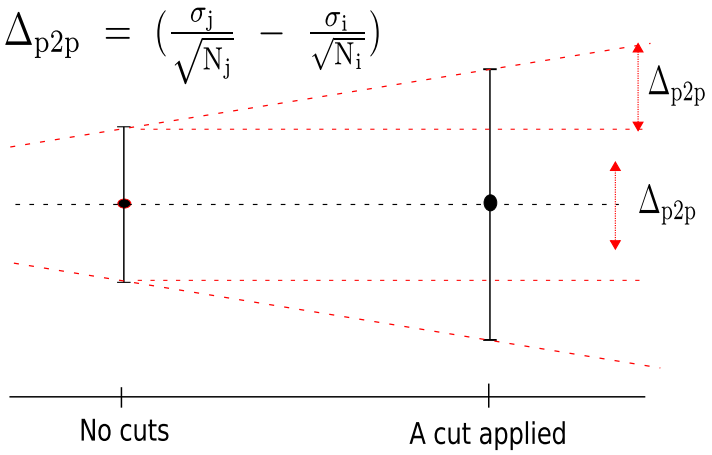

Figure D.1: The statistical fluctuation when a cut is applied to remove subset of data.

D.2 Main Detector Asymmetry Definitions: How and Why?

The total scattered rate from the Čerenkov detectors,

$$\begin{aligned} R^{L/R} &= L^{L/R} \int_{\Delta\Omega} \frac{d\sigma^{L/R}}{d\Omega} d\Omega \\ &= L^{L/R} \cdot \sigma^{L/R}(\Delta\Omega) \end{aligned} \tag{D.1}$$

where $L^{L/R}$ is the luminosity and $\frac{d\sigma^{L/R}}{d\Omega}$ is the differential cross section for L/R helicity states. The $L^{L/R} \propto I^{L/R}$. The parity violating asymmetry is measured between $\sigma^{L/R}(\Delta\Omega)$,

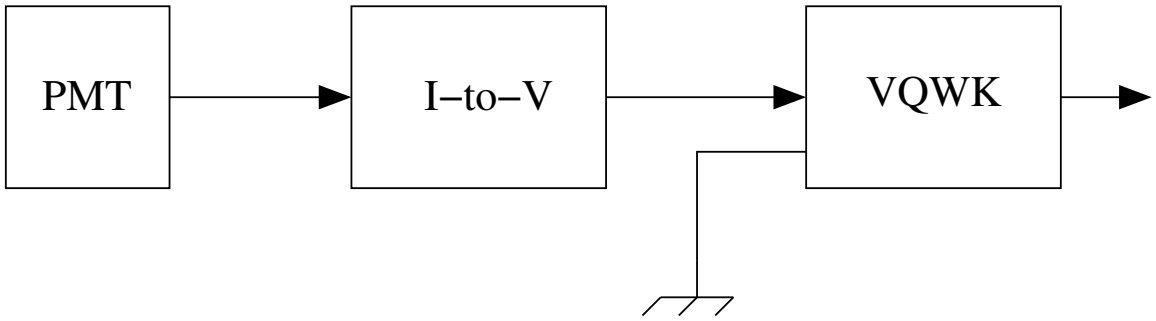

Figure D.2: Detector+Electronic chain up-to raw data for a PMT

$$A^{raw} = \frac{\sigma^{R}(\Delta\Omega) \ - \ \sigma^{L}(\Delta\Omega)}{\sigma^{R}(\Delta\Omega) \ + \ \sigma^{L}(\Delta\Omega)} \tag{D.2}$$

The measured PMT yield (see Figure D.2),

$$Y_{raw} = V_{det} \cdot N_{s} \tag{D.3}$$

where the V_{det} is proportional to the PMT current, T_{det} and N_s is the number of samples read out by the VQWK.

$$\begin{aligned} Y^{L/R} &= \frac{\frac{(Y^{L/R}_{raw} \ - \ Y_{ped}) \times g_{det}}{N_s}}{I^{L/R}_{beam}} \\ &\propto \sigma^{L/R}(\Delta\Omega) \end{aligned} \tag{D.4}$$

The normalized yield, $Y^{L/R}$, is a measure of the scattered cross section. Therefore, the parity violating asymmetry,

$$A^{raw} = \frac{Y^{R} \ - \ Y^{L}}{Y^{R} \ + \ Y^{L}} \tag{D.5}$$

D.3 Main Čerenkov Detector Asymmetry Schemes

The final experimental asymmetry can be computed using individual PMT asymmetries and PMT yield weighted asymmetry. For the simplicity the asymmetry

is compared for a single octant. The two PMT are named p and n in each octant detector. The weighted yield for an octant,

$$Y_{bar}^{L/R} = \frac{Y_p^{L/R} W_p + Y_n^{L/R} W_n}{W_p + W_n} \tag{D.6}$$

where $Y_{\pm}^{L/R}$ and W_{p}/n are p/n PMT yield and weight, respectively for L/R helicity states. The weights are defined as,

$$W_{p/n} = \frac{1}{< Y_{p/n} >} \tag{D.7}$$

where the $< Y_{p/n} >$ are the average MPS based PMT yields over time period of couple of hours. We can write the light yield for the ^{i}th track goes through the quartz bar,

$$\begin{aligned} Y_{p,i}^{R/L} &= g_p S_{track}^{R/L}(1 - \alpha x_i) \\ Y_{n,i}^{R/L} &= g_n S_{track}^{R/L}(1 - \alpha x_i) \end{aligned} \tag{D.8}$$

where $Y_{p/n,i}^{R/L}$ is the light generated by the i^{th} track on positive (p) and negative (n) PMTsn the R/L represents the heilicity of the track, α is linear attenuation coefficient, $S_{track}^{R/L}$ is the PMT signal for tracks incident at x_i=0 where x_i is the position of the incident track from the center of the bar, the $g_{p/n}$ is the PMT gain. We get N such tracks per R/L helicity states and the PMT yield per each helicity state can be derived,

$$\begin{aligned} Y_p^R &= g_p S^R(1 + \alpha\Delta^R) \\ Y_p^L &= g_p S^L(1 + \alpha\Delta^L) \\ Y_n^R &= g_n S^R(1 - \alpha\Delta^R) \\ Y_n^L &= g_n S^L(1 - \alpha\Delta^L) \end{aligned} \tag{D.9}$$

For the rest of the discussions lets assume (see Figure D.3),

$$\Delta^{R} = -\Delta^{L} = \Delta \tag{D.10}$$

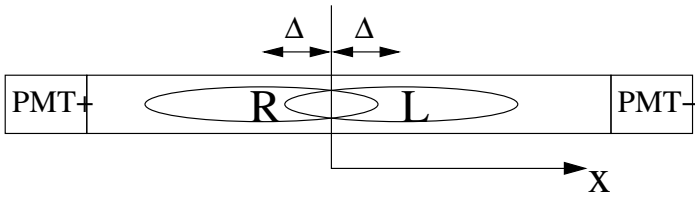

Figure D.3: The absolute shift of the beam envelope is defined parallel to the bar along the x-direction from the center (x = 0)

where Δ is the relative shift of the beam envelope parallel to the bar from the center for a given helicity state.

Yield based MD Bar Asymmetry

The MD bar yield is weighted by normalization factor to match the gains between PMTs and then the asymmetry is computed for the bar. The wieghted yield is defined as,

$$Y_{bar}^{R/L} = \frac{Y_{p}^{R/L}W_{p} + Y_{n}^{R/L}W_{n}}{W_{p} + W_{n}} \tag{D.11}$$

where the $Y_{p/n}^{R/L}$ are from the equation D.9, and the weights are,

$$W_{p} = \frac{1}{< Y_{p} >}$$
$$W_{n} = \frac{1}{< Y_{n} >} \tag{D.12}$$

then the yield weighted MD bar asymmetry can be write as,

$$A_{bar}^{yield} = \frac{(Y_{bar}^{R1} + Y_{bar}^{R2}) - (Y_{bar}^{L1} + Y_{bar}^{L2})}{(Y_{bar}^{R1} + Y_{bar}^{R2}) + (Y_{bar}^{L1} + Y_{bar}^{L2})} \tag{D.13}$$

where the asymmetry is computed from a quartet (QRT) (R1 L1 L2 R2 or L1 R1 R2 L2). Using equations D.9 and D.10, and the assumption of $< \Delta > = 0$ we can simplify the equation D.13 to,

$$A_{bar}^{yield} \simeq g_{pn} \cdot \alpha\Delta + A_S + (-\delta \cdot \alpha\Delta - (\delta \cdot \alpha\Delta)^2) \cdot A_S^2 + \cdots \tag{D.14}$$

where the symmetry breaking gain factor, δ is,

$$\delta = \frac{\frac{g_p}{< g_p >} - \frac{g_n}{< g_n >}}{\frac{g_p}{< g_p >} + \frac{g_n}{< g_n >}} \tag{D.15}$$

where one can assumed that $< g_p > \simeq < g_n >$. The ideal PMT asymmetry from $S^{R/L}$ is defined,

$$A_S = \frac{(S^{R1} + S^{R2}) - (S^{L1} + S^{L2})}{(S^{R1} + S^{R2}) + (S^{L1} + S^{L2})} \tag{D.16}$$

PMT Averaged MD Bar Asymmetry

We can calculate the average asymmetry of the left and right PMTs. First the left and right PMT asymmetries are calculated using equations D.9,

$$\begin{aligned} A_p &= \frac{(Y_p^{R1} + Y_p^{R2}) - (Y_p^{L1} + Y_p^{L2})}{(Y_p^{R1} + Y_p^{R2}) + (Y_p^{L1} + Y_p^{L2})} \\ A_n &= \frac{(Y_n^{R1} + Y_n^{R2}) - (Y_n^{L1} + Y_n^{L2})}{(Y_n^{R1} + Y_n^{R2}) + (Y_n^{L1} + Y_n^{L2})} \end{aligned} \tag{D.17}$$

and the averaged of A_L and A_R is the PMT averaged bar asymmetry,

$$A_{bar}^{pmt} = \frac{A_p + A_n}{2} \tag{D.18}$$

the equation D.18 can be simplified to,

$$A_{bar}^{pmt} \simeq A_S + \alpha\Delta \cdot A_S^2 + \cdots \tag{D.19}$$

D.4 Nonlinearities in the Main Čerenkov Detector Chain

Non-linearities exist in the BCM signal, main Čerenkov detector signal, and at the Q_{weak} target density.

$$\begin{aligned} I_{BCM} &= I(1 = \alpha \cdot I) \\ S &= c \cdot R(1 + \gamma \cdot I) \\ \rho_{tgt} &= \rho_o(1 + \beta \cdot I) \end{aligned} \tag{D.20}$$

where $\alpha,\ \beta$ and, γ are constants, I_{BCM} is the measured beam current, I is the actual beam current, S is the detector signal, c is a constant, $R \propto \rho_{tgt} I$ is the detected rate and putting all together to get the measured detector signal,

$$\begin{aligned} S &= c \cdot \rho_o \cdot I(1 + \beta \cdot I)(1 + \gamma \cdot I) \\ Y &= \frac{S}{I_{BCM}} \\ &= Y_o(1 + \gamma + \beta - \alpha)I \end{aligned} \tag{D.21}$$

The asymmetry computed using non-linear yield (equation D.21) generates a false asymmetry due to the non-linearity term $(\gamma + \beta - \alpha) \cdot I$,

$$A_{false}^{non-lin} = (\gamma + \beta - \alpha) \cdot I_o \cdot A_Q \tag{D.22}$$

where $I_o = \frac{I^R + I^L}{2}$ and charge asymmetry $A_Q = \frac{I^R - I^L}{I^R + I^L}$. If the average charge asymmetry is non-zero, then there is a false asymmetry contribution due to non-linearities in the main Čerenkov yield (equation D.21),

$$< A_{false}^{non-lin} >= (\gamma + \beta - \alpha) \cdot I_o \cdot < A_Q > \tag{D.23}$$

D.5 List of Wien-0 Runlets

Follow the e-log 651 made by Katherine Myers

D.6 Individual Contributions to Final Asymmetry

Let,

$$R_{Other} = R_{RC} \times R_{Det} \times R_{Acc}$$

$$A_{Tree} = R_{Other} \times \frac{\{\frac{A_{msr}}{P_e} - f_{b1} \cdot A_{b1} - f_{b2} \cdot A_{b2} - f_{b3} \cdot A_{b3} - f_{b4} \cdot A_{b4}\}}{(1 - f_{Other})}$$

$$A_{Tree} = A_{msr} + \Delta A_{P_e} + \Delta A_{b1} + \Delta A_{b2} + \Delta A_{b3} + \Delta A_{b4} + \Delta A_{R_{Other}} \tag{D.24}$$

Individual Corrections

$$\Delta A_{P_e} = \frac{R_{Other}}{(1 - f_{Total})}\{\frac{A_{msr}}{P_e} - A_{msr}\} \tag{D.25}$$

$$\Delta A_{b_1} = -1 \cdot \frac{R_{Other}}{(1 - f_{Total})}\{f_{b_1} \cdot A_{b_1}\} \tag{D.26}$$

$$\Delta A_{R_{Other}} = \frac{R_{Other} \cdot A_{msr}}{(1 - f_{Total})} - A_{msr} \tag{D.27}$$

D.7 Beam-line Asymmetry Estimation

The beamline background asymmetry is assumed to be the measured asymmetry on the main Čerenkov detectors in octant 1 and 5 (MD1 and MD5) during the blocked-octant runs. The measured MD1 and MD5 combined asymmetry during a blocked-octant period (run 18849) [132],

$$A_{MD\_1\_5\_blocked} = 94 \pm 5 \text{ ppm} \tag{D.28}$$

The measured beam-line background dilution [133] (and [119]), $f_{b3} = 0.00193 \pm 0.00064$. Then the contribution to the measured asymmetry due to beam-line background asymmetry is,

$$\begin{aligned} f_{b3} \cdot A_{b3} &= 0.00193 \times A_{MD\_1\_5\_blocked} \\ &= 0.00193 \pm 0.00064 \times 94 \pm 5 \text{ ppm} \end{aligned} \tag{D.29}$$

The background detector, MD9, signal is also diluted due to the blocked octants and it's dilution,

$$f_{MD9} = \frac{\text{blocked\_yield}}{\text{unblocked\_yield}} = 0.094 \tag{D.30}$$

Now using the MD9 dilution measurement the beam-line background can be related to the measured asymmetry from the unblocked MD9.

$$A_M D\_9\_\text{unblocked} = f_{MD9} \cdot A_{MD\_9\_blocked} \tag{D.31}$$

and

$$\begin{aligned} f_{b3} \cdot A_{b3} &= 0.00193 \times A_{MD\_1\_5\_blocked} \times \frac{A_{MD\_9\_unblocked}}{A_{MD\_9\_unblocked}} \\ &= 0.00193 \times A_{MD\_1\_5\_blocked} \times \frac{A_{MD\_9\_unblocked}}{f_{MD9} \cdot A_{MD\_9\_blocked}} \\ &= 0.044 \times A_{MD\_9\_unblocked} \equiv 0.044 \times A_{MD\_9} \end{aligned} \tag{D.32}$$

The equation D.32 relates the beam-line background asymmetry to unblocked background detector, MD9. Now to relate the MD9 and US luminosity monitor asymmetries,

$$\frac{A_{MD\_9}}{A_{US\_LUMI}} = 0.21 \tag{D.33}$$

using the equations D.32 and D.33 the beam-line background asymmetry is related to the US luminosity monitor asymmetry and this is used to compute the beam-line background asymmetry during Wien0 data set.

$$f_{b3} \cdot A_{b3} = 0.0092 \times A_{US\_LUMI} \tag{D.34}$$

Note that the background corrections are done after the beam polarization is corrected. Therefore the beam-line asymmetry estimated from the above analysis is multiplied by the factor, $1/P_e = 1/0.8895$ [132].

D.8 Light-yield weighting effects on A_{RC}^{sim} and $< Q^2 >_{RC}^{sim}$

In the experiment we can not measure the $< Q^2 >^{exp}$ for each asymmetry measurements due to the integrating of all the electron tracks to measure the yield. In tracking mode we can measure,

- Detector un-bias $< Q^2 >^{exp}$: $< Q^2 >_{unbiased}^{exp}$
- Detector bias $< Q^2 >^{exp}$: $< Q^2 >_{biased}^{exp}$

and in simulations we can measure,

- Detector un-biased:$A_{unbiased}^{sim}$ and $< Q^2 >_{unbiased}^{sim}$
- Detector biased: A_{biased}^{sim} and $< Q^2 >_{biased}^{sim}$

If the assumption, $A \propto Q^2$ is valid, then

$$\frac{A_{no\_bias}^{sim}}{A_{bias}^{sim}} \simeq \frac{< Q^2 >_{no\_bias}^{sim}}{< Q^2 >_{bias}^{sim}} \tag{D.35}$$

and if the simulation program is properly benchmarked then experimentally measured and simulated results should agree each other (equation D.36). This is verified in an analysis [134], [122].

$$\frac{< \mathrm{Q}^2 >^{\mathrm{exp}}_{\mathrm{no\_bias}}}{< \mathrm{Q}^2 >^{\mathrm{exp}}_{\mathrm{bias}}} \simeq \frac{< \mathrm{Q}^2 >^{\mathrm{sim}}_{\mathrm{no\_bias}}}{< \mathrm{Q}^2 >^{\mathrm{sim}}_{\mathrm{bias}}} \tag{D.36}$$

but the simulation results have shown that [122],

$$\frac{\mathrm{A}^{\mathrm{sim}}_{\mathrm{no\_bias}}}{\mathrm{A}^{\mathrm{sim}}_{\mathrm{bias}}} > \frac{< \mathrm{Q}^2 >^{\mathrm{sim}}_{\mathrm{no\_bias}}}{< \mathrm{Q}^2 >^{\mathrm{sim}}_{\mathrm{bias}}} \tag{D.37}$$

This discrepancy has not yet been resolved and therefore the $\delta \mathrm{Q}^2$ is applied to $\mathrm{R}_{\mathrm{Det}}$ as a correction.

$$\delta \mathrm{Q}^2 = \frac{\frac{\mathrm{Q}^{2\mathrm{data}}_{\mathrm{nobias}}}{\mathrm{Q}^{2\mathrm{sim}}_{\mathrm{nobias}}}}{\frac{\mathrm{Q}^{2\mathrm{data}}_{\mathrm{bias}}}{\mathrm{Q}^{2\mathrm{sim}}_{\mathrm{bias}}}} \tag{D.38}$$

The $\delta \mathrm{Q}^2$ is applied to $\mathrm{R}_{\mathrm{Det}}$ as an additional correction,

Appendix E: A Text Summary Output

I have developed a script to summarize a text output for runs taken during Q_{weak} experiment. It is available in the Q_{weak} software repository.

```
svn --no-auth-cache --username [your JLab username] checkout
    https://qweaksvn.jlab.org/repos/QwAnalysis/trunk ~/QwAnalysis
```

After check out, the code can be found at

`Analysis_dir/Extensions/Macro/Parity/QwPromptSummary.cc`

Text summaries were saved in http://qweak.jlab.org/textsummaries/. A sample output from this script is given below,

```
======= BEGIN =======

        RUN = 13873

Root file on which this analysis based =

/home/cdaq/qweak/QwScratch/rootfiles/QwPass1_13873.000.histos.root

/home/cdaq/qweak/QwScratch/rootfiles/QwPass1_13873.001.histos.root

/home/cdaq/qweak/QwScratch/rootfiles/QwPass1_13873.002.histos.root

/home/cdaq/qweak/QwScratch/rootfiles/QwPass1_13873.003.histos.root

/home/cdaq/qweak/QwScratch/rootfiles/QwPass1_13873.004.histos.root

/home/cdaq/qweak/QwScratch/rootfiles/QwPass1_13873.005.histos.root

/home/cdaq/qweak/QwScratch/rootfiles/QwPass1_13873.006.histos.root

/home/cdaq/qweak/QwScratch/rootfiles/QwPass1_13873.007.histos.root

/home/cdaq/qweak/QwScratch/rootfiles/QwPass1_13873.008.histos.root

/home/cdaq/qweak/QwScratch/rootfiles/QwPass1_13873.009.histos.root

/home/cdaq/qweak/QwScratch/rootfiles/QwPass1_13873.010.histos.root

/home/cdaq/qweak/QwScratch/rootfiles/QwPass1_13873.011.histos.root

================================================================================
```

```
ANALYSIS CHECKS :
-----------------
number of good quartets in this run = 735934
based on this number the run lasted = 49.1 minutes

based on this total charge accumulated = 439.1 mC
================================================================================
BEAM PARAMETERS
---------------
 Beam Properties at the Target
--------------------------------------------------------------------------------
      quantity |      value |               Asym/Diff | Asym/Diff width
      ........ | (uA,mm,mrad) |         (ppm,nm,murad) | (ppm,nm,murad)
        charge |     149.15 |       +0.29 +/-    0.62 |     +533.24
      target x |      0.153 |     +27.808 +/-  22.863 |  +19603.991
      target y |     -1.392 |     -22.907 +/-  15.658 |  +13426.368
       angle x |     -0.301 |      +0.001 +/-   0.001 |      +0.497
       angle y |     -0.403 |      -0.000 +/-   0.001 |      +0.475
 Note: Angles are in radians while angle differences are still presented
    in gradient differences
  Energy (dP/P) |     -0.001 |      +0.000 +/-   0.000 |      +0.000
================================================================================
MAIN DETECTOR PARAMETERS
------------------------
      quantity |      value |                    asym |    asym width
      ........ |     (V/uA) |                   (ppm) |    (ppm)
           MD1 |      0.035 |      -0.397 +/-   0.815 |    +682.681
```

```
          MD2 |       0.033 |      -1.155 +/-   0.816 |    +683.384
          MD3 |       0.029 |      -1.727 +/-   0.828 |    +693.710
          MD4 |       0.029 |      +0.910 +/-   0.846 |    +708.431
          MD5 |       0.039 |      +0.973 +/-   0.851 |    +712.462
          MD6 |       0.034 |      -0.213 +/-   0.832 |    +696.966
          MD7 |       0.033 |      -0.765 +/-   0.813 |    +681.333
          MD8 |       0.041 |      +0.023 +/-   0.816 |    +683.377
   MD_AllBars |       0.034 |      -0.386 +/-   0.331 |    +277.060
  MD_EvenBars |       0.034 |      -0.196 +/-   0.438 |    +367.219
   MD_OddBars |       0.034 |      -0.654 +/-   0.440 |    +368.296
 ======== END of SUMMARY========
Expert mode is ON.
======== END ========
Please contact Rakitha Beminiwattha for any queries and suggestions
rakithab@jlab.org
```

Thesis and Dissertation Services